Beyond the Standard Model searches with b-jets and hadronically decaying τ-leptons with the ATLAS detector

Adam Jackson Parker

Department Of Physics

Lancaster University

Declaration

I declare that the work in this thesis is my own, except where clearly stated in the text, and that no portion of this work has been submitted for consideration for any other degree.

<div align="right">

Adam Jackson Parker

August 2018

</div>

Acknowledgements

Abstract

This thesis describes the search for resonant and non-resonant Higgs boson pair production in the $b\bar{b}\tau^+\tau^-$ decay channel. The main focus of this document is on the final state where both τ-leptons decay hadronically. The search is performed using 36.1 fb^{-1} of data collected by the ATLAS detector in proton-proton collisions at a centre-of-mass energy of 13 TeV during 2015 and 2016. The cross-section for non-resonant di-Higgs production is found to be 16.4 times the Standard Model prediction in the fully hadronic channel at a 95% confidence level. Combining the result with the semi-leptonic channel produces a measured signal strength of $\mu = 12.7$ at a 95% confidence level when compared to the Standard Model prediction.

Resonant Higgs boson pair production excludes bulk Randall-Sundrum gravitons G_{KK} in the mass range 325 GeV $< m_{G_{KK}} <$ 885 GeV for $k/\overline{M}_{PL} = 1$. For the simplified hMSSM minimal supersymmetric model for $\tan\beta = 2$, resonances are excluded in the mass range 305 GeV $< m_H <$ 402 GeV.

Finally, a re-interpretation of the Higgs boson pair production analysis is presented as a search for third-generation scalar leptoquarks. Pair-produced third-generation scalar leptoquarks decaying to $b\tau b\tau$ are excluded at 95% confidence level for $m_{LQ} <$ 1030 GeV.

Contents

Chapter 1

Introduction

The discovery of the Standard Model Higgs boson at the Large Hadron Collider in 2012 [1, 2] by the ATLAS [3] and CMS [4] experiments was a huge success for particle physics. A new generation of physics quickly followed focusing on the measurement of the Higgs boson properties. The discovery prompted many searches for physics beyond the Standard Model and continues to drive a large amount of research currently taking place at the Large Hadron Collider and future experiments.

The main topic of this thesis is a search for resonant and non-resonant Higgs boson pair production in the $b\bar{b}\tau^+\tau^-$ final state in pp collisions at $\sqrt{s} = 13$ TeV with the ATLAS detector. The search addressed here focuses primarily on the fully hadronic channel, but also presents a full combination with the semi-leptonic analysis. The resonant search concentrates on theories predicting the decay to two Standard Model Higgs bosons, such as a spin-2 Kaluza-Klein (KK) graviton in the bulk Randall-Sundrum (RS) model [5] and a heavy spin-0 scalar in the two Higgs doublet model (2HDM) [6]. Whereas the non-resonant search aims to test the electroweak symmetry breaking of the Standard Model by establishing the strength of the Higgs boson tri-linear self-coupling (λ_{hhh}). Deviations from the Standard Model could introduce new physics through modifications to the top Yukawa coupling and/or λ_{hhh}.

Various methods are used throughout this analysis to boost the sensitivity to a di-Higgs signal such as: boosted decision tree multivariate techniques, statistical evaluation and data-driven background estimators. The $b\bar{b}\tau\tau$ channel suffers from a large multi-jet background that reproduces the signature of two hadronically decaying τ-leptons. This thesis describes a data-driven multi-jet background estimation using an ABCD method as an alternative to Monte Carlo predictions for this background.

The interest in searches for di-Higgs production has recently grown in both the theory sector and collider experiments. The di-Higgs analysis outlined in this thesis has presented results at ICHEP 2018 and has been submitted to Physics Review Letters. A search for di-Higgs production in the $b\bar{b}\tau\tau$ channel was previously completed by ATLAS using data collected in 2012 with a centre-of-mass energy of $\sqrt{s} = 8$ TeV. The analysis set upper limits on the cross-section for non-resonant di-Higgs production of 160 times the SM prediction (1.6 pb) using 20.3 fb^{-1} and set limits on the production cross-section for resonances within a mass range 260 GeV $< m_X < 1$ TeV. However, only the semileptonic channel was considered [7]. A combination of the $bbbb$ [8], $bb\gamma\gamma$ [9] and $WW\gamma\gamma$ [7] channels by the ATLAS experiment yielded an upper limit on the non-resonant di-Higgs production of 70 times the SM prediction (0.67 pb). The CMS experiment has also performed a search for resonant and non-resonant di-Higgs production in the $b\bar{b}\tau\tau$ mode at $\sqrt{s} = 13$ TeV with 35.9 fb^{-1} [10]. Non-resonant di-Higgs production was excluded for cross-sections greater than 28 times the SM prediction.

The most sensitive result to date for non-resonant Higgs boson pair production comes from the ATLAS search in the $b\bar{b}b\bar{b}$ channel, the observed (expected) limit excludes a cross-section greater than 13.0 (20.7) times the SM prediction at 95% confidence level.

Additionally, this document briefly presents a search for pair production of scalar leptoquarks [11–17] decaying to $b\tau$ at $\sqrt{s} = 13$ TeV with the ATLAS detector. The di-Higgs analysis is re-interpreted to become sensitive to decays from resonant third-generation leptoquarks. The strategy for both analyses is very similar and they share many techniques but any differences are cleared stated in the relevant analysis chapters.

ATLAS has already excluded leptoquarks decaying to bτbτ final states below masses of 534 GeV using 4.7 fb^{-1} collected at $\sqrt{s} = 7$ TeV [18]. CMS has also performed a search for pair-produced leptoquarks decaying to bτbτ, excluding them below 740 GeV using 19.7 fb^{-1} collected at $= 8$ TeV [19].

The structure of this thesis is as follows. Chapter 2 describes the theoretical background of the Standard Model and the relevant theory and motivation for the di-Higgs and leptoquark analyses. Details of the CERN accelerator complex are provided in Chapter 3 along with

specifics of the ATLAS detector. Object reconstruction for the ATLAS experiment is described in Chapter 4 before discussing a τ-lepton vertex study in Chapter 5. The study was performed in 2015 as an ATLAS authorship task and aimed to improve current τ-lepton vertex association.

The common analysis strategy for the two analyses discussed is described in Chapter 6, including preselection, multivariate techniques, statistical analysis and systematics. Chapter 7 outlines in detail the ABCD method for the data-driven multi-jet estimation and the results of the di-Higgs and leptoquark analyses are presented in Chapters 8 and 9, respectively. Finally, Chapter 10 summarises the thesis and provides any concluding remarks. Any additional material is given in the Appendices.

The author joined the experimental particle physics group at Lancaster University in 2014 and shortly after became a member of the ATLAS collaboration. Throughout the PhD qualification, the author has been a main contributor to the $hh \rightarrow b\bar{b}\tau\tau$ analysis group during Run 2 of the LHC and has also helped towards the operation of the ATLAS experiment. The author was a part of the Run 2 di-Higgs analysis for its entirety and contributed mostly to the fully hadronic decay channel. Overseeing the cut-based analysis was the initial focus before becoming a more integral part of the recently released Run 2 result published in Physics Review Letters [20]. Many of the authors significant contributions are documented within this thesis.

The vertex association study for tau-jet reconstruction set out in Chapter 5 was performed by the author and implemented in the upcoming ATLAS software release. The algorithm and performance plots are documented in an ATLAS public note [21]. The di-Higgs analysis was originally a cut-based analysis and unblinded data in late 2015. However, the result was never published and the analysis moved to multivariate techniques. It is not documented here but the author was one of the few involved in the cut-based result and made significant contributions to the running of the analysis and helped produce final limits. During the multivariate di-Higgs analysis presented, the author was responsible for the running of the fully hadronic channel analysis framework and producing input files and histograms for the final statistical evaluation and limit setting. The analysis strategy outlined in Chapter 6 was implemented in the MIA analysis framework before histograms in the relevant signal and control regions are filled and background modelling studies were performed. The boosted decision tree (BDT) classifiers were introduced to MIA and the author provided BDT score distributions to other members of the group for limit setting. The Run 2 Higgs boson pair production result is presented in Chapter 8.

The main contribution of the author was to develop a data-driven multi-jet background estimation. The technique was based on a fake factor method and was optimised to include momentum information from both τ-leptons. The method and relevant systematics are outlined in Chapter 7. The data-driven multi-jet background estimation was used in the final di-Higgs result and was later re-optimised for the third-dimension scalar leptoquark analysis presented in Chapter 9. The scalar leptoquark result is currently being combined with other analyses and hopes to publish soon [22].

The author made substantial contributions to other areas throughout the four years of PhD study but they could not be presented in this document. These include: making significant efforts to develop the CxAOD derivation framework and the MIA analysis framework, maintenance of the framework trigger tool and performing numerous additional studies needed for the data-driven multi-jet background estimation.

Chapter 2

Theory

This Chapter describes the theoretical framework of particle physics in brief, known as the Standard Model, in Section 2.1. Theory for the behaviour of subatomic particles is presented, in addition to the Higgs boson and the mechanism responsible for mass generation in Section 2.1.1. Finally, a summarised overview of theoretical interpretations beyond the Standard Model is outlined for di-Higgs production and third-generation scalar leptoquarks in Section 2.2.1, two analyses addressed throughout this thesis.

2.1 The Standard Model of Particle Physics

The Standard Model (SM) [23–31] is currently the most successful theory in describing how fundamental particles behave and the interactions acting between them. The SM has been praised for its ability to not only propose the existence of previously unknown matter but also predict their associated properties.

However, the SM does not currently account for unexplained phenomena such as: neutrino oscillations, gravitational interaction and matter-antimatter asymmetry of the known universe. Despite this, the SM provides a powerful description of the world around us.

The known matter in the universe is made up of *quarks* and *leptons*. These half-integer spin elementary particles are known as *fermions*; interactions between fermions are mediated by integer spin particles called *bosons*. The strong, electromagnetic and weak interactions are mediated by spin one vector bosons in the SM. The massless gluon and massless photon govern the strong and electromagnetic forces, respectively, while the massive Z and $W^{\pm}$ bosons mediate the weak interaction.

The gravitational interaction currently has no place in the Standard Model but is not expected to greatly contribute due to its weaker nature. The strength of the gravitational force is measured to be orders of magnitude lower than the other forces, in particular it can be roughly 40 orders smaller than the strong nuclear force experienced at collider energies today.

The Standard Model is described by a non-abelian gauge theory based on the product of the groups $SU(3)_C \otimes SU(2)_L \otimes U(1)_Y$. The non-abelian $SU(3)_C$ group describes the strong interactions between quarks and gluons formerly known as Quantum Chromodynamics (QCD). The electroweak sector and the hypercharge sector are governed by $SU(2)_L \otimes U(1)_Y$ respectively.
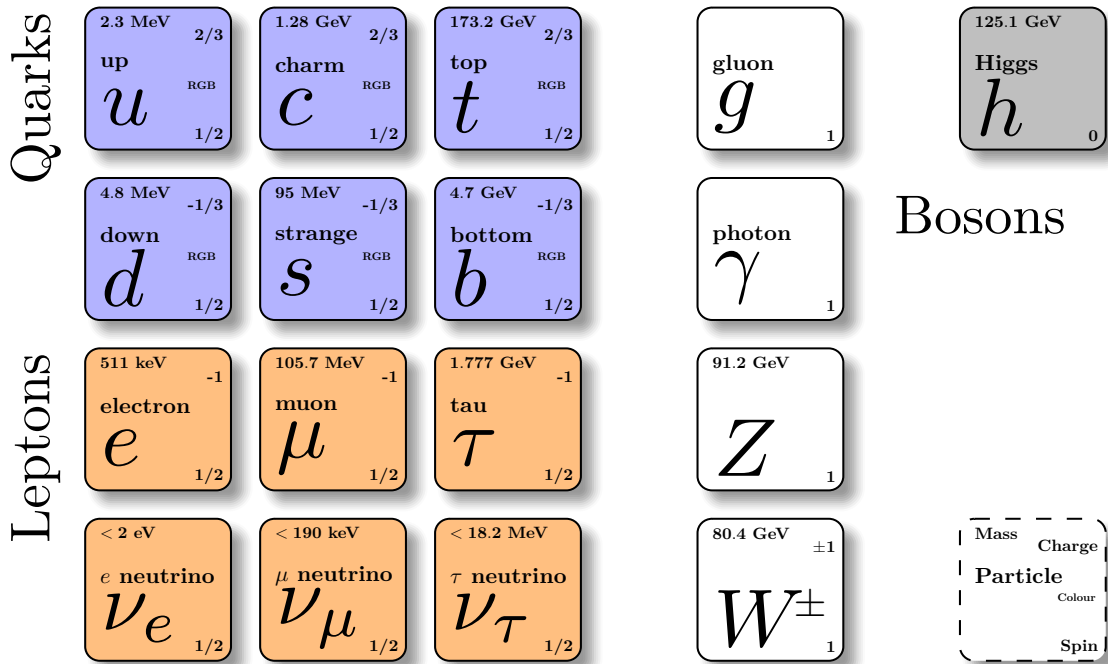
Figure 2.1: A simplified illustration of the Standard Model's fundamental particles, showing the spin, charge and mass of each. The quarks, shown in blue, and the gluon also carry colour charge. Values are taken from [32].

The fermionic content of the SM is arranged into three generations and consists of six quarks and six leptons. Each fermion has its own anti-particle according to relativistic quantum mechanics. SM particle content and fundamental properties are shown in Figure 2.1.

Quantum Chromodynamics is the description of the strong interaction between quarks and gluons described by the non-abelian $SU(3)_C$ *colour* symmetry group. The simplest respresentation of the theory allows for the families of quarks for each flavour, $N_c = 3$, along with $(N_c^2 - 1) = 8$ massless gluons all carrying colour charge. The theory proposes when gluons, mediating the strong force, interact with quarks they rotate the quark's colour in $SU(3)$ space through the orthogonal colour states of QCD.
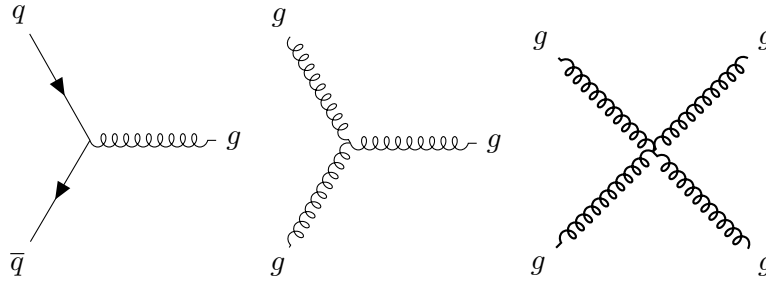
Figure 2.2: The Feynman diagrams for leading order QCD interactions

Due to the non-abelian nature of QCD, the eight massless gluons carry colour charge unlike the neutral photon in the similarly charged environment of QED. The fact the gluons carry a colour charge allows them to couple to each other and produce multiple-gluon interaction vertices shown in Figure 2.2. The gluon self-interaction in QCD has interesting consequences on the strong coupling constant dependence, α_s, to the momentum scale, Q^2, of the interaction. The running coupling of α_s leads to *asymptotic freedom* when $Q^2 \gg 1$ GeV; $\alpha_s(Q^2)$ is small at short distances so quarks and gluons are weakly coupled and can be described almost as free particles. Therefore, perturbative theory can be used in production calculations at high energy colliders. Furthermore, large $\alpha_s(Q^2)$ at large distances (small Q^2 values) leads to *colour confinement* where quarks and gluons can only exist as colour-singlet (colour-neutral) bound states known as mesons or baryons.

Electroweak (EW) theory unifies the $SU(2)_L$ weak isospin symmetry with the $U(1)_Y$ group from weak hypercharge. The violation of parity conservation in the $SU(2)_L$ gauge group implies that the weak isospin current couples only to left-handed fermions where the spin projection onto the particles momentum is negative. Neutral currents conserve lepton flavour, whereas the charged currents change the flavour of left-handed fermion fields.

The electroweak (EW) gauge symmetry group $SU(2)_L \otimes U(1)_Y$ is associated with weak hypercharge, Y^W and the weak analogue of isospin, weak isospin, T. The electric charge Q can be expressed as the sum of the weak hypercharge and the third component of the weak isospin: $Q = (T^3 + \frac{1}{2}Y^W)$. The full family of fermions in the electroweak sector are shown in Table 2.1.

Fermion	Electric Charge Q	Weak Hypercharge Y^W	Weak Isospin T^3
ν_L^l	0	-1	$+\frac{1}{2}$
l_L^-	-1	-1	$-\frac{1}{2}$
l_R^-	-1	-2	0
u_L, c_L, t_L	$+\frac{2}{3}$	$+\frac{1}{3}$	$+\frac{1}{2}$
d_L, s_L, b_L	$-\frac{1}{3}$	$+\frac{1}{3}$	$-\frac{1}{2}$
u_R, c_R, t_R	$+\frac{2}{3}$	$+\frac{4}{3}$	0
d_R, s_R, b_R	$-\frac{1}{3}$	$-\frac{2}{3}$	0

Table 2.1: The full family of fermions in the electroweak sector with their corresponding values of weak isospin and weak hypercharge.

The theory requires the existence of four massless mediating particles to carry the unified EW interaction. However, the existence of massive EW mediators is suggested by the apparent short range of the weak interaction. For this to be the case, there must be a breaking of the underlying $SU(2)_L \otimes U(1)_Y$ symmetry that gives rise to the masses of the $W^\pm$ and Z vector bosons but also omits the massless photon.

Between 1964-1965, the idea of symmetry breaking was implemented by Kibble, Guralnik and Hagen [33], Brout and Englert [34] and Higgs [35, 36] to give what is now known as the Brout-Englert-Higgs (BEH) mechanism. The theory was later applied in 1967 by Weinberg [24] and Salam [37] to the original $SU(2)_L \otimes U(1)_Y$ EW gauge theory introduced by Glashow. The ATLAS and CMS collaborations reported the discovery of a new particle in 2012 [38, 39] which seems consistent with the associated spin-0 Higgs boson of the BEH mechanism.

2.1.1 Brout-Englert-Higgs Mechanism and Spontaneous Symmetry Breaking

The Brout-Englert-Higgs mechanism introduces spontaneous symmetry breaking of the $SU(2)_L \otimes U(1)_Y$ symmetry group through the addition of a complex scalar field, ϕ, which takes the form of a self-interacting $SU(2)$ doublet in the SM.

Introducing a scalar field doublet with a weak hypercharge $Y = \frac{1}{2}$ relative to $U(1)_Y$

$$\phi = \begin{pmatrix} \phi^+ \\ \phi^0 \end{pmatrix} = \begin{pmatrix} \phi_1 + i\phi_2 \\ \phi_3 + i\phi_4 \end{pmatrix}, \tag{2.1}$$

where ϕ_3 and ϕ_4 are the CP-even and CP-odd neutral components and ϕ^+ is the complex charged component of the Higgs doublet. The scalar Higgs part of the Lagrangian now takes the form

$$\mathcal{L}_{Higgs} = (D^\mu \phi)^\dagger (D_\mu \phi) - V(\phi). \tag{2.2}$$

The covariant derivative of ϕ, in this case

$$D_\mu \phi = \left(\partial_\mu + \frac{i}{2} g \sigma^a W_\mu^a + \frac{i}{2} g' B_\mu \right) \phi, \tag{2.3}$$

where W^a and B represent the $SU(2)_L$ and $U(1)_Y$ gauge fields, respectively, with their gauge couplings g and g'. The Pauli matrices are given by σ^a ($a = 1,2,3$).

To maintain $SU(2)_L \otimes U(1)_Y$ invariance, the Higgs potential $V(\phi)$ must take the form of the most general renormalisable scalar potential with constants $\lambda, \mu \in \mathbb{R}$ given by

$$V(\phi) = -\mu^2 \phi^\dagger \phi + \lambda \left(\phi^\dagger \phi \right)^2. \tag{2.4}$$

The values of μ and λ have consequences on the configuration of the potential.

– A negative value for λ leads to $V(\phi)$ having no stable minima;

– values of $-\mu^2\phi^\dagger\phi$, $\lambda > 0$ gives a potential well with minimum energy at $\phi = 0$, preserving the symmetries of the Lagrangian.

– The case where $-\mu^2$ is negative and λ is positive results in the interesting potential where the minimum energy does not sit at $\phi = 0$.

The Higgs potential does not have a minimum at $\phi = 0$ and produces the so-called *Mexican hat* potential shown in Figure 2.3. The neutral component of the scalar field acquires a nonzero vacuum expectation value (VEV), v, for the ground state which induces the spontaneous symmetry breaking of the SM gauge symmetry. Note that there are an infinite number of degenerate states with minimum energy satisfying the Higgs potential; the convention is arbitrarily choosing the ground state to be

$$\langle\phi\rangle = \frac{1}{\sqrt{2}} \begin{pmatrix} 0 \\ v \end{pmatrix} \qquad \text{with} \qquad v = \sqrt{\frac{-\mu^2}{\lambda}}. \tag{2.5}$$
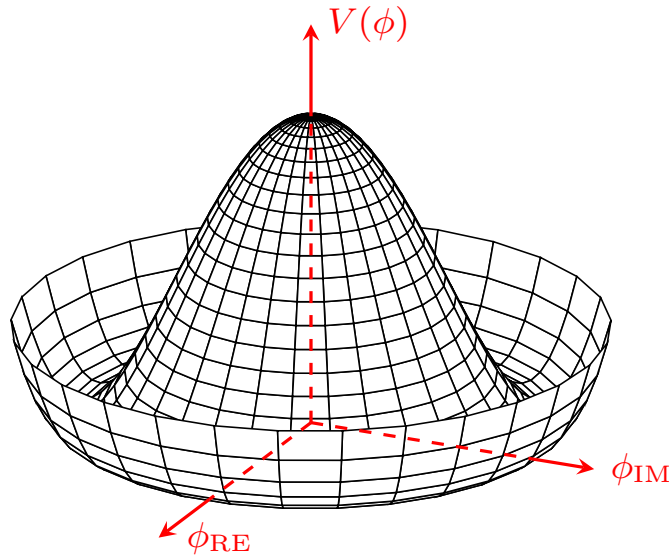

Figure 2.3: Representation of the scalar field potential $V(\phi)$, commonly known as the *Mexican hat* potential.

By using a unitary gauge configuration and rewriting ϕ_3 as an expansion of the VEV, v, small perturbations around the ground state are considered in the scalar doublet as

$$\phi = \frac{1}{\sqrt{2}} \begin{pmatrix} 0 \\ v + h \end{pmatrix}, \tag{2.6}$$

where h is a real scalar field. The expression for ϕ in the potential leads to a $\lambda v^2 h^2$ term in the Lagrangian, representing the physical scalar Higgs boson with mass $m_h = v\sqrt{2\lambda}$.

The Higgs field couples to the W and B gauge fields associated with $\text{SU}(2)_\text{L} \otimes \text{U}(1)_\text{Y}$ local symmetry through the covariant derivative shown in equation 2.3. As a result of choosing the unitary gauge, the values of $\phi_1 = \phi_2 = \phi_4$ have vanished from the original complex scalar field. The fields represent three massless Goldstone degrees of freedom which are actually absorbed to become the longitudinal components of the W and Z physical gauge bosons. The extra degree of freedom is manifested as mass and through the covariant derivative of the kinetic term in the Higgs Lagrangian, the Z and W gauge bosons acquire mass.

Simplifying the Higgs potential to omit any h-mixed terms from equation 2.8 demonstrates this generation of the gauge boson masses, the idea follows from

$$D_\mu \phi = \left(\partial_\mu + \frac{i}{2} g \sigma^a W_\mu^a + \frac{i}{2} g' B_\mu \right) \frac{1}{\sqrt{2}} \begin{pmatrix} 0 \\ v \end{pmatrix}$$

$$\tag{2.7}$$

$$= \frac{v^2}{8} \begin{pmatrix} g W_\mu^1 - i g W_\mu^2 \\ -g W_\mu^3 + g' B_\mu \end{pmatrix}.$$

The kinetic term of the Lagrangian with the simplified Higgs field becomes

$$(D^\mu \phi)^\dagger (D_\mu \phi) = \frac{v^2 g^2}{8} (W^{1\mu} - i W^{2\mu})(W_\mu^1 + i W_\mu^2) + \frac{v^2}{8} (g' B^\mu - g W^{3\mu})^2 \tag{2.8}$$

This term of the Lagrangian density describes a linear combination of fields, which can be interpreted as new fields, corresponding to massive particles. The physical gauge fields can now be defined as

$$W_\mu^+ \equiv \frac{1}{\sqrt{2}}(W_\mu^1 - iW_\mu^2), \tag{2.9}$$

$$W_\mu^- \equiv \frac{1}{\sqrt{2}}(W_\mu^1 + iW_\mu^2). \tag{2.10}$$

Thereby the Lagrangian term becomes

$$\frac{1}{2}\left(\frac{gv}{2}\right)^2 W_\mu^\dagger W^\mu \tag{2.11}$$

with the corresponding W mass

$$m_W = \frac{gv}{2} \tag{2.12}$$

The remaining neutral gauge bosons, Z and A, are defined as

$$Z_\mu \equiv \frac{1}{\sqrt{g^2 + g'^2}}\left(gW_\mu^3 - g'B_\mu\right) \qquad \text{with mass} \qquad m_Z = \frac{v}{2}\sqrt{g^2 + g'^2}, \tag{2.13}$$

$$A_\mu \equiv \frac{1}{\sqrt{g^2 + g'^2}}\left(g'W_\mu^3 + gB_\mu\right) \qquad \text{with mass} \qquad m_A = 0. \tag{2.14}$$

A_μ describes the massless vector field associated to the EM photon field, the nonzero VEV yields the breaking scheme $\text{SU}(2)_\text{L} \otimes \text{U}(1)_\text{Y} \to \text{U}(1)_{EM}$ which remains conserved in electroweak spontaneous symmetry breaking (EWSSB). Finally to note, including the h term in the scalar doublet and allowing it to propagate through to the SM Lagrangian, interaction terms arise between the gauge fields and the scalar Higgs field. Additionally, the quadratic term of the Higgs potential (2.4) leads to three and four self-interaction vertices of the Higgs field.

Fermion masses appear from the Yukawa term of the Lagrangian through the Yukawa coupling to the Higgs field,

$$\mathcal{L}_{\text{Yukawa}} = -g_f(\bar{\chi}_{L,f}\phi\psi_{R,f} \ + \ \bar{\psi}_{R,f}\bar{\phi}\chi_{L,f}) \tag{2.15}$$

where the isospin doublet of the left-handed fermions χ and the isospin singlet states for right-handed fermions ψ are included. The coupling of the Higgs field to the fermion field is necessary to ensure the Lagrangian is invariant under $\text{SU(2)}_L \otimes \text{U(1)}_Y$ and forms a singlet vertex $\bar{\chi}_{L,f}\phi\psi_{R,f}$ with coupling g_f for all fermion flavours.

Using the Higgs field from Equation 2.6, the Yukawa Lagrangian for leptons becomes

$$\mathcal{L}_{\text{Yukawa}}^{\text{leptons}} = -\frac{g_l}{\sqrt{2}}\left((\bar{\nu},\bar{l})_L \begin{pmatrix} 0 \\ v+h \end{pmatrix} l_R + \bar{l}_R(0, v+h) \begin{pmatrix} \nu \\ l \end{pmatrix}_L \right) \tag{2.16}$$

$$= -\frac{g_l(v+h)}{\sqrt{2}}(\bar{l}_L l_R + \bar{l}_R l_L) \tag{2.17}$$

$$= \frac{g_l}{\sqrt{2}}v\bar{l}l - \frac{g_l}{\sqrt{2}}h\bar{l}l. \tag{2.18}$$

From this it can be seen that the non-zero vacuum expectation value of the Higgs field leads to lepton masses given by

$$m_l = \frac{g_l v}{\sqrt{2}}, \tag{2.19}$$

and a lepton-Higgs coupling term arises in the Lagrangian in the form

$$g(h\bar{l}l) = \frac{m_l}{v}. \tag{2.20}$$

The model does not predict the lepton masses but it can be seen that the Higgs coupling is proportional to the lepton mass. τ-lepton signatures are therefore very important at collider experiments for Higgs searches. In the quark sector, it is little more difficult to obtain mass terms because of quark-mixing but the final result is very similar to leptons. Equation 2.19 for the lepton masses stands for all fermions with coupling g_f.

2.1.2 Higgs Production

The SM Higgs boson couples to both fermions and weak vector bosons. The main processes for Higgs production at hadron colliders are illustrated in Table 2.2. The primary production mechanisms include: gluon-gluon fusion (ggF), vector boson fusion (VBF), associated Wh and Zh production (Vh) and processes involving the production of a Higgs with a $t\bar{t}$ or $b\bar{b}$ pair.

The cross-sections for these processes in proton-proton collisions at the LHC are shown in Figure 2.4 for a centre-of-mass energy of 13 TeV versus the mass of the Higgs boson.

Production Mechanism	Cross-section	Diagram
Gluon-gluon fusion	43.92 pb	
Vector boson fusion	3.748 pb	
V-associated	Wh: 1.380 pb Zh: 0.8696 pb	
$t\bar{t}$-associated	0.5085 pb	
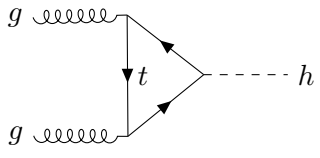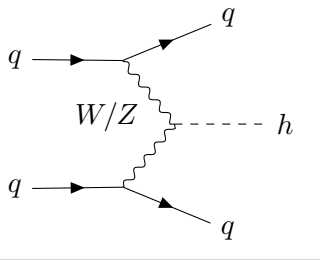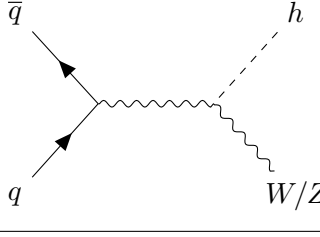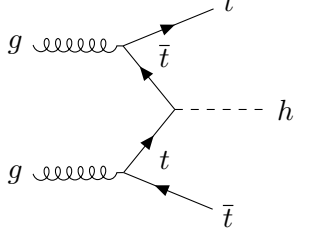
Table 2.2: The main production mechanisms for Standard Model Higgs boson production and their corresponding cross-sections for a $m_h = 125.0$ GeV Higgs boson at $\sqrt{s} = 13$ TeV. [40]

Gluon-gluon fusion

The dominant Higgs production mechanism is gluon-gluon fusion, $gg \to h + X$ (ggF). The leading order Feynman diagram for ggF features a quark loop in the SM usually through the exchange of a virtual heavy top quark. Although the cross-section is dominated heavily by the contribution from the top quark because of its comparable mass to the Higgs boson, other lighter quark can contribute. However, cross sections for lighter quark contributions are proportional to m_q^2 and are therefore heavily suppressed. The cross-section depends on the parton distribution function (PDF) of the colliding protons and also QCD radiative corrections with the next-to-leading order (NLO) corrections in α_s [41, 42].

The majority of corrections to the cross-section come from the emission of soft, virtual and collinear gluons. This is the leading contribution in the soft limit where the partonic centre of mass, $\hat{s}$, edges towards the Higgs mass m_h^2. Corrections due to soft-gluon radiation have been performed at next-to-next-to-leading logarithmic (NNLL) and partial NNNLL accuracy [43, 44].

The cross-section has been approximated by evaluating the leading top-quark contribution in the limit $m_t \to \infty$ where the ggH coupling becomes pointlike. The corresponding Feynman diagrams have one less loop; N3LO [45], NNLO [46–48] and NLO [49, 50] calculations have been completed using this approximation. Higher-order QCD corrections are necessary in the ggF cross-section predictions because of the slow convergence in α_s of the perturbative expansion. However, N3LO corrections show perturbation series to be rather stable with a small 3% enhancement [45] and insensitivity to resummation effects. The current cross-section value for ggF production to a 125 GeV Higgs boson is shown in Table 2.2 with a 13 TeV centre-of-mass energy at the LHC. N3LO corrections are combined with soft-gluon resummations at NNLL, and partial NNNLL accuracy along with secondary EW corrections [51, 52].

Vector boson fusion

The Higgs boson production mode with the second largest cross-section in the SM is vector boson fusion, $qq \to qqh$ (VBF). Despite the cross section being an order of magnitude below ggF production, VBF is very important in discriminating signal from background in

pp collisions because of its characteristic final state. The mechanism occurs by the scattering of two (anti-)quarks through the exchange of a W or Z boson in the t- or u-channel; the Higgs boson radiates from the weak propagator. The resulting quarks in the final state produce two hard jets at high rapidities due to the momentum transfer of the scattering quarks being of the order $m_V \ll \sqrt{s}$. Gluon emission is strongly suppressed because of the color-singlet state of the W and Z bosons. The two scattering quarks are not interacting through colour fields and so jets develop mostly in the quark directions.

Computation of the cross section with full QCD corrections have been completed to an accuracy of NLO [53, 54] with additional EW corrections of the order 10% at NLO. Approximate NNLO corrections are presented in Ref. [55].

Vector boson associated production Vh

The production of a Higgs boson in association with a weak vector boson, also known as *Higgs-strahlung*, has a very small cross-section compared with ggF. Vh production is dominated by quark-quark induced subprocesses ($q\bar{q}Vh$). However, in the case of a Z boson produced in association with the Higgs, there are large contributions from gluon-gluon initiated mechanisms. The gluon component leads to larger QCD corrections and the top quark loop introduces a scale dependence to the scattering amplitude.

Full QCD corrections to the cross section are available up to NNLO with NLO EW and gluon-gluon channel corrections in Vh@NNLO [56].

$t\bar{t}$ associated production

Despite having one of the smallest cross sections, Higgs production in association with a $t\bar{t}$ pair has great importance to the SM because it gives the opportunity to probe the top-Higgs Yukawa coupling which other mechanisms do not provide. QCD corrections to the order of NLO are presented in Refs. [57–60].
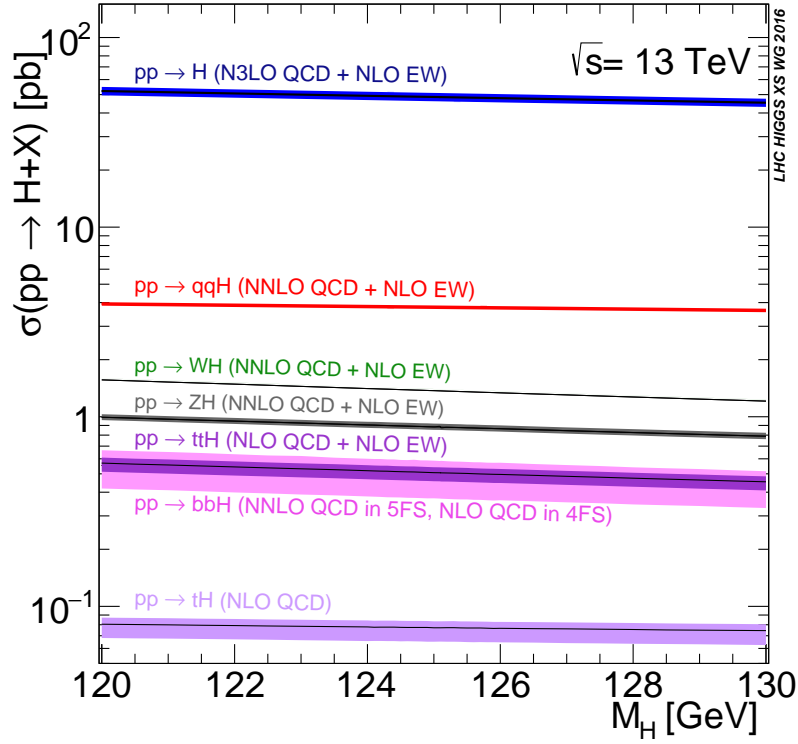
Figure 2.4: Standard Model Higgs Boson production cross-sections at $\sqrt{s} = 13$ TeV as a function of the Higgs mass [61].

2.1.3 Higgs Boson Decay

The Standard Model Higgs is unstable and the couplings of the Higgs to the different final state particles determines the decay branching ratios. Vertex diagrams for all processes and associated couplings are depicted in Figure 2.5.
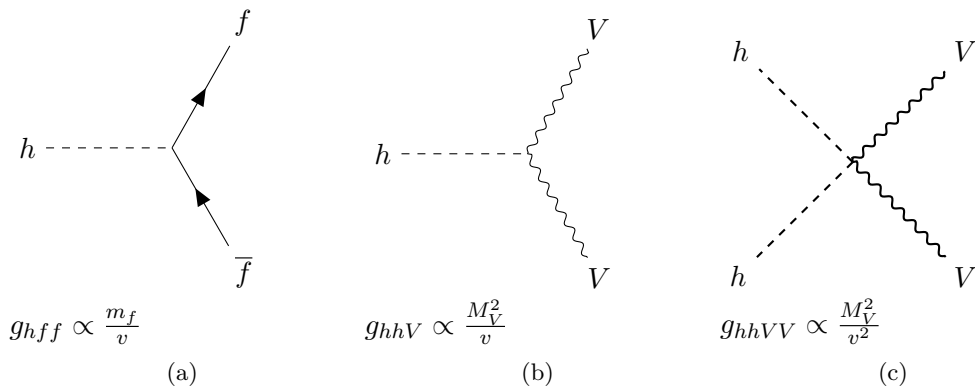

Figure 2.5: Higgs interaction vertices and their associated coupling, Higgs-fermion (a) and Higgs-vector boson (b) triple and (c) quartic interaction vertices.

For a 125 GeV Higgs boson, the dominant decay modes are to pairs of fermions through the Yukawa interactions and also into pairs of *W* or *Z* bosons, where one of which is *off-shell*. Additionally, di-photon pairs can be produced through a fermion loop similar to the gluon pair decay mode mediated by quark loops.
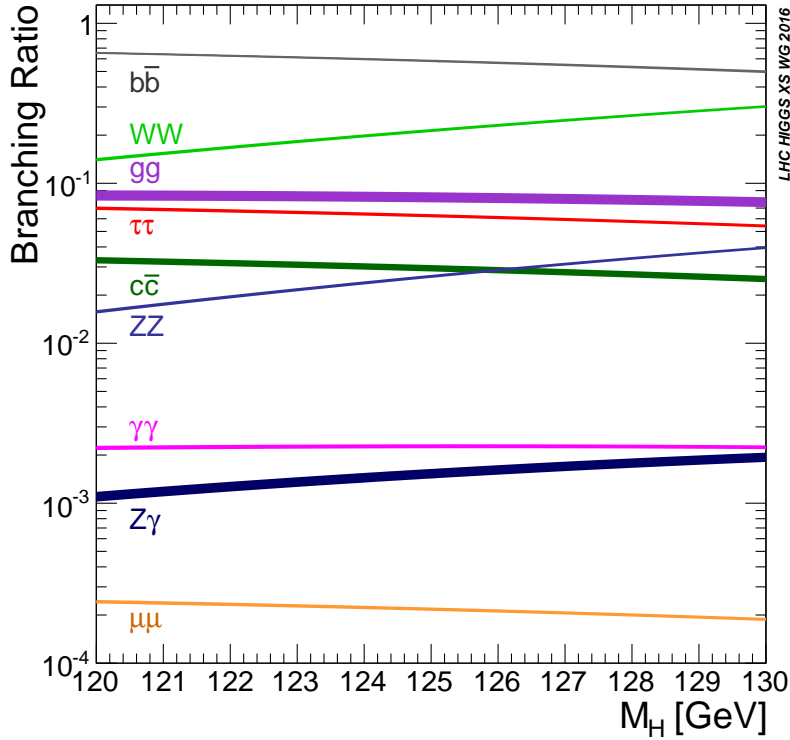

Figure 2.6: Standard Model Higgs boson decay branching ratios [61].

The main decay mode for a Standard Model Higgs boson is to a pair of *b*-quarks, $h \rightarrow b\bar{b}$, because this is the heaviest particle which can be produced on-shell from a Higgs decay. The branching ratio of $h \rightarrow \gamma\gamma$ is small but has a very clean signature in hadron collider experiments of two energetic photons. The di-photon decay mode was the first confirmed discovery channel for the Higgs boson due to the high $\gamma\gamma$ invariant mass resolution of both ATLAS and CMS [1, 2]. Other Higgs decay modes include $h \rightarrow WW^*$, $h \rightarrow ZZ^*$, $h \rightarrow c\bar{c}$ and $h \rightarrow gg$; however, the latter two suffer from a high QCD di-jet background. The decay branching ratios (*BR*) are given in Figure 2.6 as a function of the Higgs mass.

2.2 Di-Higgs Boson Production

The production of a Higgs boson with another Higgs is a process of particular interest at the LHC. One of the primary aims of the proposed high luminosity LHC (HL-LHC) [62] is to probe the di-Higgs production mechanism because of the many implications it can have beyond the Standard Model (BSM). Many theories exist to describe di-Higgs production at the LHC.

In the standard model, Higgs bosons can be pair-produced via top loops or the Higgs boson self-coupling. Establishing the strength of the Higgs boson tri-linear self-coupling (λ_{hhh}) is a crucial test of EWSSB and can act as a closure test for the Standard Model.

The cross-section for Higgs boson pair-production is very small in current theories and would be impossible to measure with the current data collected by the LHC. However, extensions to the Standard Model can enhance this cross-section. Higgs pair-production at the LHC is dominated by gluon-gluon fusion and is loop-initiated at LO. Contributing diagrams are shown in Figure 2.7 where the box top-loop and Higgs self-interacting spin-0 configurations destructively interfere. Consequently, the SM cross-section for Higgs pair-production at 13 TeV centre-of-mass energy with $m_h = 125.09$ GeV, is very small, $33.41^{+4.3\%}_{-6.0\%} \pm 5.0\% \pm 2.3\% \pm 2.1\%$ pb [61, 63–65]. The uncertainties quoted are the scale uncertainty, theory uncertainty, α_s uncertainty and parton distribution function (PDF) uncertainty. This value of the cross-section is NNLO matched to NNLO cross-sections for $gg \to hh$ and also includes reweighting (RW) for all top-quark mass effects at NLO taken from [65]. This cross-section corresponds to a cross-section times branching ratio to the $b\bar{b}\tau\tau$ final state of $2.44^{+0.18}_{-0.22}$.

It is also important to note that results are also presented in this thesis with a cross-section $37.91^{+2.2\%}_{-5.0\%} \pm 2.6\% \pm 2.1\% \pm 2.1\% \pm 3.0\%$ pb[61, 63, 64] without the full top-quark mass reweight at NLO.
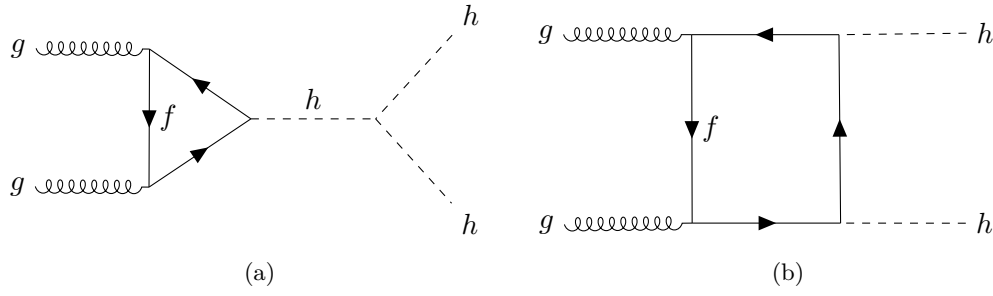
Figure 2.7: The contributing diagrams to non-resonant di-Higgs production at leading order. The *triangle* process is shown in (a) and the *box-diagram* is shown in (b).

2.2.1   Beyond the Standard Model

In the search for new physics beyond the Standard Model (BSM), many theories exist for Higgs pair-production. A heavy spin-0 scalar, H, in the two Higgs doublet model (2HDM) [6, 66–68] and spin-2 Kaluza Klein (KK) excitations of the graviton G^*_{KK} in the bulk Randall-Sundrum (RS) model [69, 70] are examples of heavy resonances decaying to a pair of Higgs bosons.

Additionally, modifications to λ_{hhh} or the existing top Yukawa coupling result in significant enhancements to non-resonant cross-sections along with introducing new couplings [71–74].

Other theories exist for extensions to the Standard Model such as: MSSM [75, 76], NMSSM [77–79], Little Higgs [74, 80], Higgs Portal [81, 82] and Composite Higgs models [73, 83] but these are not addressed in this thesis.
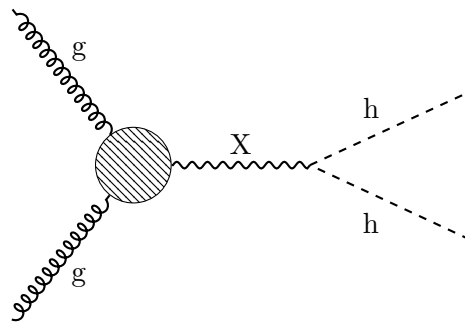

Figure 2.8: An example process diagram for resonant Higgs pair production beyond the Standard Model, X can be replaced with a Heavy Higgs in the two Higgs doublet model (2HDM) or a Kaluza Klein graviton.

Randall-Sundrum Kaluza-Klein Model

Resonant Higgs pair-production can occur through the creation of a spin-2 Kaluza Klein (KK) Graviton in Warped Extra Dimension (WED) models and can provide a solution to the Planck-weak hierarchy problem of the Standard Model [84, 85]. The existence of new particles at the ~TeV scale is an area of interest at the LHC, provided the new states have a non-negligible coupling to the SM particles. One scenario explains the hierarchy problem through the introduction of an anti-de Sitter (AdS) geometry in an extra dimension.

The solution is based on the Randall-Sundrum framework with a five dimensional Graviton field arising from the space-time quantum fluctuations of the metric after the inclusion of the additional dimension. Definition of the ultraviolet (UV) and infrared branes (IR) addresses the large hierarchy and pertubations on the space-time project to the four dimensional effective theory as a tower of KK states. The zero mode corresponds to the massless four-dimensional graviton whereas the first massive excitation is the KK-graviton.

Depending on the scenario, SM fields can be localized in the IR brane ("RS1") or be allowed to explore the 5th dimension as well. A well motivated configuration (known as the bulk-RS model) [5], predicts that the Higgs doublet is localized in the IR brane with the gauge bosons, while the other SM matter fields are localized in the UV brane and are allowed to propagate in the extra dimensional bulk. The KK-Graviton couples preferentially with the h, Z, W and t and the couplings to light fermions would be dramatically reduced in the bulk-RS model. Since couplings to fermions are suppressed, gluon fusion through a $t\bar{t}$ loop is the dominant process for KK-Graviton production at the LHC [86].

The decay widths of the KK-gravitons are proportional to the value of

$$c = \frac{k}{\overline{M}_{\mathrm{Pl}}}, \tag{2.21}$$

where k corresponds to the curvature of the warped extra dimension and $\overline{M}_{\mathrm{Pl}} = 2.4 \times 10^{18}$ GeV is the reduced four-dimensional Planck scale.

WEDs are considered as a model resonant double Higgs production searches at the LHC. Branching ratios of the massive KK-Graviton production are available in [85, 86]. The KK-Graviton is considered in this thesis as a possible resonance decaying to two Standard Model Higgs bosons for the $c = 1$ and $c = 2$ configurations.

Two-Higgs Doublet Model

The two-Higgs Doublet Model (2HDM) is an alternative to the SM and a minimal expansion that introduces additional Higgs bosons but maintains consistency with current experimental data, making it an interesting model to probe at the LHC. It is possible to build a CP-conserving theory that has been shown to be stable at LO [87, 88] and gives rise to a general renormalisable potential that is invariant under $\text{SU}(2) \otimes \text{U}(1)$.

Following on from the general idea of the BEH mechanism by introducing a second additional complex $\text{SU}(2)$ doublet with 4 degrees of freedom (similar to Equation 2.1), the potential then becomes

$$V(\Psi_1, \Psi_2) = m_1^2 \Psi_1^\dagger \Psi_1 + m_2^2 \Psi_2^\dagger \Psi_2 + (m_{12}^2 \Psi_1^\dagger \Psi_2 + h.c) + \frac{1}{2}\lambda_1(\Psi_1^\dagger \Psi_1)^2 + \frac{1}{2}\lambda_2(\Psi_2^\dagger \Psi_2)^2$$

$$+ \lambda_3(\Psi_1^\dagger \Psi_1)(\Psi_2^\dagger \Psi_2) + \lambda_4(\Psi_1^\dagger \Psi_2)(\Psi_2^\dagger \Psi_1) + \frac{1}{2}\lambda_5[(\Psi_1^\dagger \Psi_2)^2 + h.c],$$

$$(2.22)$$

where Ψ_i are the complex $\text{SU}(2)$ doublets. If the $\text{SU}(2)$ symmetry is broken, analogous to the BEH mechanism, the theory produces two charged Higgs bosons, $\text{H}^\pm$, one CP-odd state, A^0, and two CP-even Higgs states denoted by h and H [6].

Two-Higgs doublet models are often characterised by the value of $\tan\beta = v_2/v_1$, the ratio of the vacuum expectation values of the two Higgs doublets. A particular case of the 2HDM is a model where the up-type quarks couple to Ψ_2, down-type quarks couple to Ψ_1 and charged leptons couple to Ψ_1. One particular model that describes this scenario is known as the Minimal Supersymmetric Standard Model (MSSM) [75, 76].

After the discovery of the Higgs boson, the MSSM finds it difficult satisfy the constraint of the Higgs mass $m_h \approx 125$ GeV and so a simpler and almost model independent approach was put forward, called the hMSSM [89, 90]. In this framework, the mass of the Higgs is accounted for and the model can access the full (m_A, β) parameter space without conflicting current LHC data. The hMSSM is considered in this thesis with a value of $\tan\beta = 2$ as a possible heavy Higgs resonance decaying to two Standard Model Higgs bosons.

2.2.2 Exotics in the $b\tau\bar{b}\tau$ Final State

The existence of leptoquarks is predicted by many theories beyond the Standard Model such as techni-colour, superstrings, composite models, PatiSalam SU(4), and SU(5) grand unification [11–17]. Leptoquarks are hypothesised to couple to both quarks and leptons via the Yukawa interaction for all three fermion generations. They are said to carry non-zero lepton and baryon number, colour charge and fractional electric charge. Figure 2.9 shows gluon-initiated diagrams which dominate below very large leptoquark masses. At the LHC, leptoquarks could be produced in pairs through gluon-gluon fusion and quark-antiquark annihilation. Not only are leptoquarks well theoretically motivated, they have the potential to explain deviations from SM measurements given by Belle, BaBar and LHCb [91–93] in the branching ratios for B meson decays to leptons,

$$R(D^*) = \frac{BR(B^0 \to D^* \tau \nu)}{BR(B^0 \to D^* \mu \nu)}.$$
(2.23)

This thesis describes a search for pair-produced scalar leptoquarks decaying to bτbτ final states in the ATLAS detector. The analysis is based on reinterpreting the di-Higgs$\to bb\tau\tau$ search for evidence of leptoquarks and examine the sensitivity available. The search is carried out for an up-type (LQ$_3^u \to t\nu/b\tau$) and a down-type (LQ$_3^d \to b\nu/t\tau$), where the di-Higgs reinterpretation is sensitive to both. The branching ratio, B, of the leptoquarks decaying to charged leptons is considered to be B = 1 for the results presented in this document.
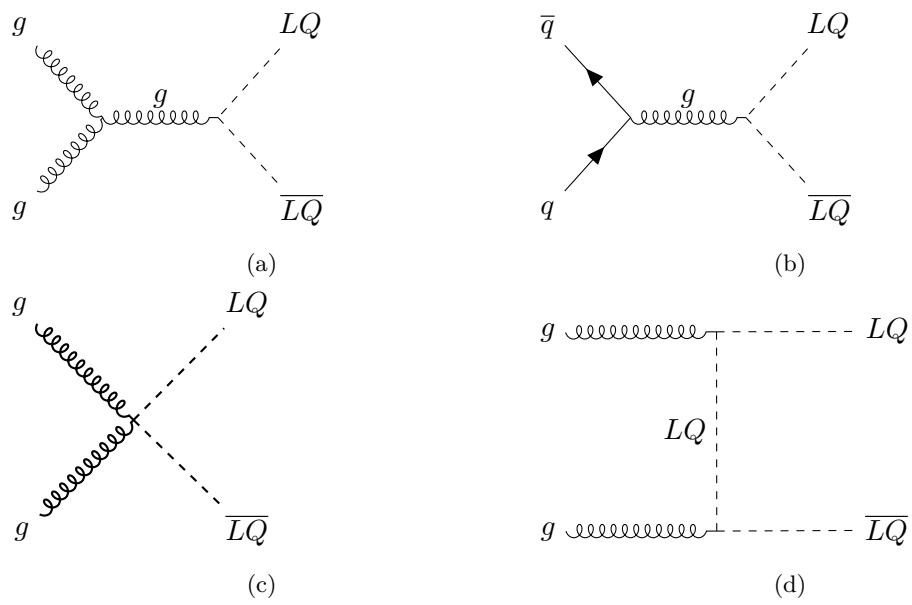
Figure 2.9: Dominant leptoquark pair production at the LHC.

Chapter 3

The ATLAS Experiment

In this chapter, an introduction to CERN and the ATLAS experiment is presented. Section 3.1 describes the Large Hadron Collider and the ATLAS experiment is then outlined in detail in Section 3.2 including all detector sub-components, the trigger system and the common nomenclature. All data presented in the analysis results of this thesis has been collected with the ATLAS experiment at the LHC.

3.1   The Large Hadron Collider

The Large Hadron Collider (LHC) is a 26.7 km superconducting ring accelerator located approximately 100 m below the surface at the CERN facility near to the French-Swiss border. The CERN accelerator complex [94, 95], shown in Figure 1, is capable of proton-proton (pp), proton-lead (p-Pb) or lead-lead (Pb-Pb) collisions where the beams are designed to intersect at four main experiments around the circumference of the ring: ATLAS [3], CMS [4], LHCb [96] and ALICE [97]. The current collision centre-of-mass energy is $\sqrt{s} = 13$ TeV with the intention of upgrading to 14 TeV in the near future. The main aim of the LHC is to probe physics beyond the Standard Model.

During pp-collisions, protons are accelerated through several stages inside the CERN accelerator complex before emerging from the Super Proton Synchrotron (SPS) to be injected into the main collider ring at 450 GeV. The two proton beams are then accelerated further, up to world leading energy of 6.5 TeV per beam ($\sqrt{s} = 13$ TeV). Collisions occur at precise interaction points in each experiment when the proton bunches are orientated to cross paths.

The two general purpose detectors, ATLAS (A Toroidal LHC ApparatuS) [3] and CMS (Compact Muon Solenoid) [4], both boast a peak instantaneous luminosity of $L = 10^{34}$ cm^{2}s^{-1} for proton operation. The two detectors are sensitive to a wide range of physics at this high luminosity such as: extensions to the Standard Model, supersymmetric searches and precise Higgs boson measurements. The one dedicated LHC heavy ion experiment, ALICE (A Large Ion Collider Experiment), researches heavy ion collions and quark-gluon plasma, whereas LHCb specialises more in studying *b*-physics.

During 2015 and 2016, many months of successful data taking with a reduced bunch spacing (25 ns) resulted in a total integrated luminosity of 36.1 fb^{-1} collected data. Run 2 aims to deliver 100-300 fb^{-1} over the coming years.
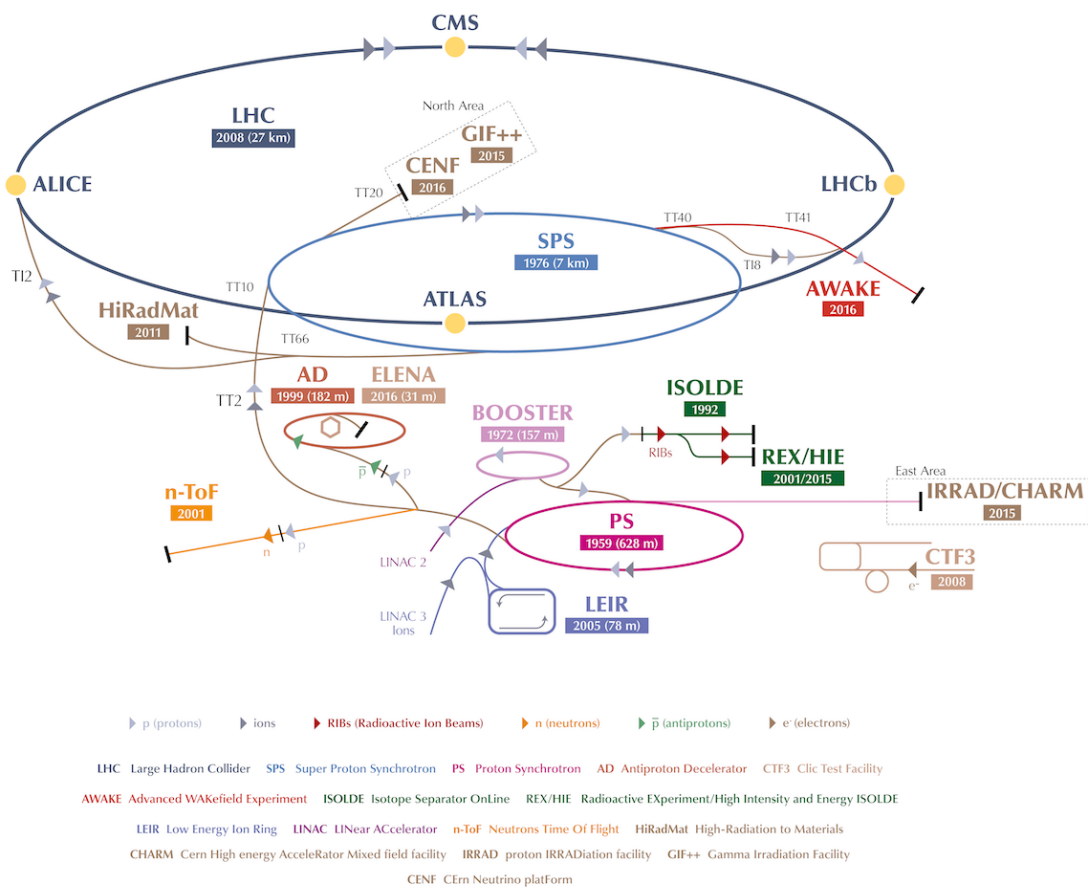
Figure 3.1: The CERN accelerator complex and the major experimental collaborations [98].

3.2   The ATLAS Detector

3.2.1   Overview

As previously stated, the ATLAS detector is one of two multi-purpose detectors on the LHC ring located approximately 93 m underground at Point 1. The detector has an almost cylindrical forward-backward symmetric design with a diameter of 25 m and an overall length of 44 m. The purpose of the ATLAS detector is to record the energies and trajectories of particles emerging from the collisions with the help of numerous sub-detector components.

The inner detector (ID) surrounds the interaction point and is made up of high-resolution semiconductor pixels, silicon microstrip trackers (SCT) and a transition radiation tracker (TRT) all encompassed within a 2 T solenoidal magnetic field. In 2014, the ATLAS insertable B-layer (IBL) was introduced as a fourth layer to the present pixel detector around the beam pipe. This was to ensure tracking efficiency and precision throughout Run-2 and the future HL-LHC operations and protect against any degradation of the equipment over time.

Electromagnetic (ECAL) and hadronic (HCAL) sampling calorimeters make up a large portion of the ATLAS detector. High granularity liquid-argon (LAr) is used with lead for the ECAL, whereas the HCAL uses an arrangement of steel and scintillator tiles for a large majority of the rapidity range, discussed in more detail in a following section. Both calorimeters ensure good containment of electromagnetic and hadronic showers while providing excellent performance in terms of energy and position resolution.

Surrounding the two calorimeters is a muon spectrometer (MS) which defines the overall dimension of the ATLAS detector. Utilising the combination of precision measurement and fast-trigger detectors, the MS achieves excellent muon momentum resolution.

A full cut-away view of the ATLAS detector components is presented in Figure 3.2.
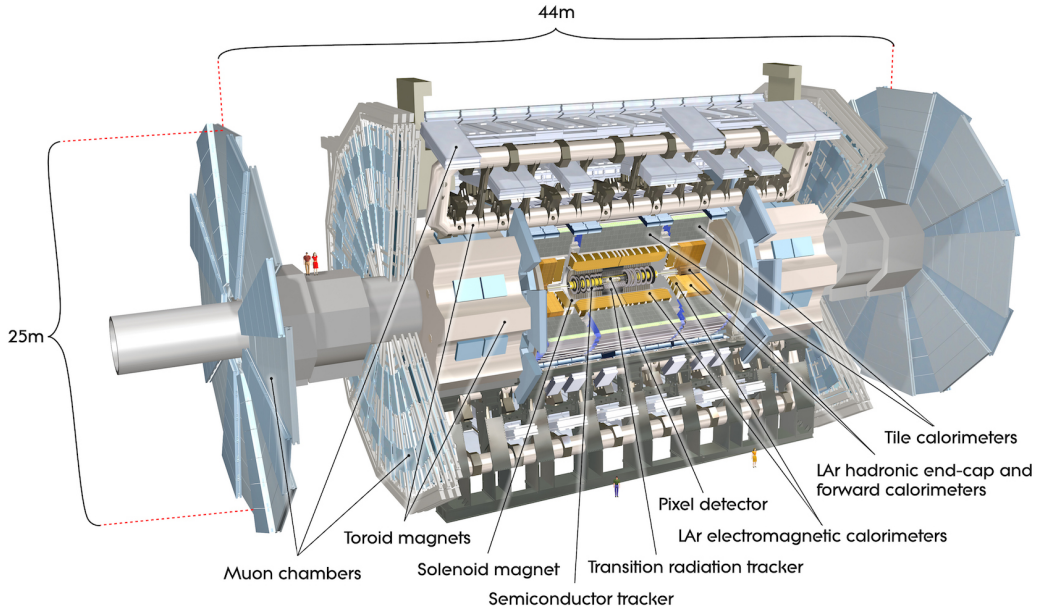
Figure 3.2: The ATLAS detector, taken from [3].

3.2.2 The ATLAS Coordinate System

The coordinate system used by ATLAS aims to consistently describe the particles emerging from pp collisions and the orientation with respect to the detector. The system is right-handed with the origin defined as the nominal collision interaction point. Beam direction is said to be the z-axis and the x-y plane is transverse to this. The y-axis is designed to be positive pointing upwards and the positive x direction points towards the centre of the LHC ring from the interaction point.

The coordinates are based on a cylindrical system with the transverse plane often described in terms of r and ϕ. The azimuthal angle ϕ is measured around the beam axis and the radial coordinate measures the distance from the beam line.

The polar angle θ is the angle from the beam line in the positive z direction which directly relates to a popular variable known as *pseudorapidity*, defined as

$$\eta = -\ln\left(\tan\frac{\theta}{2}\right). \tag{3.1}$$

Alternatively in the case of massive objects such as jets, rapidity is used

$$y = \frac{1}{2} \ln \left(\frac{E + p_z}{E - p_z} \right), \tag{3.2}$$

where E is a particles energy and p_z is the z-component of the momentum.

Finally, the distance ΔR in the pseudorapidity-azimuthal angle space within the detector is given by

$$\Delta R = \sqrt{\Delta \eta^2 + \Delta \phi^2}. \tag{3.3}$$

The convention is usually to express the kinematics of objects in the x-y plane of the detector, the momentum and energy of the particles can be expressed as variables transverse to the beam line using θ relations. The transverse momentum and energy are given by

$$p_{\text{T}} = |\mathbf{p}| \sin \theta, \tag{3.4}$$

$$E_{\text{T}} = E \sin \theta, \tag{3.5}$$

where $\mathbf{p}$ is the three-momentum vector of the particle.

3.2.3 Inner Detector

The inner detector (ID) [99, 100] is a sophisticated collection of sensors designed to measure the trajectory of charged particles as they traverse through the early stages of the detector. The resolution requirements needed for standard physics processes are difficult to reach, especially in a high track density environment emerging from the interaction point (IP) every 25 ns. The ID works with the combination of high granularity pixel and silicon microstrip (SCT) trackers, and the straw tubes of the TRT. The sub-detectors are based on two technologies: silicon sensors and straw drift tubes. Incident particles pass through the silicon sensors and deposit energy, generating electron-hole pairs which are accelerated in the electric field and drift to the nearest electrodes determining the local position of the particle. Straw drift tubes work in a similar manner where charged particles ionise a gas contained within the straw and the excited electrons drift to a central wire. The combination of three separate sub-detectors shown in Figure 3.3, all utilising different technologies, is designed to achieve optimal momentum and spatial resolution while minimising cost.

The silicon pixel detector [101] is located closest to the beam pipe and spans the radial distance of 33–150 mm. It is arranged as three concentric cyclindrical layers in the barrel region $|\eta| < 1$ and two end-caps with three disks each.

With over 80 million pixels in total, the pixel detector hosts 1744 identical pixel-sensor modules and each module contains 46080 pixels with a size of 50 μm (r-ϕ) $\times$ 400 μm (z). The arrangement of the cylinders and end-caps ensures three pixel layers are typically traversed by each particle track.
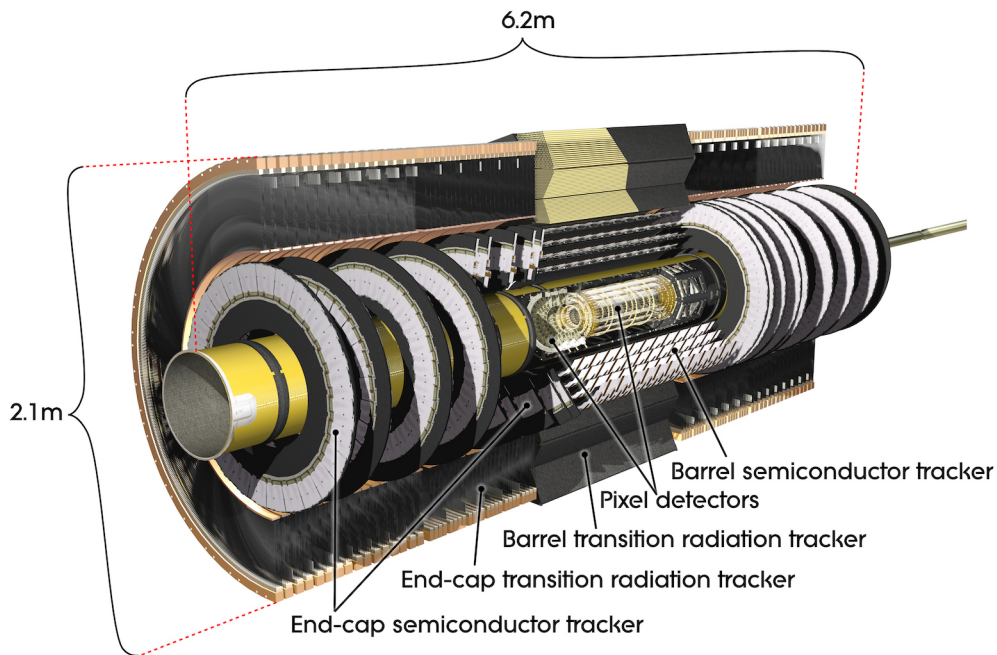
Figure 3.3: A cut-away view of the ATLAS inner detector showing the many sub-detectors and systems. Taken from [3]

The SCT covers the radial region 299–560 mm and consists of 4088 silicon microstrip modules distributed between four barrel layers and two end-caps with nine disks each. In the barrel region, each module consists of two 6.4 cm layers of silicon microstrip sensors glued back to back with a relative stereo angle of 40 mrad. Typically the SCT provides between four and nine spatial measurments from a particle track crossing eight strip layers.

The transition radiation tracker is the largest sub-detector and makes up the outermost layer of the ID, it is comprised of more than 350,000 gas-filled straw tubes with a diameter of 4 mm. These tubes typically provide an average of 36 (at least 32) hits per track and enable track-following up to $|\eta| = 2.0$. Each tube is around 1.5 m in length in the barrel and

0.4 m in length in the end-caps. The gas mixture filling the tubes consists of 70% Xe, 27% CO_2 and 3% O_2 and the spaces between the straws are filled with polymer fibres. In addition to tracking information, the TRT can provide particle identication through the detection of transition radirion. The transition radiation emitted by charged particles propagating through the TRT differs for electrons compared to charged hadrons at the same momentum so separation is possible.

In 2014, the insertable B-layer (IBL) was newly installed and is now the innermost pixel layer of the ID and boasts over 12 million silicon pixels covering the region $|\eta| < 3.03$. The IBL was designed to maintain robust tracking while directly improving track and vertex reconstruction until the planned inner detector replacement in 2025. Performance measurements of the IBL show a 40% increase in both transverse and longitudinal impact parameter resolution for tracks with a p_T around 0.5 GeV [102].

Figure 3.4 provide a detailed view of the inner detector sub-components.
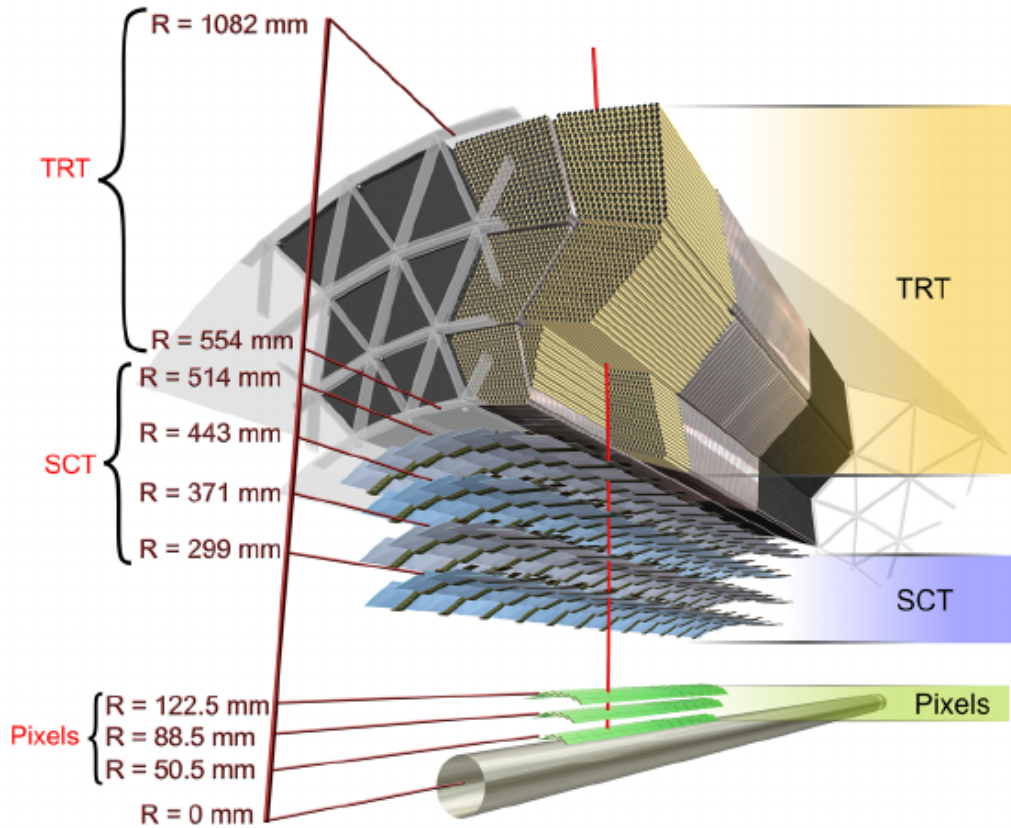
Figure 3.4: Schematic view of (a) the ATLAS detector, with (b) a detailed layout of the Inner Detector (ID), including the new Insertable B-Layer (IBL). Taken from [103].

3.2.4 Calorimeters

Calorimeters within the ATLAS detector, shown in Figure 3.5, are designed to measure the energy and trajectory of both charged and neutral particle showers. The ATLAS calorimeters only measure a fraction of the energy deposited by an incident particle and then deduce the full energy of the shower from the observed deposit, this is known as *sampling* calorimetry. The setup of the calorimeters covers the range $|\eta| < 4.9$ and incorporates many different techniques to investigate the physics processes of interest across this full scope. The ECAL within the barrel is more suited to the precise measurement of electrons and photons due to the fine granularity but the remaining calorimetry equipment is required for jet reconstruction and E_T^{miss}. Both the ECAL and HCAL deliver good containment of particle showers with minimal punch-through into the muon system [104].
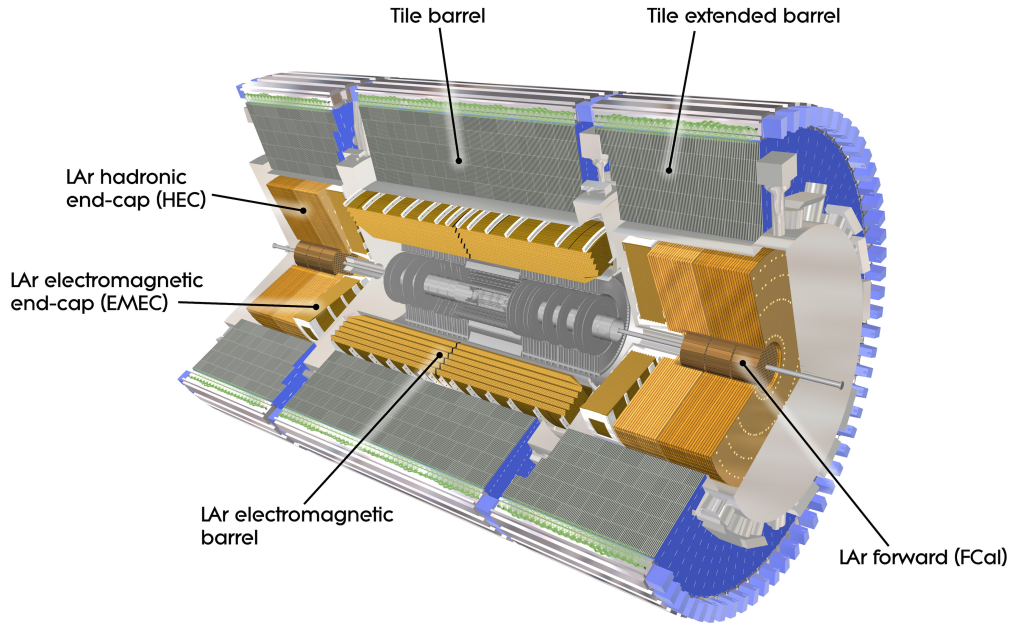
Figure 3.5: A cut-out view of ATLAS calorimeters, taken from [105]

Electromagnetic Calorimeters

The electromagnetic calorimeters encompass the ID and separate into two main parts. A barrel component is made up of two identical half-barrels isolated from each other by a 4 mm gap at $z = 0$ and covers $|\eta| < 1.475$. Two coaxial wheels make up the end-caps of the EM calorimeter with the outer wheel spanning the region $1.375 < |\eta| < 2.5$ and the

inner wheel responsible for $2.5 < |\eta| < 3.2$. The EM calorimeter is a lead-LAr detector with kapton electrodes assembled into an accordian-shape. The complex geometry avoids azimuthal cracks and gives complete symmetry in ϕ [106].

Hadronic Calorimeters

Hadronic calorimetry is provided by a scintillator/steel-tile calorimeter (TileCal) [107] within $|\eta| < 1.7$. Steel is used as the absorber and scintillating tile is the active material in this case. A TileCal barrel provides coverage up to $|\eta| < 1.0$ and two additional barrels extend past this to cover the rapidity range quoted above and provide enough depth to successfully capture the full collimated shower from incident particles. The tile calorimeter is divided azimuthally into 64 modules and separated in depth into three layers. With a total thickness of 9.7 interaction lengths at the outer edge of the tiles perpendicular to the beam line, the tile calorimeter makes up a significant portion of the ATLAS detector. Wavelength shifting fibres read from both sides of the scintillator and travel into two separate photomultiplier tubes.

To complement the tile calorimeter, two additional parellel-plate copper-LAr hadronic endcaps (HEC) cover the $1.5 < |\eta| < 3.2$ region. The two independent wheels are built from 32 identical wedge-shaped modules and provide four longitudinal calorimeter layers. The HEC is positioned directly behind the EM end-cap calorimeter and shares the same LAr cryostats. The inner wheels are constructed from 25 mm parallel copper plates with a radius of 0.475 m. The wheel end-caps furthest from the interaction point use 50 mm copper plates and possess a radius of 2.03 m. The copper plates are partitioned by 8.5 mm LAr gaps and act as the active medium for the calorimeter.

Finally, the forward calorimeter (FCal) provides coverage over the range $3.1 < |\eta| < 4.9$, close to parallel with the beam line. The FCal uses cylindrical modules comprised of tubes parallel to the beam axis with concentrically positioned rod electrodes on the inside. LAr was chosen again to fill the narrow gaps and avoid ion buildup at high rates, the whole apparatus is around 10 interaction lengths deep. The immediate module electrode is made of copper and has been optimised for electromagnetic measurements with 269 μm gaps. Whereas, the subsequent two modules are made from tungsten and predominantly measures hadronic interaction energy with gaps of 375 and 500 μm, respectively.

3.2.5 Muon Spectrometer

The muon spectrometer (MS) is the outermost ATLAS sub-detector, the layout is shown in Figure 3.6. A system of three large air-core superconducting toroid magnets provide a 0.5 T magnetic field to deflect muon tracks in the high-precision tracking chambers. One barrel ($|\eta| < 1.05$) and two end-cap sections make up the MS. Resistive plate chambers (RPCs) are used for low pseudorapidity ranges, $|\eta| < 1.05$, and thin gap chambers continue up to $|\eta| < 2.4$. These are arranged in layers of three and serve as trigger chambers for detection. Position measurements (η,ϕ) are achieved with a spatial resolution of 5-10 mm and precise muon momentum measurements are provided by three layers of monitored drift tube (MDTs) chambers ($\eta < 2.7$).
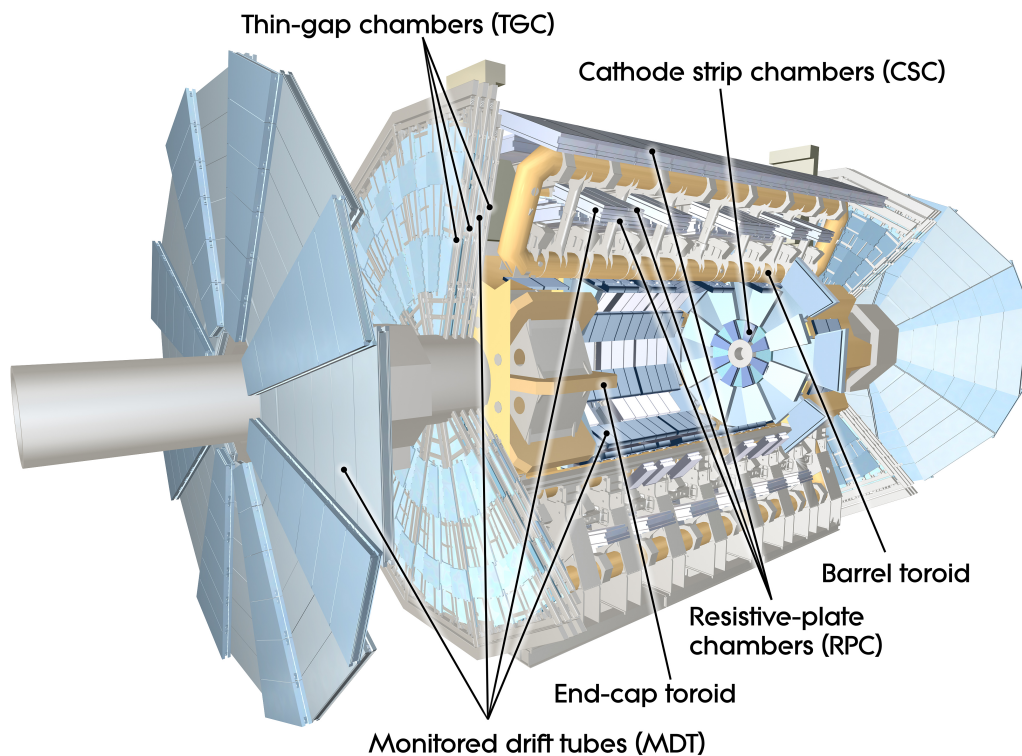
Figure 3.6: A cut away diagram of the ATLAS muon spectrometer, [108]

3.2.6 Magnets

The ATLAS detector takes advantage of three separate magnet systems [109] to alter the trajectory of traversing charged particles and measure their momentum. The magnetic fields are generated using coils of NbTi/Cu superconductor, stabilised by Al and cooled by a liquid He system. A solenoidal magnet surrounds the inner detectors and an array of three large air-core toroids generate the muon sprectrometer magnetic field. A schematic of the ATLAS magnet components is shown in Figure 3.7.

The solenoidal magnet [110] is around 5.8 m in length and 10 cm thick and immerses the inner detector while providing a 2 T, approximately uniform, longitudinal magnetic field. The muon spectrometer and calorimeters are surrounded by the system of toroid magnets that produce an azimuthal magnetic field. The toroid coils are designed into a discorectangle or 'racetrack' shape and split into a barrel toroid and two end-cap toroids. The barrel toroid magnet [111] covers $|\eta| < 1.4$ and the eight coils are arranged symmetrically around the central region, each contained in their own cryostat. Two end-cap toroids [112] are positioned at the sides of the detector, each with eight coils, and cover a range of $1.6 < |\eta| < 2.7$. The barrel and end-cap magnets are capable of providing a magnetic field strength of 0.5 T and 1.0 T, respectively. The bending power is lower in the transition regions where the two magnets overlap $(1.4 < |\eta| < 1.6)$.
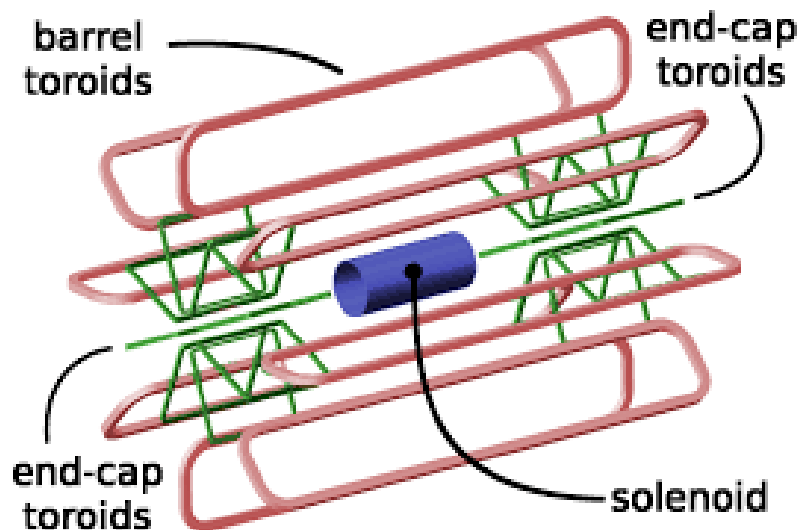
Figure 3.7: A schematic of the ATLAS magnet systems, taken from [113]

3.2.7   Trigger and Data Acquisition

Data acquisition is an important part of the ATLAS experiment and introduces a challenge of recording the properties of processes of interest. The LHC must operate at a high rate to produce analysable quantities of rare events. The ATLAS detector must deal with a bunch crossing rate of 40 MHz and filter out events to an acceptable rate for storage while still capturing the most important physics processes. The ATLAS *Trigger and Data Acquisition* system (TDAQ) is in place to reduce data to an adequate level for storage but this must be done in real-time. Decision-making and reconstruction at the triggering stage is known as *online*, whereas general ATLAS reconstruction is referred to as *offline*. The trigger works in two stages, firstly a hardware trigger is in place followed by a secondary software based trigger system. The hardware component is known as the *Level 1* (L1) [114] trigger which first encounters all *pp* collisions. The rejection of events to ultimately reduce the rate to 70 kHZ is mostly based on calorimeter and muon sub-detector information. The L1 trigger is the fastest part of the system and the inner detector algorithms cannot process events at such a high rate so ID information is omitted at this stage. The *High Level Trigger* (HLT) [115] is composed of the software triggers and is split into two parts: *Level 2* (L2) and the *Event Filter* (EF). The HLT reduces the event storage rate even further to around 700-1000 Hz.

The initial stages of the L1 trigger are based on identifying high-p_T objects or events with high $E_\mathrm{T}^\mathrm{miss}$ using basic calorimeter clustering and track information from the muon spectrometer. The performance of the detector is sacrificed for the purpose of speed. Granularity of the EM calorimeter is reduced and only some compartments of the muon system are used for read out. Regions of Interest (RoIs) are identified by the L1 trigger in $\eta - \phi$ space for each event if they pass certain threshold requirements, these are then passed on the *Central Trigger Processor* (CTP) to be matched to a set menu of triggers.

The HLT receives the RoIs from L1 and begins to process the events using full reconstruction, calibration and identification algorithms similar to those applied offline. The L2 stage utilises additional detector information where necessary and then transfers the events to the EF to fully reconstruct the entire event and perform the final selection.

Chapter 4

Object Reconstruction

The ATLAS experiment relies heavily on the reconstruction, identification and calibration of objects within the detector for all physics analyses. Reconstructing tracks from charged particles and locating collision and decay vertices constitute the basis of ATLAS reconstruction. The association of tracks to the primary vertex (PV) and determination of track parameters with respect to a given vertex offers the opportunity to suppress pile-up effects. Pile-up is where physics objects are reconstructed from interactions other than the hard scatter collision within a bunch crossing.

Energy deposits in the calorimeters form the basic constituents of jets which are supplemented by track and vertex information to define objects such a b-jets and τ-leptons. Both of which are important for the final state addressed in this thesis. This chapters aims to give an overview of the reconstruction algorithms and identification procedures for all physics objects used within ATLAS.

4.1   Tracks and Vertices

Track reconstruction for charged particles begins in the pixel and SCT detectors with cluster creation. Hits in the pixel and strip sensors are grouped into *clusters* where the energy produces a charge above threshold. Three-dimensional measurements called space-points are created from the clusters to represent the point at which the particle crossed the sensor. The total collected charge in a pixel sensor is proportional to the length of the traversing path through the medium. Calorimeter cell clustering can aid in recovering trajectory information using the incident angle of the particle and the intersection point. Additional information utilising the TRT can be found in [116].

Track seeds are defined as a combination of three space-points and must satisfy strict criteria to be identified as a track. An iterative track finding algorithm uses a combinatorial Kalman filter [117] to build track candidates and combine additional space-points compatible with the preliminary trajectory. Following this, ambiguity solving and track-fitting rejects track candidates and calculates more precise track parameters [118, 119].

Basic track quality criteria includes:

- $p_T > 400$ MeV,

- $|\eta| < 2.5$,

- minimum of 7 pixel and SCT clusters (12 are expected),

- maximum of one shared pixel cluster or two shared SCT clusters on the same layer,

- $|d_0^{BL}| < 2.0$ mm,

- and $|z_0^{BL} \sin\theta| < 3.0$ mm.

Impact parameters of a track, shown in Figure 4.1, are estimated using a perfect helical trajectory in a uniform magnetic field but compensated by particle energy loss throughout the material. Once the track candidates are fully reconstructed particle charge and momentum are calculated and added to perigee parameters particular to each track. The charged particles follow a circular trajectory in the transverse plane of the ID magnetic field and are described by a set of parameters with respect to the primary vertex. Parameters include: the inverse transverse momentum q/p_T, where q is the particle charge, the azimuthal (ϕ) and polar (θ) angles, and the transverse (d_0) and longitudinal (z_0) impact parameters. The impact parameters are defined as the point of closest approach to the beam line (BL).

The **vertex reconstruction** strategy for ATLAS Run-2 mirrors that used in Run-1 where an iterative vertex finding algorithm aims to find a common origin point from the several charged particle tracks tagged in the ID. Vertex seeds are constructed from the reconstructed tracks z-positions at the crossing point with the beam line [120, 121]. The general algorithm is as follows.
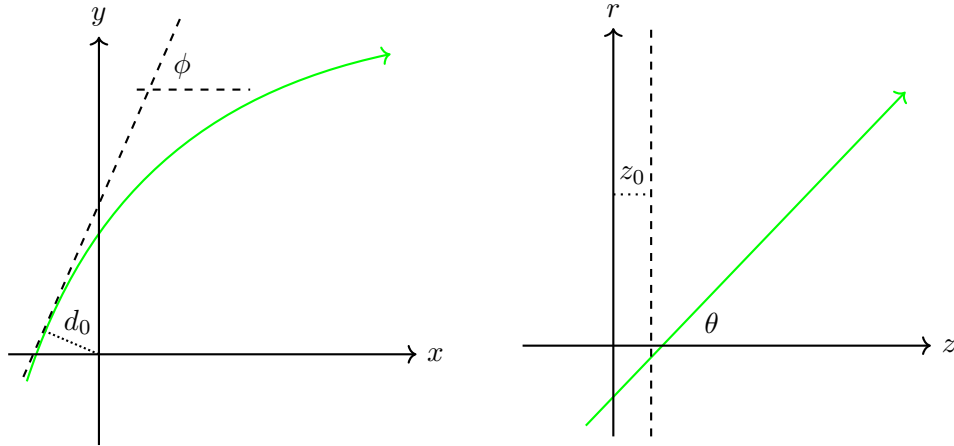
Figure 4.1: Diagrams of the transverse and longitudinal coordinate systems to define impact parameters with respect to the point of closest approach to the primary vertex.

- Select tracks that pass vertex reconstruction selection criteria [122].

- Perform a χ^2 fit to find a common vertex using a jet seed and collected tracks.

- Iteratively perform the fit procedure and down-weight tracks as they become more incompatible and recompute the vertex position. Tracks displaced from the fitted vertex by $> 7\sigma$ of the three-dimensional Gaussian distribution are removed and used to seed a new one.

- After determining a vertex position, incompatible tracks are removed from the associated set and can be used to refit another vertex.

- The procedure is repeated until there are no free tracks left in the event or no additional vertex can be computed from the remaining tracks.

  - All vertices require association to at least two tracks.

The algorithm outputs a set of the vertex objects with their three-dimensional vertex position, covariance matrices and the associated tracks. A luminous region inside the ATLAS detector where proton collisions occur is known as the beamspot position. The shape and position of the beamspot can be used to constrain the transverse position resolution of vertices reconstructed from a small collection of tracks [123, 124].

The efficiency of the vertex reconstruction is dependent on the average number of inelastic pp interactions per bunch crossing, $<\mu>$. Ideally the reconstruction efficiency would remain

constant as a function of $<\mu>$ but effects such as vertex merging, fake tracks and split vertices cause the efficiency to decrease. The main primary vertex where the hard scatter collision of the event occurred is identified as the vertex with the largest sum-p_T-squared of associated tracks. ATLAS vertex reconstruction performance plots are shown in Figure 4.2.
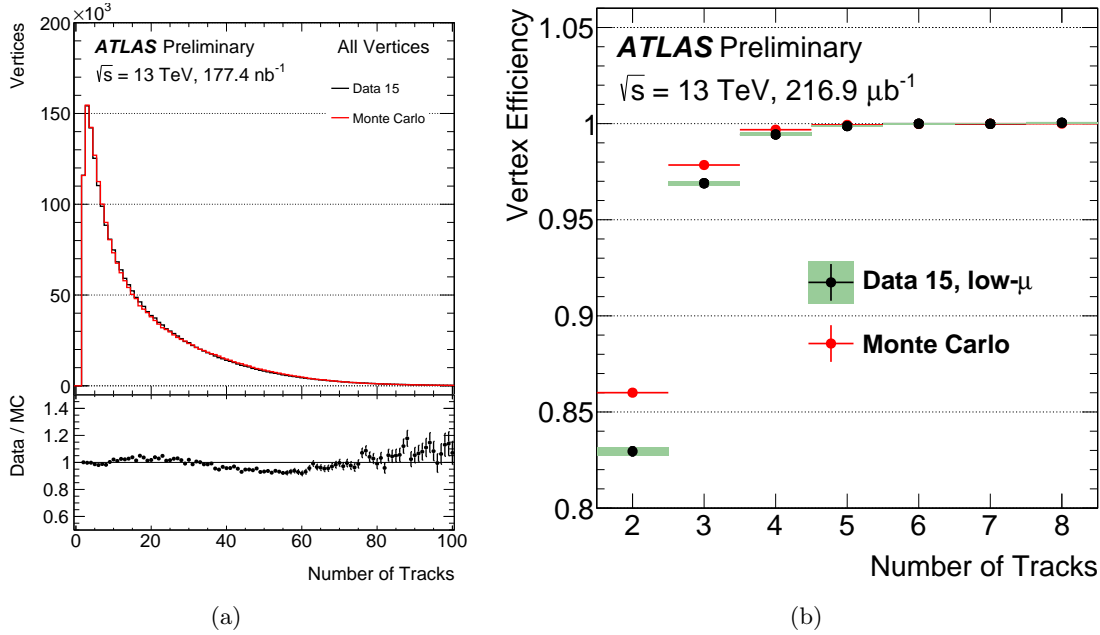
Figure 4.2: ATLAS performance plots with (a) showing the comparison between the number of tracks associated to the reconstructed vertex for all vertices in high-μ 2015 data and simulation. The vertex reconstruction efficiency as a function of the number of tracks in low-μ data compared to Monte Carlo simulation is shown in (b). Taken from [124].

4.2 Lepton Reconstruction

Electrons within the ATLAS detector are reconstructed using the energy clusters in the ECAL and an associated ID reconstructed track. High energy electrons dominantly interact with matter by the emission of a photon through a *Bremsstrahlung* radiation process, whereas high energy photons primarily produce an electron-positron pair in the active material. Electron reconstruction relies heavily on the properties of the resulting electromagnetic showers in the calorimeters. The longitudinal and tranverse shapes of the EM calorimeter showers, ID tracking and the track-to-cluster matching quantities are of particularly use in electron object determination [125, 126]. The efficiency of this ECAL cluster search ranges from 95% at $E_T = 7$ GeV to more than 99% above $E_T = 15$ GeV [127].

The EM clusters in the calorimeter are formed by using a sliding window algorithm and seeded by deposits with a total cluster transverse energy above 2.5 GeV. A sliding window size, corresponding to the granularity of the ECAL middle layer (3 x 5 in units of 0.025 x 0.025), is used to search for seed electron clusters. Selected tracks consistent with electron candidates are then loosely matched to EM clusters based on the $\eta - \phi$ position in relation to the cluster barycentre. The four-momentum of the reconstructed electrons are computed using the properties of the associated track (matched to the primary interaction vertex) and the final calibrated energy of the EM cluster.

Candidates go through a separate identification procedure to distinguish electrons from background-like objects such as hadronic jets, electrons from photon conversions and non-isolated electrons. The distinguishing variables for the identification algorithms are defined in detail in [127]. Several changes were made to the input variables for Run-2 to take advantage of the IBL. Three levels of identification operating points are output using a multivariate (MVA) technique to separate signal- and background-like electrons, *Loose, Medium* and *Tight*, in order of increasing background rejection. Many analyses require a separate isolation criteria on electrons to further discriminate between signal and background. Run 2 electron reconstruction efficiency remains very similar to the Run 1 performance, the efficiencies for each ID working point are shown in Figure 4.3.
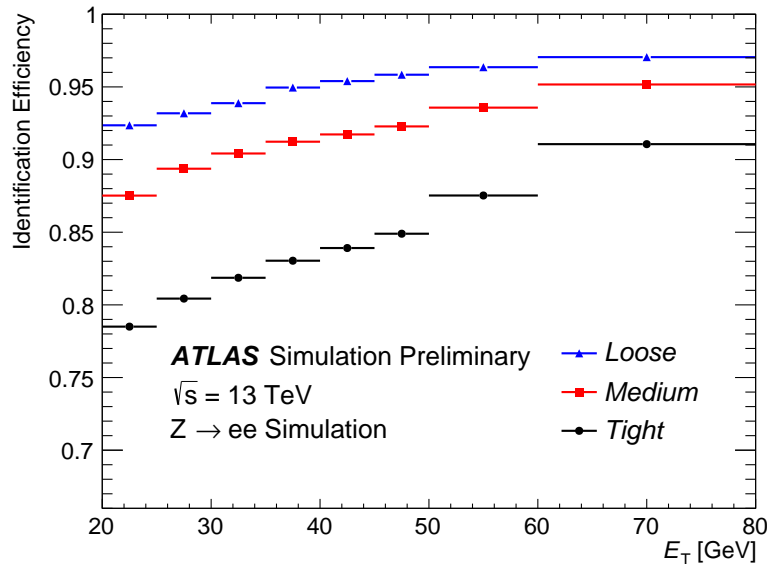
Figure 4.3: Electron identification efficiency to identify electrons from $Z \rightarrow ee$ decays obtained using Monte Carlo simulations and measured with respect to reconstructed electrons [128].

Muons produced by *pp* collisions are approximated by minimum ionising particle with a momentum of 1 to 100 GeV. Therefore, they can traverse the entire detector before decaying due to their 2.2 x 10^{-6} s mean life time. Reconstruction has to combine information from both the MS and the ID. Calorimeters can additionally be used to improve pseudorapidity coverage and momentum resolution but is not always used.

Muon reconstruction is first done independently by the two ATLAS sub-detector systems. Track reconstruction is performed in the ID like any other charged particle, whereas, tracks in the MS are pieced together by identifying hit patterns inside the muon chamber to form segments. Muon track candidates are then built by fitting hits from multiple segments in different layers. The acceptance of the ID and MS however is limited and some regions are not adequately equipped for this reconstruction. This is where calorimeter cluster information is often utilised. The combination of the sub-detectors leads to the classification of four types of muon objects [129, 130].

- **Extrapolated muons (ME)**

  Muons are reconstructed solely within the MS where muons that traverse two layers of MS chambers are considered track candidates. These are then extrapolated back to the beam line to determine track parameters with respect to the interaction point after energy loss throughout the calorimeters has been taken into account.

- **Calorimeter-tagged muons (CT)**

  When only an ID track is available, energy deposits within the calorimeter consistent with that of a minimum ionising particle are used. Deposits are matched to the track from the ID to define the muon candidate. No information from the MS is used so the purity of CT muons is the lowest, but utilising the calorimeters recovers acceptance in regions where the ATLAS muon system is partially implemented.

- **Segment-tagged muons (ST)**:

  Tracks reconstructed in the ID that can be extrapolated and matched to a track in the MS that crosses at least one segment, are considered to be a muon object. This muon type is necessary to recover low-p_T muons that only traverse one layer or appear in a region with reduced MS acceptance.

- **Combined muons (CB)**:

  Track candidates are independently built in the ID and MS and then combined to a single track. Many algorithms exist for the global fit procedure but the most common is an outside-in pattern recognition, where muon reconstruction is first performed in the MS and then extrapolated towards the beam line to link up with an ID track. The four-momentum and charge of these muons is obtained from the combined track, exhibiting excellent efficiency and resolution for muons with p_T below 100 GeV.

Corrections are made to the simulated muon momentum scale and resolutions to obtain agreement between data and simulation. MC events are also adjusted to compensate for isolation and trigger mismodelling. Finally, before physics analysis takes place, muons are classified as *Tight, Medium* and *Loose* at the identification stage, similar to that of electrons [130]. Figure 4.4 shows the performance of muon reconstruction and isolation algorithms.

(a)　　　　　　　　　　　　　　(b)
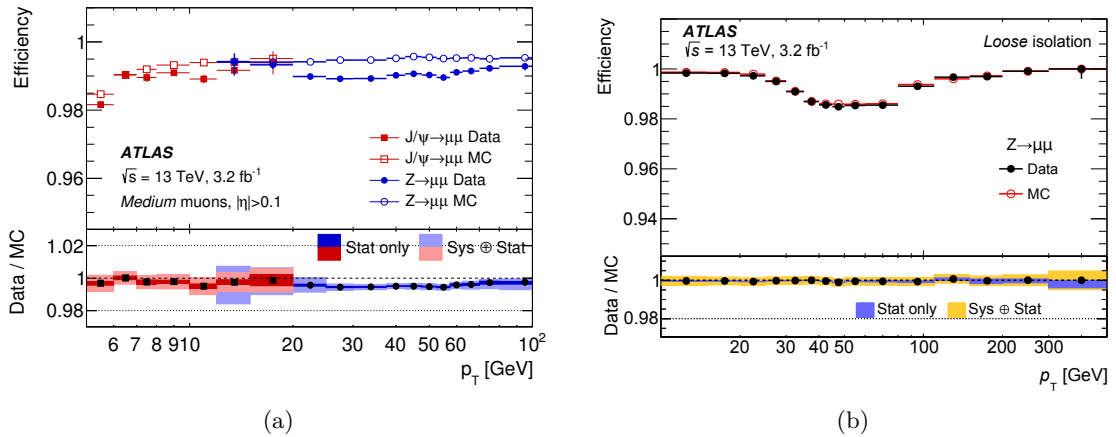
Figure 4.4: ATLAS muon performance plots with (a) showing the reconstruction efficiency for Medium muon selection as a function of the p_T of the muon in the region $0.1 < |\eta| < 2.5$. The isolation efficiency for the *Loose* muon isolation working point is shown in (b) as a function of the muon transverse momentum p_T, measured in $Z \to \mu\mu$ events. Taken from [124].

4.3 Jets

Whenever partons are produced in pp collisions at the LHC they hadronise. Quarks and gluons are unable to exist as free particles due to confinement and therefore fragment and become collimated sprays of energetic colourless hadrons. The radiation of gluons and splitting into $q\bar{q}$ pairs continues until the partons bind to colourless states. However, states are often themselves unstable which leads to the production of more hadrons, leptons and photons. The resulting shower is the experimental signature in particle detectors known as a jet. As a dominant final state in high-energy collisions, jets play a significant part in precision measurements and searches for new phenomena.

The hadronisation mechanism for parton showers is not well described by theory but with a standard definition of jet objects between theory and experiment [131], the features of a jet can fit experimental observations to physical objects. For example, it is implied that the momenta and parameters associated to that of the hadron closest to the jet axis mirrors that of the original parton. Throughout hadron collider experiments, the accepted definition requires a clustering of calorimeter cells in the $\eta - \phi$ plane.

Several algorithms exist for jet formation and they are mostly defined as either sequential or cone algorithms. An important feature of jet finding algorithms is how they evolve and handle the emission of soft or collinear particles throughout hadronisation. Sequential algorithms work by adding objects together without being restricted by a predefined shape, their configuration is by construction insensitive to soft and collinear emission. For the calculation of cross-sections in perturbation theory, the jet must be defined in a way as to which it remains independent of the presence of infinitesimally soft gluons. Cone based jets tend to be collinear unsafe due to the seeding objects being heavily affected by splitting.

The anti-$k_\mathbf{T}$ jet reconstruction algorithm [132, 133] is the sequential algorithm of choice within ATLAS, the close to conical shape and almost insensitivity to soft radiation is beneficial in high pile-up conditions seen at the LHC. ATLAS uses a topological cluster (topocluster) to act as input to the jet finding algorithms. Topoclusters have both three-dimensional shape and location information and are created by grouping neighbouring cells that have significant energy relative to expected noise. Cells with a large energy significance above a large threshold act as a seed and surrounding clusters are added if

their energy exceeds a secondary smaller energy threshold. Contrary to a sliding window algorithm for cluster grouping with a fixed-size, topological clustering leads to clusters with a variable number of cells [134, 135].

Sequential algorithms in general work by calculating the *distance* between these clusters, d_{ij}, and then iteratively combining these objects until no clusters are left in the event. The distance parameter is defined as

$$d_{ij} = min(p_{\text{T},i}^{2 \cdot p}, p_{\text{T},j}^{2 \cdot p}) \frac{\Delta R_{ij}^2}{R^2}. \tag{4.1}$$

The definitions of p_T and ΔR can be found in Chapter 3.2.2. In the case of the anti-k_T algorithm the parameter p is chosen to be $p = -1$ to prioritise clusters from hard particles so jets grow outwards around the hard seed. The energy weighted distance parameter becomes

$$d_{ij} = min\Big(\frac{1}{p_{\text{T},i}^2}, \frac{1}{p_{\text{T},j}^2}\Big) \frac{\Delta R_{ij}^2}{R^2}. \tag{4.2}$$

ATLAS tends to choose the value of 0.4 for the radius parameter R. The full algorithm is labelled as follows, using topologically-related calorimeter clusters:

- Scan objects and calculate d_{ij} between all pair combinations. Recognise the pair of objects with the smallest value of d_{ij}.

- If d_{ij} is smaller than $min\Big(\frac{1}{p_{\text{T},i}^2}, \frac{1}{p_{\text{T},j}^2}\Big)$, the two objects are merged using a four-momentum recombination scheme.

- However, object i is considered a jet and removed from the list if d_{ij} is greater than $\frac{1}{p_{\text{T},i}^2}$.

- The procedure is repeated until no clusters are left in the event.

After the jet candidates are reconstructed, ATLAS employs a rigorous jet energy scale calibration scheme. At each stage of the calibration, the full four-momentum of the jet is corrected with adjustments aiming to reduce pile-up effects. The complete chain of corrections is shown in Figure 4.5 but some of the more important are described here in detail. The origin correction redefines the jet direction to coincide with the hard scatter vertex and the momentum is recalculated and keeping the energy constant.

Additionally, the jets four-momentum is corrected to the particle-level energy scale derived using truth jets in dijet MC events [136–138].
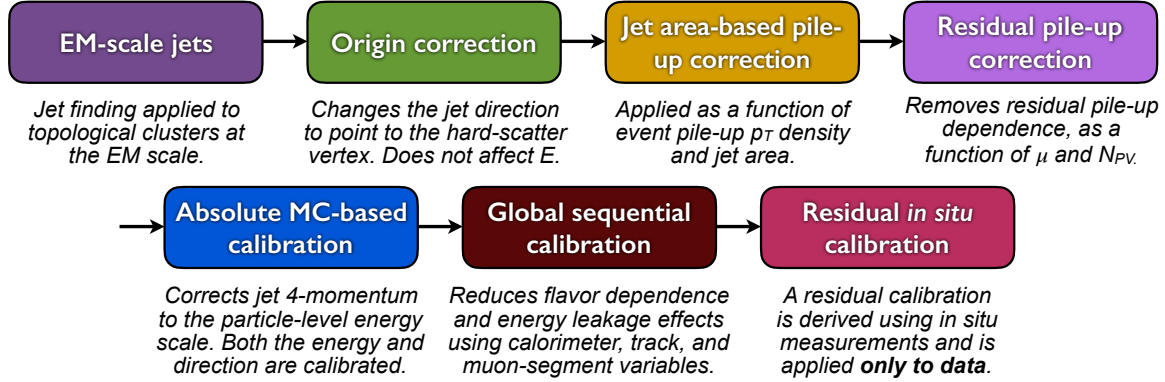
Figure 4.5: The many stages of the EM-scale jets calibration, taken from [138], all calibrations are applied to the four-momentum of the jet.

Accounting for pile-up is a challenge in ATLAS jet reconstruction, especially looking forward to the future at the LHC and the HL-LHC. With the switch from 50 to 25 ns bunch spacing, the amount of out-of-time pile-up has increased and topocluster thresholds have to be increased to control the impact of pile-up on the jet energy scale (JES). The main changes from Run 1 to Run 2 are explained in detail in [137] but it is worth noting that jet reconstruction has a separate regime to remove spurious pileup jets originating from other pile-up vertices.

A jet vertex fraction (JVF) variable is defined as the scalar transverse momentum sum of the tracks that are associated to the jet and originate from the hard-scatter vertex (PV_0) divided by the scalar p_T sum of all associated tracks [139]. Including those originating from the n-th primary vertex (PV_n). JVF is defined as follows

$$\text{JVF} = \frac{\Sigma_k \ p_\text{T}^{\text{trk}_k}(\text{PV}_0)}{\Sigma_l \ p_\text{T}^{\text{trk}_l}(\text{PV}_0) + \Sigma_{n\geq 1}\Sigma_l \ p_\text{T}^{\text{trk}_l}(\text{PV}_n)}. \tag{4.3}$$

The jet vertex fraction is bound between 0 and 1 with -1 reserved for jets with no associated tracks. This parameter measures the fractional p_T from tracks associated to the hard-scatter vertex and was initially used as a minimum criteria to reject pile-up jets. However, JVF has a strong dependence on the number of reconstructed primary vertices in an event (N_{vtx}). Therefore the jet reconstruction group developed the jet-vertex-tagger, where two new variables R_{pT} and corrJVF are introduced as

$$\text{corrJVF} = \frac{\Sigma_k \, p_T^{\text{trk}_k}(\text{PV}_0)}{\Sigma_l \, p_T^{\text{trk}_l}(\text{PV}_0) + \frac{\Sigma_{n \geq 1} \Sigma_l \, p_T^{\text{trk}_l}(\text{PV}_n)}{k \cdot n_{\text{trk}PU}}}, \tag{4.4}$$

$$R_{pT} = \frac{\Sigma p_T^{\text{trk}_k}(\text{PV}_0)}{p_T^{jet}}. \tag{4.5}$$

Where the scaling factor k is roughly taken as the slope of p_T^{PU} with n_{trk}^{PU}, in this case pileup values are defined using PU. CorrJVF is a modified JVF variable to remain stable against the number of reconstructed vertices in the event, whereas R_{pT} combines calorimeter and tracking information to further identify pileup jets. The jet-vertex-tagger (JVT) is constructed using these two parameters as a two-dimensional likelihood discriminant to suppress pileup jets in the event, depicted in Figure 4.6 [139, 140]. The idea of the JVF is applied to tau-jets in Chapter 5.

(a)

(b)
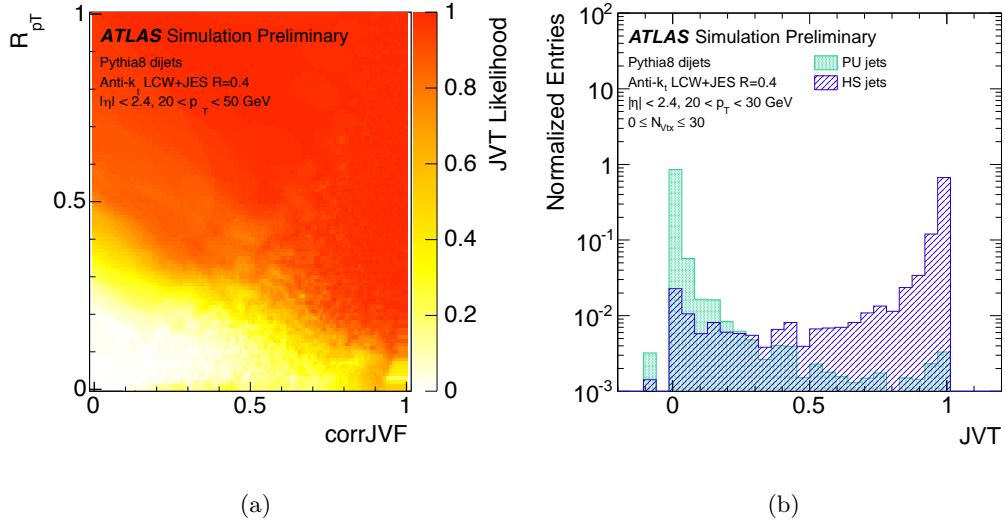
Figure 4.6: The 2-dimensional JVT likelihood as a function of corrJVF and R_{pT} is shown in (a), the distribution of JVT for pileup and hard-scatter jets with $20 < p_T < 30$ GeV is shown in (b) [139].

4.4 *b*-**tagging**

The ability to distinguish jets originating from *b*-quarks rather than those with different flavour origin such as *c*-jets or light(u, d, s-quark or gluon *g*)-jets is clearly crucial in an analysis with *b*-quarks in the final state. The performance of *b*-jet identification, known as *b*-tagging, can have significant impact on the signal sensitivity of an analysis. Many algorithms have been developed at ATLAS to 'tag' *b*-jets and these are either lifetime-based or based on the decay of *b*- and *c*-hadrons, usually to soft muons. The *b*- and *c*-hadrons are relatively short lived particles but are able to relativistically traverse a few mm inside the detector before decaying. Therefore, at least one displaced vertex can be reconstructed within the jets. Impact parameters of the tracks emerging from the flavour decay and the reconstruction of a secondary displaced vertex are crucial to *b*-tagging algorithms. The impact parameter represent the point of closest approach to the primary vertex (PV) of the extrapolated tracks from the *b*-hadron decay, illustrated in Figure 4.7.
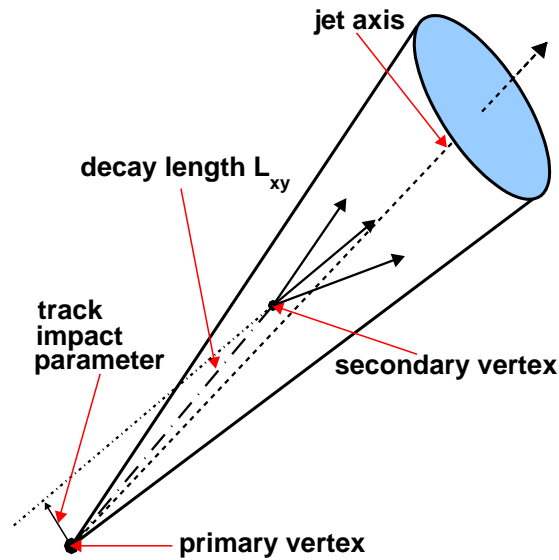
Figure 4.7: Schematic view of a *b*-hadron decay inside a jet resulting in a secondary vertex with three charged particle tracks. The vertex is significantly displaced with respect to the primary vertex, thus the decay length is macroscopic and well measurable [141].

Impact parameter based algorithms:

- **IP2D tagger** uses the transverse impact parameter significance, d_0/σ_{d_0}, as the discriminating variable to distinguish between tracks coming from the PV and those produced from a *b*-hadron decay.

- **IP3D tagger** makes use of both the tranverse impact parameter information and also the longitudinal impact parameter significance, $z_0 \sin\theta/\sigma_{z_0 \sin\theta}$, in a two-dimensional template to account for correlation and produce a more powerful discriminator.

Both the IP2D and IP3D taggers compare predetermined two-dimensional probability density functions (PDF) for *b*-jets, *c*-jets and light-jets obtained from reference histograms derived from Monte Carlo simulation. The ratio of the template PDF for the different jet flavour hypotheses is used as input to a log-likelihood ratio (LLR) method. Each ratio of the probabilities defines the track weight. The LLR discriminant is computed as the sum of the per-track contributions, $\Sigma_{i=1}^{N}\log\frac{P_b}{P_{light}}$, where N is the number of tracks of a given jet and P defines the particular likelihood. P_b and P_{light} are the template probability density functions (PDF) for the b- and light-flavour jet flavour hypotheses, respectively. The discriminating power of the LLR can be applied to separate *b*-jets from *c*-jets and also *c*-jets from light-flavour jets. Example LLR outputs are shown in Figure 4.8.
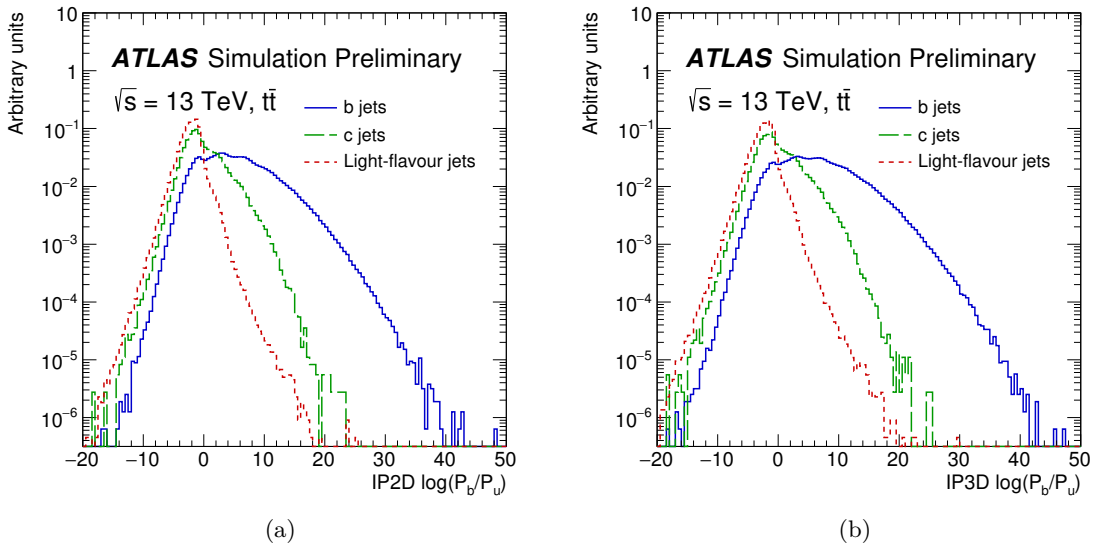
Figure 4.8: The log-likelihood ratio for for *b*- (solid blue), *c*- (dashed green) and light-flavour (dotted red) jets in $t\bar{t}$ events for the IP2D (a) and IP3D (b) [142].

Vertex based algorithms

Secondary vertex-based algorithms (SV) aim to explicitly reconstruct a displaced secondary vertex within the jet. Two-track pairs within the jet are tested to form vertex candidates which are then rejected if they are likely to have originated from the decay of a long-lived particle or from interactions within the detector material [143]. The secondary vertex can provide a number of discriminating variables for different jet-flavours such as: the invariant mass of the tracks, $m(\mathrm{SV})$, at the secondary vertex assuming pion masses and also the distance between primary and secondary vertices divided by its uncertainty, S_{xyz}.

JetFitter is a decay chain multi-vertex algorithm [144] that aims to fully reconstruct the *b*-hadron decay chain. The decay of *b*-hadrons primarily results in at least one *c*-hadron inside the jet and additional vertices can then be reconstructed. JetFitter takes advantage of the *b*- and *c*-hadron topological structure to resolve multiple vertices and flight paths along the approximated original *b*-hadron flight path, even when only a single track is attached. Again, the JetFitter algorithm produces discriminating variables and these can be used as input to more sophisticated *b*-tagging algorithms. Secondary vertex reconstruction rates are shown in Figure 4.9.
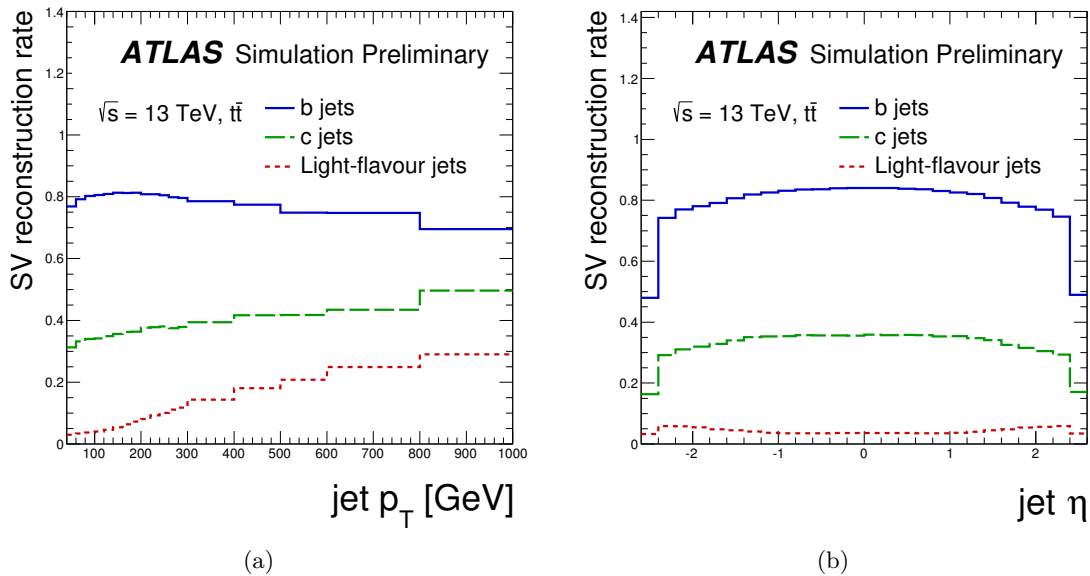
Figure 4.9: Secondary vertex reconstruction rates as a function of jet p_T (a) and jet η (b) [142]

MV2 multivariate b-tagging algorithm

The basic b-tagging algorithms addressed above are combined to achieve greater discriminating power using a Boosted Decision Tree (BDT) algorithm known as the MV2 algorithm [142, 145]. The BDT takes variables from the basic algorithms as input and combines kinematic properties of the jets, namely p_T and $|\eta|$, to take advantage of correlations between input variables [145]. The efficiency working point of the multivariate classifier chosen can produce a gain in b-tagging efficiency but in turn changes the light and c-jet rejection depending on the physics analysis requirements. MV2 has been optimised to produce three variants, MV2c00, MV2c10 and MV2c20, where the names of the taggers indicate the c-jet percentage in the BDT training. More information on b-tagging calibration and performance can be found in [146].

4.5 Tau Reconstruction

The reconstruction of hadronically decaying tau objects is based on information from the ID and the calorimeters. The τ-lepton candidates are seeded by a jet formed using the anti-k_T algorithm with a distance parameter $R = 0.4$. As with general jet reconstruction, inputs to the τ-jets algorithm are TopoClusters calibrated using the local hadronic calibration scale (LC) [147]. Additionally, b-tagging is performed at a 77% efficiency working point to veto jets associated to a b-quark decay. Jets seeding taus are also required to have $p_T > 20$ GeV and $|\eta| < 2.5$. Jets within the transition region, $1.37 < |\eta| < 1.52$, are vetoed.

The vertex association for tau candidates incorporates the idea of the JVF in jet pileup suppression to pair the tau candidate to the vertex with the largest fraction of momentum from tracks in a *core* region $(0 < \Delta R < 0.2)$. This idea is explained in more detail in Chapter 5 with an accompanying study and optimisation for tau-jet vertex association. Tracks from the jet are associated to the tau *core* and *isolation* $(0.2 < \Delta R < 0.4)$ regions if the following criteria are met with respect to the tau vertex (TV):

- $p_T > 1$ GeV,

- at least two associated hits in the pixel detector,

- at least seven hits in total in the pixel and SCT detectors,

- $|d_0| < 1$ mm,

- $|\Delta z_0 \sin(\theta)| < 1.5$ mm.

The vertex is used to determine the direction of the hadronic tau and build a coordinate system for the object which identification variables are calculated with respect to. The vectorial sum of three-dimensional TopoClusters found within $\Delta R < 0.2$ of the seed barycentre are combined with the tau vertex origin point to define a tau axis and direction. The mass of the tau candidate is initially defined to be zero and therefore the tau momentum is computed from the transverse energy, E_T.

Note the reconstructable visible hadronic components of the tau decay, often indicated as $\tau_{\text{had-vis}}$, are being referenced when mentioning hadronic tau candidates and calculating variables. The tau candidate is defined according to the number of associated tracks (charged particles) in the core region: 1-prong, 3-prong or multi-prong. Track selection is optimised to maximise the fraction of 1- and 3-prong tau decays reconstructed with the correct number of charged particles [21, 148].

Leptonically decaying taus rely on general lepton reconstruction with particular isolation criteria and fake rejection taken into account. Classification of τ_{lep} takes place at an identification stage later.

4.5.1 Tau Energy Calibration

Similar to the jet energy, tau-jets are reconstructed from energy deposits in the electromagnetic and hadronic calorimeters and need to be calibrated to correct the measured tau energy to the true tau-jet energy. Due to the larger fraction of electromagnetic energy in tau-jets compared to QCD jets, the tau energy scale (TES) is different to that of jet energy scale calibrations. Tau energy calibration has two stages, firstly energy contributions originating from pileup interactions are subtracted and secondly a correction is applied to remedy effects where the tau decay products do not deposit enough energy to form TopoClusters, fall outside of the tau-jet core region or simply do not reach the calorimeter. Calibration functions are described in detail in [148] where a newly implemented technique known as "Tau Particle Flow" [149] is introduced to improve energy resolution at low-p_T.

4.5.2 Tau Identification

Hadronic tau objects and QCD jets have a similar signature in the detector. The aim of tau identification is to identify real taus and minimise the number of quark- and gluon-initiated jets mis-identified as taus. This is of high importance for physics analyses with a hadronic tau final state. Identification uses a boosted decision tree (BDT) where 1-prong and 3-prong taus are trained separately. The identification working points for 1-prong (3-prong) are labelled *loose, medium and tight* and target efficiencies of 0.6 (0.5), 0.55 (0.4), 0.45 (0.3) respectively. The full list of BDT input variables in Run-2 reconstruction is given in [148].

All taus considered in this thesis use the Medium tau-ID working point because of the relatively high efficiency and sufficient fake tau rejection.

4.6 Missing Transverse Energy

Missing tranverse momentum ($E_{\mathrm{T}}^{\mathrm{miss}}$) is defined as the momentum carried by particles undetected by the ATLAS detector. A non-zero value implies the existence of SM neutrinos but could also suggest the production of new particles beyond the standard model.

$$E_{x(y)}^{\mathrm{miss}} = -\Sigma p_{x(y),i} \tag{4.6}$$

Calculating $E_{\mathrm{T}}^{\mathrm{miss}}$ is difficult because it depends on the reconstruction of all the other objects in the event after calibration, involves all of the detector subsystems and is restricted by the limitations of the detector and pileup interactions [150, 151].

The $E_{\mathrm{T}}^{\mathrm{miss}}$ is determined from x- and y-components of the E^{miss} given by

$$E_{\mathrm{T}}^{\mathrm{miss}} = \sqrt{(E_x^{\mathrm{miss}})^2 + (E_y^{\mathrm{miss}})^2}, \tag{4.7}$$

$$E_{x(y)}^{\mathrm{miss}} = E_{x(y)}^{\mathrm{miss},e} + E_{x(y)}^{\mathrm{miss},\gamma} + E_{x(y)}^{\mathrm{miss},\tau_{\mathrm{had}}} + E_{x(y)}^{\mathrm{miss},jets} + E_{x(y)}^{\mathrm{miss},\mu} + E_{x(y)}^{\mathrm{miss, \, Soft \, term}}, \tag{4.8}$$

$$\phi^{\mathrm{miss}} = \tan^{-1}\left(\frac{E_y^{\mathrm{miss}}}{E_x^{\mathrm{miss}}}\right), \tag{4.9}$$

where in the transverse plane:

- $E_{x(y)}^{\text{miss},e}$ is the total energy associated to electrons,

- $E_{x(y)}^{\text{miss},\gamma}$ is the total energy associated to photons,

- $E_{x(y)}^{\text{miss},\tau_{\text{had}}}$ is the total energy associated to hadronically decaying taus,

- $E_{x(y)}^{\text{miss},jets}$ is the total energy associated to jets,

- $E_{x(y)}^{\text{miss},\mu}$ is the total energy associated to muons,

- $E_{x(y)}^{\text{miss, Soft term}}$ is the total energy of topological clusters or ID tracks not associated to any previously reconstructed object.

Chapter 5

Tau-Jet Vertex Association

As briefly described in Chapter 4, ATLAS reconstructs many vertices per bunch crossing. The hard scatter vertex, where the main physics collision occured, is identified as the vertex with the highest $\sum p_T^2$ of all the tracks associated to it. The remaining reconstructed vertices within the event come from pile-up interactions.

The majority of ATLAS objects are associated to the highest $\sum p_T^2$ vertex. However, truth information from MC shows this is not always the vertex tau objects originate from in the event. Tau-jet vertex association (TJVA) is a necessary step in tau reconstruction and calibration. This chapter outlines the details of the TJVA and presents a study on track selection optimisation for the algorithm to be included in an upcoming ATLAS reconstruction software release.

This study was the main part of the author's qualification task for ATLAS authorship.

5.0.1 Tau-Jet Vertex Association Algorithm

The $\tau_{\text{had-vis}}$ track selection and reconstruction is sensitive to the vertex associated to the tau candidate, particularly at high pile-up conditions at $\sqrt{s} = 13$ TeV. Tracks can fail a $|z_0|$ requirement if the tau is assigned to the incorrect vertex or a pile-up interaction is defined as the hard scatter vertex.

A vertex is associated to the tau candidate by the tau-jet vertex association algorithm (TJVA) which is based on the JVF pileup suppression variable used in jet reconstruction. The JVF is calculated for each jet with respect to the hard scatter vertex, shown in Equation 4.3. JVF is defined as the scalar p_{T} sum of tracks associated to the jet and that originate from the primary vertex divided by the scalar sum p_{T} of all tracks regardless

of which vertex they originated as long as they pass selection criteria. The idea follows that the JVF output is used as a discriminator and a threshold is chosen to distinguish between jets originating from the primary vertex and those coming from pile-up vertices.

Figure 5.1 depicts the JVF and corresponding values for a scenario involving two jets. The JVF is described in detail in Section 4.3.
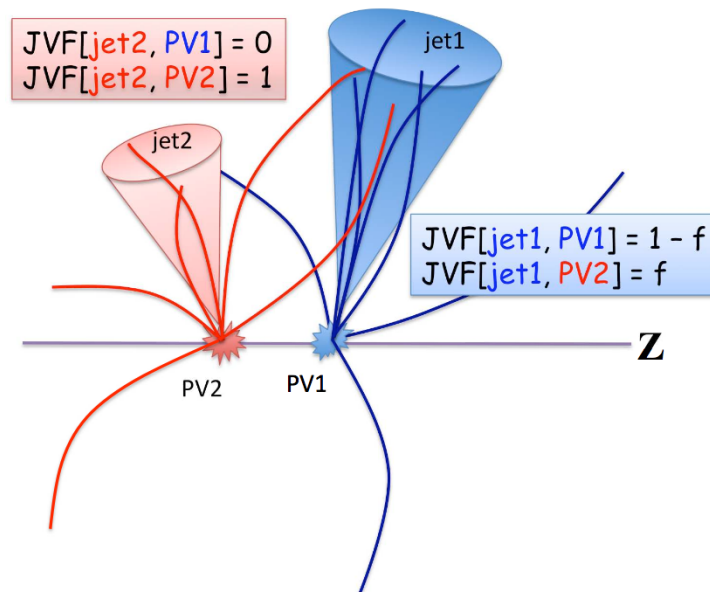
Figure 5.1: A representation of the jet vertex fraction (JVF) discriminant corresponding to the fraction of a jet, f, originating from a particular vertex [152].

Tau reconstruction can adapt the JVF variable to calculate a tau-jet vertex fraction (TJVF) where a tau-jet is evaluated with respect to each reconstructed vertex vtx_j using the associated tracks trk_k of the tau-jet τ_i, defined as

$$\text{TJVF}(\tau_i, vtx_j) = \frac{\sum_k p_{\text{T}}(trk_k^{\tau_i}, vtx_j)}{\sum_{n,l} p_{\text{T}}(trk_l^{\tau_i}, vtx_n)}. \tag{5.1}$$

The TJVF can be thought of as the scalar sum p_T of the tracks, from the tau, associated to the vertex in question divided by the total scalar sum p_T of all tracks within the tau-jet. The vertex with the highest TJVF value is taken as the primary vertex the tau originated from.

Traditionally, the tracks used to evaluate the TJVF are those passing the track selection criteria given in Section 4.1 and fall within $\Delta R < 0.2$ with respect to the TopoCluster barycentre of the reconstructed tau object. However, this track selection is not always optimal and a study was necessary to investigate the efficiency of the TJVA algorithm in selecting the correct vertex for the current ATLAS software release.

5.1 TJVA Algorithm Efficiency Study

Associating the reconstructed tau candidate to the correct primary vertex, where the tau originated, is important and can impact the characteristics of the final tau object. The efficiency of the TJVA algorithm can be assessed by its ability to associate a τ-lepton to the correct production vertex in MC events. Truth information in MC provides the coordinates of the primary vertex in the detector and the *correct* reconstructed vertex is considered to be the one closest to the truth vertex in z.

The TJVA algorithm is validated with events at $\sqrt{s} = 8$ TeV and then the algorithm track selection is optimised for $\sqrt{s} = 13$ TeV events. All studies are performed using $Z \to \tau\tau$ MC samples generated by PYTHIA8

Note, analysis tools provided by the ATLAS tau working group were implemented to apply the tau selection and also match objects in the sample to truth particles. Hadronic tau candidates used in the efficiency calculations and following plots were required to have met basic criteria: all reconstructed tau leptons were required to have been matched to a truth tau, $p_{\mathrm{T}} > 20$ GeV and $|\eta| < 2.5$. The crack region of the ATLAS detector is excluded.

5.1.1 TJVA Efficiency at 8 TeV

The TJVA algorithm performed well in Run 1 analyses at $\sqrt{s} = 8$ TeV. The technique was implemented in this study to validate and to provide benchmark efficiency results to improve on at 13 TeV. Efficiency tests were performed for both 1-prong and 3-prong taus separately. Plots for 8 TeV showed a recovery in efficiency for the TJVA algorithm over the default primary vertex chosen in reconstruction, the highest $\sum p_T^2$ of the associated tracks to the vertex. It is important to note there was a BDTMedium requirement on the

taus which unknowingly introduced a bias to the TJVA algorithm causing an almost 100% efficiency, particularly for 3-prong decays. This requirement was removed for the remainder of the study.

The efficiency of the TJVA algorithm in identifying the correct primary vertex experienced the highest gain at low p_{T}^{τ} when compared to the default primary vertex, an almost 10% increase in effcency is shown in Figure 5.2a. Additionally, the TJVA method improves efficiency when there is a high number of reconstructed vertices, which is important in higher pile-up environments.

5.1.2 Split Vertices

Events where the TJVA selected an incorrect vertex were suspected to be because of *split vertices*, where a truth vertex is reconstructed as two vertices very close to each other. The cases where the TJVA algorithm was incorrect could have been because the other vertex of the split which was in fact not closest to the truth vertex, therefore labelled as incorrect.

A simple sorting algorithm was used to identify the closest and second closest vertex to the truth vertex from the container of reconstructed vertices. The distance used here is in the longitudinal direction along the beam line. The algorithm aims to find the closest and second closest vertex by minimising $\Delta z = (z_{\mathrm{Truth}} - z_i)$ where z_i is the position of vertex i along the z-axis between the truth vertex and the reconstructed vertices. The distance transverse to the beampipe was negligible.

Figure 5.3 shows the Δz between the truth vertex and the second closest vertex. Events where the distance between the second closest and the truth is comparable to the vertex resolution of the detector implies splitting. It is unlikely to be this close and still not be the closest reconstructed vertex with current vertex reconstruction.

It is important to identify vertices that were split using the Δz between the truth vertex and the tau vertex (TV) chosen by the TJVA method. The distribution of Δz produced three regions of interest: $|\Delta z| < 0.5$ mm, 0.5 mm $\leq |\Delta z| < 3$ mm and $|\Delta z| \geq 3$ mm. These values for $|\Delta z|$ between the truth vertex and the TJVA chosen vertex, when incorrect, were used to separate regions of $|\Delta z|$ between the closest and second closest vertices. If this $|\Delta z|$

is less than 0.5 mm, the vertices are considered to be one vertex for this event that have been reconstructed as two.

Primary vertex resolution for taus from events with split vertices was similar to that of the primary vertex resolution for all taus. Taking into account all of the cases where the TJVA algorithm identifies the wrong vertex, only 2% of the time it is due to splitting. More is shown in Appendix B.1.

5.1.3 TJVA Efficiency at 13 TeV

The TJVA was implemented for Run 2 using a track selection criteria where all tracks associated to the $\tau_{\text{had-vis}}$ candidate were used in the calculation and the efficiency shown in Fig. 5.5. Although the TJVA method performed better than the default primary vertex association method, it was still not optimised and gave the opportunity to maximise efficiency.

To optimise the track selection for the TJVF calculation, the d_0 and $z_0 \sin\theta$ restrictions are removed. The expected recovery of efficiency is seen particularly at low p_T and high pileup conditions, performance is similar to that of 8 TeV. The optimised track selection efficiencies are shown in Figure 5.6 and resulted in a $\sim$1-2% efficiency increase. The TJVA technique with optimised track selection is implemented in Release 21 of ATLAS reconstruction.
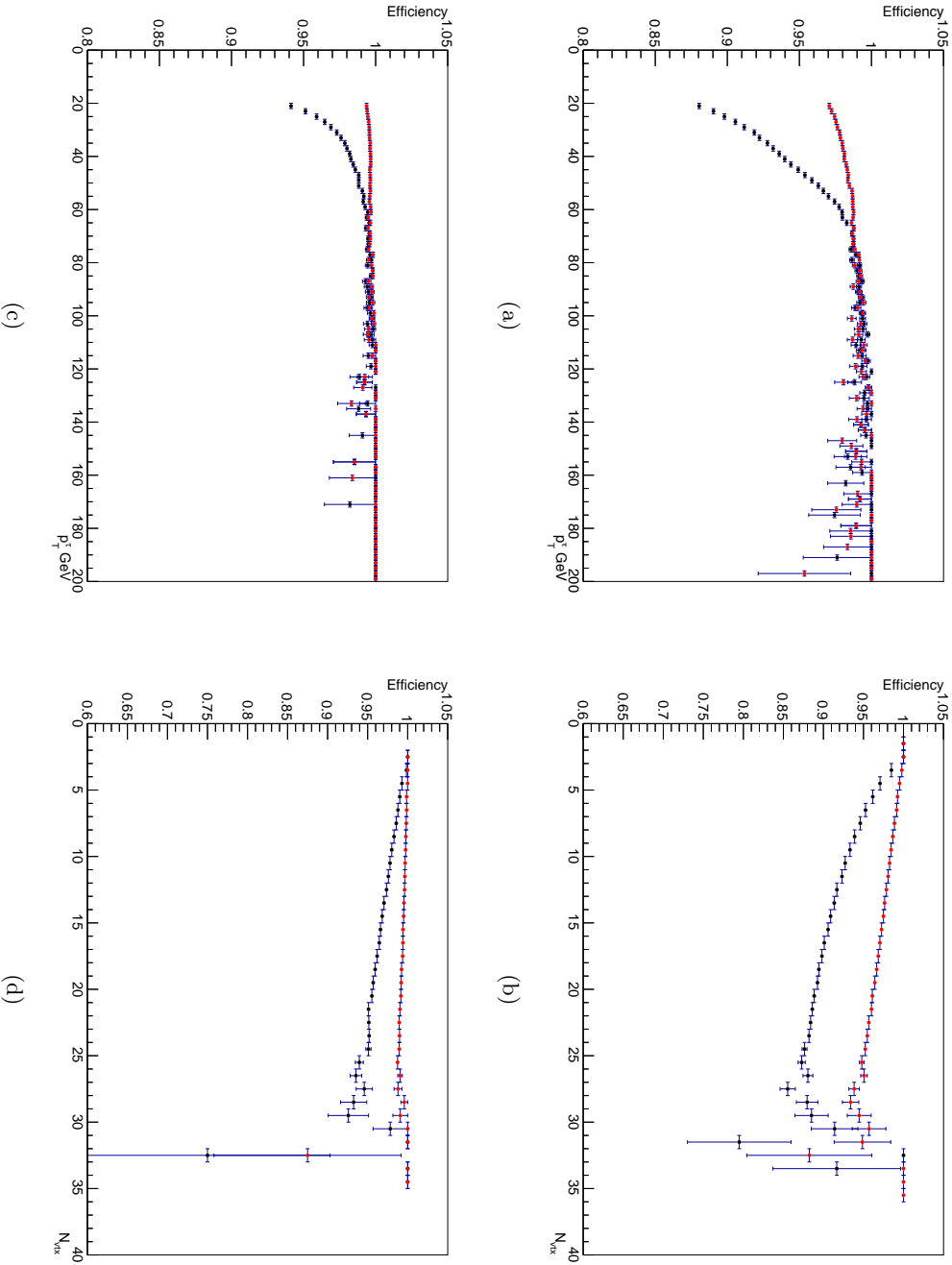
Figure 5.2: Efficiency for correct production vertex assignment in 1-prong (top) and 3-prong (bottom) τ decays for the **TJVA algorithm** and the **default choice of the vertex** with the highest $\sum p_T^2$. Efficiency is shown in (a) and (c) as a function of $\tau_{\text{had-vis}}$ p_T and the number of reconstructed vertices (b) and (d) in the event.
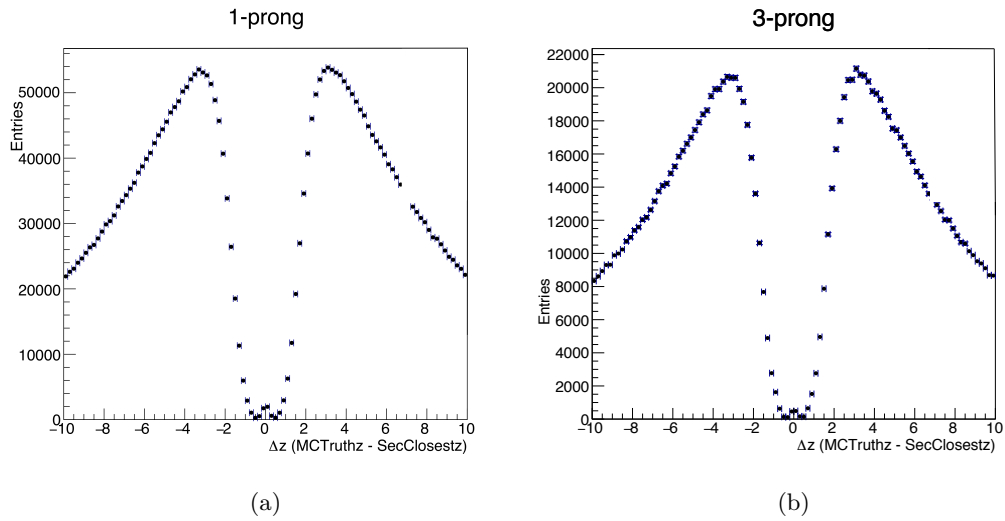
Figure 5.3: The Δz between the truth vertex and the second closest reconstructed vertex for 1-prong τ decays (a) and 3-prong τ decays (b).
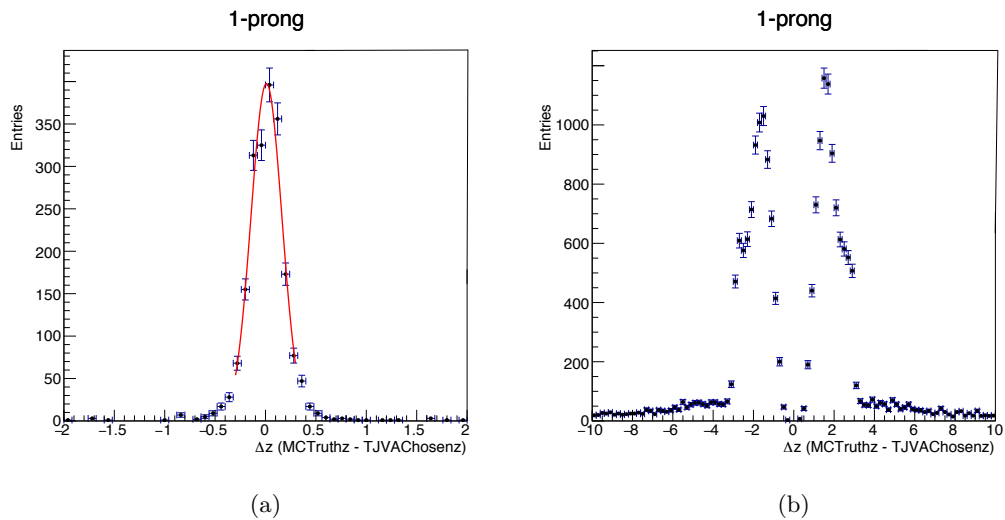
Figure 5.4: The Δz between the truth vertex and reconstructed vertex chosen by the TJVA algorithm when it is incorrect at different distances between the closest and second closest vertices to the truth vertex. (a) shows taus from events with a distance of less than 0.5 mm between the closest and second closest vertices and 0.5 mm - 3.0 mm, (b).
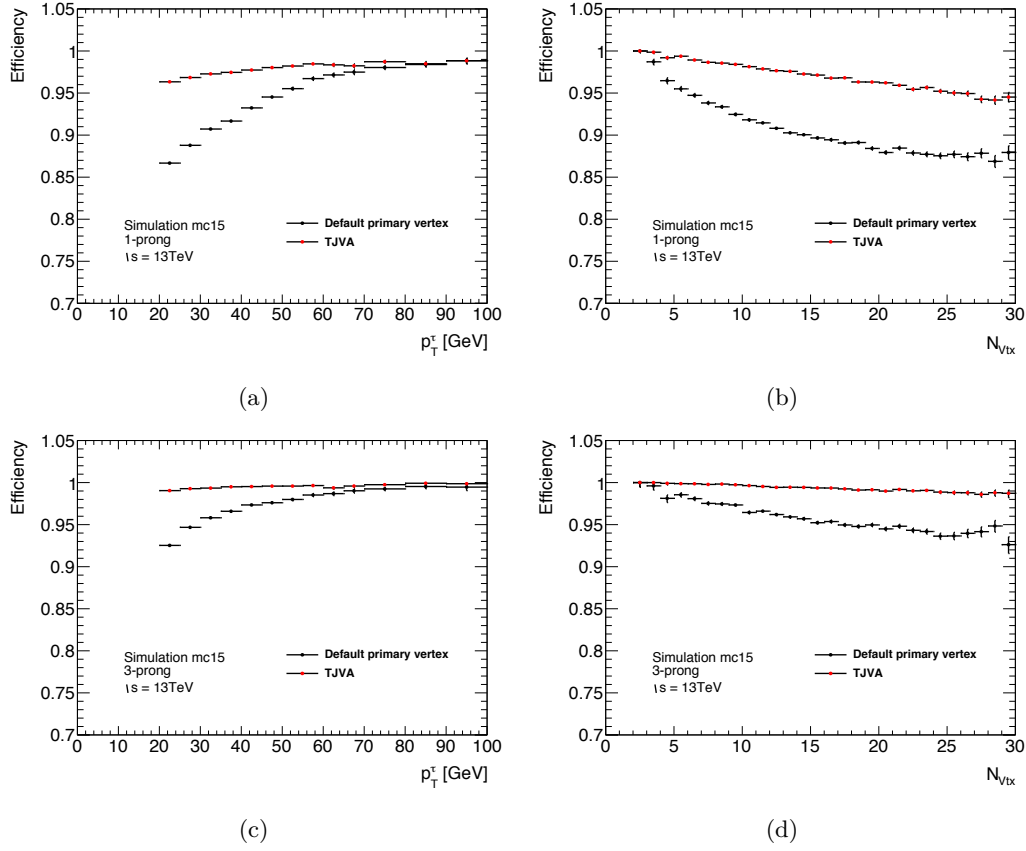
Figure 5.5: Efficiency for production vertex assignment in 1-prong and 3-prong τ decays for the tau reconstruction algorithm without optimal track selection and the default choice of the vertex with the highest $\sum p_{\mathrm{T}}^2$, as a function of $\tau_{\mathrm{had\text{-}vis}}$ p_{T} (a,c) and of the number of reconstructed vertices in the event (b,d) from MC.
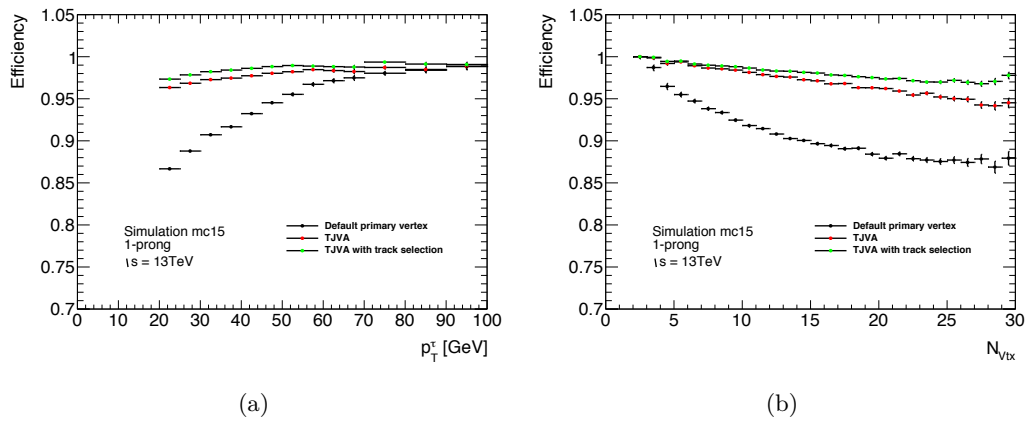
Figure 5.6: Efficiency for production vertex assignment without optimal track selection in 1-prong τ decays for the tau reconstruction algorithm and the default choice of the vertex with the highest $\sum p_{\mathrm{T}}^2$, compared to the correct production vertex assignment. Efficiency as a function of $\tau_{\mathrm{had\text{-}vis}}$ p_{T} (a) and of the number of reconstructed vertices in the event (b) from MC.

Chapter 6

Analysis Strategy

This chapter describes the strategy employed in the di-Higgs analysis where a selection is applied to select events compatible with a $b\bar{b}\tau_{\mathrm{had}}\tau_{\mathrm{had}} + E_{\mathrm{T}}^{\mathrm{miss}}$ final state. This analysis is then reinterpreted for a third-generation scalar leptoquark search with a final state of $b\tau_{\mathrm{had}}\bar{b}\tau_{\mathrm{had}}$. Both anaylses are very similar in their method and the commonalities associated are explained in detail throughout this chapter, including preselection, final multivariate discriminant strategy, signal and backgrounds used and also systematic uncertainties. Any figures and tables shown in this chapter are taken from the di-Higgs analysis.

The two analyses differ in a few areas such as signal samples used, boosted decision tree (BDT) discriminating variables and selection. All details of differences are stated within each relevant results chapters and references to this common analysis strategy chapter are made very clear to avoid confusion.

6.1   General Strategy

The general strategy for analyses addressed in this thesis begins with initial preselection with trigger matching for a final state of two hadronically decaying taus and two anti-k_T jets with a radius parameter of $R = 0.4$. Control regions are then defined to validate background modelling and develop data-driven methods if MC is inadequate. Events are divided into subcategories depending on the number of b-tagged jets, primarily 0-tag, 1-tag and 2-tag regions. Finally, a boosted decision tree is trained on major backgrounds and when applied to the analysis, the final BDT score is used to compare to signal hypotheses and set exclusion limits if no significant excess is present.

6.1.1 Object Selection

In addition to the basic ATLAS object reconstruction, further object selection and identification is required before the analysis specific event selection.

- Hadronic taus

    - $p_{\mathrm{T}} > 20$ GeV

    - $|\eta| < 2.5$ (veto $1.37 < |\eta| < 1.52$)

    - one or three tracks

    - unit charge

    - Pass BDTMedium ID working point.

- Jets

    - Anti-k_{T} with a radius parameter $R = 0.4$

    - $p_{\mathrm{T}} > 20$ GeV

    - $|\eta| < 2.4$ (veto $1.37 < |\eta| < 1.52$)

- b-jets

    - Jets originating from b-quarks are identified using the MV2c10 multivariate discriminant described in Chapter 4

    - Working point that corresponds to an average tagging efficiency of 70% for b-jets in $t\bar{t}$ events.

6.1.2 Fake Taus

Jets are often mis-identified as tau candidates and can be notoriously difficult to model in Monte Carlo estimations and in the signal region. To introduce an alternative method for estimating *fake* taus, it is important to design a control region in which there is an abundance of jets faking the experimental signature of hadronic taus (fakes) using an *anti-tau* selection. Anti-taus are defined as tau candidates that have a tau-ID BDT score above the threshold of 0.35, which is always less than loose selection. The minimum BDT score in the selection

ensures the jets in the region still have tau-like properties and makes sure the composition of gluon and quark jets is closer to the Medium ID signal region. Note, anti-taus are considered to be tau candidates when it comes to E_T^{miss} calculations.

6.1.3 Triggers

To select events with a final state of two hadronic taus, both analyses use two unprescaled triggers for the entire 2015-2016 dataset. Offline reconstructed τ-leptons are required to match to online taus that pass either the Single Tau Trigger (STT) or the Di-Tau Trigger (DTT) for the event to be considered. The specific triggers used changes depending on the run period and in the scenario where both triggers are matched the STT events take precedence.

The single τ trigger requires a p_{T} threshold of 80, 125 or 160 GeV on the leading tau (depending on the data-taking period), while the di-τ trigger requires a p_{T} threshold of 35 (25) GeV on the leading (sub-leading) tau. During the 2016 data-taking period, the di-tau trigger also required the presence of an additional jet at Level-1 passing a 25 GeV p_{T} threshold.

The triggers used are listed below.

- Single tau triggers:

  - 2015 and 2016 Period A: HLT_tau80_medium1_tracktwo_L1TAU60

  - 2016 Periods B - D3: HLT_tau125_medium1_tracktwo

  - 2016 Periods D4 - end of 2016: HLT_tau160_medium1_tracktwo

- Di-tau triggers:

  - 2015: HLT_tau35_medium1_tracktwo_tau25_medium1_tracktwo_L1TAU20IM_2TAU12IM

  - 2016: HLT_tau35_medium1_tracktwo_tau25_medium1_tracktwo_L1TAU20IM_..._L1J25

6.2 Mass Reconstruction

The invariant mass reconstruction of experimental final states is crucial in the search for new physics and also in resonance precision measurements. Difficulty arises when a resonance decays to a pair of τ-leptons. Neutrinos in the process can carry a significant portion of energy and then evade detection leading to inaccurate reconstructed mass values. The sensitivity of analyses searching for resonances in mass final discriminants depends on the width of the signal invariant mass distributions compared to often wide background process spread. In an analysis involving the reconstruction of a Higgs decay to two hadronic taus, invariant mass reconstruction can directly impact final di-Higgs searches.

Hadronic tau decays involve the creation of one neutrino whose full energy cannot be correctly determined in *pp* collisions. The missing transverse energy object used in ATLAS is essentially the total transverse momentum of all neutrinos (and other undetected particles) in the event. This can be a problem for processes with multiple neutrinos because more than one particle is treated as one and information is lost. Heavy resonances decaying to a di-tau system offers another level of complexity where the two τ-leptons are usually produced back-to-back. In the decay of the τ-lepton pair, any missing energy from one tau decay is carried away by a neutrino. However, this is partially counterbalanced by the missing energy from another neutrino from the τ-lepton pair with respect to a missing energy calculation. As a result, the invariant mass of the heavy resonance is not easily reconstructed from visible τ-decay products and E_T^{miss}. Many techniques exist for di-tau mass reconstruction.

Previously, common hadron collider methods to reconstruct the mass of di-tau final states led to very broad distributions with long tails for signal processes which makes them difficult to separate from background. For example, the "Collinear Approximation Technique" was first proposed to reconstruct a Higgs boson decay to $\tau\tau$ with an additional energetic jet requirement [153]. This method was frequently used at the LHC [154, 155]. As the name suggests it relies on the assumption that the two neutrinos are collinear with respect to the visible components of the tau decays and also all missing tranverse energy is due to solely neutrinos in the event.

The total momentum carried away by the neutrinos from each tau decay can be estimated using these equations for the x and y components of the missing energy

$$E_{\mathrm{T},x}^{\mathrm{miss}} = p_{\mathrm{miss}_1} \sin\theta_{vis_1} \cos\phi_{vis_1} + p_{\mathrm{miss}_2} \sin\theta_{vis_2} \cos\phi_{vis_2}, \tag{6.1}$$

$$E_{\mathrm{T},y}^{\mathrm{miss}} = p_{\mathrm{miss}_1} \sin\theta_{vis_1} \cos\phi_{vis_1} + p_{\mathrm{miss}_2} \sin\theta_{vis_2} \cos\phi_{vis_2} \tag{6.2}$$

where:

- $p_{\mathrm{miss}_{1,2}}$ are the momenta of the missing component of the τ decay products,

- $\theta_{vis_{1,2}}$ and $\phi_{vis_{1,2}}$ are the polar and azimuthal angles of the missing τ decay products.

Then the invariant mass of the whole system can be described as

$$M_{\tau\tau} = \frac{m_{\mathrm{vis}}}{\sqrt{x_1 \cdot x_2}}, \tag{6.3}$$

$$x_{1,2} = \frac{p_{vis_{1,2}}}{p_{vis_{1,2}} + p_{miss_{1,2}}}, \tag{6.4}$$

where:

- $p_{\mathrm{vis}_{1,2}}$ are the momenta of the visible τ decay products,

- $m_{\mathrm{vis}_{1,2}}$ are the invariant mass of the visible components of the di-τ decay products.

Although the collinear approximation technique is successful in achieving a reasonable mass resolution for events where the di-tau system is boosted, this is only a small fraction of events and the whole method is very sensitive to the $E_{\mathrm{T}}^{\mathrm{miss}}$ resolution. This leads to an over-estimation of the $\tau\tau$ mass and gives tails to the resulting mass distribution which in turn causes undesirable consequences in the low-mass regime near the Higgs and $Z \to \tau\tau$ peak.

The Missing Mass Calculator

To improve upon the collinear approximation method, the Missing Mass Calculator (MMC) [156] allows for a complete reconstruction estimation of the di-tau system without the limitations of previous methods and without a sacrifice in reconstructed mass resolution. Perfect detector resolution is assumed and that there are no other neutrinos in the event

other than those resulting from $\tau\tau$ decays. Using the measured value for the tau lepton invariant mass, M_τ, the equations to construct the MMC become

$$E_{\mathrm{T},x}^{\mathrm{miss}} = p_{\mathrm{miss}_1} \sin\theta_{vis_1} \cos\phi_{vis_1} + p_{\mathrm{miss}_2} \sin\theta_{vis_2} \cos\phi_{vis_2}, \tag{6.5}$$

$$E_{\mathrm{T},y}^{\mathrm{miss}} = p_{\mathrm{miss}_1} \sin\theta_{vis_1} \cos\phi_{vis_1} + p_{\mathrm{miss}_2} \sin\theta_{vis_2} \cos\phi_{vis_2}, \tag{6.6}$$

$$M_{\tau_1}^2 = m_{vis_1}^2 + m_{miss_1}^2 + 2\sqrt{p_{vis_1}^2 + m_{vis_1}^2}\sqrt{p_{miss_1}^2 + m_{miss_1}^2}$$
$$- 2p_{vis_1}p_{miss_1} \cos\Delta\theta_{vm_1}, \tag{6.7}$$

$$M_{\tau_2}^2 = m_{vis_2}^2 + m_{miss_2}^2 + 2\sqrt{p_{vis_2}^2 + m_{vis_2}^2}\sqrt{p_{miss_2}^2 + m_{miss_2}^2}$$
$$- 2p_{vis_2}p_{miss_2} \cos\Delta\theta_{vm_2}, \tag{6.8}$$

where:

- $E_{\mathrm{T},x}^{\mathrm{miss}}$ and $E_{\mathrm{T},y}^{\mathrm{miss}}$ are the x- and y-components of the $E_{\mathrm{T}}^{\mathrm{miss}}$ vector,

- $p_{\mathrm{vis}_{1,2}}$ are the momenta of the visible τ decay products,

- $m_{\mathrm{vis}_{1,2}}$ are the invariant masses of the visible τ decay products,

- $\theta_{vis_{1,2}}$ and $\phi_{vis_{1,2}}$ are the polar and azimuthal angles of the visible τ decay products.

- Finally, $\Delta\theta_{vm_{1,2}}$ is the angle between the vectors p_{miss} and p_{vis} for each tau.

For hadronic decays, $m_{\mathrm{miss}_{1,2}}$ are set to 0 because of the single neutrino involved in the decay. The number of unknown parameters exceeds the number of constraints so there is not enough information to find an exact solution. However, knowledge of the τ-lepton decay kinematics can distinguish between the more likely solutions from the rare cases. The additional knowledge on the tau decay topologies is incorporated as probability density functions in a global likelihood scan to provide additional constraints and obtain a better estimation of $M_{\tau\tau}$. The MMC is the technique used to reconstruct the di-tau mass in this thesis in the di-Higgs analysis, where $m_{\tau\tau}^{\mathrm{MMC}}$ acts as an important discriminating variable. Note, this variable is omitted for the leptoquark search because the τ-leptons are not paired and do not originate from the same parent particle, therefore the variable is not applicable.

6.3   Event Preselection

Preselection is the first stage of the event selection to filter objects and introduce a number of requirements to select signal-like events and reject unwanted events. The common preselection for all analyses addressed in the thesis is summarised below.

- **Good Runs List (GRL)**: During data recording in ATLAS, the quality of the data is monitored continuously by online software and additional shifter monitoring. The GRL is a list of data runs used by all analyses where the entire ATLAS detector was completely operational and working as intended.

- **Vertex Selection**: Only events where at least one primary vertex with a minimum of two associated tracks are used (track $p_{\mathrm{T}} > 400$ MeV).

- **Jet Cleaning**: Events containing bad jets are discarded. Bad jets are defined as those not associated to any real energy deposits in the calorimeter due to beam conditions and hardware problems.

- **DTT events**:

  - A total of two hadronic taus with $|\eta| < 2.5$. The highest p_{T} (leading) tau must have a $p_{\mathrm{T}} > 40$ GeV and the second (sub-leading) tau is required to have a $p_{\mathrm{T}} > 30$ GeV. Figure 6.1 shows a hadronic tau trigger efficiency turn on curve, demonstrating the need for a large offline p_{T} cut.

  - At least two jets are required in each event. Due to the lowest unprescaled DTT having a Level-1 trigger requirement, there is a p_{T} threshold on both jets. The leading (sub-leading) jet must have a $p_{\mathrm{T}} > 80$ (20) GeV to operate at an acceptable trigger efficiency of approximately 90%.

- **STT events**:

  - A total of two hadronic taus with $|\eta| < 2.5$. Depending on data taking period, the leading tau is required to have a $p_{\mathrm{T}} > 100$, 140 or 180 GeV to ensure high trigger efficiency with the trigger thresholds of 80, 125 or 160 GeV. The sub-leading tau must have a $p_{\mathrm{T}} > 20$ GeV.

  - At least two jets with $p_{\mathrm{T}} > 45$ (20) GeV in the event.

- **Leptons**: Events with electrons or muons that meet the object selection criteria are vetoed.

- **Charge**: Both taus are required to be of opposite charge.
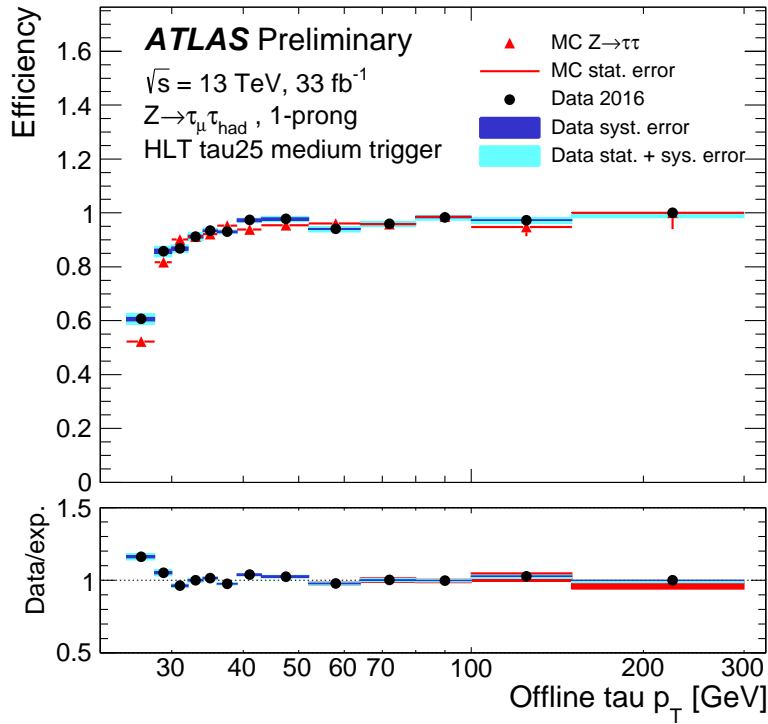
Figure 6.1: Efficiencies of the HLT tau25 medium trigger as a function of the p_T of the offine τ_{had} probe selected in $Z \to \mu\tau_{had}$ [157].

6.3.1 Overlap Removal Strategy

When physics objects are reconstructed within a certain distance to each other, defined by ΔR between objects, a procedure must be in place to give priority and avoid bias in the event. The table below describes the approach for a selected particle and the overlapping object in $\eta - \phi$ space.

Physics Object	Overlapping Object	Within ΔR	Priority
Electron	Jet	0.2	Electron
Jet	Electron	0.4	Jet
Muon	Jet	0.4	Muon
Jet	Muon	0.4	Jet
Electron	Muon	0.2	Muon
Muon	Tau-jet	0.2	Muon
Electron	Tau-jet	0.2	Electron
Tau-jet	BDTMedium tau-jet	0.2	Best reconstructed object
	b-tagged jet		
	Anti-tau		
	Light jet		

Table 6.1: Overlap removal procedure.

6.4 Background Estimation

Accurately predicting background contributions is essential for any analysis to draw meaningful conclusions from statistical interpretations of the observed data. The main contributing backgrounds considered throughout this thesis are $t\bar{t}$, $Z/\gamma* \to \tau\tau$ produced in association with heavy-flavour jets (bb, bc, cc), and multi-jet events. The majority of background processes are taken from Monte Carlo simulations such as $t\bar{t}$ events where both hadronic taus are real, $Z \to \tau\tau$ + heavy-flavour (HF) jets, $W \to \tau\nu$+jets and di-boson events.

Multi-jet and $t\bar{t}$ events where one or more hadronic taus comes from mis-reconstructed jets (so-called 'fakes' or 'fake taus') are estimated using data-driven methods. The complete procedure for estimating multi-jet events is described in the following chapter where selected hadronic taus are replaced by anti-taus to better represent the jet contribution to the selection. Control regions and event categories are constructed to validate the performance of the background modelling to develop trust in the method for final hypothesis testing.

6.4.1 Fake Tau Background Estimation for $t\bar{t}$ Events

Estimating the portion of $t\bar{t}$ events with at least one jet faking a τ-lepton is done by using the MC as a template and then applying a *fake rate* correction that has been derived in a control region. For the $\tau_{\mathrm{had}}\tau_{\mathrm{had}}$ channel, a control region is constructed to calculate fake

rates using a $\tau_{\text{lep}}\tau_{\text{had}}$ channel where one of the taus decays leptonically. The motivation for this comes from the fact it is much easier to create a data sample rich in semi-leptonic $t\bar{t}$ events to derive a fake rate (FR) compared to the fully hadronic channel. The selection for this control region requires the use of a single lepton trigger (SLT) and additional selection as follows:

- Single lepton triggers:

  - 2015

    - HLT_e24_lhmedium_iloose_L1EM20VH || HLT_e60_lhmedium || HLT_e120_lhloose

    - HLT_mu24_imedium || HLT_mu50

  - 2016 Periods A - D3

    - HLT_e24_lhmedium_ivarloose || HLT_e60_lhmedium_nod0 || HLT_e140_lhloose_nod0

    - HLT_mu24_imedium || HLT_mu50

  - 2016 Periods D4 - end of 2016

    - HLT_e26_lhtight_ivarloose || HLT_e60_lhmedium_nod0 || HLT_e140_lhloose_nod0

    - HLT_mu26_ivarmedium || HLT_mu50

- **SLT events**:

  - Exactly one *tight* electron or one *medium* muon at ID level with p_{T} a minimum of 1 GeV above the threshold for the trigger currently in use for that period of data taking.

  - One hadronic tau with $p_{\text{T}} > 20$ GeV and $|\eta| < 2.3$.

  - At least two jets with $p_{\text{T}} > 45$ (20) GeV in the event.

In addition to this selection, a cut is made on the transverse mass, m_T^W, between the lepton and E_T^{miss}. Given by

$$m_T^W = \sqrt{2 p_T^l E_T^{miss} (1 - \cos \Delta\phi)}, \qquad (6.9)$$

where p_T^l is the transverse momentum of the lepton. A cut of $m_T^W > 80$ GeV is required because signal events tend to have a lower m_T^W than the $t\bar{t}$ process. The transverse mass of a lepton and neutrino decaying from a W boson in a $t\bar{t}$ event tends to peak at $m_W \approx 80$ GeV.

The fake rate (FR) is defined as the probability for a jet to pass tau ID requirements

$$FR = \frac{N(\text{pass})}{N(\text{total})}, \qquad (6.10)$$

where $N(\text{pass})$ is the total number of events in which a jet passes online tau ID and the offline ID requirement of being at least *medium*. $N(\text{total})$ is all events passing SLT selection and having a tau-ID BDT score > 0.35 but also failing 'Medium' ID. Fake rates are calculated separately for 1-prong and 3-prong taus as a function of tau η inclusively across both electron and muon channels. All $t\bar{t}$ components and other backgrounds with true τ-leptons are subtracted from the control region.

The template fake tau $t\bar{t}$ events where the fake rates are applied are taken from MC and selected as those that pass the $\tau_{had}\tau_{had}$ channel event selection but fail any other trigger or offline tau ID to avoid biasing the prediction. Threshold cuts on the p_T to mimic DTT selection are applied to be closer to that of the signal region. Fake rates are applied to all tau candidates in this $t\bar{t}$ selection that are not matched to a hadronic tau at generator level. In the event where both reconstructed taus are fake the FR is applied separately to each tau, not on a per-event basis.

Figures 6.2 shows the fake rates for the di-Higgs analysis for 1-prong and 3-prong taus separately as a function of tau p_T.
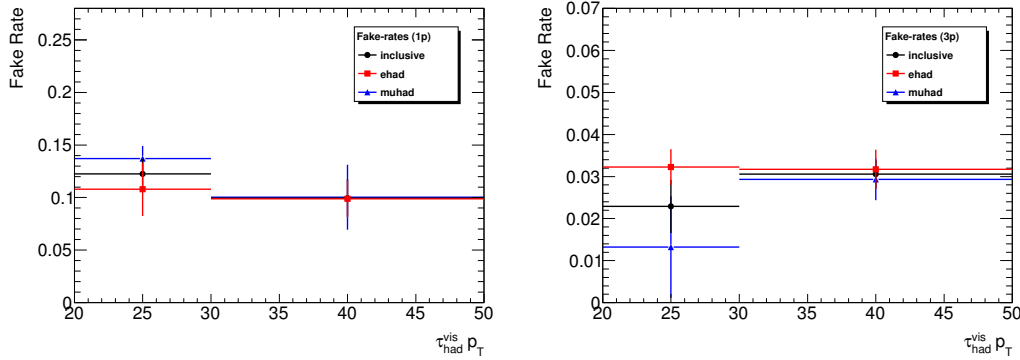
Figure 6.2: Fake rates for 1-prong (left) and 3-prong (right) taus for the $t\bar{t}$ background estimation procedure in the $\tau_{\mathrm{had}}\tau_{\mathrm{had}}$ channel. The categories 'ehad' and 'muhad' refer to the semi-leptonic decay modes with $e\tau_{had}$ and $\mu\tau_{had}$ final states, respectively for the di-Higgs analysis.

6.5 Boosted Decision Trees

The main goal of any physics analysis is to maximally reject background while obtaining the highest signal detection efficiency possible. *Cut based* analyses make use of several single observables to consecutively discriminate and rarely have the desired differentiating power and can fail where backgrounds have similar topologies to that of the signal. In addition to this, cut based analyses often leave the signal region with too few events to statistically evaluate, making it impossible to build meaningful results. High energy physics analyses have widely used techniques to combine several observables to build a multivariate (MVA) method and a more powerful final discriminant. This technique is used particularly in analyses where cut based methods have reached their limitations.

Boosted decision trees (BDT) [158] are a type of machine learning classifier and work to maximise signal and background separation through a multi-dimensional *cut* technique of several chosen variables over the whole parameter space. A BDT is able to take into account correlations between chosen input variables and optimise signal to background separation.

Decision trees [159] aim to automatically find the optimal way to split between two event classes (signal and background in this case) based on a sequence of given parameter selection requirements. Each sample is split multiple times until the specified number of splits for the tree (*MaxDepth*) or the minimum number of events in the terminal nodes (*MinNodeSize*) is reached. For many analyses the criterion used to maximise event class separation would

BDT parameter	Value
BoostType	AdaBoost
AdaBoostBeta	0.15
NTrees	200
MaxDepth	4
MinNodeSize	5%
NCuts	100

Table 6.2: Parameters used for BDT training in the $\tau_{\mathrm{had}}\tau_{\mathrm{had}}$ channel.

be the purity of the signal. Boosting [160, 161] is an extension to the method which can improve the stability and performance of decision trees into a single final discriminant. Several decision trees are combined into a 'forest' where events that were misidentified in the first tree are given higher weights or a *boost* relative to the correctly-identified events.

The boosting technique employed by this analysis is the adaptive boosting implementation of TMVA [158]. For adaptive boosting each new tree starts from the same initial sample but the events are given a new weight α_i based on how it was classed on the previous i-th tree. The weight α_i is defined as

$$\alpha_i = \left(\frac{1-\epsilon}{\epsilon}\right)^{\beta},\tag{6.11}$$

where ϵ is the fraction of misclassified events from the previous tree and β is a configurable value. After boosting, a weighted average is taken from all trees and a final discriminant is formed, known as the BDT response. This score undergoes a transformation to map the response on the interval of -1 to $+1$. For analyses addressed in this thesis, signal-like events have a score close to 1 and background-like events have score closer to -1. The criteria and values concerning BDTs throughout this thesis are shown in Table 6.2.

A multivariate analysis using BDTs goes through two stages, training and application. Using the information given by MC and the discriminating variables provided, the method is trained to recognise signal events and distinguish against background. The resulting BDT is then applied to data. Training and application samples are k-folded to make sure the trained data and application data are statistically independent.

In this case, training is performed on odd events which is then applied to even events and vice versa ($k=2$). Specific information on the training and performance of the BDT strategy is addressed in the retrospective following chapters.

For the analyses included in this thesis, training is performed using background events from $t\bar{t}$, $Z \to \tau\tau$ + heavy-flavour jets, and multi-jet estimations.

6.6   Statistical Analysis Procedure

The yields of background and signal processes can be extracted from the statistical analysis of the data and the MC predictions in the provided regions using the final BDT discriminator previously described. The process begins with background predictions being validated in control regions and a search is performed for a statistically deviation from the background-only model hypothesis shortly after unblinding the data in the signal region.

In this thesis, the CL_s method [162] approach is used to test the degree at which the data is consistent with the background expectation given by MC. In the absence of a signal or significant excess, limits are set to evaluate the compatibility of the data with a particular model. The procedure described in this chapter describes the statistical techniques employed for both, the di-Higgs analysis and the reinterpretation for a scalar leptoquark search. Nuisance parameters (NP) are included in the final statistical model that relate to the systematic uncertainties and floating normalisations of background contributions.

6.6.1   Input BDT Transformations

The output BDT score distributions are equally segmented into 1000 bins along the x–axis between values -1 and $+1$. The binning of the BDT score distributions is optimised to ensure that the background uncertainty is kept to below 50% of the signal fraction for all cases and if there is no signal in that bin the background uncertainty is required to be below 1%. Bins are consecutively merged, starting at the upper edge of the BDT spectrum, if the signal and background conditions are met and a minimum of 5 data events are within each bin. The statistical uncertainty becomes well distributed across all bins and the total background is now smooth after the transformation.

6.6.2 Likelihood Functions and Profiling

Following unblinding, the presence of a signal in the data is tested by comparing to *background-only* and *signal-plus-background* hypotheses. The test of a hypothesis is generally performed in terms of a *test statistic* where the data is reduced to one value which is able to distinguish between hypotheses and quantify the analysis. The number of events in the bins of the BDT score distributions form the basis of the compatibility measurement. The expected number of events in bin i (n_i) can be expressed as

$$n_i = \mu \cdot s_i + b_i, \tag{6.12}$$

where s_i and b_i are the number of expected signal and background events in the bin i. The signal strength factor μ is defined as the ratio of the observed or expected cross-section to that of the SM cross-section

$$\mu = \frac{\sigma_{obs}}{\sigma_{SM}}. \tag{6.13}$$

A signal strength of $\mu = 0$ represents the background-only hypothesis with an absence of any signal. Whereas a value of $\mu = 1$ agrees with the signal-plus-background hypothesis where the signal is compatible with the SM.

The statistical analysis is based on a binned likelihood function $\mathcal{L}(\mu)$ and the best estimate of the signal strength is obtained when this likelihood is maximised. The effects of systematic uncertainties on the predictions are encoded in the set of nuisance parameters θ and are incorporated into the likelihood. The total number of events in a given bin depends on μ and θ. The convention is for a value $\theta = \pm 1$ to represent a $\pm 1\sigma$ variation of a systematic while a value of $\theta = 0$ corresponds to the central nominal value of the prediction. These nuisance parameters adjust the expected yields of background and signal in each bin according to a particular uncertainty. The final values correspond to the values that best fit the data.

Throughout this thesis, the test statistic is based on a profile likelihood ratio (q_μ) defined as follows

$$q_\mu = -2 \ln \left(\frac{\mathcal{L}(\mu, \hat{\hat{\theta}}_\mu)}{\mathcal{L}(\hat{\mu}, \hat{\theta})} \right), \tag{6.14}$$

where $\hat{\mu}$ and $\hat{\theta}$ are the values of the parameters that maximise the likelihood function and $\hat{\hat{\theta}}_\mu$ are the nuisance parameter values that maximise the likelihood function for a given value of μ. This is known as profiling, where for each value μ the values of θ are chosen such that the numerator log-likelihood function $\mathcal{L}(\mu, \hat{\hat{\theta}}_\mu)$ is maximised.

The sensitivity and performance of an experiment can be characterised by the expectation value under the assumption of a particular hypothesis and obtain a distribution of the test statistic. One method is the toy-MC method where datasets are generated that randomly sample the model at all points in the parameter space and calculate the value of the test statistic for each individual dataset. On the other hand, an asymptotic approximation can be used [163] for the final statistical fit procedure, the so-called *Asimov* dataset is constructed in a way to deliver the median sensitivity. The Asimov dataset is formed from MC prediction and is able to obtain the true value of all parameters when it is used to evaluate estimators. Nuisance parameters by definition take the nominal value in the Asimov dataset. This approach is less computationally demanding [164, 165] and is the method considered in this thesis.

6.6.3   Limit Setting

In the absence of a statistically significant excess of events above the background expectation, upper limits can be set on a signal hypothesis to a particular confidence level (CL). Once the test statistic is identified, the agreement of data to a hypothesis is quantified by a p-value [164]. Given the value of the test statistic on observed data q_{obs}, the compatibility of the result with respect to the signal-plus-background hypothesis ($s+b$) and the background-only hypothesis (b) is given by the p-values

$$p_{s+b} = \int_{q_{\mathrm{obs}}}^{\infty} f(q\|s+b)dq, \tag{6.15}$$

$$p_b = \int_{q_{\mathrm{obs}}}^{-\infty} f(q\|b)dq. \tag{6.16}$$

Following the asymptotic approximation, the value of μ can be adjusted in the fit to put an upper limit on the cross section for a signal hypothesis following the CL approach [166, 167]. The 95% CL upper limit is set on the signal hypothesis using

$$CL_s = \frac{CL_{s+b}}{CL_b} = \frac{p_{s+b}}{1-p_b} \tag{6.17}$$

and adjusting μ until the value of $CL_s = 0.05$. The results quoted throughout this thesis follow this approach.

6.6.4 Pulls and Impact

While maximising the likelihood function, the fit has to "pull" a nuisance parameter from the expected value based on auxiliary measurement or MC study. The pull of a nuisance parameter θ from its expectation value θ_0 is defined as

$$\mathrm{pull}(\theta) = \frac{\hat{\theta} - \theta_0}{\sigma_\theta}, \tag{6.18}$$

where $\hat{\theta}$ is the post-fit value and σ_θ is the nuisance parameters associated uncertainty [168].

The parameter of interest calculated by the fit can change with the variation of a nuisance parameter. The measure of how much a parameter of interest varies with respect to a nuisance parameter change is known as the impact. For each nuisance parameter, the impact is defined as

$$\mathrm{Impact}(\theta) = \Delta\mu^\pm = \hat{\hat{\mu}}_{\theta_0 \pm \sigma_\theta} - \hat{\mu}, \tag{6.19}$$

where $\hat{\hat{\mu}}_{\theta_0}$ is the maximum likelihood estimation (MLE) of μ when θ is set to its expectation value plus or minus one standard deviation. All other nuisance parameters are profiled. Low impact parameters are discarded to simplify the fit procedure. The impact is sometimes given relative to the total uncertainty of the parameter of interest [165].

6.7 Heavy-Flavour Jets Background Normalisation

The Monte Carlo samples of Z boson production in association with heavy flavour (b, c) jets were generated using `Sherpa` 2.2.1 [169]. These samples do not describe data very well and have a normalisation issue for heavy-flavour jets. Figure 6.3 shows this, where the mismodelling of $Z \rightarrow \mu\mu$ + heavy-flavour jets is greatest. A control region has been defined orthogonal to the signal selection to normalise this background to data and provide a much better estimation. The control region is defined as $Z \rightarrow \mu\mu + 2$ heavy flavour jets (bb, bc, cc) events that satisfy the criteria that

- each muon must pass a single muon trigger,

- both muons have $p_{\text{T}} > 27$ GeV,

- di-muon invariant mass, $81 < m_{\mu\mu} < 101$ GeV,

- at least two jets with $p_{\text{T}} > 45$ (20) GeV in the event that fulfil b-tagging requirements,

- di-b-jet invariant mass, $m_{bb} < 80$ GeV and $m_{bb} > 140$ GeV to remove contributions from SM $Vh(h \rightarrow bb)$

This selection provides a high purity orthogonal sample which closely follows an event selection to that of signal events in the semi-leptonic di-Higgs analysis.

The normalisation is determined from the final fit by adding the control region as a single bin histogram and allowing the normalisation to float under the assumption the $Z \rightarrow \mu\mu + cc, bc, bb$ and $Z \rightarrow \tau\tau + cc, bc, bb$ normalisation factors are correlated in the two regions.

The (background-only post-fit) yields of different background processes in this region are given in Table 6.3.

Sample	Post-fit yield
$Z \to ll + (cc, bc, bb)$	8420 ± 550
Top quark	3950 ± 510
Other $(W + Z + (ll, lc, lb) + VV)$	520 ± 180
Total Background	12900 ± 110
Data	12897

Table 6.3: Event yields in the $Z \to \mu\mu + 2$ b-tag control region for a background-only fit. The category 'Other' includes contributions from W+jets, Z/γ^* + light-flavour jets, and di-boson processes.
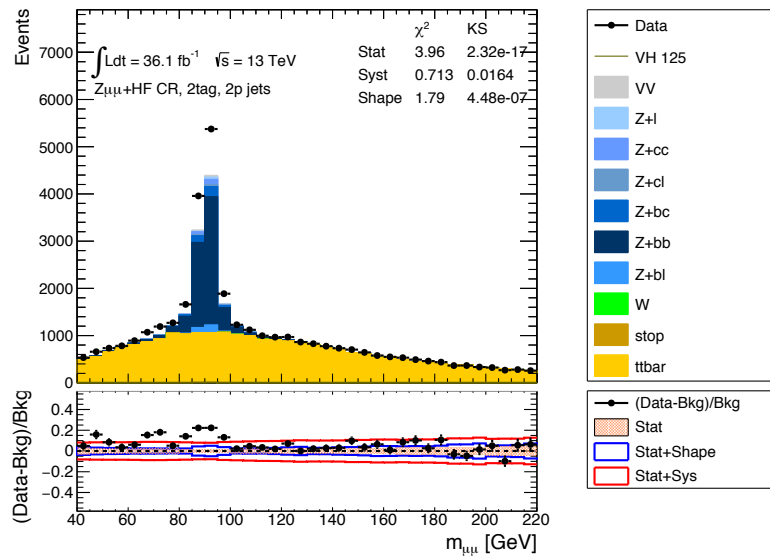
Figure 6.3: Pre-fit distribution of the di-muon invariant mass in the $Z \to \mu\mu + 2$ b-tag control region.

6.8 Systematic Uncertainties

Several sources of systematic uncertainty appear throughout the analysis and need to be properly taken into account to evaluate how compatible the observed data is to the background and signal estimations. Experimental uncertainties relate to the identification and reconstruction of physics objects as well as uncertainties originating from purely detector effects such as pile-up and integrated luminosity calculations. Measurements of background contributions from control regions can also be included in this category. Furthermore, theoretical uncertainties can arise from cross-section predictions and the Monte-Carlo event generation used. Due to some background contributions being estimated

from data, additional systematics are incorporated to address any uncertainties in the methods. This section labels the details of the analysis systematics and expresses the relative changes they may have on expected yields and distribution shapes. Note, the systematics associated with the multi-jet tau fake estimation are explained separately in detail in Chapter 7. All systematic uncertainties are included as normalisation and shape variations in the final fit. A full list and breakdown of systematics is shown in Chapter 8.

6.8.1 Experimental Uncertainties

Luminosity and Pile-up

A systematic is applied to all signal and background processes to account for uncertainties in the measurement of the integrated luminosity. It is derived from a preliminary measurement following the methods outlined in [170], where x-y beam separation scans were performed in August 2015 and May 2016. The value for the uncertainty on the integrated luminosity of the dataset is 2.1%. An additional shape and normalisation variation is included to account for any uncertainties on the pile-up reweighting procedure of the average number of interactions per bunch crossing $<\mu>$ of MC to data.

Taus

The systematic uncertainties associated with taus correspond to the reconstruction, identification and trigger efficiency. Additionally uncertainties are included for the resolution and scale of the tau energy measurements. Often systematics are calculated separately for 1- and 3-prong taus and tau objects at high-p_T some examples are as follows.

- Systematic uncertainties are included for the efficiency of reconstructing the correct number of tracks as the number of charged decay products originating from the tau lepton. Detector material, pile-up and threshold contribute most to these variations.

- Identification efficiency systematics follow a similar prescription to give an uncertainty on the efficiency for reconstructing taus but also satisfy the *Medium* working point selection criteria. The largest contribution at low-p_T comes from the detector material where the calorimeter calibration and performance can affect tau identification input variables. At high-p_T pile-up uncertainties dominate.

- Trigger efficiency systematics are applied separately for each year of data taking and are statistically dominated.

- Systematic uncertainties concerning tau-jet energy scale calibrations (TES) are made up of three independent components covering different p_T ranges: *in situ*, detector and modelling.

- Finally a systematic uncertainty is included for the tau-electron overlap removal.

Jets

Jets are complex objects compared to electrons or muons and depend heavily on calorimeter information which leads to many associated systematics on the energy scale of simulated jets (JES).

- The set of nuisance parameters associated to the jet energy scale are grouped and reduced to a small set of total JES uncertainties. These include all *in-situ* corrections, statistical, tracking and modelling uncertainty configurations as a function of p_T and η.

- A systematic uncertainty on the jet energy resolution (JER) is also taken into account.

- Finally, a small uncertainty is introduced for the efficiency of the jet-vertex-tagger (JVT).

Jet flavour tagging

Systematic uncertainties are associated with the calibration of the *b*-tagging algorithm and the misidentification of *c* and light-flavour jets as *b*-jets. Correction factors are applied to account for the differences between data and simulation for flavour-tagging efficiencies. Correction factors are calculated separately for the flavour of jet along with the associated uncertainties.

Electrons and Muons

Although not directly used in the final state for the main analysis detailed in this thesis, electrons and muons affect the final fit through control regions, overlap removal and the combination with the semi-leptonic channel. Trigger, identification and reconstruction efficiency uncertainties are included and electron isolation requirements have an associated

uncertainty. Similar uncertainties arise for muons, as well as scaling and smearing uncertainties on the corrections applied to muon p_T. Note, uncertainties associated to electrons and muon objects are small compared to those coming from jets and τ-leptons.

Missing Transverse Energy

The resolution, scale and reconstruction efficiency of tracks not associated to a physics object are a main source of uncertainty on the missing transverse energy. Errors arising from the underlying event modelling also contribute. Furthermore, the uncertainties on resolution and energy scale of all physics objects are propagated through to the $E_\mathrm{T}^\mathrm{miss}$ calculation and enter the final result.

6.8.2 Uncertainties on the Fake Tau Component of $t\bar{t}$ Background

The data-driven estimation of the fake tau contribution coming from the $t\bar{t}$ background has several sources of uncertainty associated to it.

- The MC events containing a true hadronic taus are subtracted from the region when calculating fake rates. Varying the subtracted MC up and down by 50% to be conservative and propagrating through to the final fit giving a acceptable uncertainty.

- A systematic where the m_T cut is varied from the nominal value of 80 GeV to 65 GeV to be closest to the signal region.

- Evaluation of the fake tau $t\bar{t}$ component against each theoretical uncertainty.

- Vary the derived fake rates up and down by one standard deviation of the total statistical uncertainty.

- Finally, a p_T dependent systematic is applied to account for not applying both the DTT and STT p_T threshold cuts when calculating fake rates.

Chapter 7

Data-Driven Multi-jet Fake Estimation

This chapter describes the data-driven multi-jet fake estimation used in both the di-Higgs search and the scalar leptoquark analysis. The estimation is based on an 'ABCD' method which is outlined in Section 7.1 and then the specifics of the application to the analyses in this thesis are described in Section 7.2. Details of the trigger dependence on the method and the associated systematic uncertainties follow before plots of the *fake factors*, detailed in Section 7.1, themselves are presented. Note that all factors for fake estimation and plots introduced in this chapter are associated with the di-Higgs analysis and the corresponding leptoquark plots are given in Appendix C.

For many physics analyses, a large source of background comes from object mis-identification. The rate of mis-identification is often not modelled accurately by MC, so there is motivation to derive an estimation for this background from data. For a final state of two b-jets and two hadronically decaying taus, a considerable contribution to the analysis background comes from multi-jet processes where tau-jets are actually reconstructed from mis-identified jets. The mis-identification of jets as taus originate from many sources such as: $Z(\to ll)$+jets, top processes and $W(\to l\nu_l)$+jets. However, a significant amount of fake taus originate from multi-jet events via non-resonant production of quarks and gluons. The production cross section of jets at the LHC is many orders of magnitudes higher than signal processes.

Monte Carlo simulation does not accurately describe all features of the QCD background, in particular poor modelling is observed for the detector performance of QCD jets mis-identified as taus. Detector simulation of the calorimeter shower can be time consuming and the need for non-Gaussian detector response modelling of multi-jet events leads to

imperfections in the description. Moreover, multi-jet MC sample simulation suffers from insufficient statistics in signal regions due to the stringent selection of the analysis design. Therefore an alternative method derived from data is needed, especially for the final state described in this thesis, where many jet types exist: gluon-initiated jets, quark-initiated jets and heavy-flavour jets. The description for these types can be very different.

7.1 The 'ABCD' Method

ABCD methods are a commonly used data-driven procedure to estimate background contributions coming from physics object mis-identification. The idea behind the method is simple: use two uncorrelated variables to define four separate regions in two dimensions, one of which is the signal region and the remaining control regions are used to extrapolate an estimation of the background in the signal region. Similar to using an analysis side-band region to interpolate the backgrounds within the signal region. The method requires the definition of a control region rich in the desired background to be estimated and then relate these events to the identification in the signal region using an extrapolation factor applied to a template. The basis of the method relies on the fact that the background mis-identification occurring in the control region can be related to the particle mis-indentification in the signal region by this extrapolation factor only, meaning a reasonable estimation for the mis-identified background is possible. For the purpose of this thesis, the factor described is referred to as the *fake factor*.

Note, the *fake factors* used in this analysis are not those coming from a general fake factor method [171, 172], used in many analyses, defined as the number of objects passing the selection N_{Pass} over the number of objects failing the selection N_{Fail},

$$FF = \frac{N_{Pass}}{N_{Fail}}. \tag{7.1}$$

To describe the ABCD method clearly, the representation in Figure 7.1 shows the control regions.

Selection control Region

A
Signal Region

B

Selection control Region

C

D
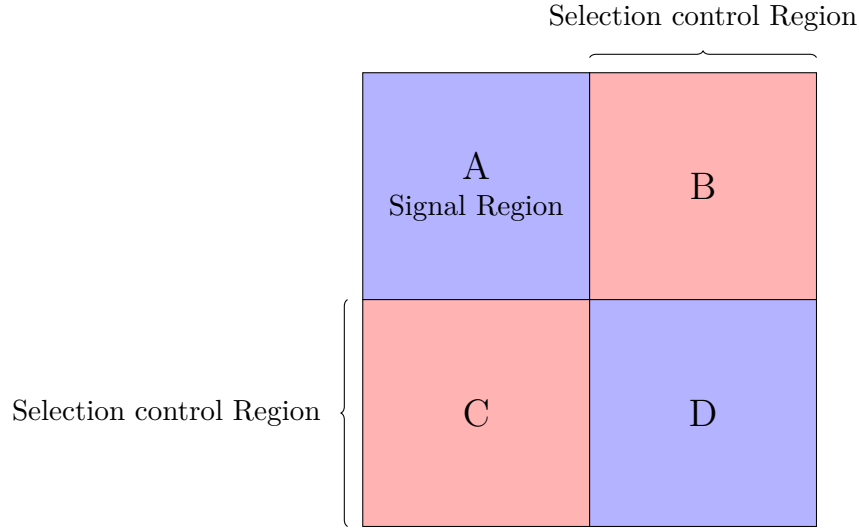
Figure 7.1: A simplified representation of the regions used in the ABCD method.

The fake factor (FF) can be calculated in the control region using the number of reconstructed events satisfying the full particle selection (B) to the number of reconstructed events passing the selection of the fake-rich control region (D).

$$FF = \frac{N_B}{N_D} \tag{7.2}$$

The factors cannot be determined in a region matching the full selection of the signal region. Derivation and application to the same region would not only bias the result but also be circular and require prior knowledge of the background in that region. Not only this, this would have significant signal contamination and would not give a good estimation for the fake background. Therefore, an additional control region must be defined to effectively give four regions with independent selections using the two uncorrelated variables.

The resulting estimation for the number of background events in the signal region (SR) $N_{SR,A}$ described by this data-driven method is given by

$$N_{SR,A} = FF \times N_C, \tag{7.3}$$

where the event yield of the fake-rich control region template N_C is weighted by the extrapolation factor.

Often the fake factors (FF) has a kinematic dependence on the rate of mis-identified objects and must be calculated in bins of a particular variable to provide shape information to the fake estimation. If the FF is applied bin-by-bin, the estimation becomes

$$\mathrm{N}_{SR,A}^{j} = \sum_{i} \mathrm{FF}^{i} \times \mathrm{N}_{C}^{i,j}, \tag{7.4}$$

where the final yield $\mathrm{N}_{SR,A}^{j}$ in bins j of the distribution being modelled and i labels the bin of the kinematic distribution where the FF was derived.

The calculation of FFs can become complicated but the general idea is simple so long as careful consideration is taken when defining control regions and selection criteria to avoid contamination from signal.

7.2 Implementation

The ABCD method is applied to the analyses in this thesis with a $b\bar{b}\tau_{\mathrm{had}}\tau_{\mathrm{had}}$ final state. Firstly, to enrich a region with a high number of multi-jet events and jets faking hadronic τ-leptons, the definition of anti-taus from Section 6.1.2 is used to define an anti-ID control region as a selection with at least one anti-tau. The anti-ID selection region can have either one BDTMedium tau with an anti-tau or two anti-taus passing selection. This ensures complete orthogonality from the signal selection of two BDTMedium, opposite-sign (OS), hadronic taus. The control region where the fake factor is derived is the so-called "same-sign" (SS) selection where both objects selected (tau or anti-tau) have the same electric charge. A summary of the regions for this fake factor procedure is shown in Figure 7.2. The choice of the charge sign selection and tau-ID selection to define the four separate regions of the ABCD separation led to the extrapolation factor being referred to as the fake factor. The calculation of this comes from a 'pass' tau-ID region divided by an anti-ID 'fail' region so the technique for fake estimation for this analysis is almost a pseudo-fake factor method.

Note, fake contributions from other background sources are small and are considered to be modelled correctly by MC. Subtracting MC from each region to give a pure QCD multi-jet
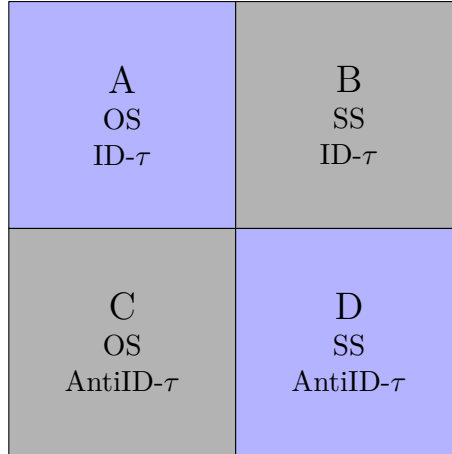
Figure 7.2: A representation of the regions involved in the calculation and application of fake factors for the multi-jet fake estimation used throughout this thesis.

fake estimation reduces any effects from the modelling of other MC and any fakes originating from MC background.

Equation 7.3 now becomes

$$N^{\tau}_{\text{OS } Data-MC,i} = N^{\text{anti}-\tau}_{\text{OS } Data-MC,i} \frac{N^{\tau}_{\text{SS } Data-MC,i}}{N^{\text{anti}-\tau}_{\text{SS } Data-MC,i}}, \qquad (7.5)$$

where $\frac{N^{\tau}_{\text{SS } Data-MC,i}}{N^{\text{anti}-\tau}_{\text{SS } Data-MC,i}}$ is the fake factor.

The fake factor is parametrised by the p_{T} of the leading and sub-leading taus whilst also being calculated separately for 1- and 3-prong taus. The mis-identification rate for jets faking τ_{had} is different for 1- and 3-prong taus because of the shape differences in the reconstruction signature, 1-prong taus usually have a lower mis-identification rate.

The signal selection requires two b-tagged jets but in the SS region this selection does not have enough events to give meaningful results when parameterised in both, p_{T} and prong of the tau or anti-tau. However, the 0-tag and 1-tag regions can be used to calculate fake factors for the 2-tag region and a transfer factor is applied to extrapolate to the 2-tag signal region. The 0-tag region is an effective test for the data-driven fake factor method but the 1-tag region is a more motivated choice to derive the fake factors with it being closer to the signal region selection. The four 1-tag regions used in the fake factor calculations are shown in Figure 7.3 before a fake estimation is included.
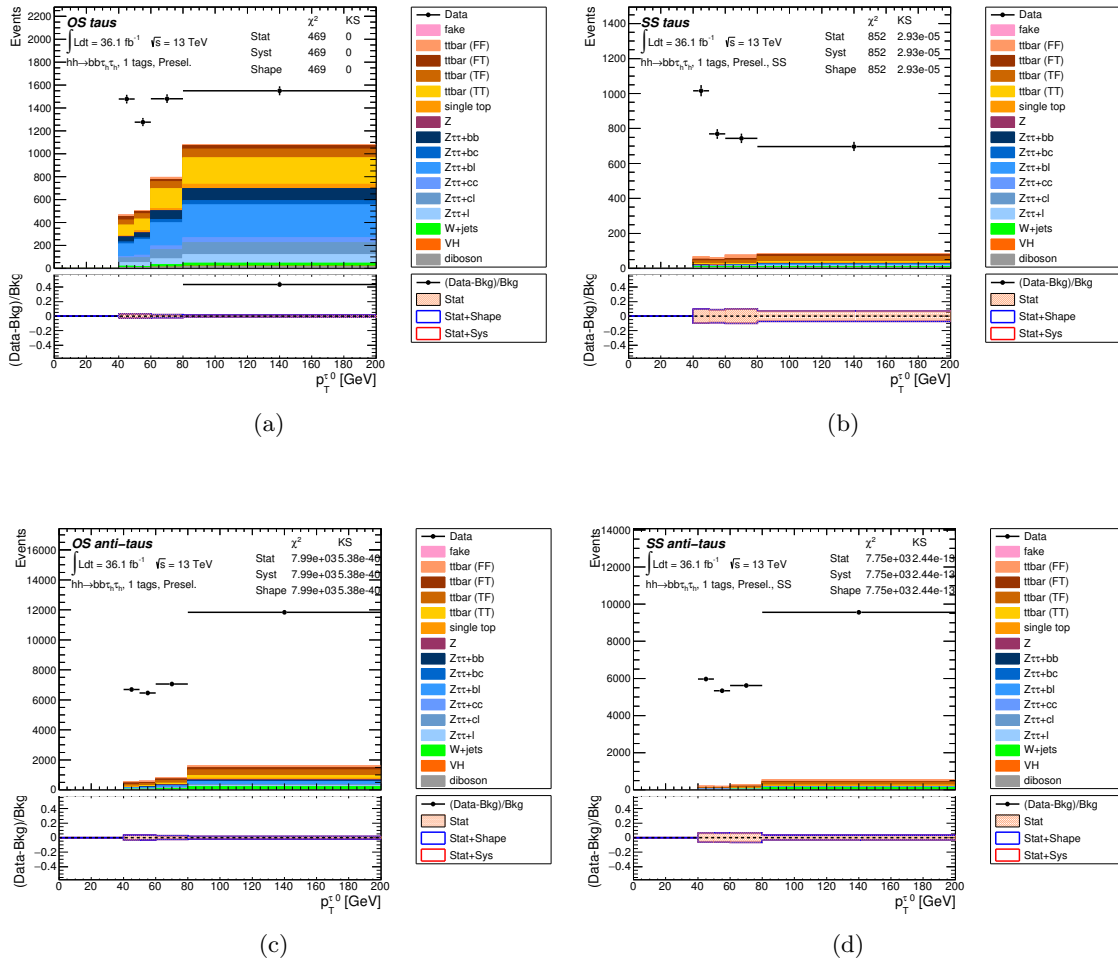
Figure 7.3: Leading tau p_{T} in all regions used for the fake factor method in the di-Higgs analysis.

7.2.1 Trigger Dependence

As previously stated, the multi-jet background is comprised of many different types of jet. The p_T thresholds on the di-tau trigger and single tau trigger, along with additional jet requirements, can affect the fraction of quark-jets to gluon-jets in the sample. In general for multi-jet events, gluon initiated jets dominate low-p_T with the fraction of quark initiated jets being much larger at higher p_T. A separate treatment of fake factor derivations is needed for each trigger separately to reduce quark- to gluon-jet fraction effects and biases.

Di-tau trigger events

The number of di-tau trigger events (DTT) exceeds that of the single tau trigger (STT) and so there is enough statistics available to parametrise the FFs in tau p_T and *prongness*.

The binning of the leading and sub-leading tau p_τ parametrisation is optimised to ensure enough events in the SS region after MC subtraction and to avoid meaningless negative bins. The chosen binning is shown below, each value representing the lower bin edge up to 1000 GeV.

```
float bins01P[5] = {40., 50., 60., 80., 1000.};
float bins03P[5] = {40., 50., 60., 70, 1000.};
float bins11P[4] = {20., 30., 50., 1000.};
float bins13P[5] = {20., 40., 50., 60., 1000.};
```

The resulting fake factors are stored in two-dimensional histograms of leading tau p_T vs. sub-leading tau p_T for each prong combination of the two taus: 1-prong 1-prong (1P1P), 1-prong 3-prong (1P3P), 3-prong 1-prong (3P1P) and 3-prong 3-prong (3P3P).

Figure 7.4 shows the nominal two-dimensional fake factors for the di-Higgs analysis. The separate fake factors for the leptoquark analysis are shown in Appendix C.
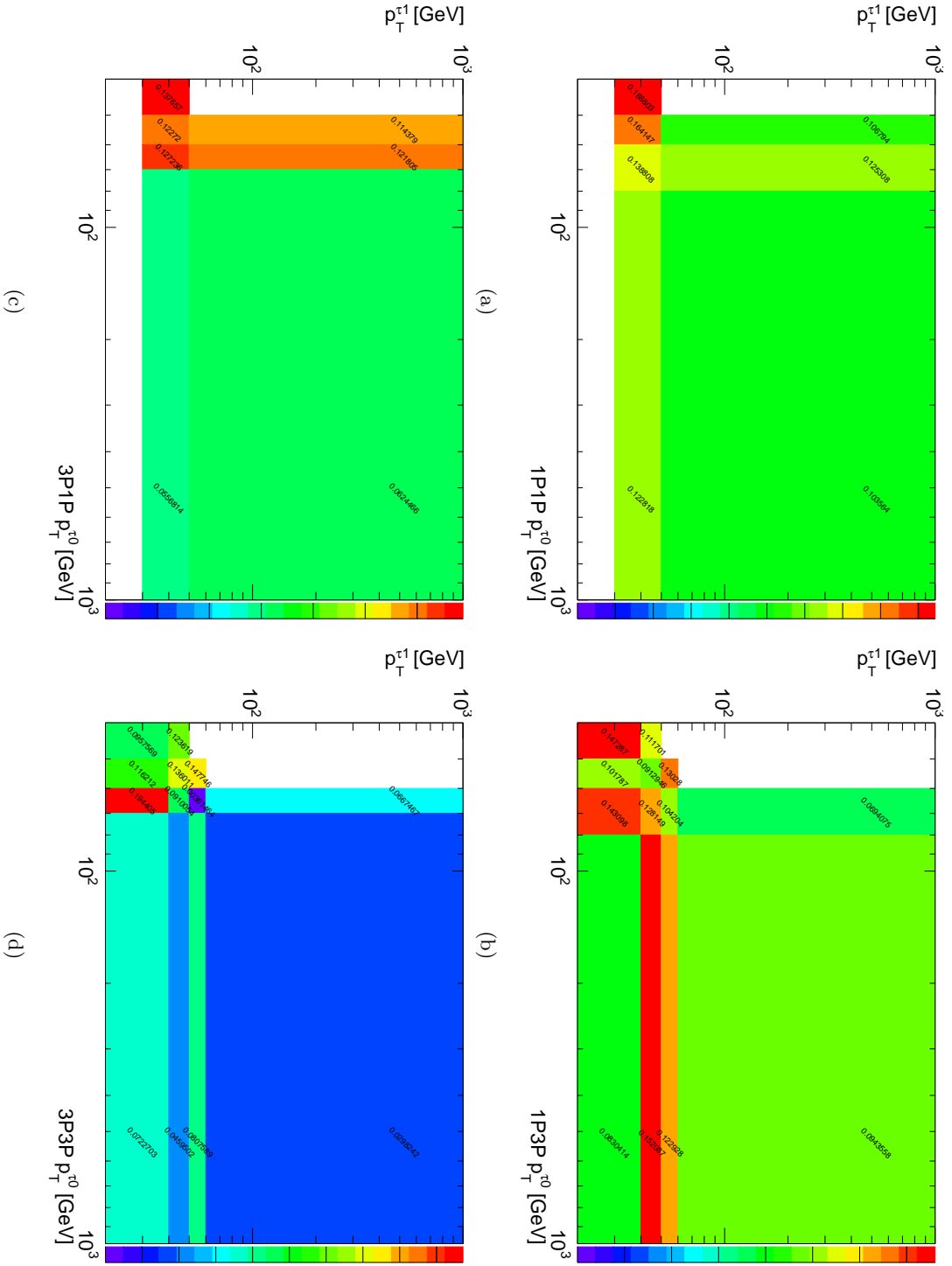
Figure 7.4: Two-dimensional fake factors of the leading tau p_T vs sub-leading tau p_T for 1-prong, 1-prong (a), 1-prong, 3-prong (b), 3-prong, 1-prong (c) and 3-prong, 3-prong (d) τ-lepton pairs with the DTT trigger, used to determine the multi-jet background in the $\tau_{had}\tau_{had}$ channel for the di-Higgs analysis.

Single tau trigger events

Events that match the single tau trigger do not have sufficient statistics to allow for the determination of p_T dependent fake factors. Therefore, the STT fake factors are derived using the total yield in the control regions for each prong combination and applied to the total distribution of the template of STT events. Like DTT events, the fake factors are calculated in the 1-tag region and then applied as an estimation for the 2-tag selection. Single tau trigger FFs for each prong combination are shown in Figure 7.5.
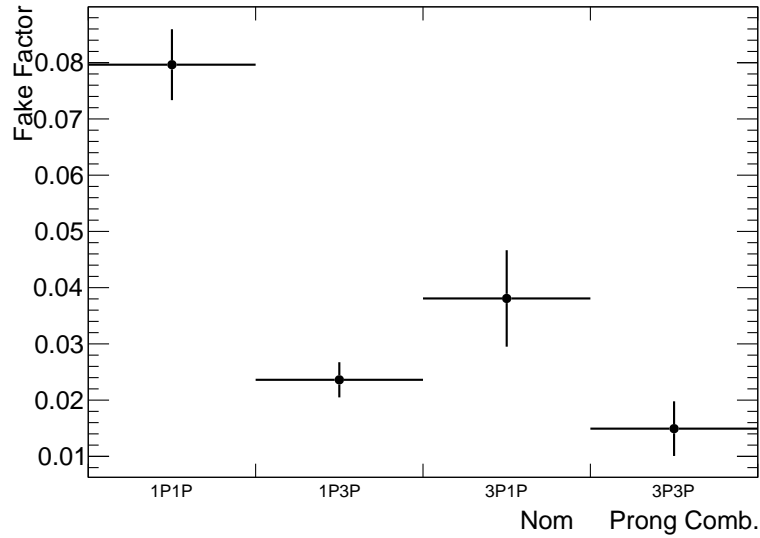
Figure 7.5: Fake factors for single tau trigger events in the di-Higgs analysis with each prong combination.

7.2.2   Transfer Factor

Any fake factors calculated in the 1-tag region may differ from those in the region with two b-tagged jets due to quark composition which affects the jet type fractions in the region as explained previously. A transfer factor is used to extrapolate between these two regions. The factor is defined as the ratio between fake-factors derived in the 1 b-tag and 2 b-tag regions for both triggers inclusively. The transfer factors (TF) are calculated inclusive of trigger used but are still parametrised by prong combination and applied to the separate 1-tag FFs for DTT and STT events. The transfer factors for the nominal fake factors are shown in Figure 7.6.
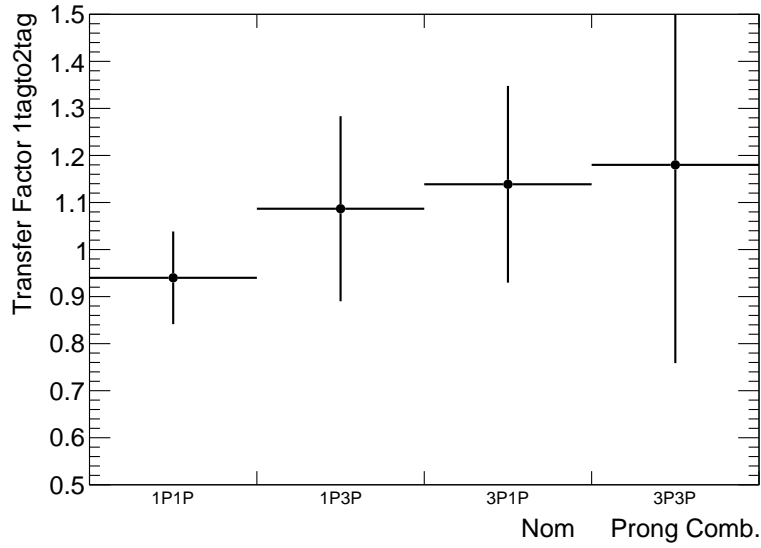
Figure 7.6: Transfer factors in the di-Higgs analysis for each prong combination.

7.3 Systematic Uncertainties

The data-driven multi-jet estimation needs a number of systematic uncertainties to cover any variation in the method. The uncertainties are constructed by varying the actual fake factors and propagating them through to a multi-jet fake background distribution in the signal region.

- **Statistical uncertainty variation**

    The nominal fake factors calculated by the method outlined previously are varied up and down by their statistical uncertainty. The variation is performed for both STT and DTT fake factors and within each parametrised bin. For example, the down variation for this systematic reduces all FFs by the lower statistical uncertainty which are then propagated through the analysis as normal, resulting in an alternative multi-jet fake background estimation.

    – `SysFFStatQCD__1up`

    – `SysFFStatQCD__1down`

- **MC Subtraction variation**

  Each region used in the fake factor calculation and application has the MC subtracted to remove effects from tau fakes coming from other Monte Carlo processes. The final systematic of the fake distribution comes from varying the subtracted MC up and down by 50%. The down variation subtracts 50% of the total MC in all regions and the up variation subtracts 150% of the total MC.

    – `SysSubtraction_bkg__1up`

    – `SysSubtraction_bkg__1down`

- **Transfer factor variation**

  To account for the fake factors being calculated in the 1 *b*-tag region, the transfer factors are applied before the fake factors are used in the 2 *b*-tag region. A systematic on the transfer factor accounts for this by varying the transfer factors up and down by their statistical uncertainty for each prong combination prior to propagating through to the final selection.

    – `Sys1tag2tagTF__1up`

    – `Sys1tag2tagTF__1down`

- **OS-SS systematic**

  The fake factors are calculated in the SS region and then applied to the OS region. To account for the difference in jet flavour composition between the two regions, fake factors are calculated for both OS and SS events in a multi-jet rich region defined as ($\Delta\phi(\tau\tau) > 2.0$). The ratio of OS FFs to SS FFs is computed for each prong combination and then fitted with a zeroth-order polynomial to obtain a value by which the nominal fake factors can be varied. Plots are shown in Figure 7.7 for the di-Higgs analysis. This is done separately for the leptoquark analysis fake estimation.

    – `SysOSSS__1up`

    – `SysOSSS__1down`

- **Multi-jet composition systematic**

  An additional systematic accounts for jet-to-tau fake composition by scanning the BDT input variables in the 1-tag OS region and uses data-MC vs. nominal multi-jet fake distribution as a closure test. The greatest closure disagreement is seen in sub-leading tau p_T for the di-Higgs analysis and leptoquark analysis. The ratio of data-MC to nominal fake background distribution is fitted with a first-order polynominal and used to vary the fake-factors. The fit on the sub-leading tau p_T distribution is shown in Figure 7.8.

  - `SysCompFakes__1up`

  - `SysCompFakes__1down`

- **Multi-jet composition systematic (Antitau BDT score variation)**

  Finally, a systematic was derived to account for the multi-jet fake composition variation. The method varied the definition of the anti-tau by using 0.45 as the minimum threshold for the tau-ID BDT score rather than 0.35. Figure 7.9 shows the composition of jets faking taus in the 0-tag region for W+jet events. The increase of the BDT score from 0.35 to 0.45 shows the composition to be flat within the ID and anti-ID region. Although this systematic was not used in the final anaylses and statistical fit, the performance was documented in this thesis.

The nominal fake factors for the DTT and the fake factors for each systematic uncertainties are given in Figure 7.10 to Figure 7.13 for each prong combination. Figure 7.14 shows the up and down variation in the data-driven fake distribution for each systematic. All fake factors corresponding to systematics are presented in Figure 7.15 for single tau trigger events and the transfer factors for each systematic are given in Figure 7.16. Finally, the leading and subleading τ-lepton p_T distributions are shown in Figures 7.17, 7.18 and 7.19 for OS and SS events in each b-tag region of the di-Higgs analysis. The data-driven multi-jet fake distribution is shown in pink.
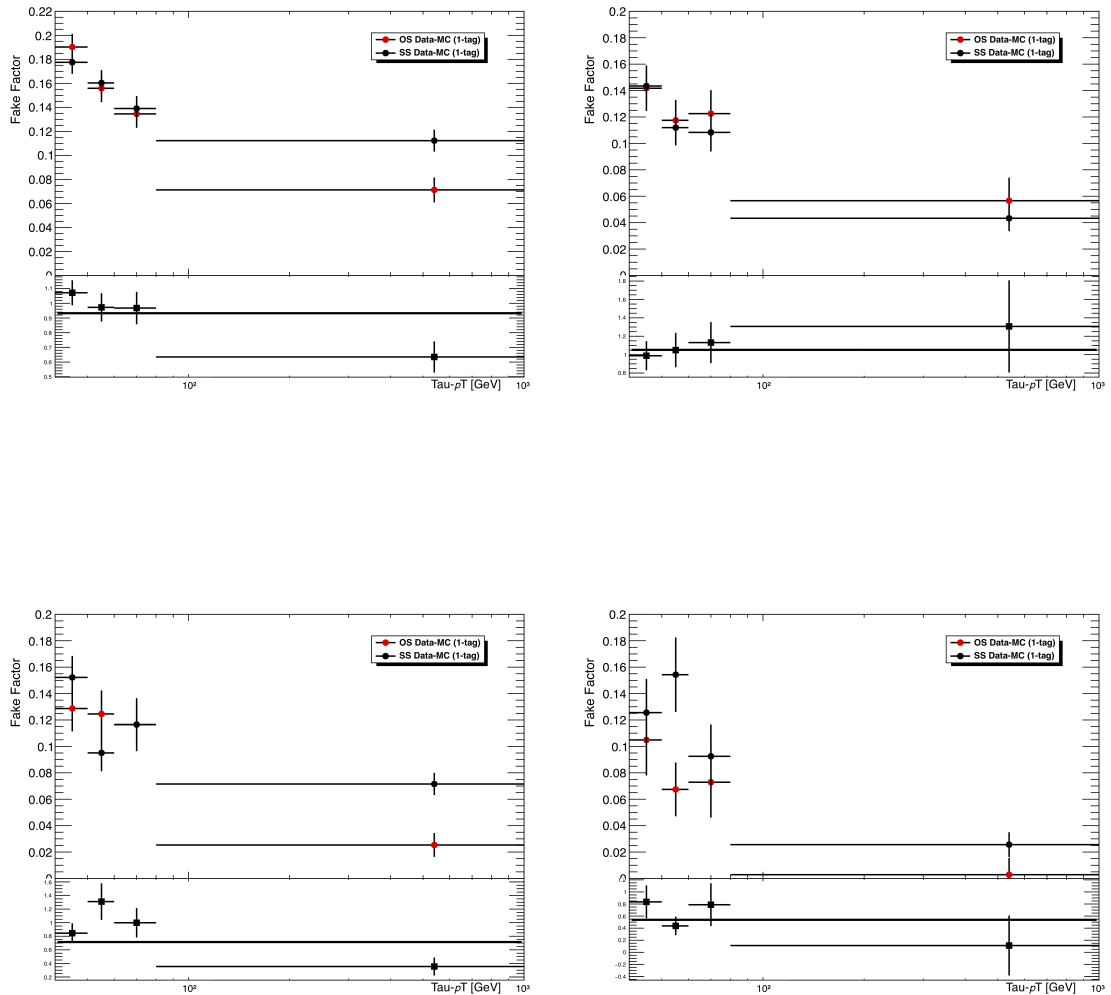
Figure 7.7: The ratio of the number of ID to anti-ID events in OS events and in SS events in the $\tau_{\text{had}}\tau_{\text{had}}$ channel QCD CR as a function of tau p_{T}. The fit to the double ratio in the bottom panels is takes as the systematic on the fake factors in the $\tau_{\text{had}}\tau_{\text{had}}$ channel.
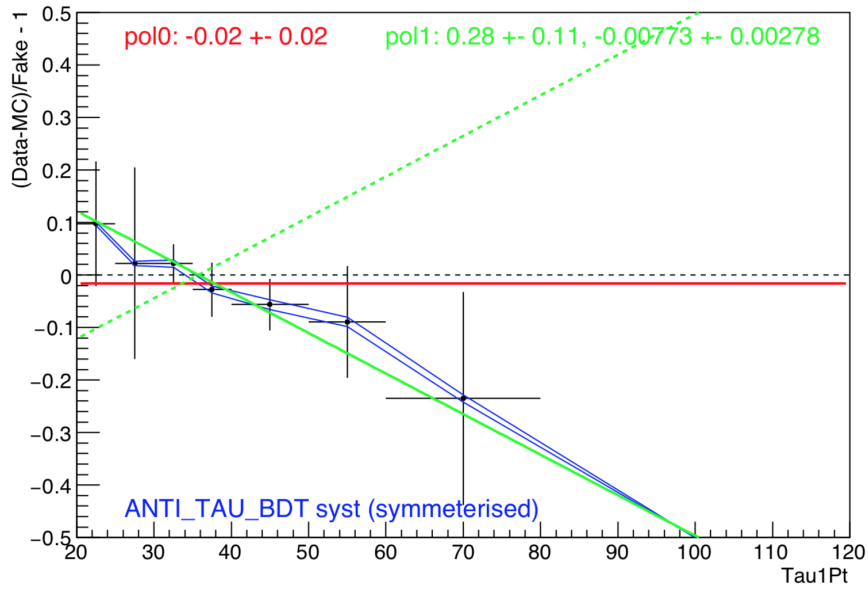
Figure 7.8: The data-MC comparison with the fake background for the sub-leading tau p_{T} in the 1-tag region. The mismodelling is fit with a first order polynomial to give a systematic uncertainty.
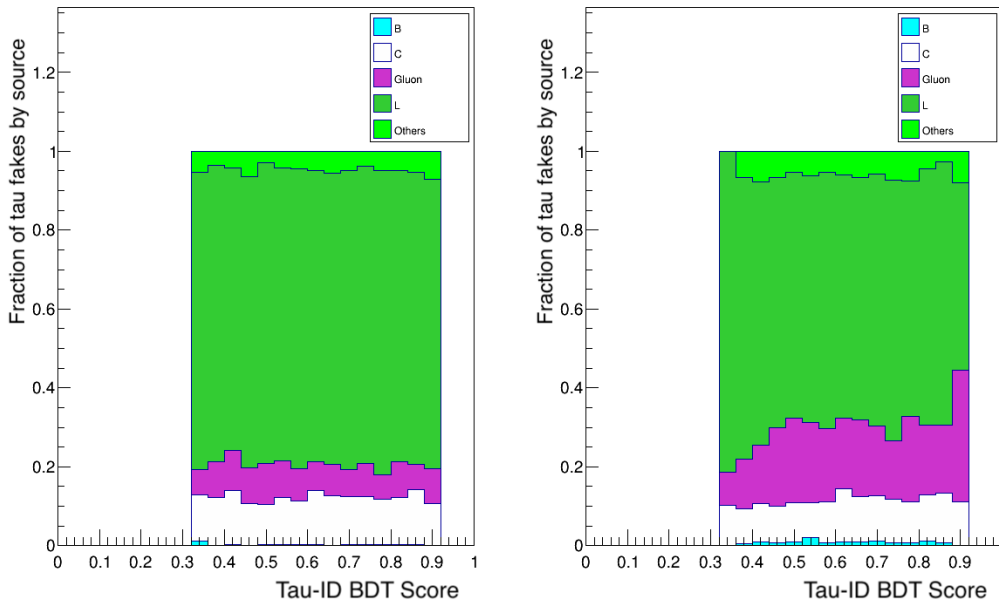
Figure 7.9: Composition of jets faking taus as a function of tau ID BDT score for W+jet events in the 0 b-tagged region for OS (left) and SS (right) events in the $\tau_{\mathrm{had}}\tau_{\mathrm{had}}$ channel.
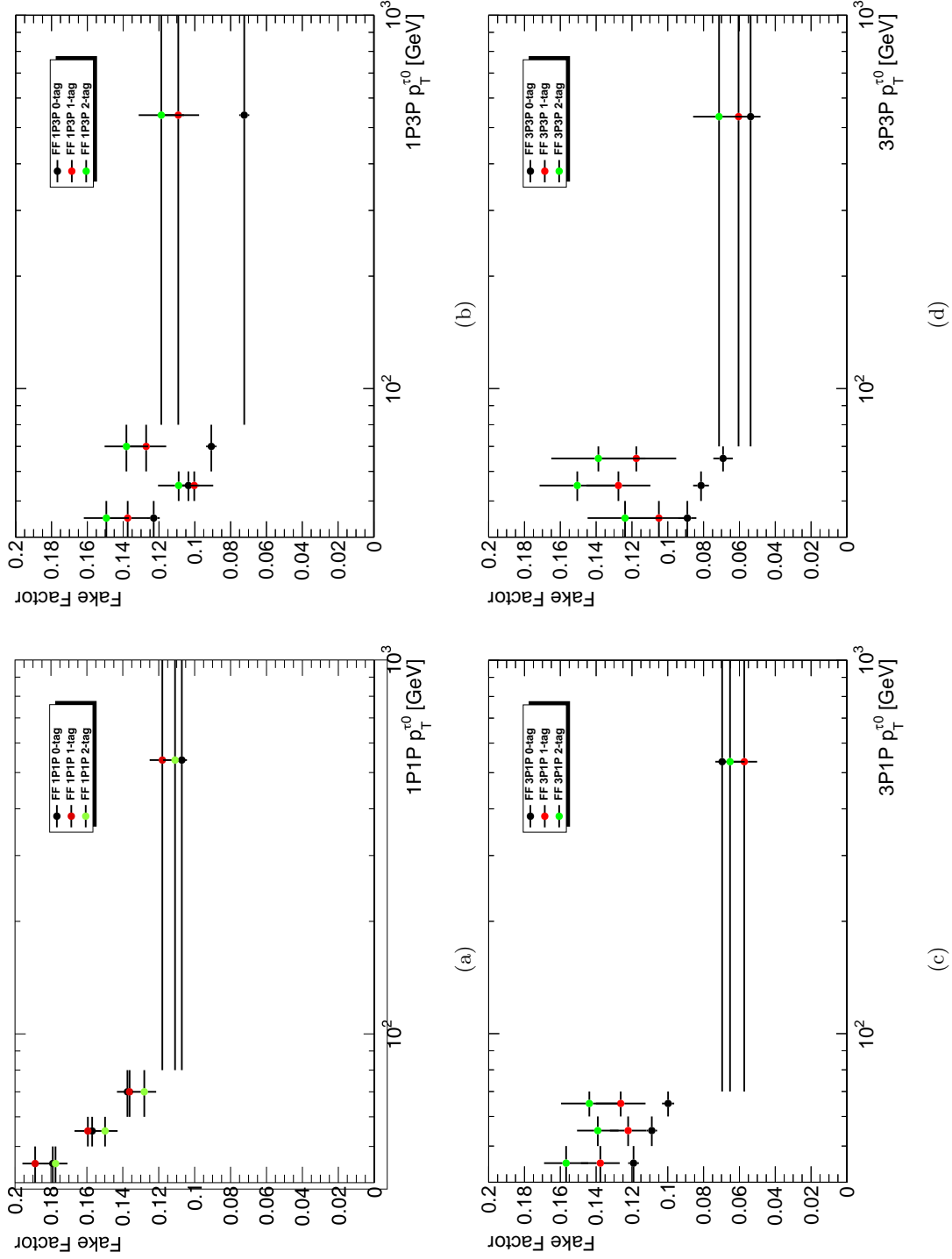
Figure 7.10: Fake factor projections onto the leading tau p_T for 1 and 2 b-tag events for 1-prong, 1-prong (a), 1-prong, 3-prong (b), 3-prong, 1-prong (c) and 3-prong, 3-prong (d) τ-lepton pairs with the DTT trigger, used to determine the multi-jet background in the $\tau_{\text{had}}\tau_{\text{had}}$ channel.
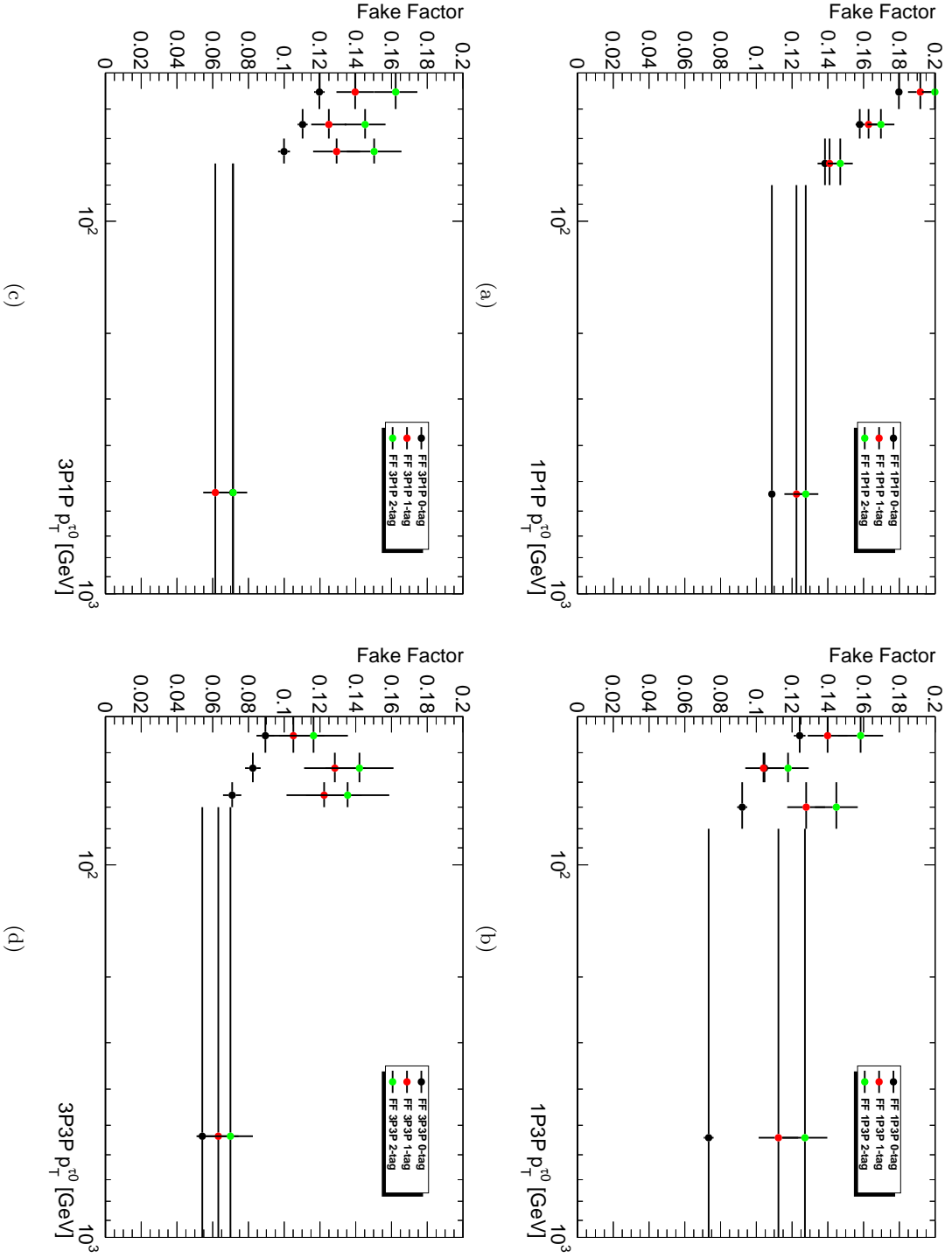
Figure 7.11: Monte Carlo subtraction upwards systematic fake factor projections onto the leading tau p_T for 1 and 2 b-tag events for τ for 1-prong, 1-prong (a), 1-prong, 3-prong (b), 3-prong, 1-prong (c) and 3-prong, 3-prong (d) τ-lepton pairs with the DTT trigger, used to determine the multi-jet background in the $\tau_{had}\tau_{had}$ channel.
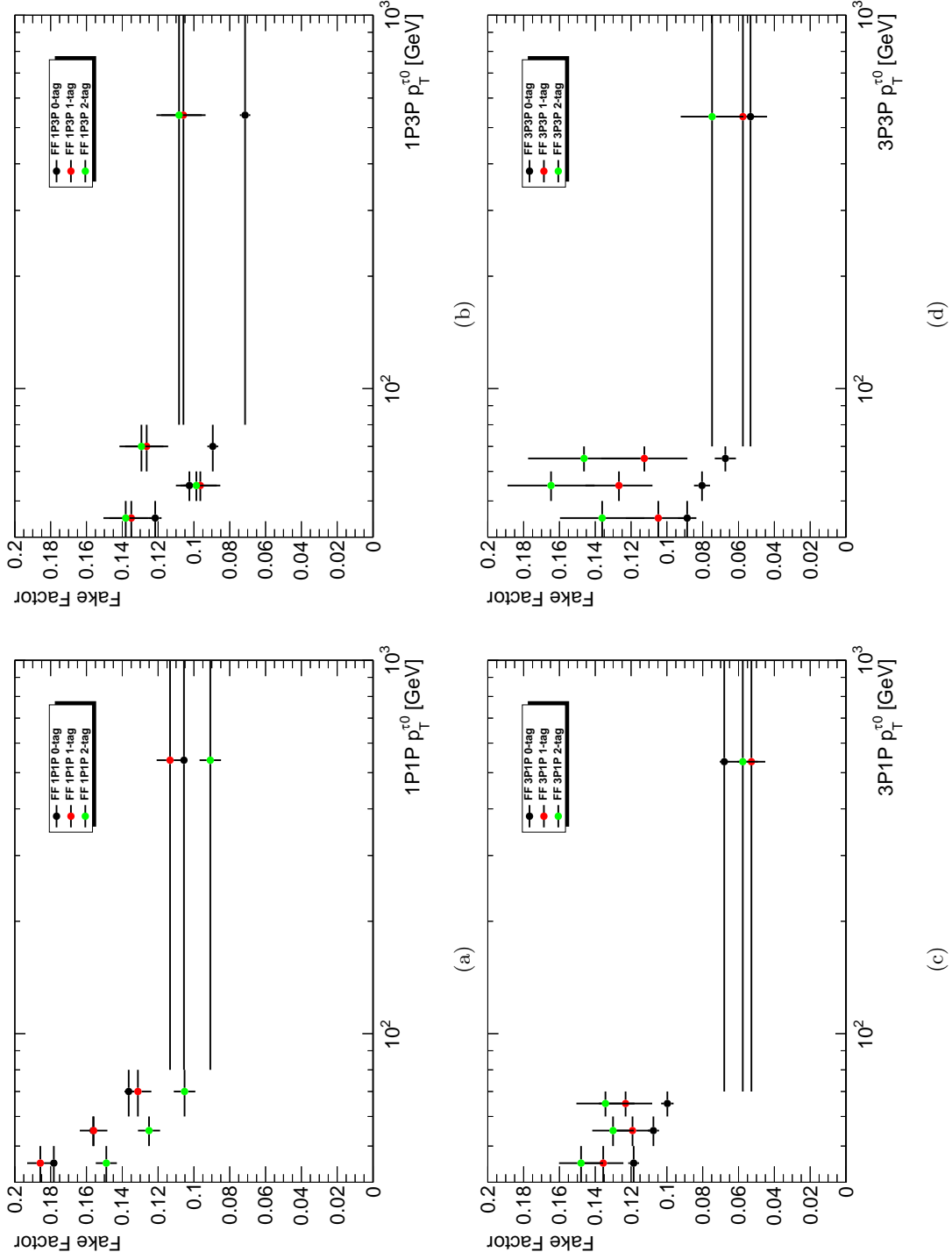
Figure 7.12: Monte Carlo subtraction downwards systematic fake factor projections onto the leading tau p_T for 1 and 2 b-tag events for 1-prong, 1-prong (a), 1-prong, 3-prong (b), 3-prong, 1-prong (c) and 3-prong, 3-prong (d) τ-lepton pairs with the DTT trigger, used to determine the multi-jet background in the $\tau_{had}\tau_{had}$ channel.
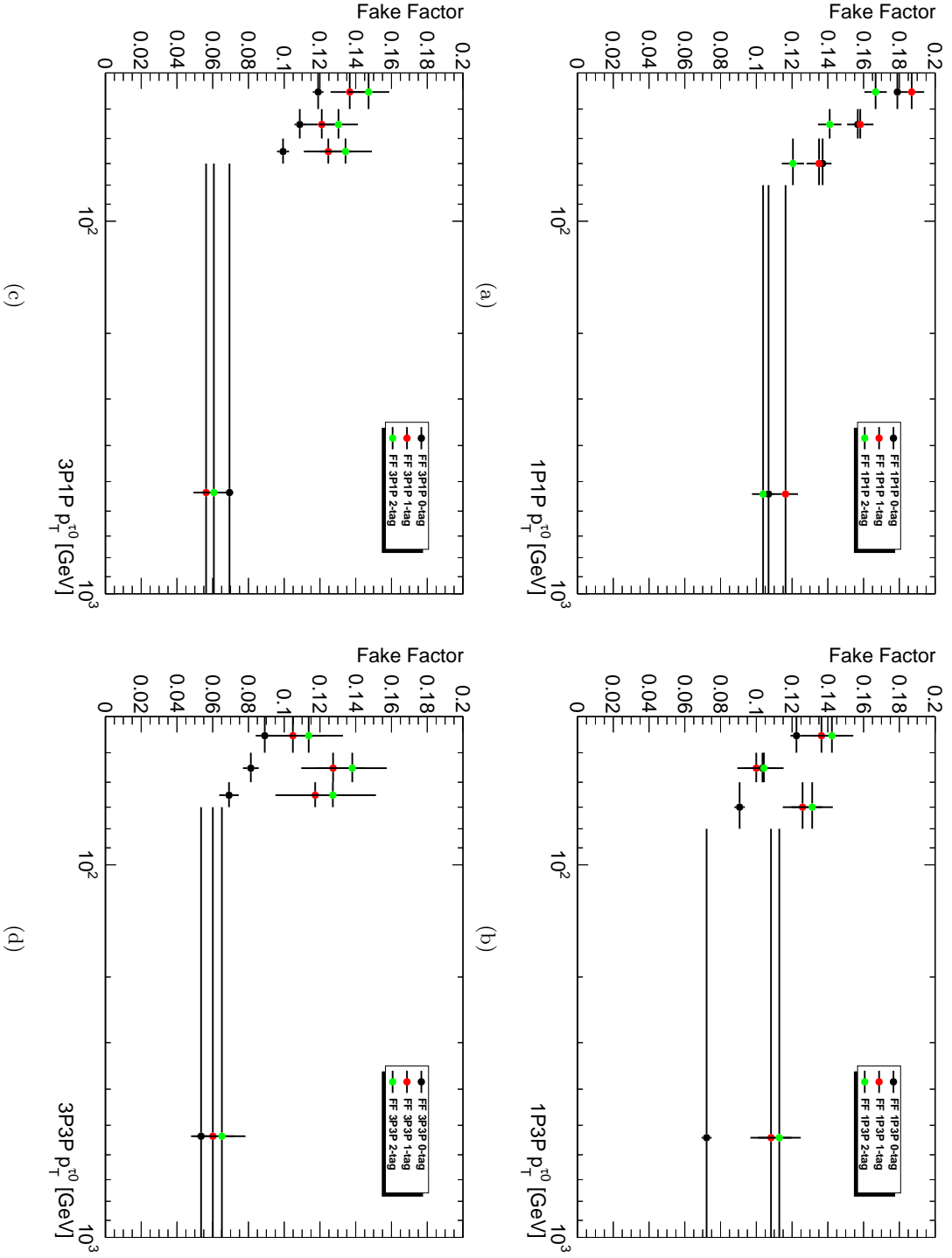
Figure 7.13: Anti-tau BDTScore variation systematic fake factor projections onto the leading tau p_T for 1 and 2 b-tag events for 1-prong, 1-prong (top left), 1-prong, 3-prong (top right), 3-prong, 1-prong (bottom left) and 3-prong, 3-prong (bottom right) τ-lepton pairs with the DTT trigger, used to determine the multi-jet background in the $\tau_{had}\tau_{had}$ channel.
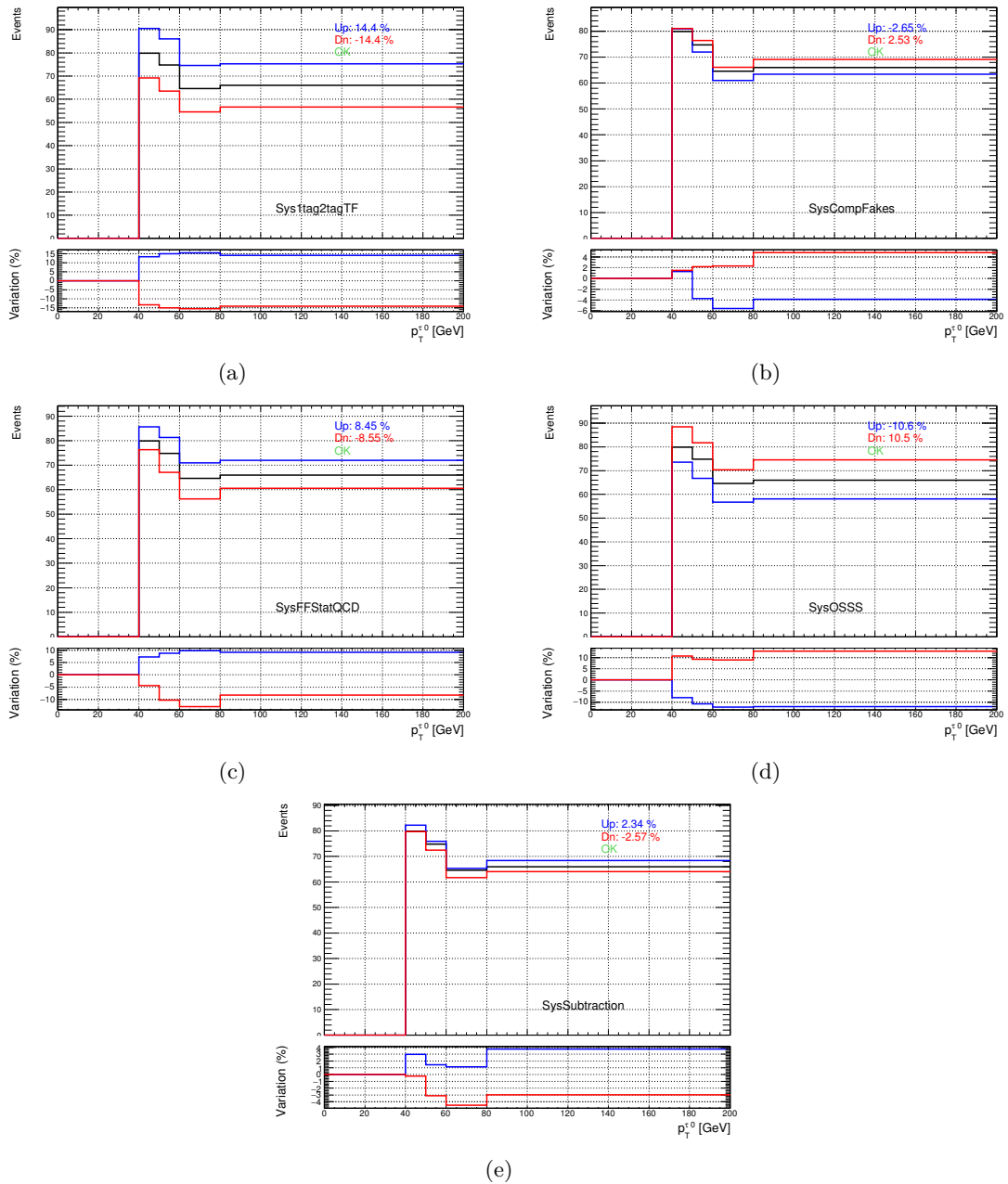
Figure 7.14: The up and down variations for each data-driven multi-jet background estimation systematic as a function of the leading-τ p_{T}.
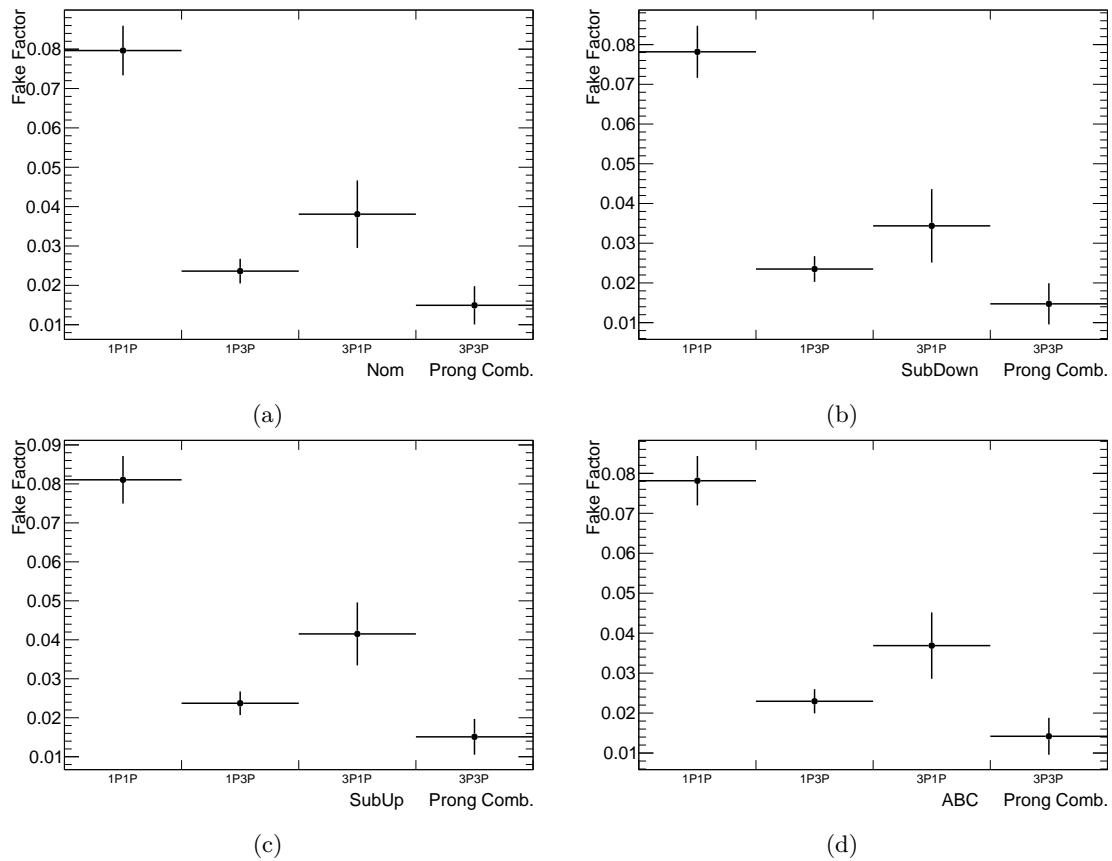
Figure 7.15: Single tau trigger fake factors for each prong combination for nominal (a), MC subtraction upwards variation (b), MC subtraction downwards variation (c) and the anti-tau BDTScore variation systematic (d), used to determine the multi-jet background in the $\tau_{\text{had}}\tau_{\text{had}}$ channel.
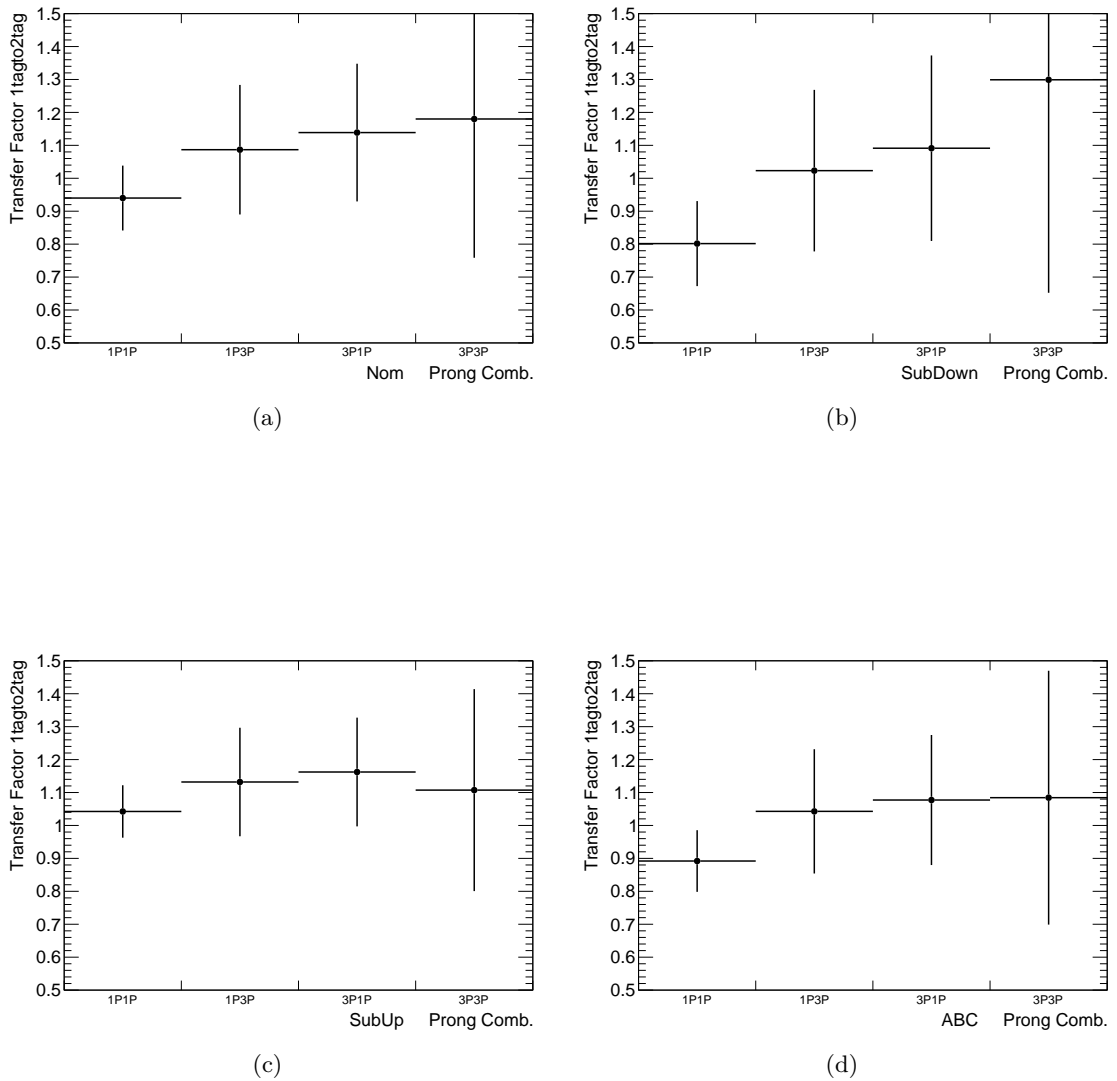
Figure 7.16: Transfer factors for each prong combination with nominal (a), MC subtraction upwards variation (b), MC subtraction downwards variation (c) and the anti-tau BDTScore variation systematic (d), used to extrapolate from 1-tag to 2-tag regions for the multi-jet background in the $\tau_{\text{had}}\tau_{\text{had}}$ channel.
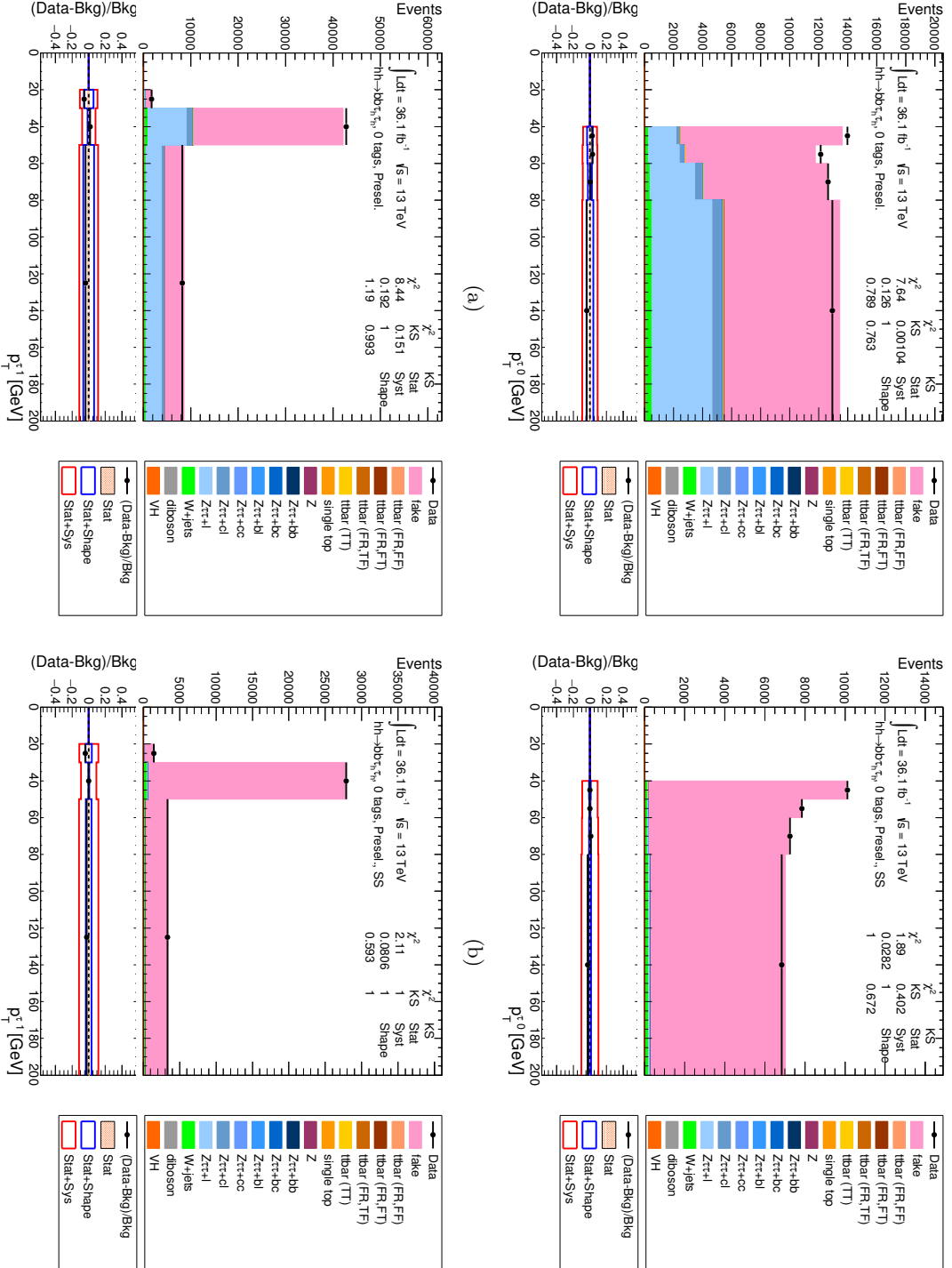
Figure 7.17: Tau p_T distributions in the separate regions used in the fake factors method for 0-tag events in the $\tau_{had}\tau_{had}$ channel of the di-Higgs analysis, showing leading tau p_T OS (a), leading tau p_T SS (b), sub-leading tau p_T OS (c), sub-leading tau p_T SS (d)
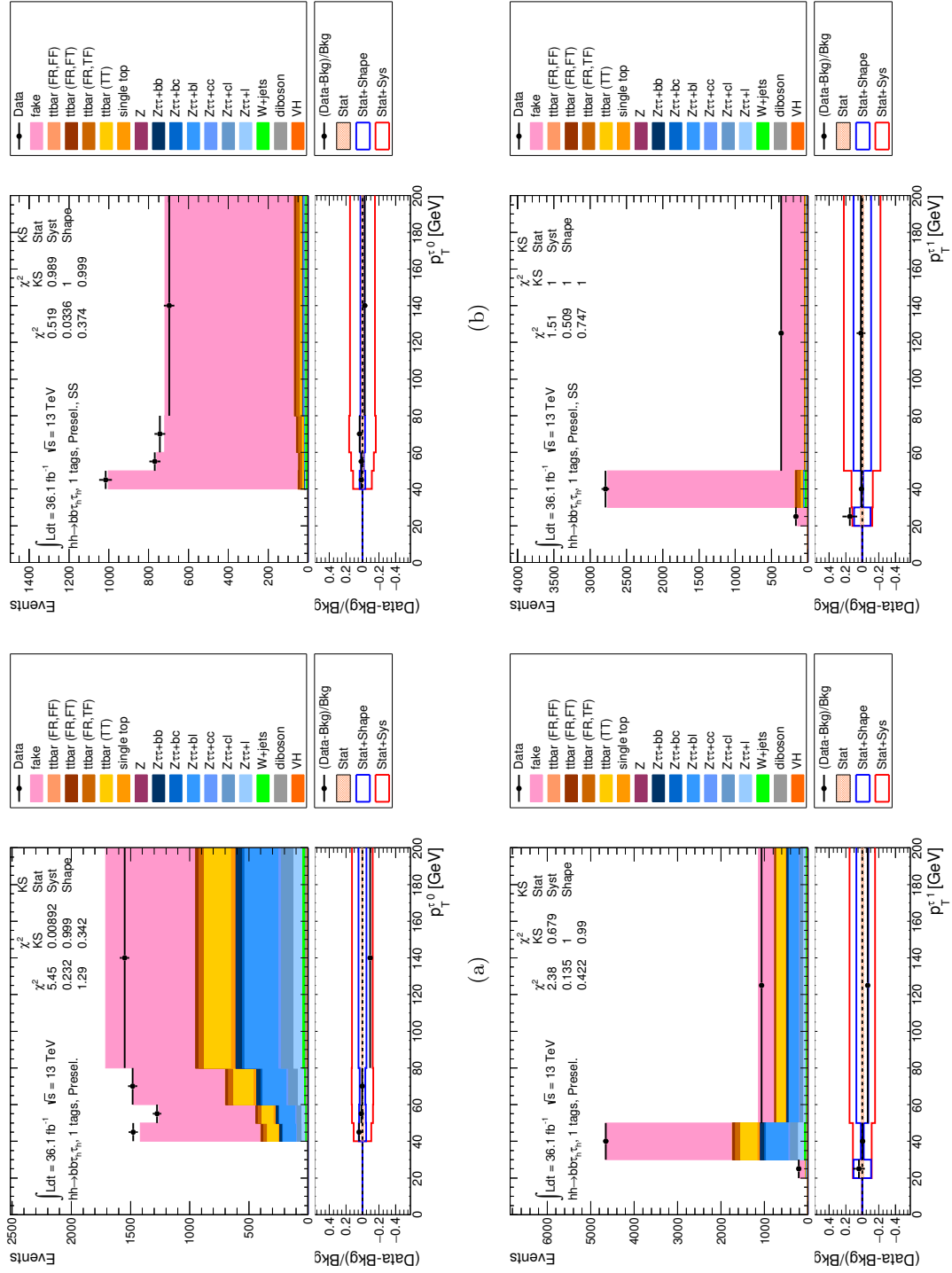
Figure 7.18: Tau p_T distributions in the separate regions used in the fake factors method for 1-tag events in the $\tau_{had}\tau_{had}$ channel of the di-Higgs analysis, showing leading tau p_T OS (a), leading tau p_T SS (b), sub-leading tau p_T OS (c), sub-leading tau p_T SS (d)
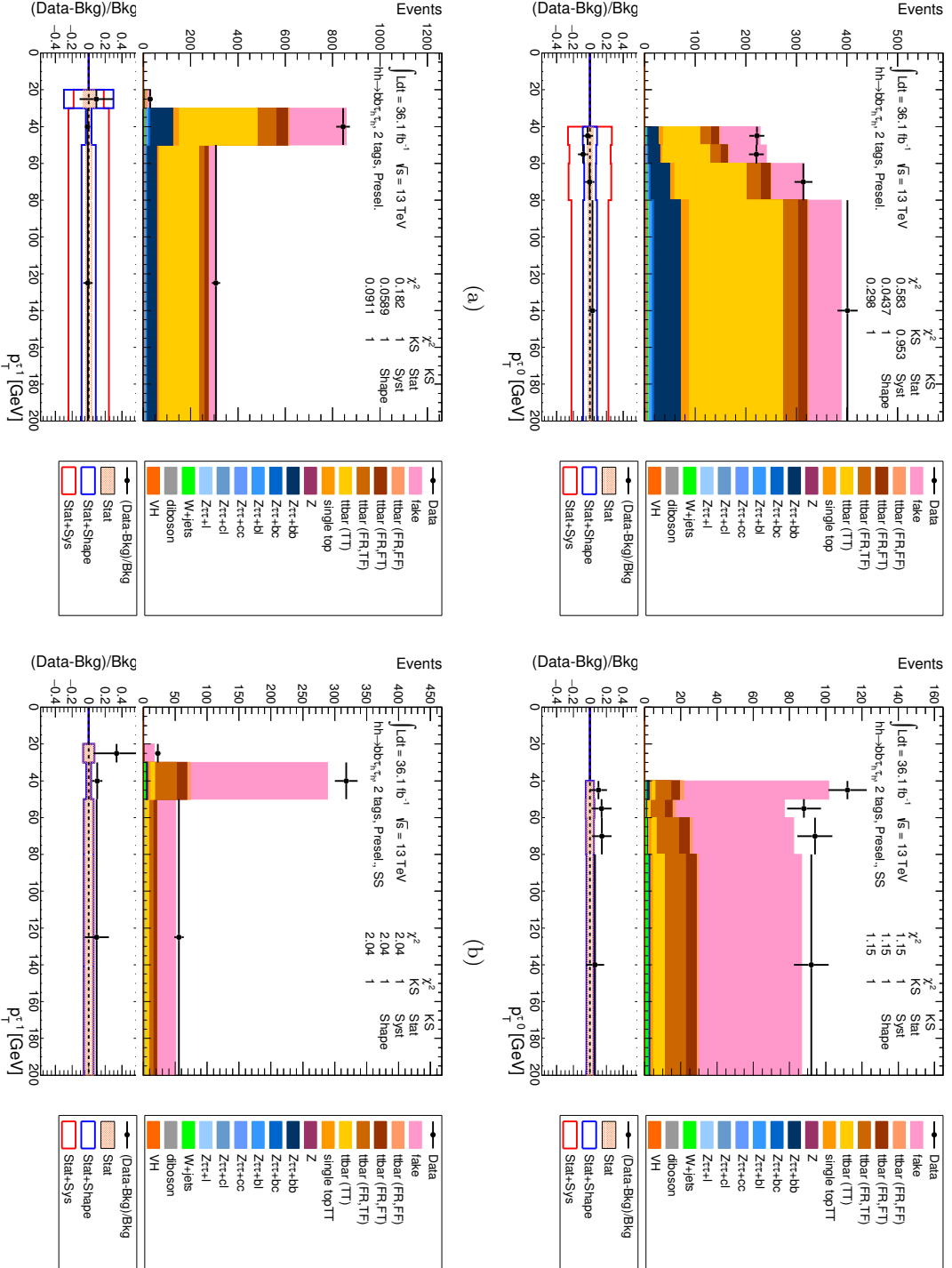
Figure 7.19: Tau p_{T} distributions in the separate regions used in the fake factors method for 2-tag events in the $\tau_{\mathrm{had}}\tau_{\mathrm{had}}$ channel of the di-Higgs analysis, showing leading tau p_{T} OS (a), leading tau p_{T} SS (b), sub-leading tau p_{T} OS (c), sub-leading tau p_{T} SS (d)

Chapter 8

Di-Higgs Production Search in the $b\bar{b}\tau\tau$ Channel

In this chapter, the result of the di-Higgs $\to b\bar{b}\tau\tau$ analysis is presented for the fully hadronic final state. Both the resonant and non-resonant results are given and a combination with the lephad channel is presented to give the latest results for comparison with other di-Higgs channels and CMS results.

The analysis strategy outlined in Chapter 6 is followed throughout, the signal strengths for Randall-Sundrum Kaluza-Klein bulk graviton, 2HDM, and non-resonant di-Higgs production are extracted using a binned profile likelihood fit on the BDT score output. This is performed in the signal region and the $Z \to \mu\mu + 2$ b-jets control region simutaneously. All sources of statistical and systematic uncertainties on the signal and background modelling described in Section 6.8 are implemented as deviations from the nominal, scaled by nuisance parameters that are profiled in the fit. The normalisations of the true $t\bar{t}$ and $Z \to \tau\tau +$ heavy-flavour jets are allowed to float in the final fit.

The measured value of μ is used to compare the observed significance to an expected significance obtained from a fit to the Asimov dataset. Limits are set at a 95% CL using the CL$_s$ method and the results of the $b\bar{b}\tau\tau$ combination are compared to $bb\gamma\gamma$, $4b$ and the CMS experiment in Section 8.3.

8.1 Boosted Decision Tree Variables and Training

The BDT score is used in this analysis as the final discriminant to improve separation between signal and background processes. The variables that give the highest discriminating

power for the fully hadronic decay channel between signal and background are as follows,

- m_{hh}: The invariant mass of the di-Higgs system is reconstructed from the di-tau and di-b-jet masses. A "Higgs mass constraint" is applied, where the Higgs mass used in simulation of 125 GeV is assumed for the di-tau and di-b-jet systems. Scale factors of m_h/m_{MMC} and m_h/m_{bb} (where m_h is the value of the Higgs boson mass used in the simulation, 125 GeV) are applied to the four-momenta of the di-tau and di-b-jet systems, respectively, in order to improve the mass resolution.

- m_{MMC}: The invariant mass of the di-tau system, calculated using the MMC.

- m_{bb}: The invariant mass of the di-b-jet system.

- $\Delta R(\tau\tau)$: The ΔR between the visible tau decay products.

- $\Delta R(bb)$: The ΔR between the two b-jets.

- E_T^{miss} ϕ centrality: This variable quantifies the position in ϕ of the E_T^{miss} with respect to the visible decay products of the two taus. It is defined as

$$E_T^{miss}\phi \text{ centrality} = \frac{A + B}{\sqrt{A^2 + B^2}}, \tag{8.1}$$

where A and B are given by

$$A = \frac{\sin(\phi_{E_T^{miss}} - \phi_{\tau_2})}{\sin(\phi_{\tau_1} - \phi_{\tau_2})}, \ B = \frac{\sin(\phi_{\tau_1} - \phi_{E_T^{miss}})}{\sin(\phi_{\tau_1} - \phi_{\tau_2})}. \tag{8.2}$$

The $E_T^{miss}\phi$ centrality is equal to:

- $\sqrt{2}$ when the E_T^{miss} lies exactly between the two taus; or

- 1 if the E_T^{miss} is perfectly aligned with either of the taus; or

- < 1 if the E_T^{miss} lies outside of the ϕ angular region defined by the two taus.

Signal events tend to have larger values of the E_T^{miss} ϕ centrality as in these cases the two taus are produced from the decay of a Higgs boson and the reconstructed E_T^{miss} ϕ angle generally falls in between the two visible tau decay products.

When training a boosted decision tree, the learner can become *overtrained* where the BDT models the signal and background differences specific to the particular training sample. Comparisons of the BDT score distributions for the training and test samples is often used to look for signs of overtraining. Differences between the BDT score distributions of the training and test samples is an indicator of overtraining. The Kolmogorov-Smirnov test (KS-test) is often used in this case to quantify the statistical probability that two samples are drawn from the same distribution, one way to quantify overtraining. Plots are shown for different mass points and signals used in the training in Figure 8.1. The distributions of the BDT input variables are presented in Figure 8.2.

It is also important to note that for the resonant BDT training, a separate boosted decision tree is trained for each resonant mass point. However, this leads to the analysis being sub-optimal for resonant masses between these discrete points. Neighbouring mass point signals are included with each training to increase the sensitivity to resonances across the whole mass range, for example a BDT would be trained for a 300 GeV graviton signal with the 260 GeV and 400 GeV signals included.

8.2 Control Regions

To give confidence in the background modelling in the signal region, especially those used in BDT training, control regions are defined to isolate backgrounds of interest. Control region plots are shown in Appendix A.

- Top control region:

    - $m_{\mathrm{MMC}} < 85$ GeV and $m_{\mathrm{MMC}} > 140$ GeV

    - $m_{bb} < 80$ GeV and $m_{bb} > 135$ GeV

- $Z \rightarrow \tau\tau$+jets control region:

    - $70 < m_{\mathrm{MMC}} < 100$ GeV

- Same-sign 2-tag region
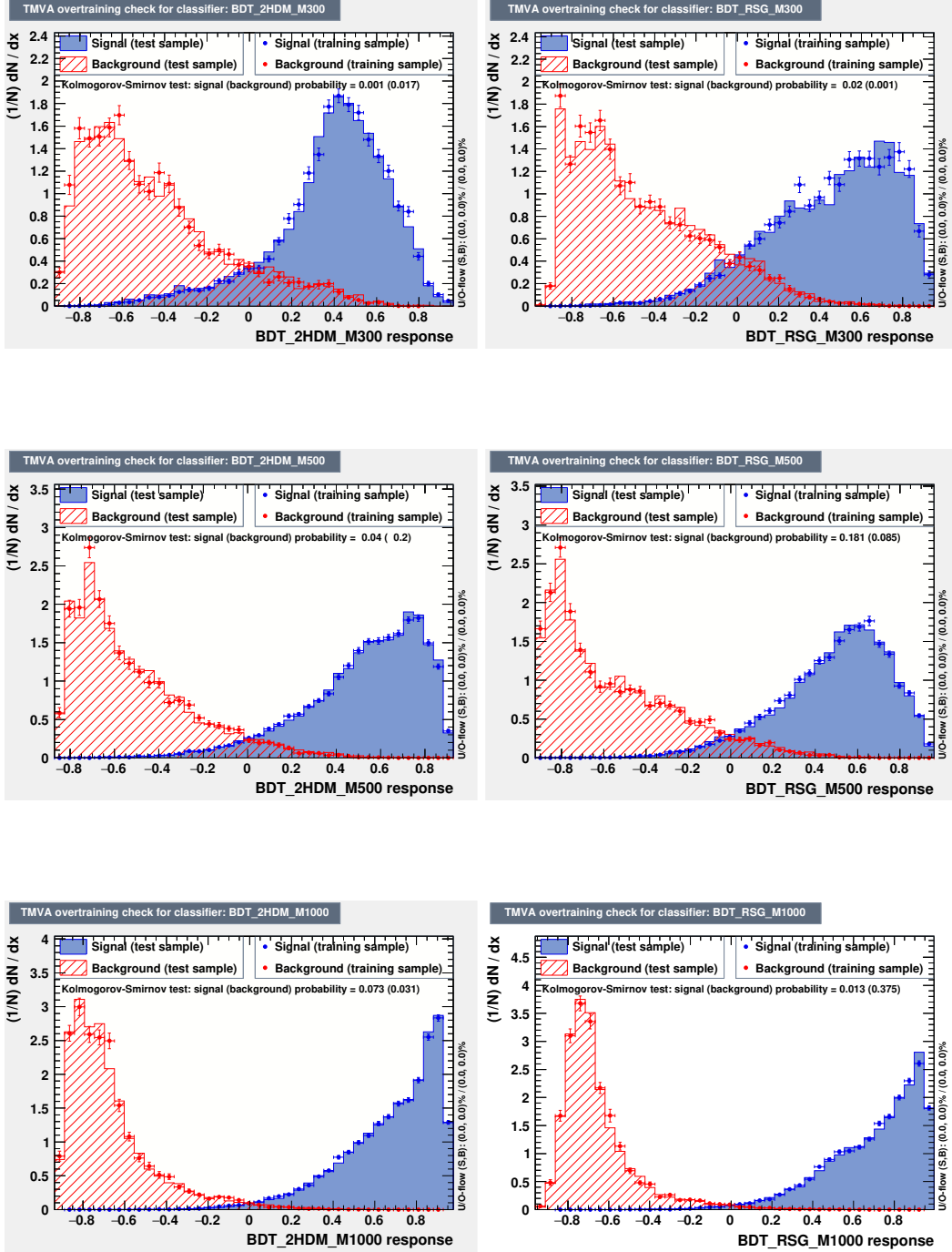
Figure 8.1: Overtraining plots for 2HDM (left) and RSG (right) signals in the $\tau_{\mathrm{had}}\tau_{\mathrm{had}}$ channel, for 300 GeV (top), 500 GeV (centre) and 1000 GeV (bottom) mass points [173].
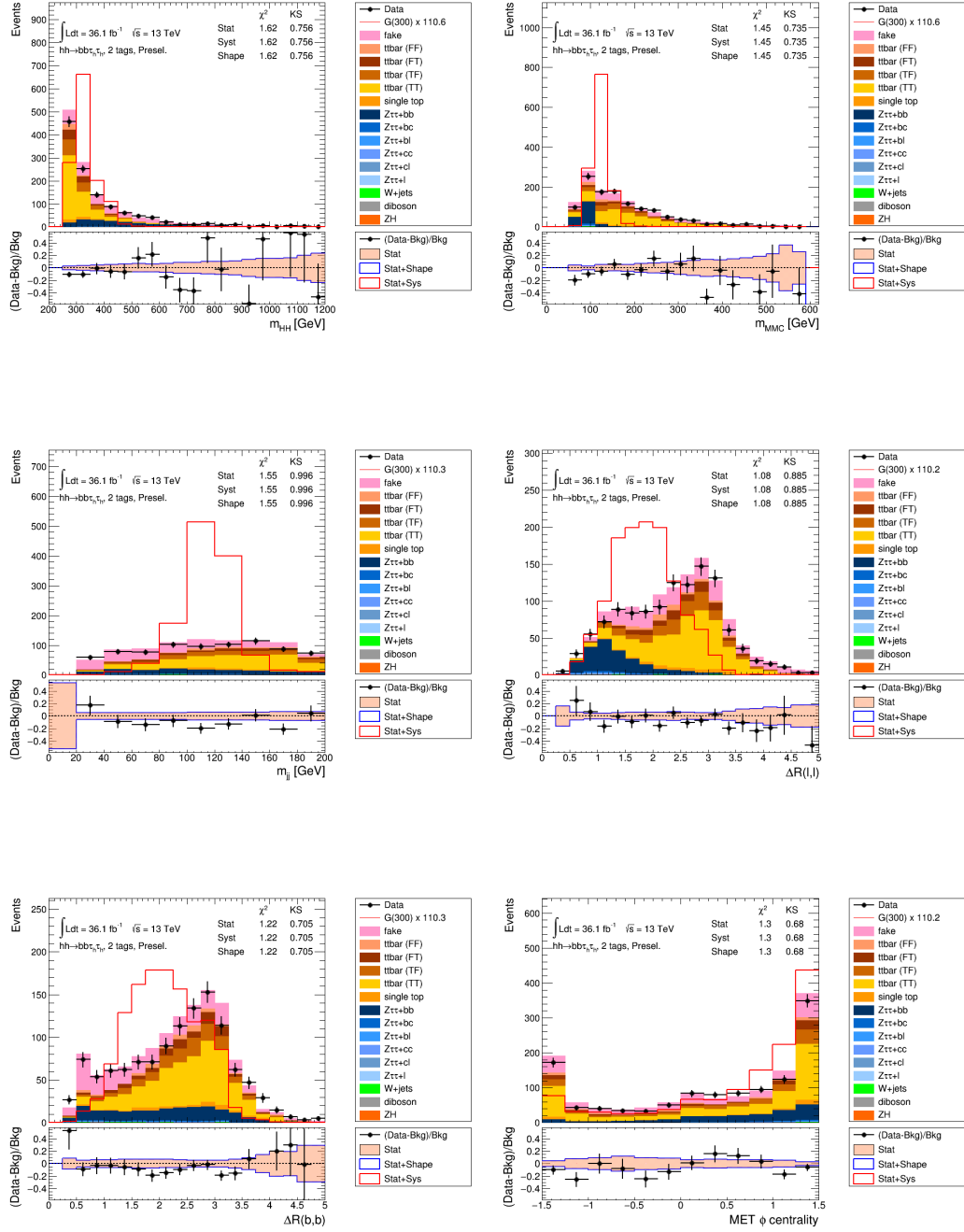
Figure 8.2: Pre-fit distributions of input variables used in the $\tau_{\mathrm{had}}\tau_{\mathrm{had}}$ channel BDT. The signal for a 300 GeV graviton is overlaid after being normalised to the total data.

8.3 Results

The BDT score output is used as the discriminating variable for all channels and places constraints on signal models. Two benchmark models for resonant di-Higgs production are considered: a spin-0 heavy Higgs boson as predicted by 2HDM models in the narrow width approximation, a spin-2 RS KK graviton for both $c=1$ and $c=2$ and also non-resonant Higgs pair-production assuming SM coupling. In all resonant cases, masses between 260 GeV and 1 TeV are considered, with the lower mass range being constrained as twice the mass of the SM Higgs boson and the heavy resonance decaying into two SM-like Higgs bosons ($m_h = 125$ GeV).

In the case of the non-resonant SM signal the result is presented with the cross-section *reweighted* (RW) by all finite top mass effects. The binning for the output BDT score distributions is optimised to ensure that the background uncertainty is kept to below 50% for all signals in the $\tau_{\mathrm{had}}\tau_{\mathrm{had}}$ channel. If there is no signal in that bin the uncertainty is required to be below 1%. In addition a minimum number of 5 events in each bin is required.

Pre-fit and post-fit distributions of the BDT score output for 2-tag OS control regions, the $Z \to \tau\tau$+jets control region and the top control region are presented in Appendix A. Good agreement between data and MC is observed in all cases but the agreement improves post-fit as expected. This can be seen also in Figure 8.3 where the BDT input variables are presented post-fit with excellent data agreement within one standard deviation of the prediction.

The BDT responses for the 2HDM and graviton searches after performing the fit when assuming a background-only hypothesis are shown in Figures 8.4 and 8.5 for the $\tau_{\mathrm{had}}\tau_{\mathrm{had}}$ channel. The post-fit output BDT score distributions for the non-resonant search are shown in Figures 8.6 with and without finite top mass reweighting.

The observed number of events are found to be compatible with the fitted number of background events. As no significant excess over the expected background from SM processes is observed, the data is used to set upper limits on resonant and non-resonant Higgs pair-production at 95% CL. As previously discussed, the results are obtained from a profile likelihood ratio test following the CLs prescription. For the fully hadronic channel,

the cross-section for non-resonant di-Higgs production is observed (expected) to be 16.4 (17.4) times the Standard Model prediction at 95% confidence level for the top mass RW signal.

The results for resonance searches are presented as exclusion limits on the hh-production cross-section, given as a function of the resonance mass. The expected limits for 2HDM and graviton signal models are shown in Figure 8.7 for the $\tau_{\mathrm{had}}\tau_{\mathrm{had}}$ channel.

The RSG c=1 has less mass points than the RSG c=2 and 2HDM. The intention was to have fine mass splitting for all the mass points for RSG c=2 and then scale the same samples down to RSG c=1. However the scaling did not close as expected and the effects were not fully understood. In addition, an uncertainty would be needed to cover for this rescaling. Therefore it was decided to abandon the scaling from RSG c=2 to RSG c=1 and use only the mass points where Monte Carlo samples were available.

8.3.1 Combination

The di-Higgs $\rightarrow b\bar{b}\tau\tau$ analysis throughout this thesis focuses on the fully hadronic channel where both taus decay hadronically, however this result has been combined with the $\tau_{\mathrm{lep}}\tau_{\mathrm{had}}$ channel where one tau decays leptonically (lephad). The $\tau_{\mathrm{lep}}\tau_{\mathrm{had}}$ group performed their analysis similarly to that of the fully hadronic channel but the analysis was split into two parts by the trigger used, the single lepton trigger (SLT) and the lepton tau trigger (LTT) analyses are included in the $b\bar{b}\tau\tau$ combination.

The results from the statistical analysis of the separate channels are presented in Table 8.1.

Expected limits at 95% CL on the cross-sections for resonant models are shown as a function of mass for the $\tau_{\mathrm{lep}}\tau_{\mathrm{had}}$ and $\tau_{\mathrm{had}}\tau_{\mathrm{had}}$ channels separately and then combined in Figure 8.8. Upper limits on the cross-section for non-resonant di-Higgs production are set and interpreted as multiples of the SM prediction for each channel separately and then combined to determine a value for μ, defined in Equation 6.13. The expected and observed results are presented in Table 8.1. The expected number of signal and background events after applying the selection criteria with exactly 2 b-jets and performing the fit assuming a background-only hypothesis are given in Table 8.2. The observed number of events in data are also shown.

The upper boundary on the cross-section for non-resonant hh production times the $hh \rightarrow bb\tau\tau$ branching ratio at 95% confidence level gives an observed (expected) limit of 30.9 fb (36.0 fb), corresponding to a value of

$$\mu = 12.7(14.8) \times \sigma_{\text{SM}}$$

The result, for all signal hypotheses, is dominated by statistical uncertainties. The percentage uncertainties on the simulated non-resonant signal strength are shown in Table 8.3 giving the effect of the various categories of uncertainty on the non-resonant result. Statistical and systematic uncertainties included in the fit, as deviations from the nominal, are not significantly contrained relative to their input value. The fractional impact and pulls of the systematic uncertainties of the combined $\tau_{\text{lep}}\tau_{\text{had}}$ and $\tau_{\text{had}}\tau_{\text{had}}$ non-resonant result are shown in Figure 8.9.

The nuisance parameter rankings for the fully hadronic channel are presented in Figure 8.10 where the contributions of the data-driven multi-jet fake estimation systematic uncertainties can be seen.

		Observed	-2σ	-1σ	Expected	$+1\sigma$	$+2\sigma$
$\tau_{\text{lep}}\tau_{\text{had}}$ (SLT)	$\sigma(hh \rightarrow bb\tau\tau)$ [fb]	52	38.2	52	72	100	134
	$\sigma/\sigma_{\text{SM}}$	21.3	15.7	21.1	29.3	40.8	55
$\tau_{\text{lep}}\tau_{\text{had}}$ (LTT)	$\sigma(hh \rightarrow bb\tau\tau)$ [fb]	326	123	165	229	319	428
	$\sigma/\sigma_{\text{SM}}$	134	50	68	94	131	175
$\tau_{\text{lep}}\tau_{\text{had}}$ Comb.	$\sigma(hh \rightarrow bb\tau\tau)$ [fb]	57	37.2	49.9	69	96	129
	$\sigma/\sigma_{\text{SM}}$	23.5	15.2	20.5	28.4	39.5	53
$\tau_{\text{had}}\tau_{\text{had}}$ RW	$\sigma(hh \rightarrow bb\tau\tau)$ [fb]	40.0	22.8	30.6	42.4	59	79
	$\sigma/\sigma_{\text{SM}}$	16.4	9.33	12.5	17.4	24.2	32.4
Combination	$\sigma(hh \rightarrow bb\tau\tau)$ [fb]	30.9	19.4	26.0	36.1	50	67
	$\sigma/\sigma_{\text{SM}}$	12.7	7.93	10.7	14.8	20.6	27.6

Table 8.1: Upper limits on the production cross-section for non-resonant di-Higgs production at 95% CL. The limits including the finite top mass correction are presented.

	$\tau_{\text{lep}}\tau_{\text{had}}$ channel		$\tau_{\text{had}}\tau_{\text{had}}$ channel
	(SLT)	(LTT)	
$t\bar{t}$	17800 ± 1100	1475 ± 94	360± 100
Single top	1130 ± 110	72.9 ± 7.6	39.7 ± 5.9
QCD fakes	-	-	294 ± 57
$t\bar{t}$ fakes	-	-	160 ± 120
Fakes	9000 ± 1100	475 ± 76	-
$Z \to \tau\tau + (cc, bc, bb)$	416 ± 97	117 ± 28	291 ± 91
Other (W + Z + DY + VV)	197 ± 32	14.5 ± 2.3	22.9 ± 5.9
SM Higgs	37.6 ± 10	4.1 ± 1	8.2 ± 2.1
Total Background	28610 ± 180	2159 ± 46	1178 ± 40
Data	28612	2161	1180
$G(300, c = 1) \to bb\tau\tau$	23.6 ± 3.7	7.5 ± 1.2	13.1 ± 2.6
$G(500, c = 1) \to bb\tau\tau$	42.4 ± 6.4	9.9 ± 1.5	36.3 ± 7
$G(1000/800(LTT), c = 1) \to bb\tau\tau$	2.56 ± 0.4	1.06 ± 0.16	2.11 ± 0.43
$G(300, c = 2) \to bb\tau\tau$	327 ± 50	82 ± 13	240 ± 46
$G(500, c = 2) \to bb\tau\tau$	193 ± 29	39.7 ± 6.1	187 ± 36
$G(1000/800(LTT), c = 2) \to bb\tau\tau$	8.6 ± 1.3	3.63 ± 0.56	7.9 ± 1.6
$H(300) \to bb\tau\tau$	39.1 ± 6.3	11.8 ± 1.9	17.9 ± 3.6
$H(500) \to bb\tau\tau$	3.41 ± 0.52	0.88 ± 0.13	2.84 ± 0.54
$H(1000/800(LTT)) \to bb\tau\tau$	0.0267 ± 0.0041	0.0228 ± 0.0035	0.0222 ± 0.0044
Non-res. hh	1.04 ± 0.14	0.290 ± 0.043	0.79 ± 0.15
Non-res.(top mass RW) hh	0.99 ± 0.13	0.225 ± 0.033	0.75 ± 0.14

Table 8.2: Post-fit expected number of signal and background events and observed number of data events after applying the selection criteria and requiring exactly 2 b-jets and assuming a background-only hypothesis. The category 'Other' includes contributions from W+jets, $Z/\gamma^* \to \ell\ell$+jets, and di-boson processes

Source	Uncertainty (%)
Total	±53.9
Data statistics	±44
Simulation statistics	±16
Experimental Uncertainties	
Luminosity	±2.4
Pile-up reweighting	±1.7
Hadronic τ-lepton	±16
Fake-τ estimation	±8.4
b-tagging	±8.3
Jets and E_T^{miss}	±3.3
Electron and muon	±0.5

Table 8.3: The percentage uncertainties on the simulated non-resonant signal strength.
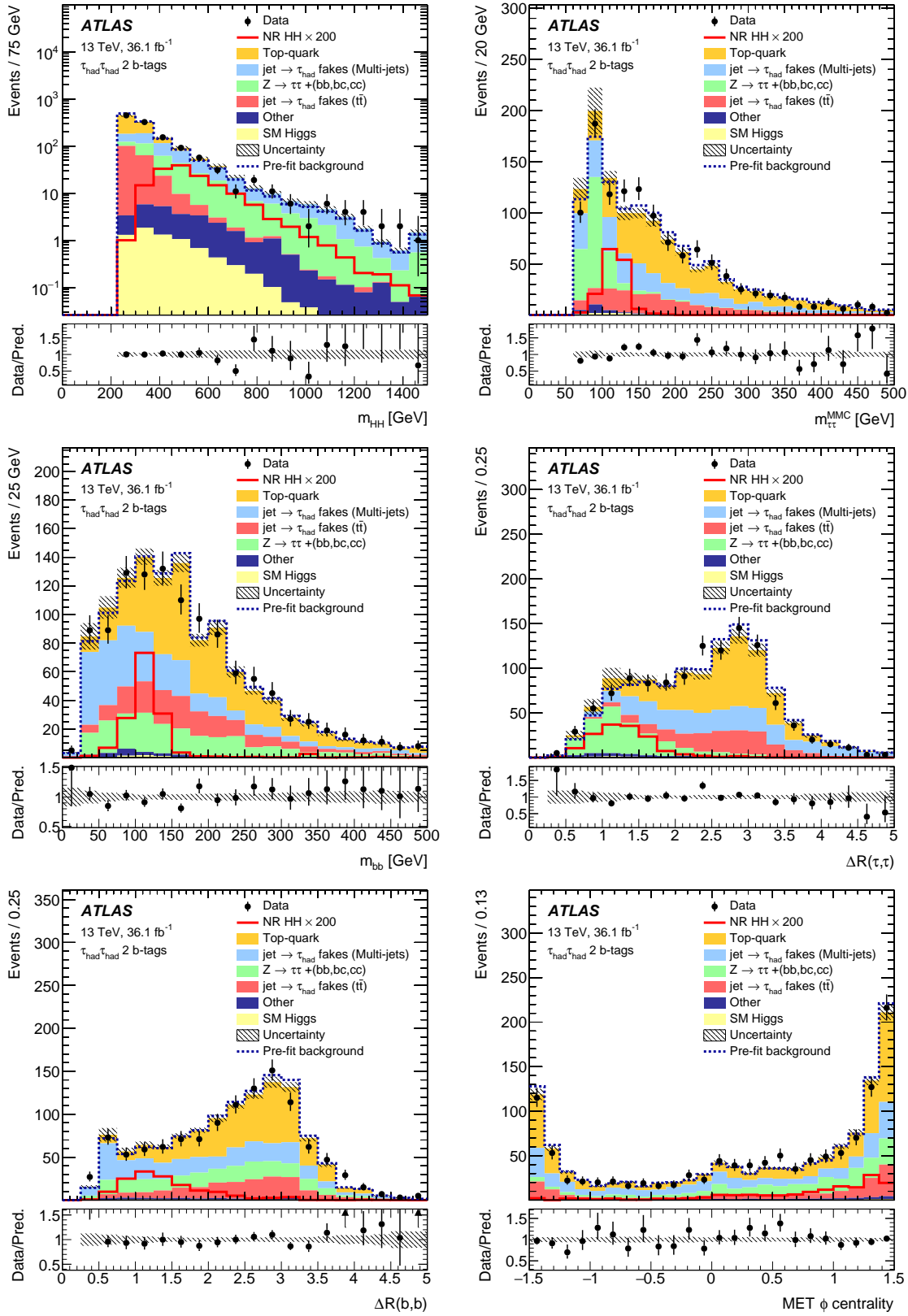
Figure 8.3: Distributions of the BDT input variables post-fit in the 2 tag OS region for the $\tau_{\text{had}}\tau_{\text{had}}$ channel [173].

(a) 2HDM ($m_{\mathrm{H}}=$ 300 GeV)

(b) 2HDM ($m_{\mathrm{H}}=$ 500 GeV)

(c) 2HDM ($m_{\mathrm{H}}=$ 1000 GeV)
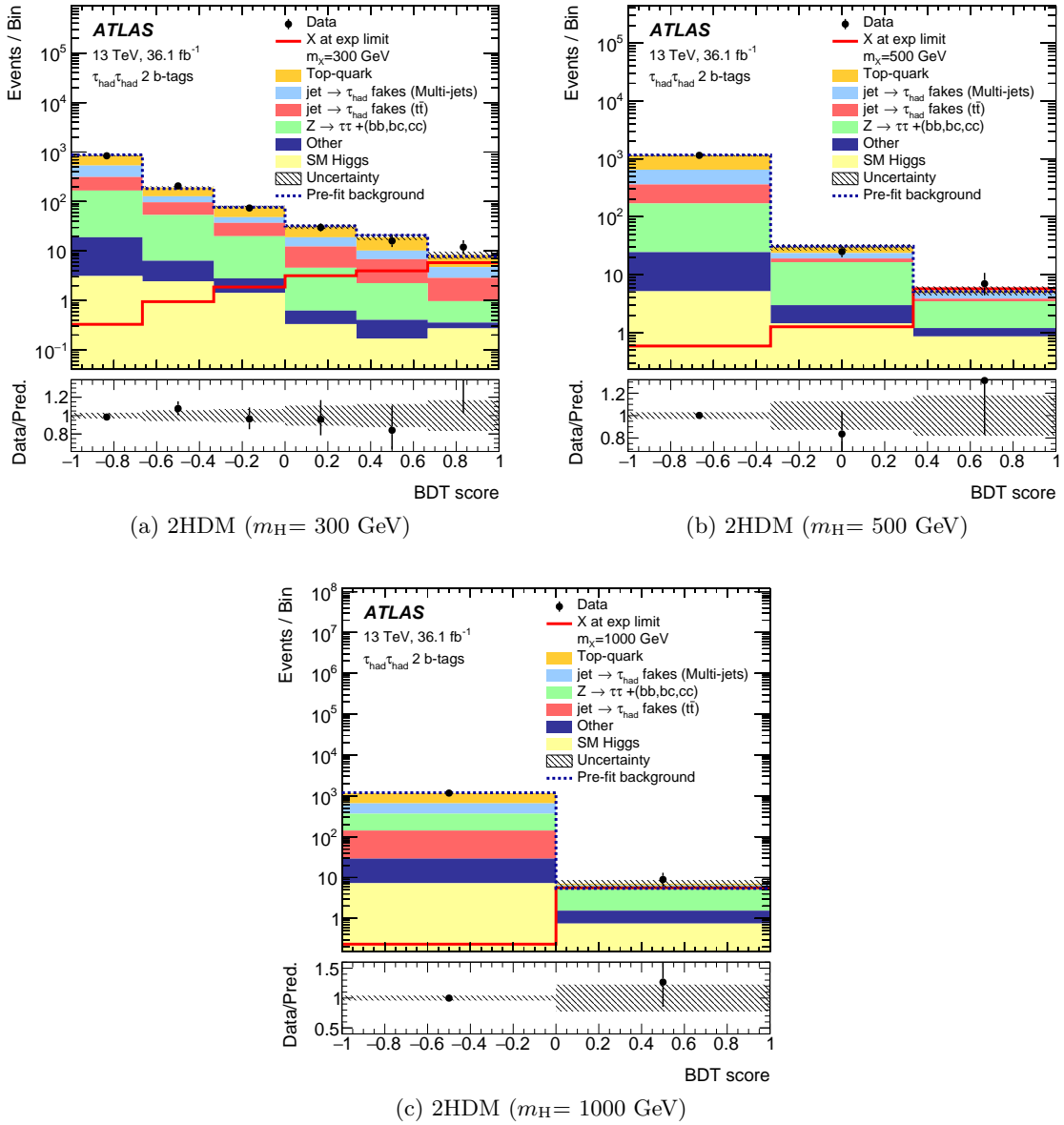
Figure 8.4: Distribution of the BDT output for 2HDM signal in the $\tau_{\mathrm{had}}\tau_{\mathrm{had}}$ channel for resonance masses of 300 GeV, 500 GeV and 1000 GeV, using the optimised binning and after performing the final fit. A background-only hypothesis is assumed [173].
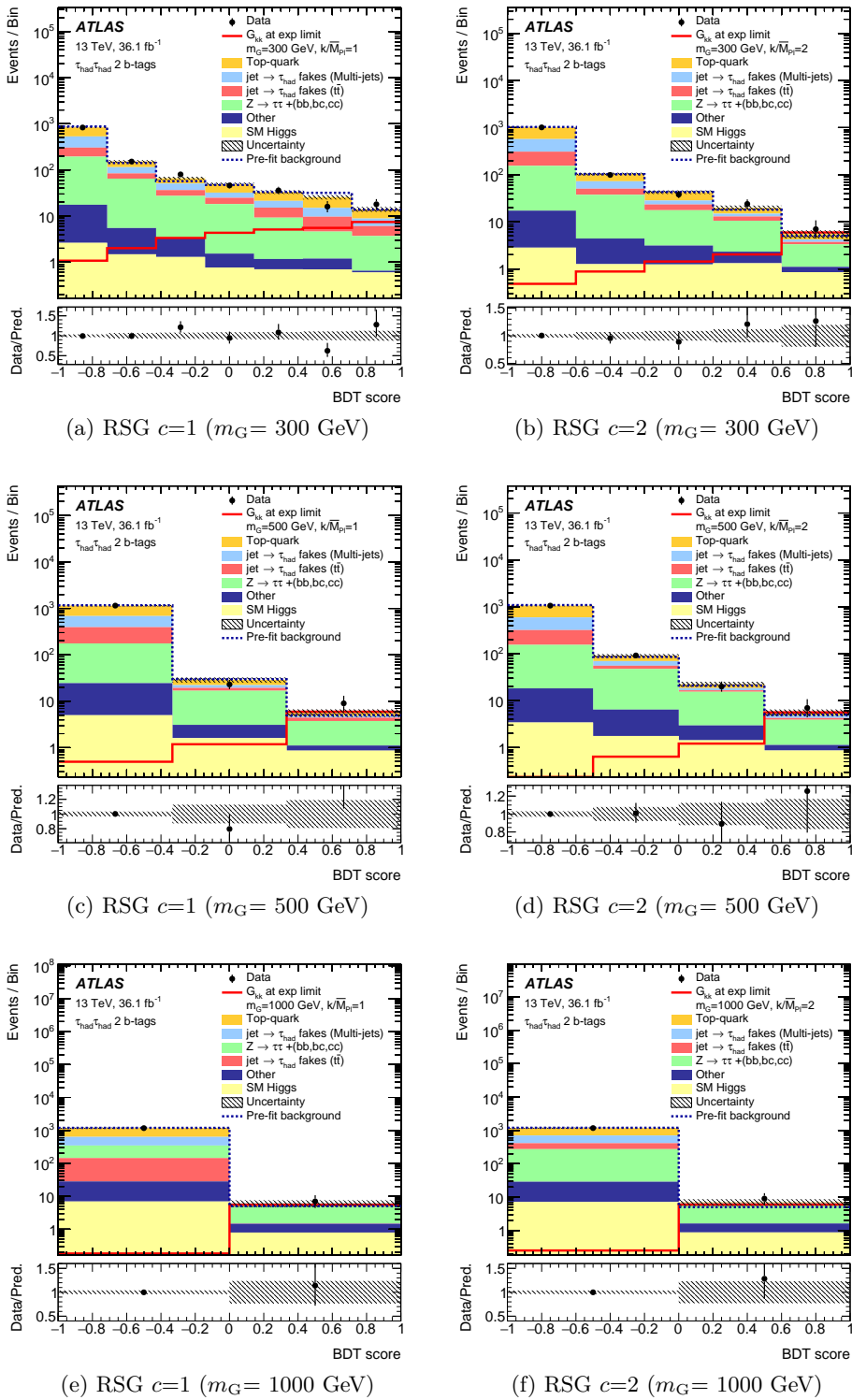
Figure 8.5: Distribution of the BDT output for RS graviton $c=1$ (left) and $c=2$ (right) signals in the $\tau_{\text{had}}\tau_{\text{had}}$ channel for resonance masses of 300 GeV (top), 500 GeV (centre) and 1000 GeV (bottom), using the optimised binning and after performing the final fit. A background-only hypothesis is assumed [173].
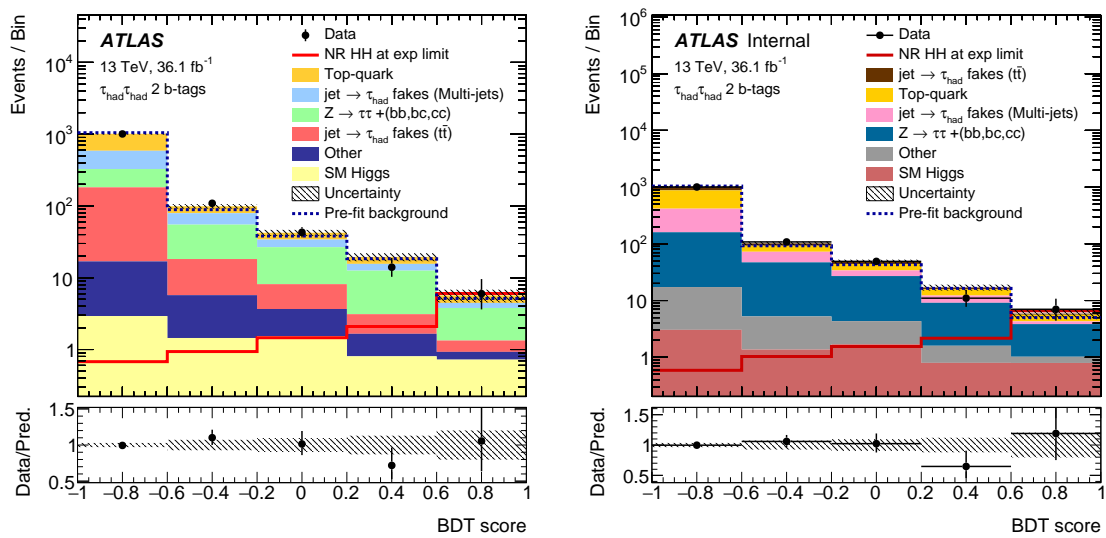
Figure 8.6: Distribution of the BDT score for the non-resonant Higgs pair-production assuming finite top mass (left) and without (right), using the optimised binning and after performing the final fit with full systematics [173].
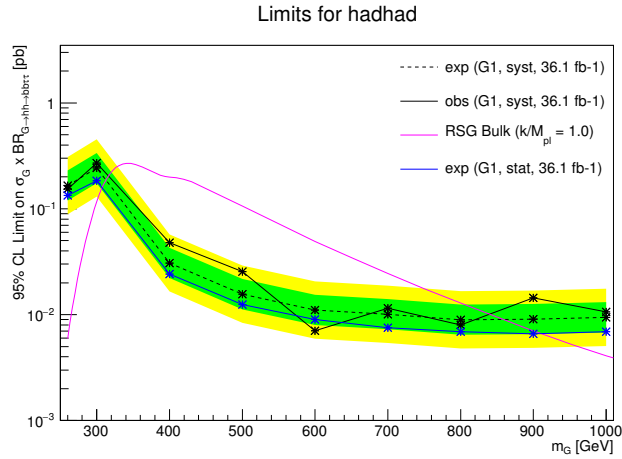
(a) RSG c=1, $\tau_{\mathrm{had}}\tau_{\mathrm{had}}$ channel
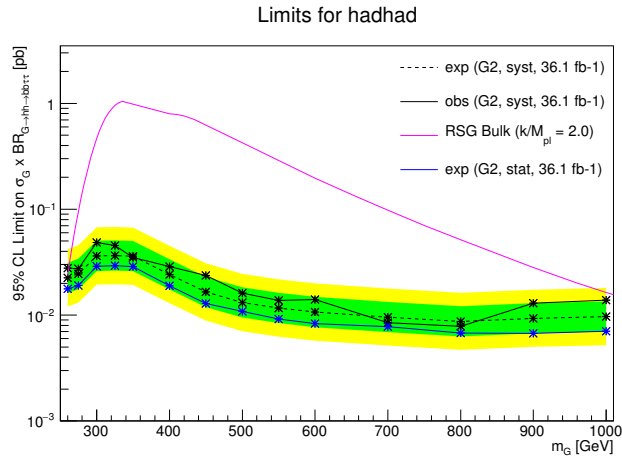
(b) RSG c=2, $\tau_{\mathrm{had}}\tau_{\mathrm{had}}$ channel
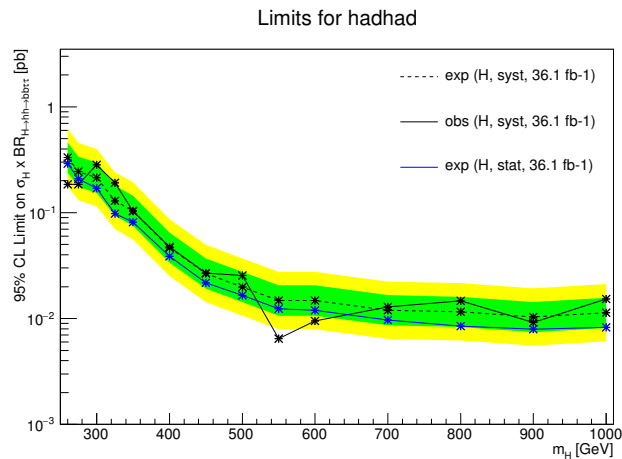
(c) 2HDM, $\tau_{\mathrm{had}}\tau_{\mathrm{had}}$ channel

Figure 8.7: Expected limits at 95% C.L. on the cross-sections of the RS $G \rightarrow hh$ c=1 (a), RS $G \rightarrow hh$ c=2 (b) and 2HDM $H \rightarrow hh$ (c) for the $\tau_{\mathrm{had}}\tau_{\mathrm{had}}$ channel. The expected cross-section for RS graviton production (assuming $c = 1.0$) is also shown in the relevant plots [173].

(a) RSG $c=1$

(b) RSG $c=2$

(c) 2HDM
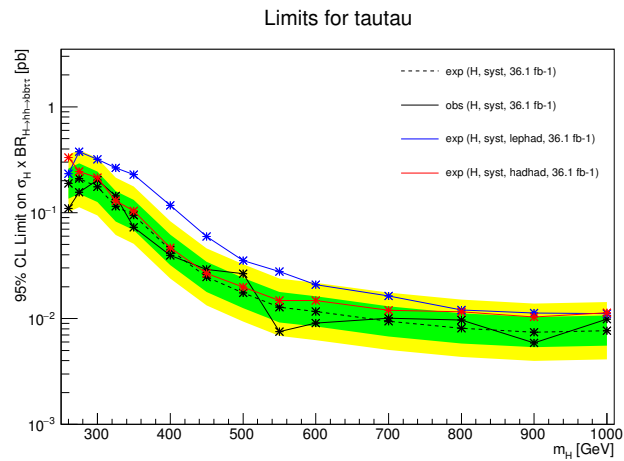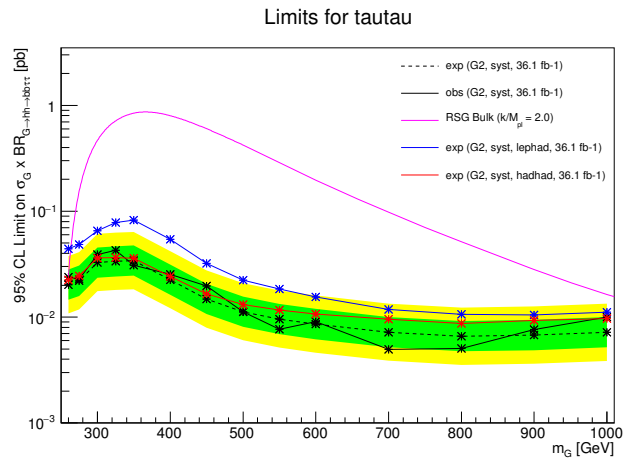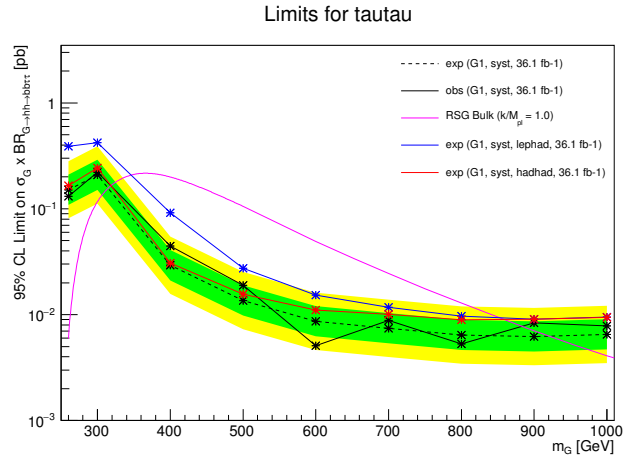
Figure 8.8: Expected limits at 95% C.L. on the cross-sections of RS $G \rightarrow hh$ for $c=1$ (a) and $c=2$ (b) and the $H \rightarrow hh$ (c) processes when combining both the $\tau_{\text{lep}}\tau_{\text{had}}$ and $\tau_{\text{had}}\tau_{\text{had}}$ channels. The expected cross-section for RS graviton production is also shown in the top two plots [173].
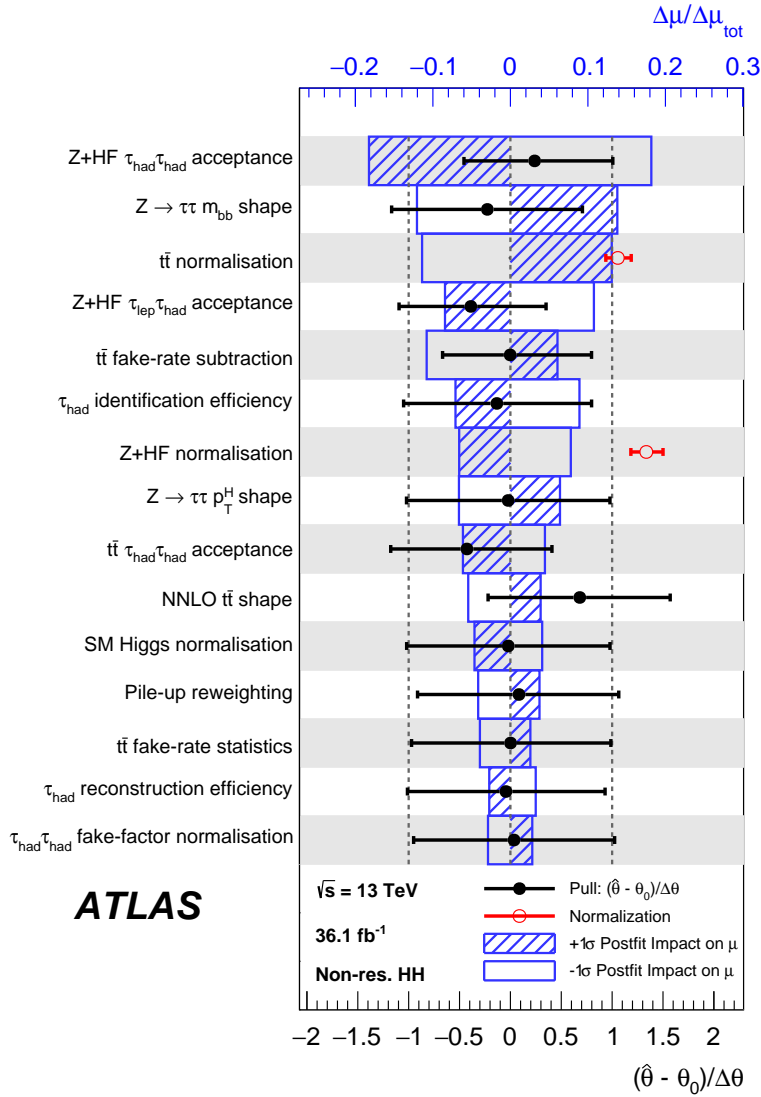
Figure 8.9: Fractional impact of systematic uncertainties for the fitted non-resonant hh signal-strength parameter μ in the combined $\tau_{\text{lep}}\tau_{\text{had}}$ and $\tau_{\text{had}}\tau_{\text{had}}$ result [173].
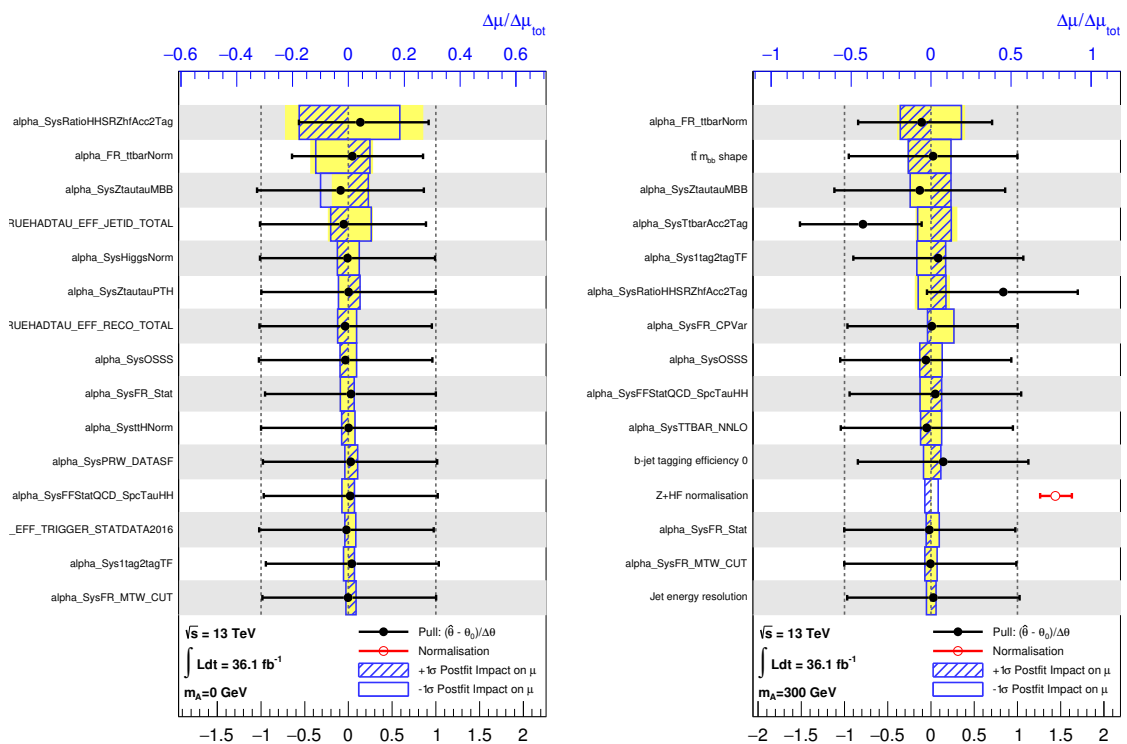
Figure 8.10: Nuisance parameter rankings in the $\tau_{\text{had}}\tau_{\text{had}}$ channel for non-resonant di-Higgs production (left) and RS graviton $c=1$ m_G=300 GeV resonant production (right) [173].

Chapter 9

Search for Third Generation Leptoquarks in the $b\tau b\tau$ Channel

This chapter describes the search for pair-produced scalar leptoquarks decaying to a $b\tau b\tau$ final state. The analysis was performed using 36.1 fb^{-1} of data taken during 2015 and 2016. The search utilises many of the same techniques used by the ATLAS di-Higgs $\rightarrow b\bar{b}\tau\tau$ search described in Chapter 8 and in more detail in [174]. The di-Higgs analysis is reinterpreted to select resonances decaying to $b\tau$ pairs rather than two Standard Model Higgs bosons decaying to bb and $\tau\tau$ [175, 176].

The analysis revolves around a boosted decision tree (BDT) and utilises the BDT score as the final discriminant outlined in Section 9.2. The statistical evaluation method performed by the di-Higgs analysis is employed here with a binned profile likelihood fit on the BDT score output to extract the signal strengths for scalar down-type and up-type leptoquark pair-production. However, if there is no clear evidence for an excess of events the signal strengths are used to produce an observed 95% CL upper limit on the cross-section for scalar leptoquark pair-production as a function of the leptoquark mass. This can be compared to the expected limit when evaluated against an Asimov dataset. The systematics enter the fit as nuisance parameters analogous to the di-Higgs analysis.

Despite the many similarities, it is important to note the differences between the scalar leptoquark search and the Higgs pair-production analysis and they are clearly stated throughout this chapter. There is no cut on the invariant mass of the di-tau system, the leading tau has a p_T minimum threshold of 60 GeV in DTT events and the 1 b-tag region is included in the fit along with the $Z \rightarrow \mu\mu + $ jets control region and the 2 b-tag selection as an additional signal region.

With a final state of two *b*-jets and two hadronically decaying taus, it is important to select the correct pairing of objects. This is studied in Section 9.1 and the final search for pair-produced scalar third-generation leptoquarks results are presented in Section 9.3.

Signal predictions within this chapter for third generation leptoquarks were generated at next-to-leading order (NLO) in QCD using the leptoquark model described in [175].

9.1   Pairing of *b*-jets and τ-leptons

It is necessary to correctly identify which *b*-jets and τ-leptons originate from the same leptoquark. Several approaches were explored in order to correctly pair the final state particles. The mass pairing strategies investigated were as follows:

- $\min|\Delta m|$ – choose the $b\tau$ pairs that minimize the mass difference between the leptoquarks.

- $\max|\Delta\phi|$ – choose the $b\tau$ pairs that maximize the sum of $\Delta\phi(b,\tau)$.

- $\min|\pi - \Delta R|$ – choose the $b\tau$ pairs that maximize the sum of $\Delta R(b,\tau)$.

All methods give approximately the same cross-section upper limit for leptoquark masses above 900 GeV. However, the $\min|\Delta m|$ pairing method gives significantly better limits at low mass and was therefore selected. An example of upper limits for each $b\tau$ pairing can be seen in Figure 9.1. The efficiencies for the different strategies are shown in Figure 9.2.
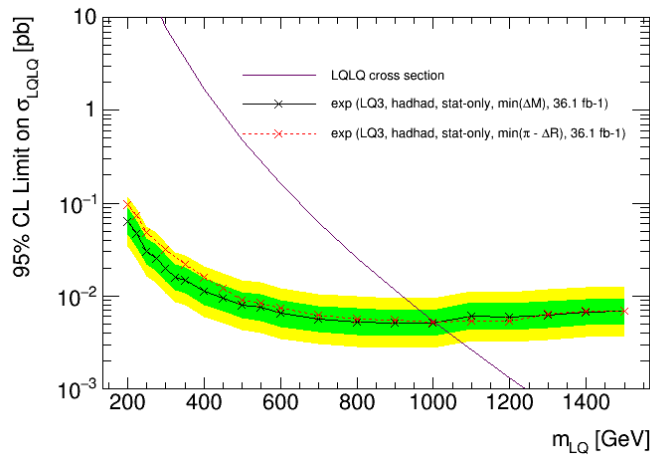
Figure 9.1: Expected limits for different pairings in the $\tau_{\mathrm{had}}\tau_{\mathrm{had}}$ channel. Leptoquark theory cross section taken from [175].
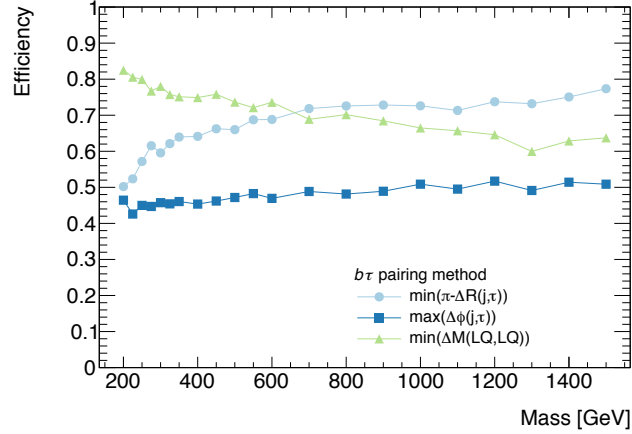
Figure 9.2: Efficiency of pairing the final state b-quarks and τ-leptons for the hadhad channel.

9.2 Boosted Decision Tree Variables and Training

As is done in the hh search, Boosted Decision Trees (BDTs) are trained to separate the signal from the expected backgrounds and the BDT score distributions are used as the final discriminant for limit-setting. Separate BDTs are trained for each signal mass point and b-tag signal regions using $Z \to \tau\tau +$ jets, fakes and $t\bar{t}$ background processes. The signal sample used in the training includes signals with neighbouring mass. The variables used as inputs to the BDT that provide good discrimination between signal and background are different to the di-Higgs analysis, as expected:

- $\Delta R(\tau_0, \text{jet})$ – The ΔR between the leading tau and leading jet.

- s_{T} – The scalar sum of missing tranverse energy in the event, the p_{T} of τ-leptons and the p_{T} of the two highest-p_{T} jets.

- $E_{\mathrm{T}}^{\mathrm{miss}}\phi$ centrality – Quantifies the position in ϕ of $E_{\mathrm{T}}^{\mathrm{miss}}$ between τs. Full definition is given in Chapter 6 and the hh paper [174].

- $m_{\tau,\mathrm{jet}}$ – The invariant mass between the leading τ and its matching jet based on a pairing that minimizes ΔM.

- p_{T}^{τ} – The p_{T} of the leading τ-lepton.

Figures 9.3 and 9.4 show the overtraining plots for the 1-tag and 2-tag regions against several leptoquark masses.
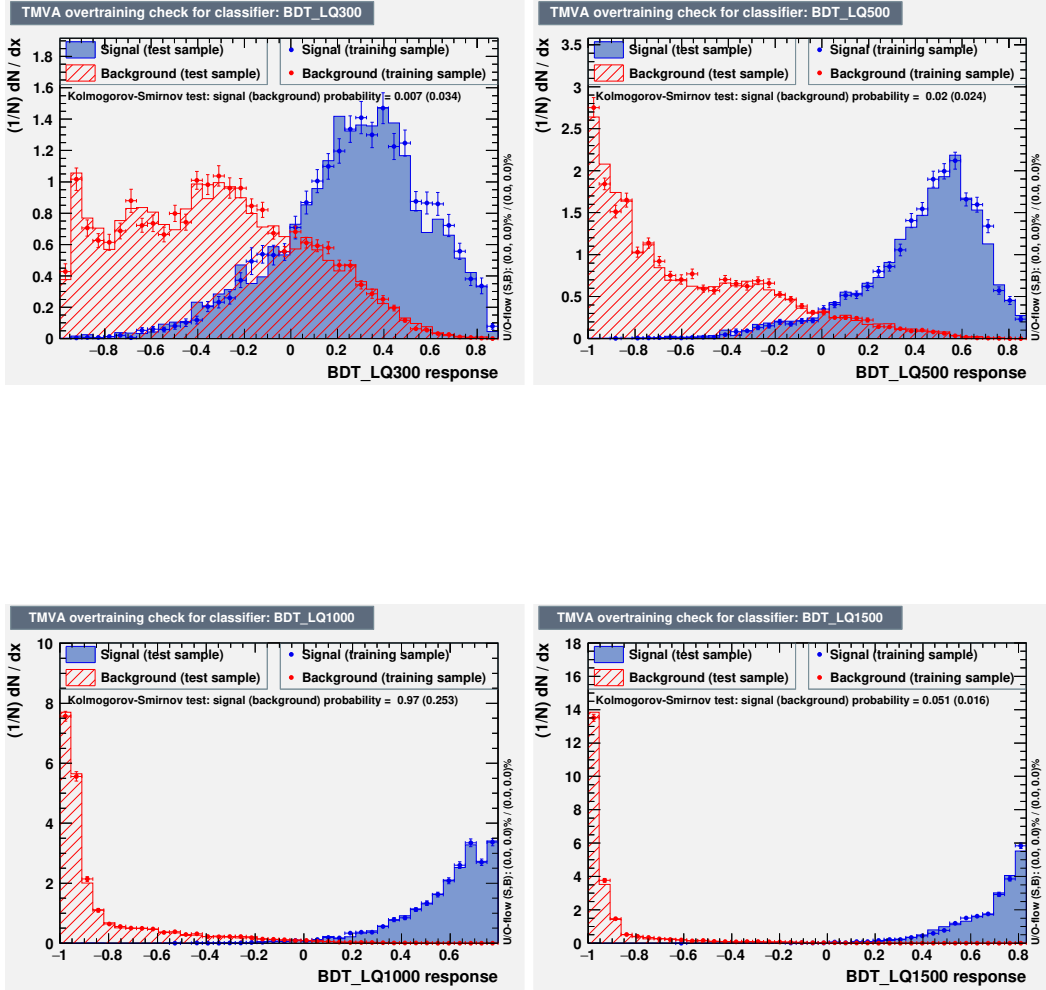
Figure 9.3: Overtraining plots for leptoquark signals in the $b\tau_{had}b\tau_{had}$ channel, for 300 GeV (top left), 500 GeV (top right), 1000 GeV (bottom left) and 1500 GeV mass points in the 1 b-tag region.
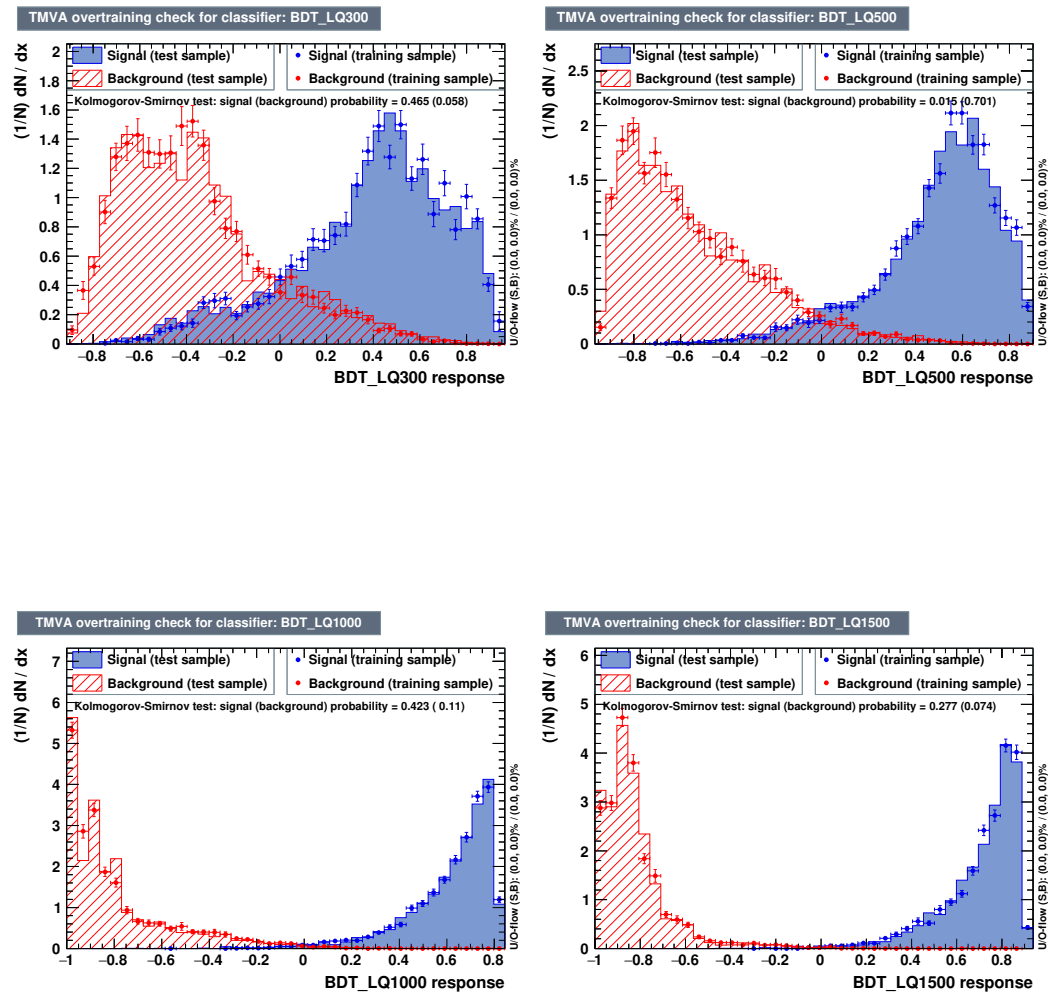
Figure 9.4: Overtraining plots for leptoquark signals in the $b\tau_{had}b\tau_{had}$ channel, for 300 GeV (top left), 500 GeV (top right), 1000 GeV (bottom left) and 1500 GeV mass points in the 2 b-tag region.

9.3 Results

The fit strategy used in this reinterpretation is identical to that of [174] and Chapter 8. The BDT output score is used as the discriminating variable for all channels and signals. The binning for the output BDT score distributions is optimised to ensure that the minimum number of events in each bin is 5 and the background uncertainty is required to be below 50% for the signal fraction in the fully hadronic channel. A profile likelihood ratio test is performed to assess the compatibility of the SM background-only hypothesis with the observations in the signal regions. Both the 1 b-tag and 2 b-tag regions are characterised as signal-like. All sources of systematic and statistical uncertainties on the signal and background modeling are implemented as deviations from the nominal model scaled by nuisance parameters that are profiled in the fit.

As in the di-Higgs analysis, a $Z \to \mu\mu$ plus 2 b-jets control region is included as a single bin in the fit in order to derive a normalisation factor for $Z + bb, bc, cc$ background processes.

The post-fit plots of the BDT input variables are presented for 1-tag and 2-tag in Figure 9.5 and Figure 9.6, respectively. Good agreement is seen between data and prediction. The BDT responses in the 1-tag and 2-tag fully hadronic signal regions are shown in Figure 9.7 and 9.8 for four representative leptoquark masses after performing the combined channel fit. Observed and expected limits on the cross-section for scalar leptoquark pair-production are shown as a function of mass in Figure 9.9 for the hadronic channel. Additionally, the comparison on the limits with and without the inclusion of the 1 tag region is shown in Figure 9.10

Yield tables in the 1-tag and 2-tag signal regions are shown for the fully hadronic channel in Table 9.1 where the numbers quoted are after performing the $\tau_{\mathrm{had}}\tau_{\mathrm{had}}$ fit.
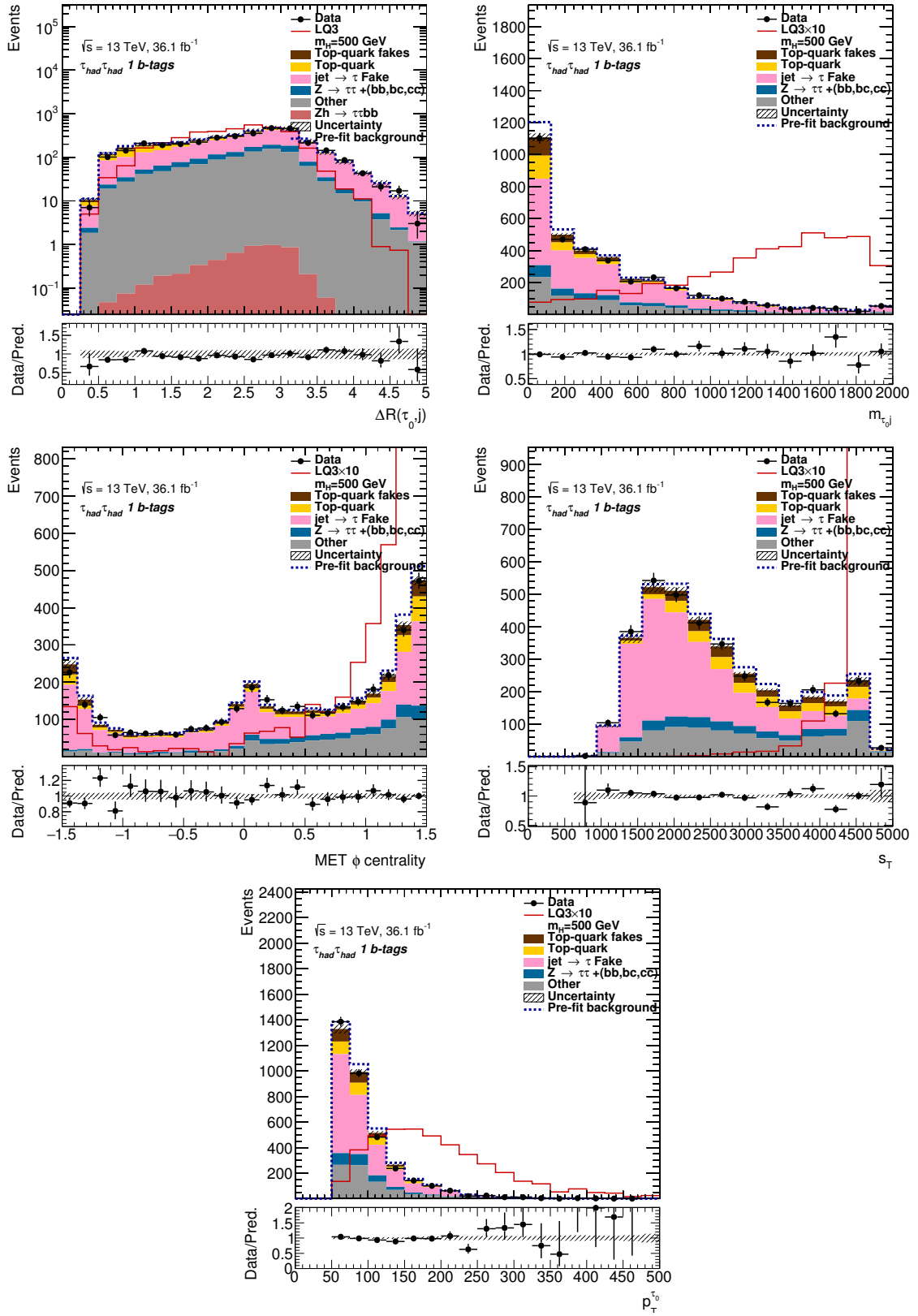
Figure 9.5: Post-fit distributions of the BDT input variables in the 1 tag OS region for the $\tau_{\mathrm{had}}\tau_{\mathrm{had}}$ channel [177].
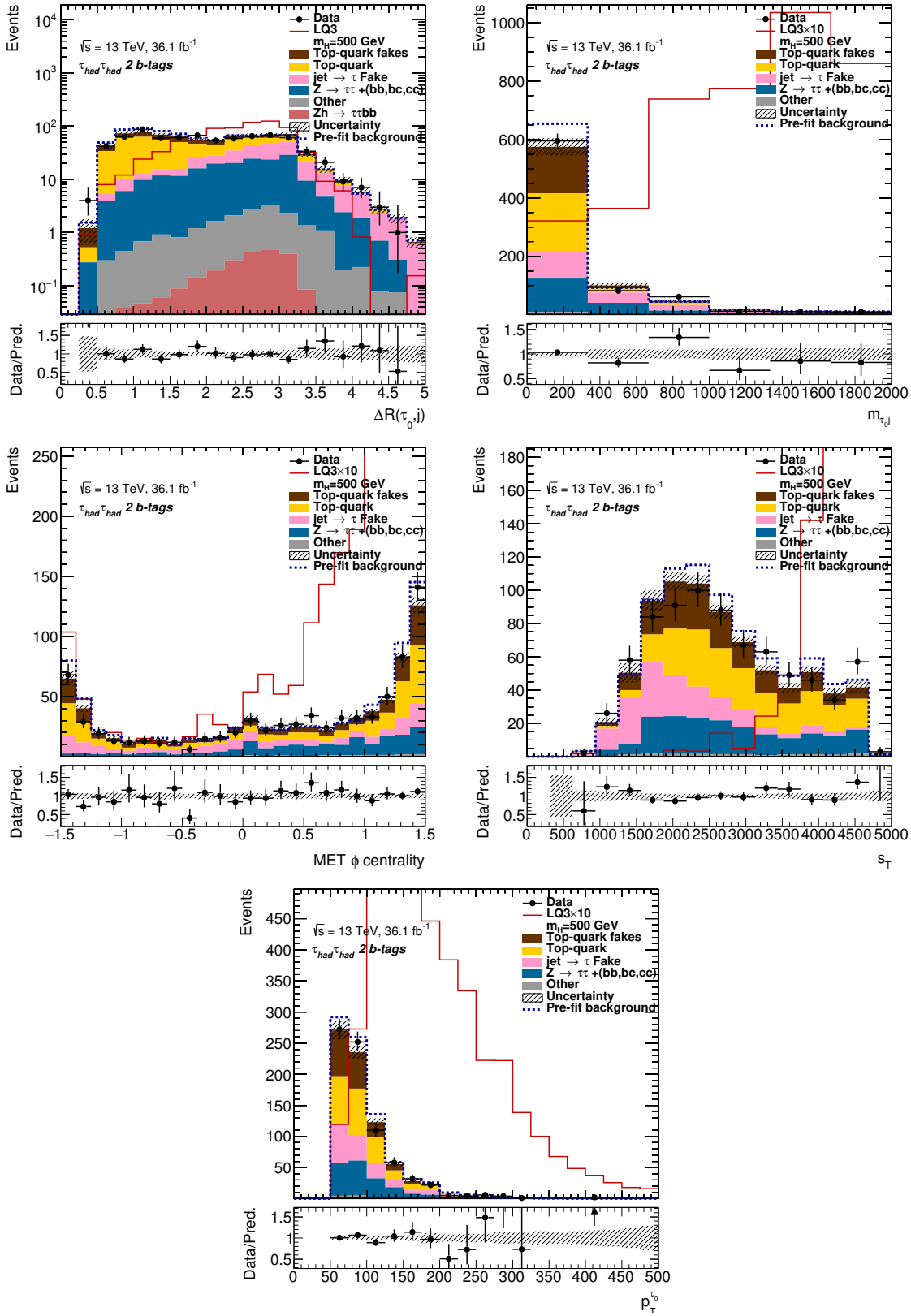
Figure 9.6: Post-fit distributions of the BDT input variables in the 2 tag OS region for the $\tau_{\text{had}}\tau_{\text{had}}$ channel [177].
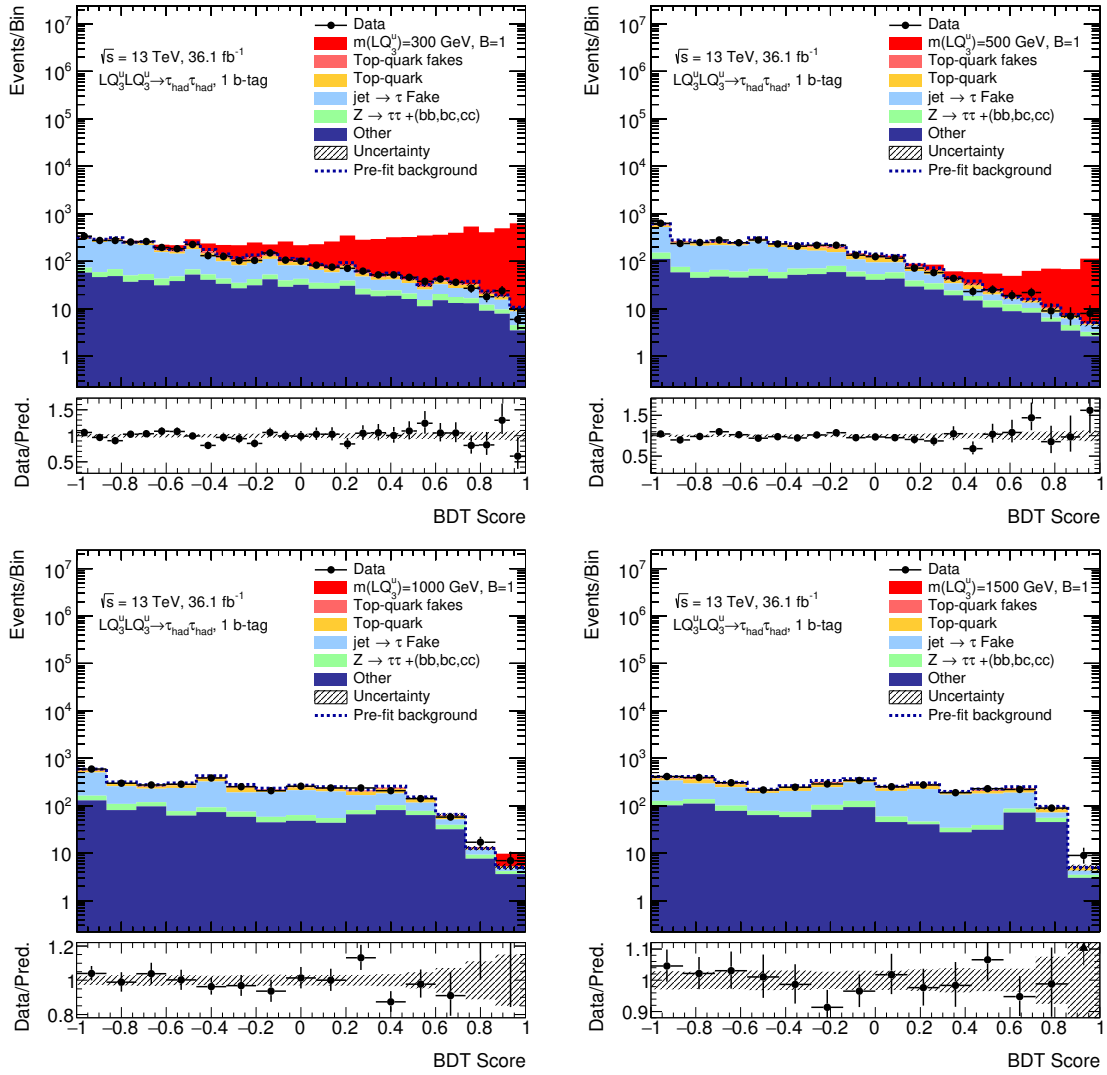
Figure 9.7: BDT score distributions for the $\tau_{\mathrm{had}}\tau_{\mathrm{had}}$ channel in the 1-tag signal region. All distributions are shown after performing the fit, 300 GeV (top left), 500 GeV (top right), 1000 GeV (bottom left) and 1500 GeV (bottom right) [177, 178].
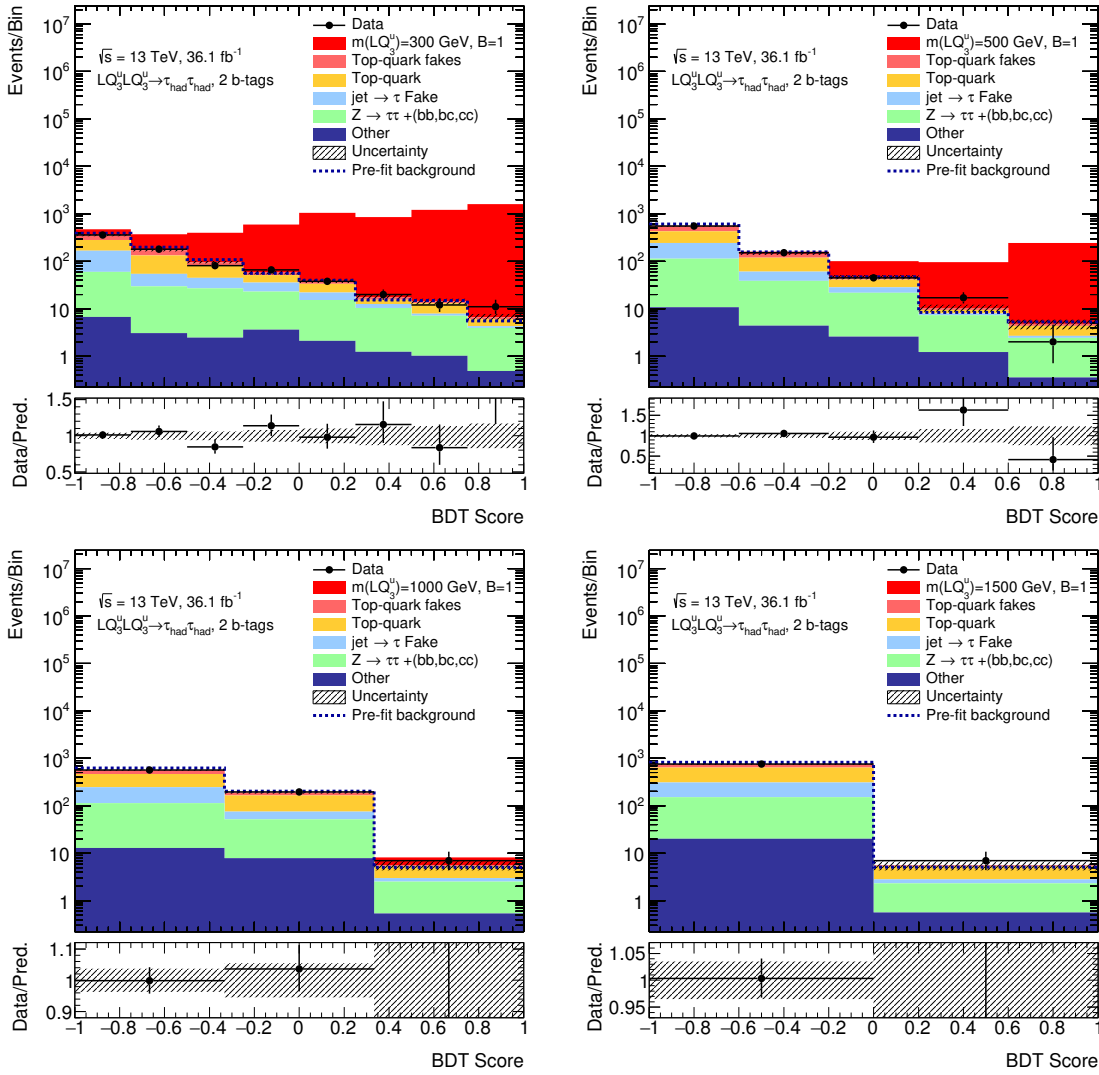
Figure 9.8: BDT score distributions for the $\tau_{\text{had}}\tau_{\text{had}}$ channel in the 2-tag signal region. All distributions are shown after performing the fit, 300 GeV (top left), 500 GeV (top right), 1000 GeV (bottom left) and 1500 GeV (bottom right) [177, 178].

	$\tau_{\text{had}}\tau_{\text{had}}$	
	1-tag	2-tag
Fakes from QCD	1760 ± 120	155 ± 35
Fakes from $t\bar{t}$	180 ± 130	125 ± 88
$Z \to \tau\tau + (cc, bc, bb)$	239 ± 76	147 ± 45
$Z \to \tau\tau + (ll, lc, lb)$	810 ± 88	7.7 ± 2.5
$Z \to \ell\ell + (cc, bc, bb)$	0.055 ± 0.019	0.0108 ± 0.0037
$Z \to \ell\ell + (ll, lc, lb)$	0.71 ± 0.2	0.0051 ± 0.0025
$t\bar{t}$	350 ± 100	287 ± 83
Single top	61.6 ± 7.6	25.3 ± 2.9
$W \to \tau\nu$	51 ± 26	4.2 ± 2.1
VV	22.7 ± 3.1	3.73 ± 0.67
VH	4.7 ± 1.4	2.17 ± 0.67
$t\bar{t}h$	4.2 ± 1.3	3.5 ± 1.1
Total Background	3478 ± 61	761 ± 26
Data	3469	768
$m_{LQ} = 300$ GeV	5600 ± 730	5810 ± 800
$m_{LQ} = 500$ GeV	442 ± 59	397 ± 56
$m_{LQ} = 1000$ GeV	5.19 ± 0.81	2.66 ± 0.45

Table 9.1: Yield table in the 1-tag and 2-tag signal regions of the $\tau_{\text{had}}\tau_{\text{had}}$ channel after performing a background-only fit. The MC background yields use the discriminant binning of the $m_{LQ} = 1000$ GeV hypothesis.
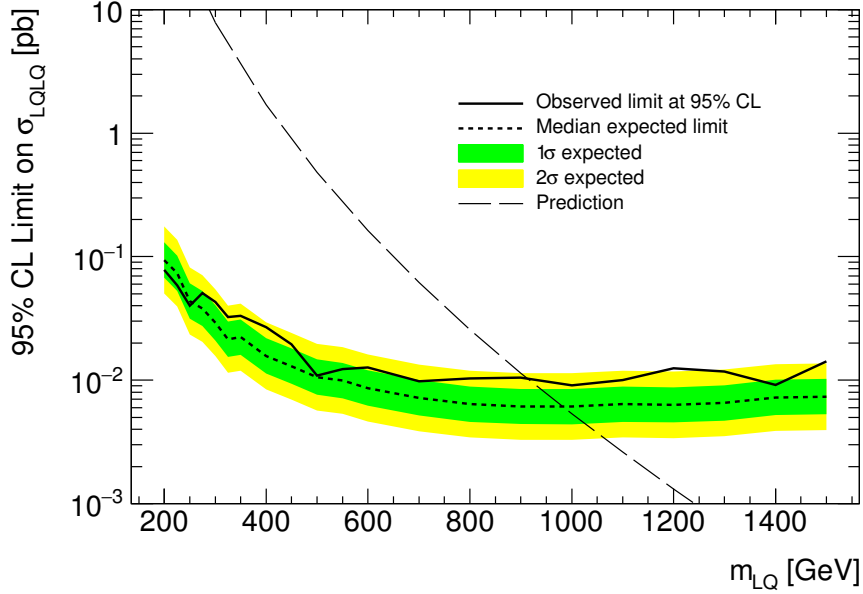
Figure 9.9: Expected 95% CL upper limits on the cross-section for scalar leptoquark pair-production as a function of leptoquark mass for the $\tau_{\text{had}}\tau_{\text{had}}$ channel [177].
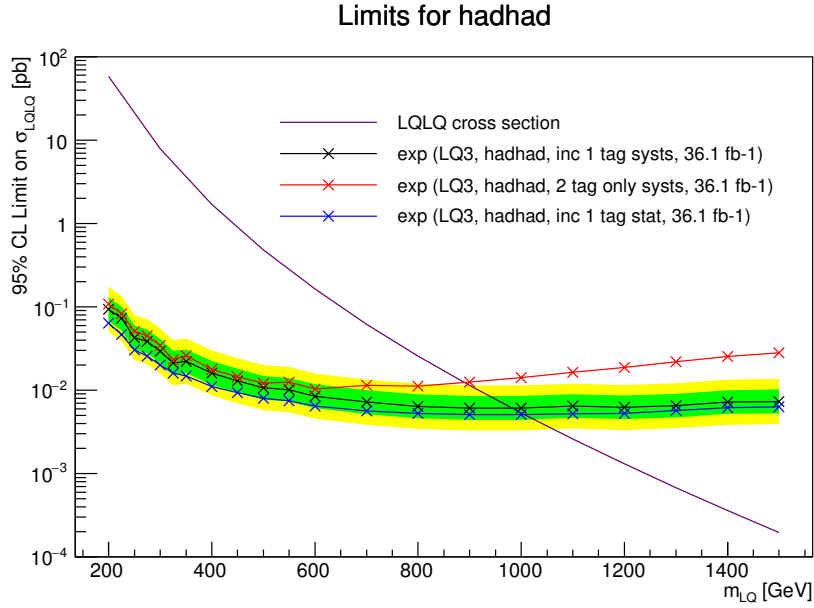
Figure 9.10: Variation of the expected 95% CL upper limits on the cross-section for scalar leptoquark pair-production as a function of leptoquark mass for the $\tau_{\mathrm{had}}\tau_{\mathrm{had}}$ channel with the inclusion of the 1 b-tag region in the fit [177].

9.3.1 Combination

The fully hadronic channel is combined with the $\tau_{\mathrm{lep}}\tau_{\mathrm{had}}$ channel the same as in the di-Higgs analysis. The combined limit including systematic uncertainties is shown in Figure 9.11 for both down-type and up-type leptoquarks, however, priority is given to the latter because the di-Higgs analysis is more sensitive to a $b\tau$ final state.

The unblinded results reveal a deficit (excess) across a large range of leptoquark masses for the separate $\tau_{\mathrm{lep}}\tau_{\mathrm{had}}$ and $\tau_{\mathrm{had}}\tau_{\mathrm{had}}$ channel results. The discrepancies between observed and predicted events is however correlated between the different mass hypotheses.
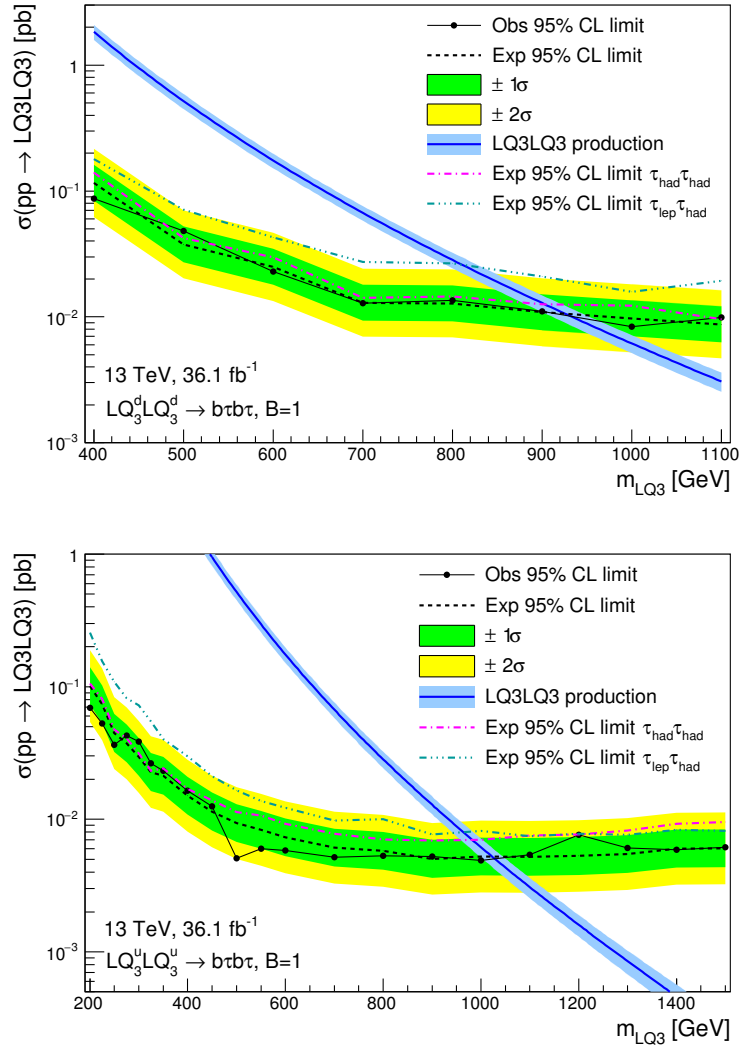
Figure 9.11: Expected and observed 95% CL upper limits on the cross-section for down-type (up) and up-type (down) scalar leptoquark pair-production, with B = 1.0, as a function of leptoquark mass for the semi-leptonic and fully hadronic channels, as well as combined, with the inclusion of systematic uncertainties. The observed limit is shown in solid black [177].

Chapter 10

Conclusion

This thesis presents searches for physics beyond the Standard Model with a final state of two b-quarks and two τ-leptons. The analyses focused mainly on the fully hadronic channel but also presented results combined with the semi-leptonic channel.

The main analysis described a search for resonant and non-resonant pair production of Higgs bosons in the $b\bar{b}\tau^+\tau^-$ final state with the ATLAS detector. The search used 36.1 fb^{-1} of the data collected at the LHC from pp collisions with $\sqrt{s} = 13$ TeV between 2015 and 2016. In the Standard Model the cross-section for Higgs boson pair production is very small due to the box top-loop and the Higgs boson self-interaction destructively interfering. Therefore, the analysis improves sensitivity by using boosted decision tree multivariate techniques to differentiate between signal and background. Statistical evaluations of the result were performed on the final BDT score discriminant.

All signals and backgrounds after event selection are simulated using Monte Carlo methods with the exception of the $t\bar{t}$ jets $\rightarrow$ taus fake background and multi-jet tau fake estimations. The latter has been presented in the thesis as an estimation coming from a data-driven fake factor method which has been shown to perform well and is a viable alternative to poor MC distributions.

The observed (expected) limit at 95% CL on the non-resonant cross-section was found to be 30.9 fb (36.0 fb) which is 12.7 (14.8) times the Standard Model prediction. For the comparison with other results, a separate analysis on the non-resonant signal without the finite top mass reweighting was conducted and produced observed (expected) limits of 37.4 fb (33.5 fb) or 15.4 (13.8) times the Standard Model prediction.

The resonant analysis has been presented in this thesis as exclusion limits on the cross-section times branching ratios of $hh \rightarrow b\bar{b}\tau\tau$ as a function of the resonance mass. The upper limits are set on resonant Higgs boson pair production for a spin-2 Kaluza-Klein graviton G_{KK} in the bulk Randall-Sundrum model and a narrow-width scalar from the two-Higgs doublet model.

The non-resonant result is the most stringent limit on hh production to date. It not only competes with other hh channels at ATLAS such as $b\bar{b}b\bar{b}$ and $b\bar{b}\gamma\gamma$ [7] but also outperforms all current results from CMS [179] which released a observed (expected) combination limit at 95% CL on non-resonant production cross-section of 21.8 (12.4) times the standard model value.

This thesis also presents a reinterpretation of the di-Higgs analysis to search for scalar leptoquarks with the ATLAS detector. Both analyses are very similar and the selection is altered slightly to reconstruct $b\tau$ pairs. Third generation scalar leptoquarks being pair produced and decaying to $b\tau b\tau$ are excluded at 95% CL for $m_{\mathrm{LQ}} < 1030$ GeV.

Looking to the future, the di-Higgs analysis aims to use the full Run-2 120 fb^{-1} dataset recorded by ATLAS and plans to release updates to the non-resonant limits in summer 2019. Extrapolating the Run-2 results presented in this thesis to $\sqrt{s} = 14$ TeV and L $= 3000$ fb^{-1} shows a promising stat-only 95% CL limit of $\mu = 0.75$ which corresponds to a significance of 2.71σ. Finally, performing a di-Higgs combination and establishing the strength of the Higgs boson trilinear self-coupling will be one of the primary physics goals for the high luminosity LHC (HL-LHC) and beyond.

List of Figures

List of Tables

Appendix A

Pre-fit and post-fit BDT distributions for di-Higgs control regions

Figure A.1: Distribution of BDT score for the SM signal pre-fit with finite mass reweighting in the 2 tag SS region for the $\tau_{\mathrm{had}}\tau_{\mathrm{had}}$ channel.
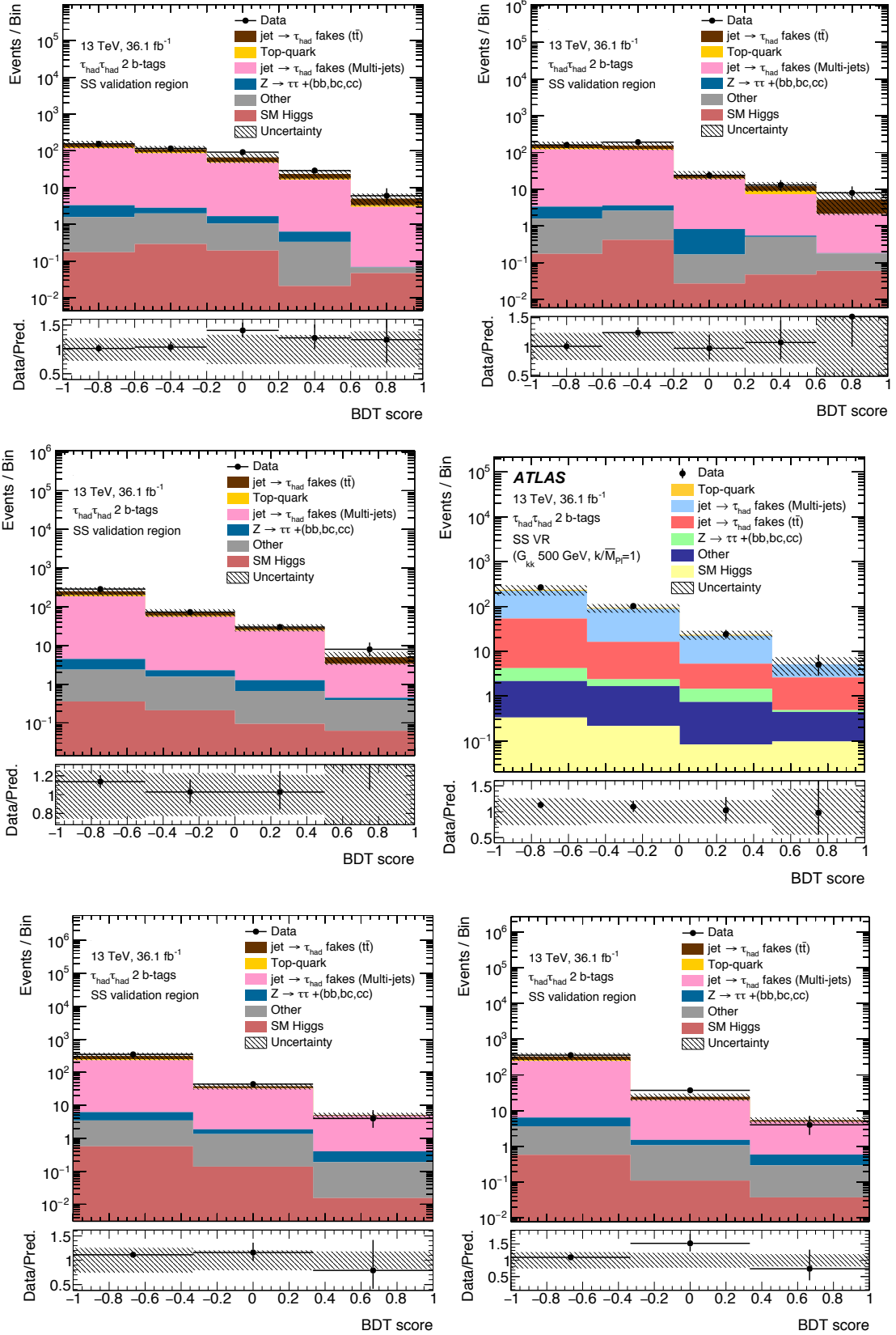
Figure A.2: Distributions of BDT scores for 2HDM (left) and RSG c=1 (right) signals at pre-fit in the 2 tag SS region for resonance masses of 300 GeV (top), 500 GeV (centre) and 1000 GeV (bottom) in the $\tau_{\mathrm{had}}\tau_{\mathrm{had}}$ channel.
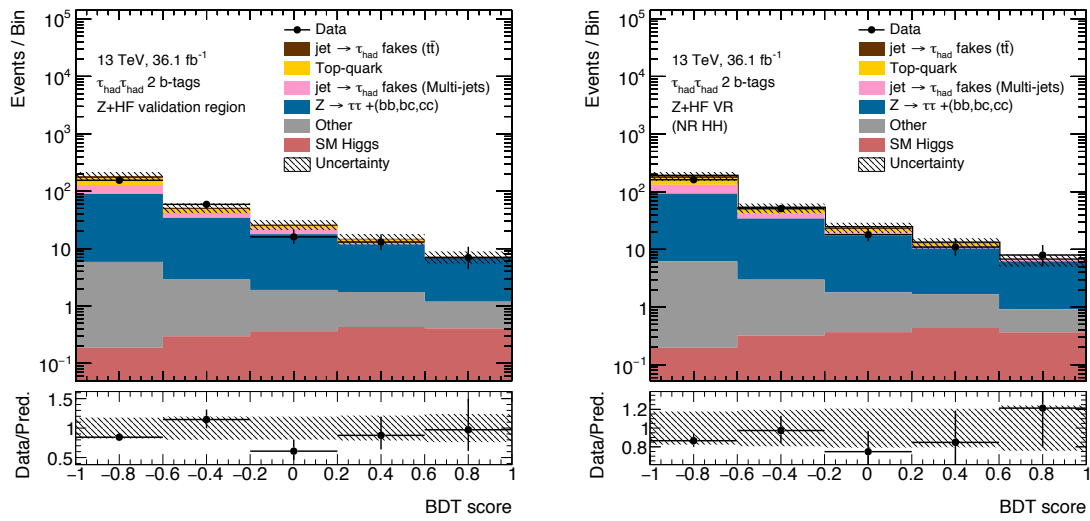
Figure A.3: Distributions of BDT score for the SM signal pre-fit with finite mass reweighting (left) and without (right) in the Z+jets control region for the $\tau_{\mathrm{had}}\tau_{\mathrm{had}}$ channel.
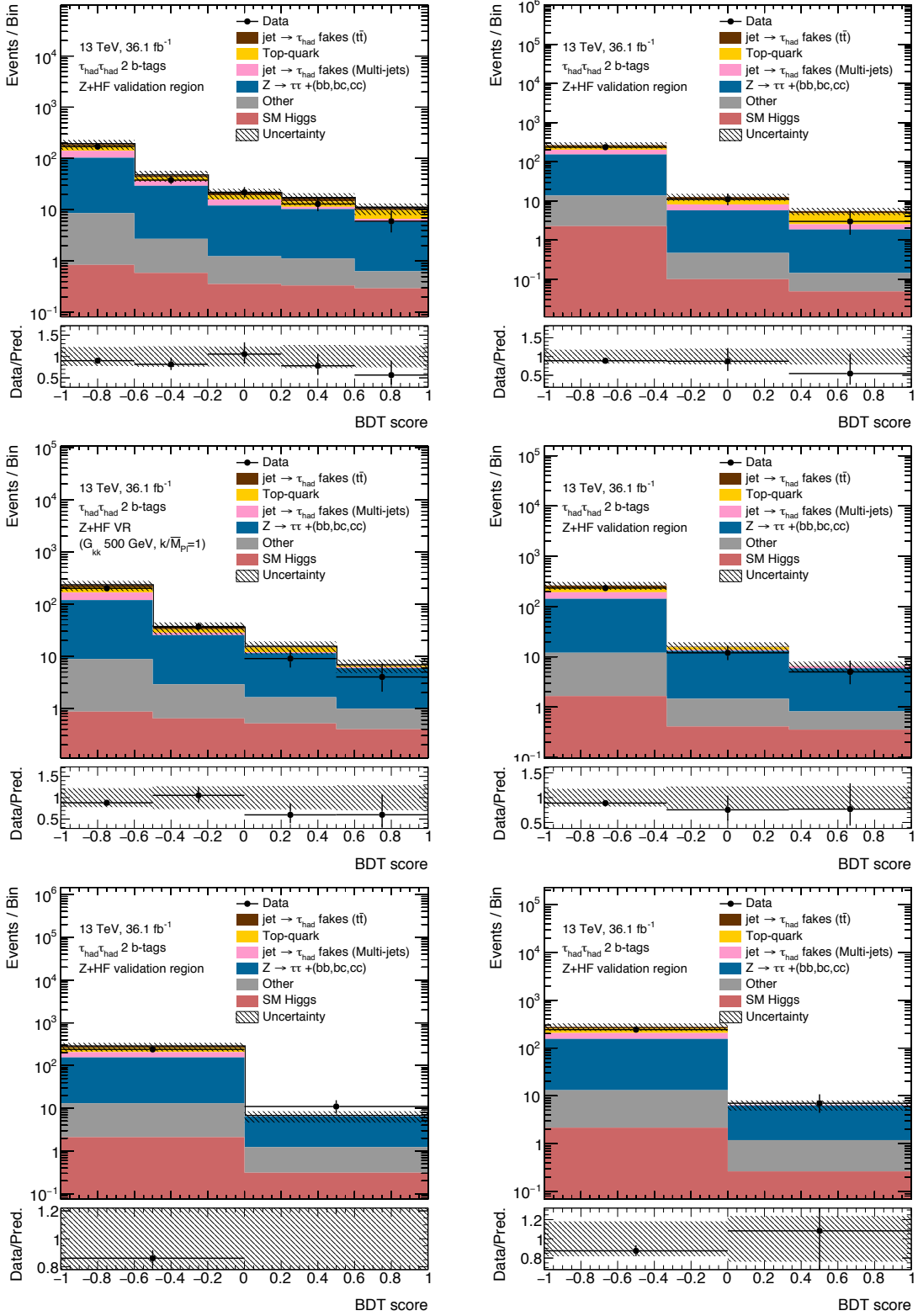
Figure A.4: Distributions of BDT scores for RSG c=1 (left) and 2HDM (right) signals at pre-fit in the Z+jets control region for resonance masses of 300 GeV (top), 500 GeV (centre) and 800 GeV (bottom) in the $\tau_{\text{had}}\tau_{\text{had}}$ channel.
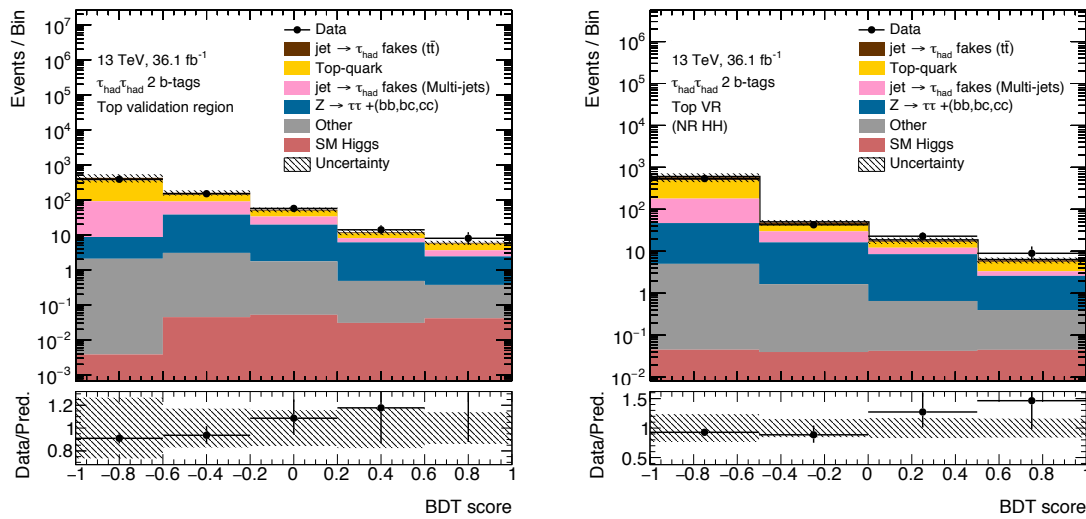
Figure A.5: Distributions of BDT score for the SM signal pre-fit with finite mass reweighting (left) and without (right) in the top control region for the $\tau_{\mathrm{had}}\tau_{\mathrm{had}}$ channel.
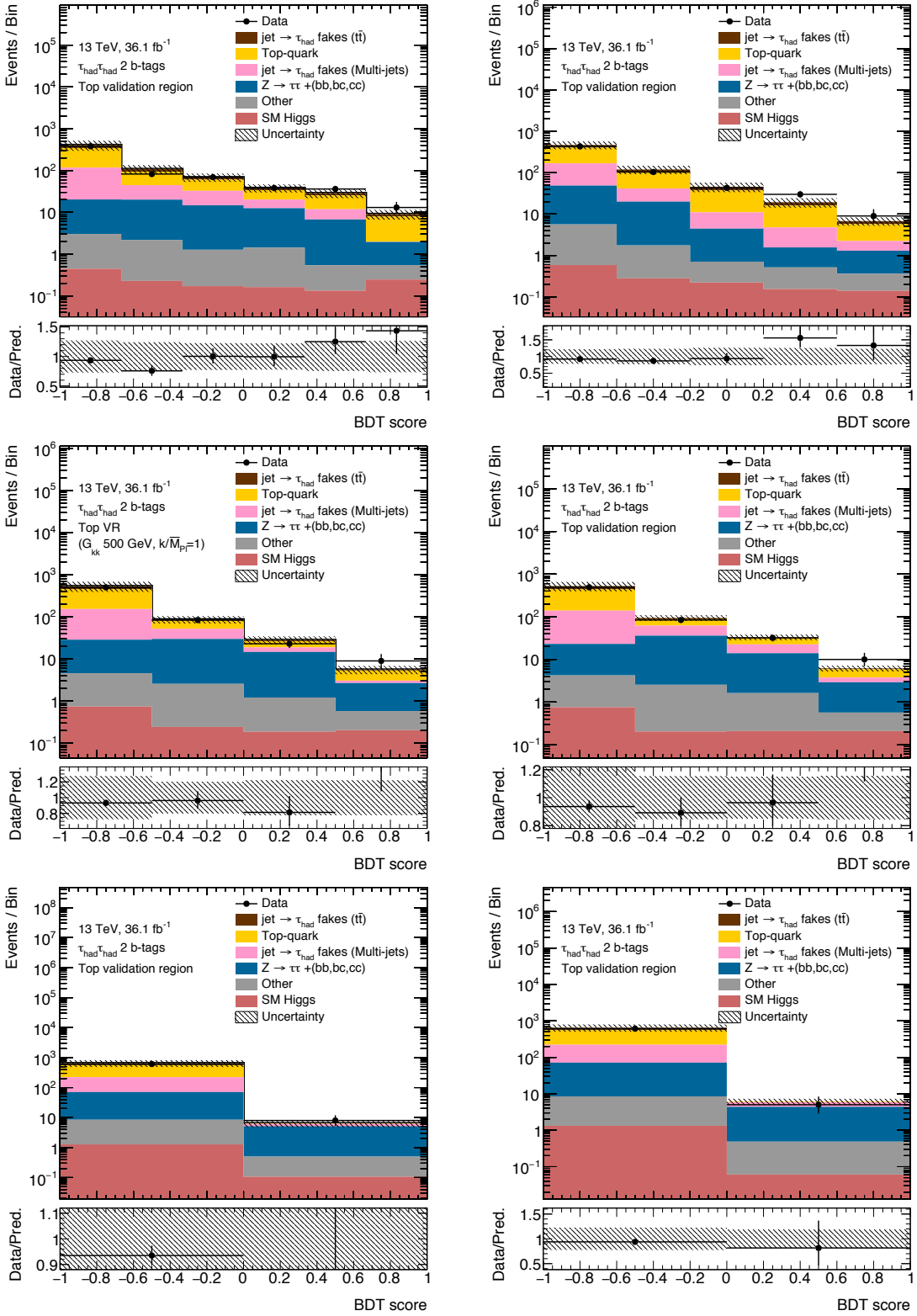
Figure A.6: Distributions of BDT scores for RSG c=1 (left) and 2HDM (right) signals at pre-fit in the top control region for resonance masses of 300 GeV (top), 500 GeV (centre) and 1000 GeV (bottom) in the $\tau_{had}\tau_{had}$ channel.
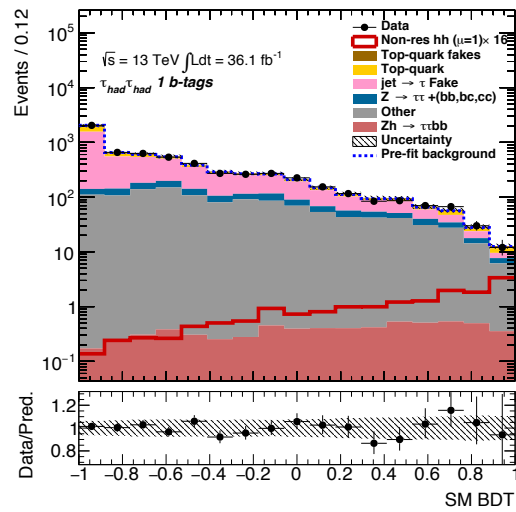
Figure A.7: Distributions of BDT score for the SM signal post-fit in the 1 tag OS region for the $\tau_{\text{had}}\tau_{\text{had}}$ channel.
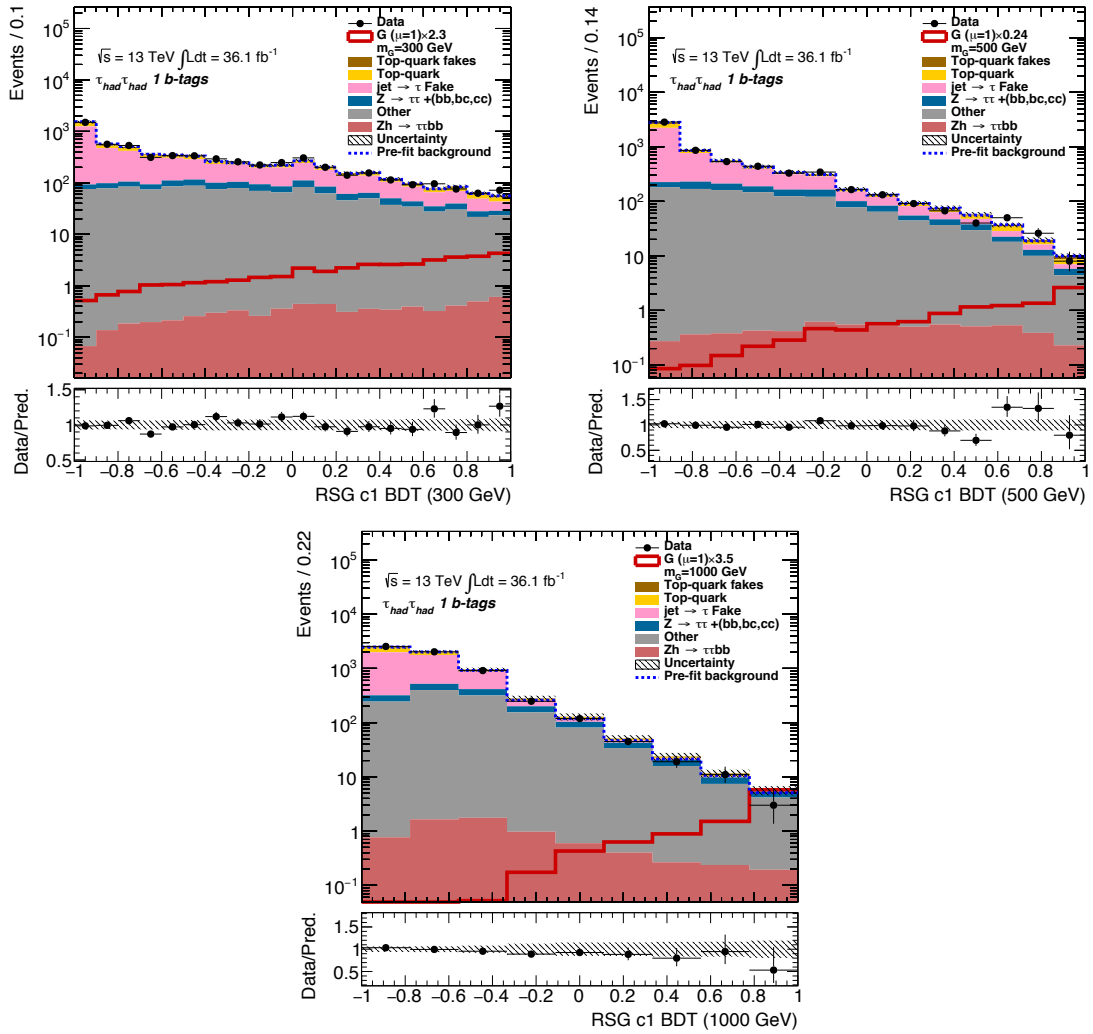
Figure A.8: Distributions of BDT scores post-fit in the 1 tag OS region for the $\tau_{\mathrm{had}}\tau_{\mathrm{had}}$ channel.
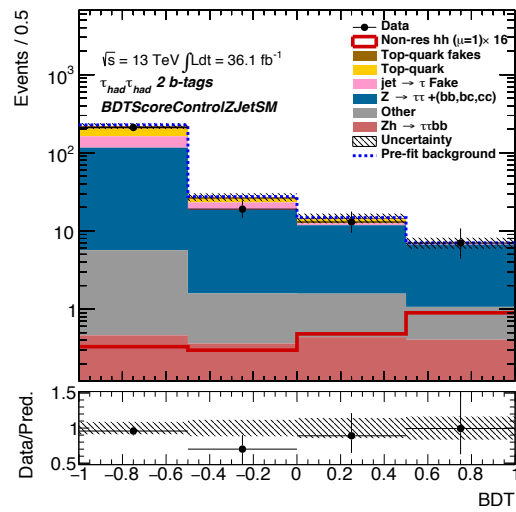
Figure A.9: Distributions of BDT score for the SM signal post-fit in the Z validation region for the $\tau_{\text{had}}\tau_{\text{had}}$ channel.
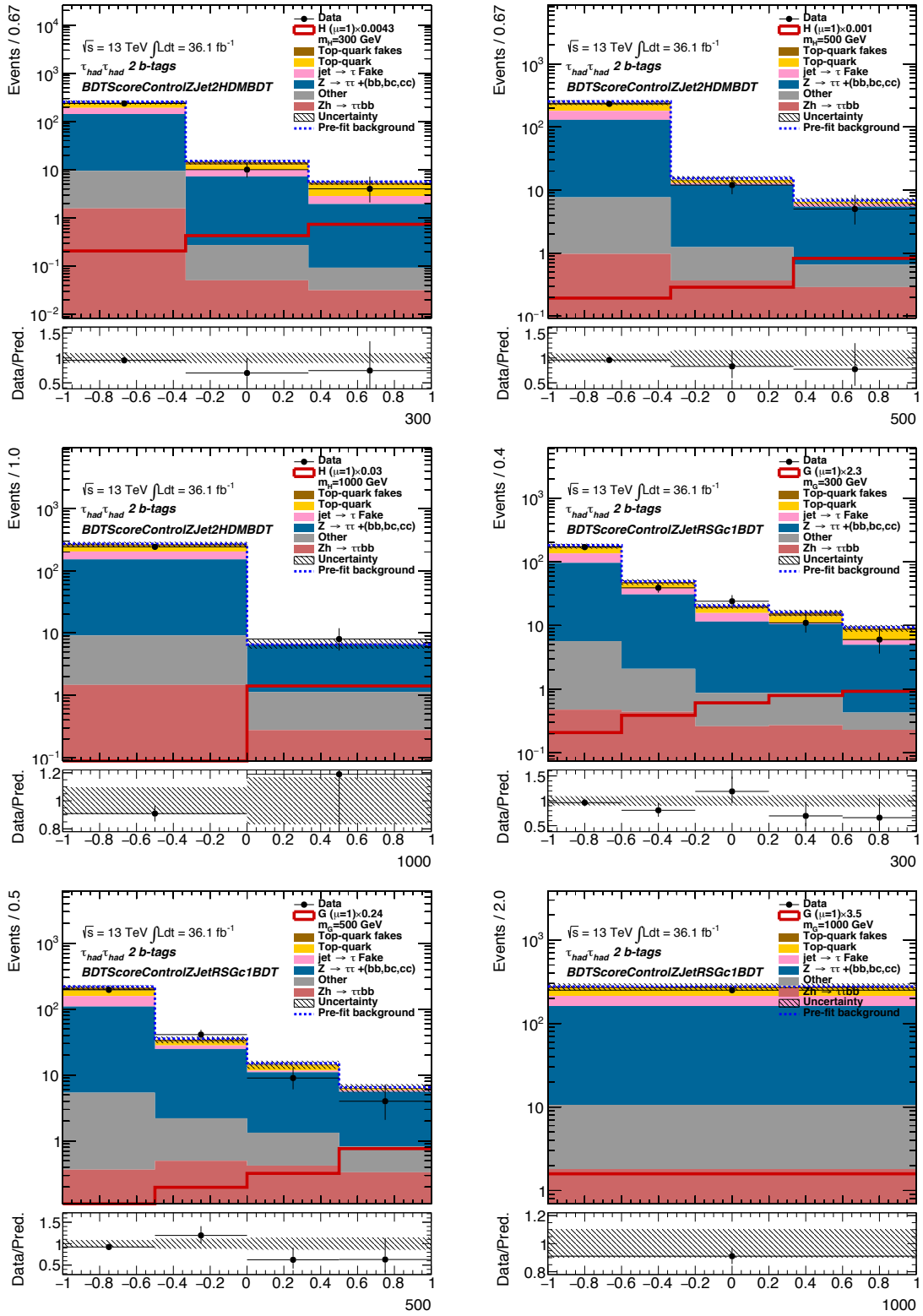
Figure A.10: Distributions of BDT scores post-fit in the Z validation region for the $\tau_{\text{had}}\tau_{\text{had}}$ channel.
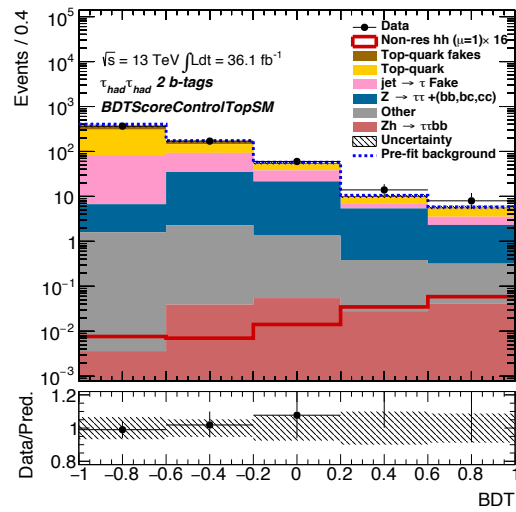
Figure A.11: Distributions of BDT score for the SM signal post-fit in the top validation region for the $\tau_{\mathrm{had}}\tau_{\mathrm{had}}$ channel.
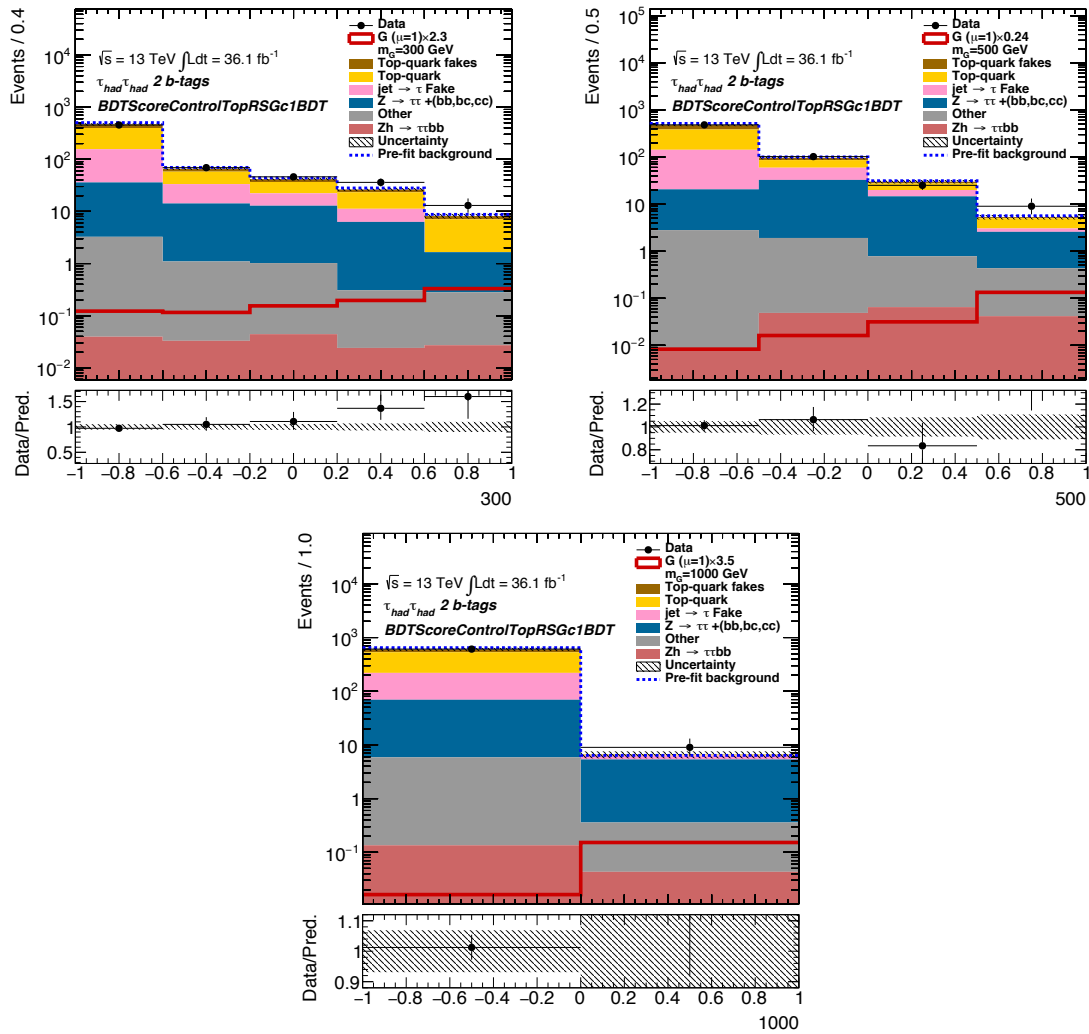
Figure A.12: Distributions of BDT scores post-fit in the top validation region for the $\tau_{\text{had}}\tau_{\text{had}}$ channel.

Appendix B

Additional Efficiency Plots for 8 TeV

(a)   (b)
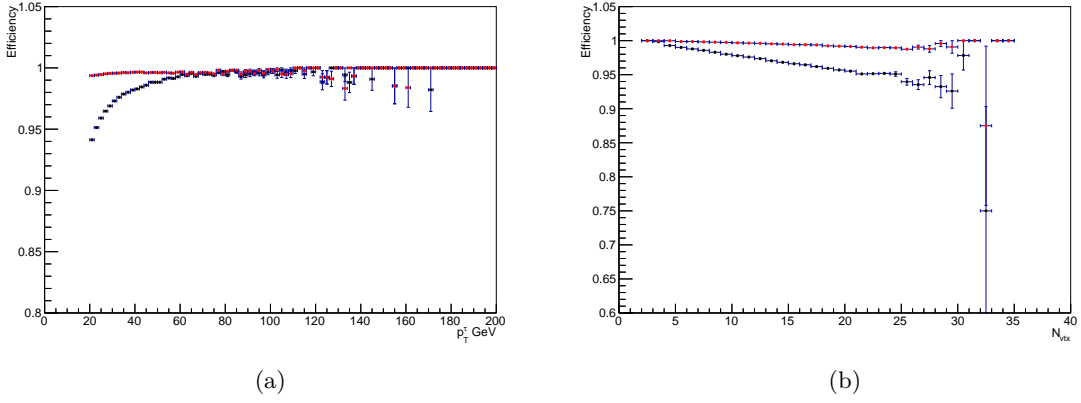
Figure B.1: Efficiency for correct production vertex assignment in 3-prong τ decays for the **TJVA algorithm** and the **default choice of the vertex** with the highest $\sum p_\mathrm{T}^2$, as a function of $\tau_\mathrm{had\text{-}vis}$ p_T (a) and of the number of reconstructed vertices in the event (b).

(a)   (b)
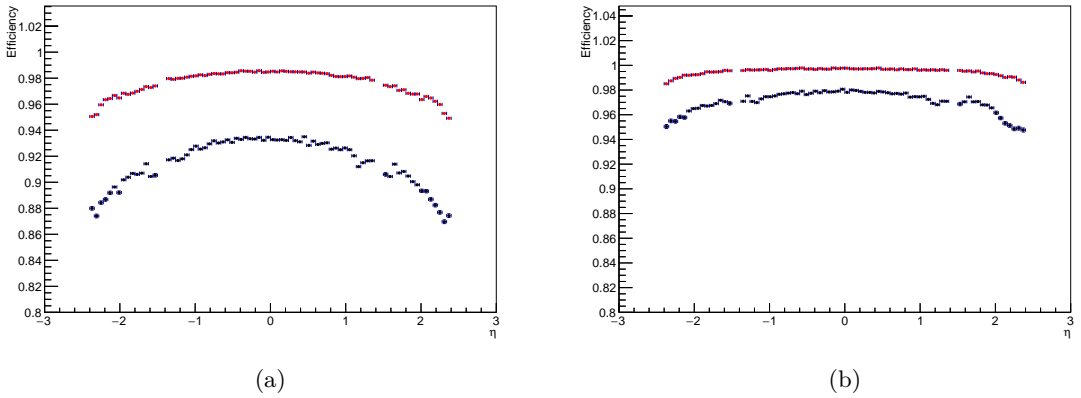
Figure B.2: Efficiency for correct production vertex assignment in τ decays for the **TJVA algorithm** and the **default choice of the vertex** with the highest $\sum p_\mathrm{T}^2$, as a function of $\tau_\mathrm{had\text{-}vis}$ η for 1-prong (a) and 3-prong taus (b).
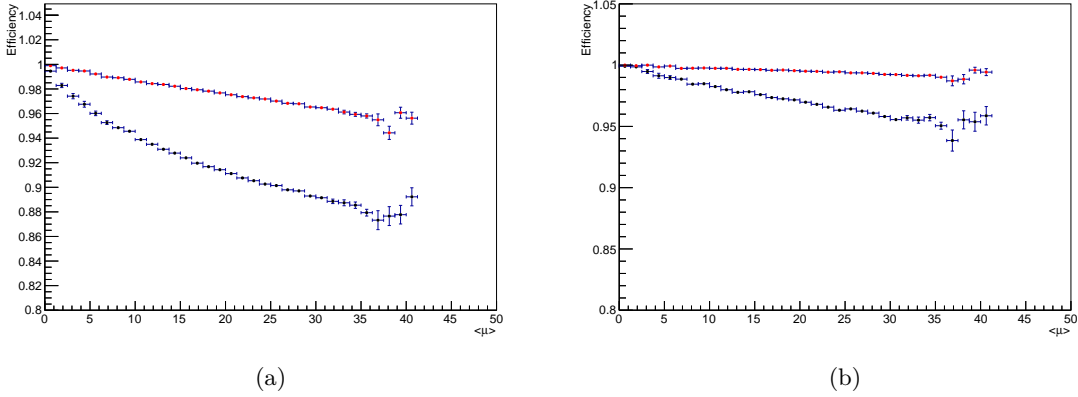
Figure B.3: Efficiency for correct production vertex assignment in τ decays for the **TJVA algorithm** and the **default choice of the vertex** with the highest $\sum p_{\mathrm{T}}^2$, as a function of the average number of interactions per bunch crossing for 1-prong (a) and 3-prong taus (b).

B.1   Table for splitting

	1-prong	3-prong
Total Taus	5281422	2028887
No. TJVA Wrong (ALL)	118898	9087
Total 0-0.5 mm	5149	1313
No. TJVA Wrong 0-0.5 mm	2272	546
No. TJVA chose SecondClosest 0-0.5 mm	2026	520
Total 0.5-3 mm	687351	274337
No. TJVA Wrong 0.5-3 mm	29077	4579
No. TJVA chose SecondClosest 0.5-3 mm	16526	3929
Total 3+ mm	4588922	1753237
No. TJVA Wrong 3+ mm	87549	3962

Table B.1: How often the TJVA algorithm identifies the wrong vertex for different distances in z between the closest and second closest vertices.

B.2   Additional Efficiency Plots for 13 TeV

(a)   (b)
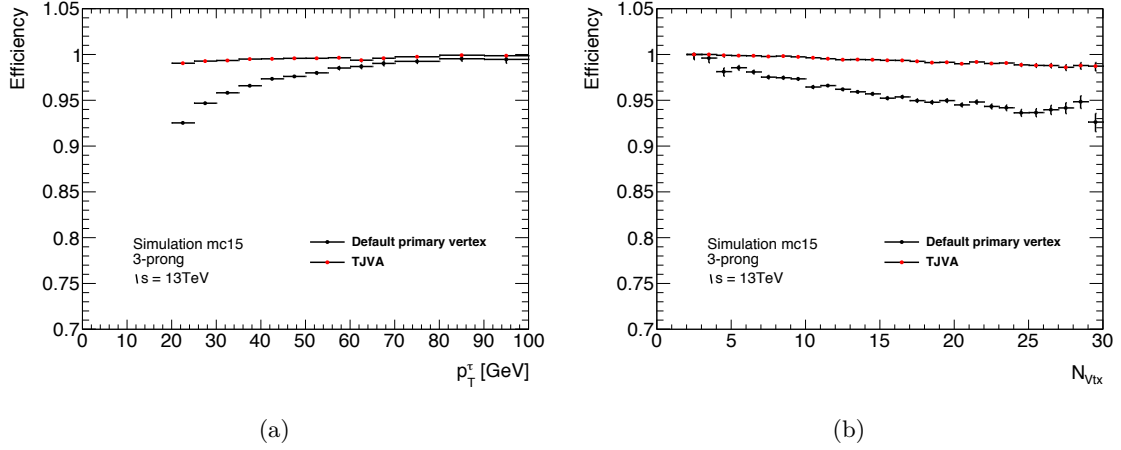
Figure B.4: Efficiency for production vertex assignment without proper tracks selection in 3-prong τ decays for the tau reconstruction algorithm and the default choice of the vertex with the highest $\sum p_T^2$, compared to the correct production vertex assignment. Efficiency as a function of $\tau_{\text{had-vis}}$ p_T (a) and of the number of reconstructed vertices in the event (b).

(a)   (b)
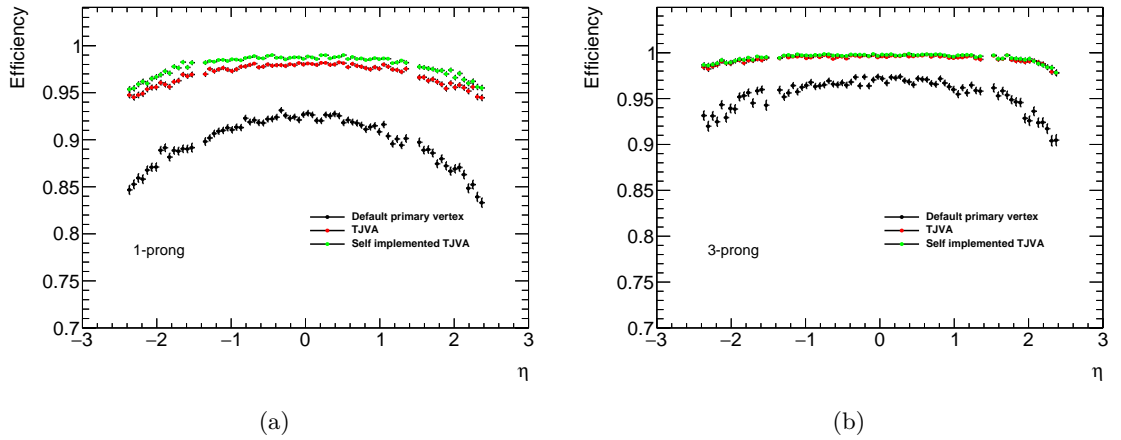
Figure B.5: Efficiency for production vertex assignment without proper tracks selection in τ decays for the tau reconstruction algorithm and the default choice of the vertex with the highest $\sum p_T^2$, compared to the correct production vertex assignment. Efficiency as a function of $\tau_{\text{had-vis}}$ η of for 1-prong (a) and 3-prong taus (b).
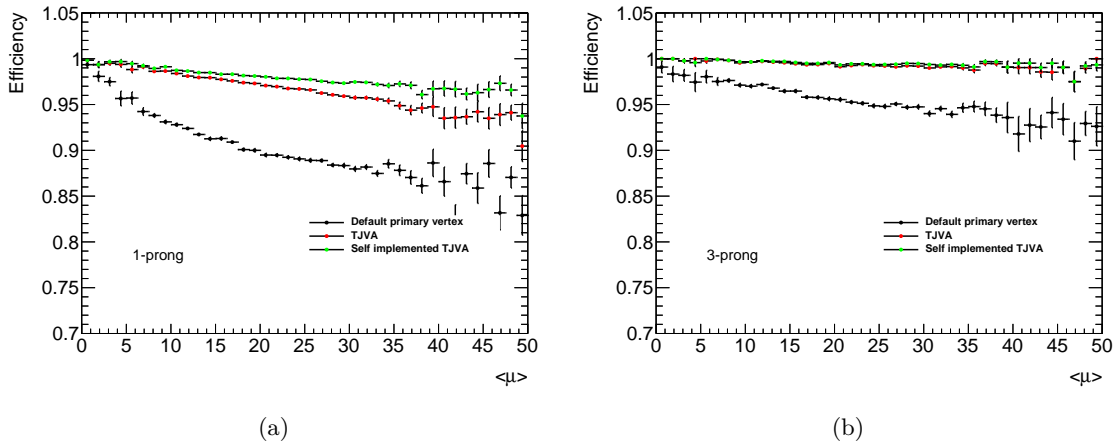
Figure B.6: Efficiency for production vertex assignment without proper tracks selection in τ decays for the tau reconstruction algorithm and the default choice of the vertex with the highest $\sum p_{\mathrm{T}}^2$, compared to the correct production vertex assignment. Efficiency as a function of the average number of interactions per bunch crossing for 1-prong (a) and 3-prong taus (b).

B.3 Data samples

Optimization of reconstruction and identification was performed using DC14 samples. Performance estimation are given applying the so established working points to a pre-production of MC15 with 25 ns bunch spacing configuration. This sample was also used to compute the energy calibration used in the release 20.1 official productions.

Systematics uncertainties have been computed using samples from both DC14 and MC15 productions, depending on the availability of the systematic variations. Most of the variations have been early performed in DC14. The different material composition for the ID was instead only available in MC15. The production with 50 ns bunch spacing in DC14 contained many updates and used a different pile-up setting, with a constant value of $\mu = 30$. It was therefore preferred to use the official MC15 50 ns production. In all cases, the systematics were evaluated comparing the differences between the varied sample and the nominal sample for the corresponding production.

DC14 samples, project `mc14_13TeV`		
Description	Dataset IDs	AMI tags
Nominal	147408	`s1982_s2008_r5787_r5853`
Nominal Drell-Yan	187451–187464	`s1982_s2008_r5787_r5853`
Di-jet background	147910–147917	`s1982_s2008_r5787_r5853`
for e fakes	147406	`s1982_s2008_r5787_r5853`
MC15 samples, project `mc15_13TeV`		
Description	Dataset IDs	AMI tags
Nominal pre-production	361108	`s2576_s2132_r6613_r6264`
Nominal pre-production Drell-Yan	301040–301054	`s2576_s2132_r6613_r6264`
5% additional inner detector material	361108 301040 − 301054	`s2606_s2183_r6785_r6282`
50 ns configuration	361108 301040 − 301054	`s2576_s2132_r6630_r6264`

Table B.2: Simulation samples used for tuning of algorithms and evaluation of systematics uncertainties.

Appendix C

Leptoquark Fake Factors
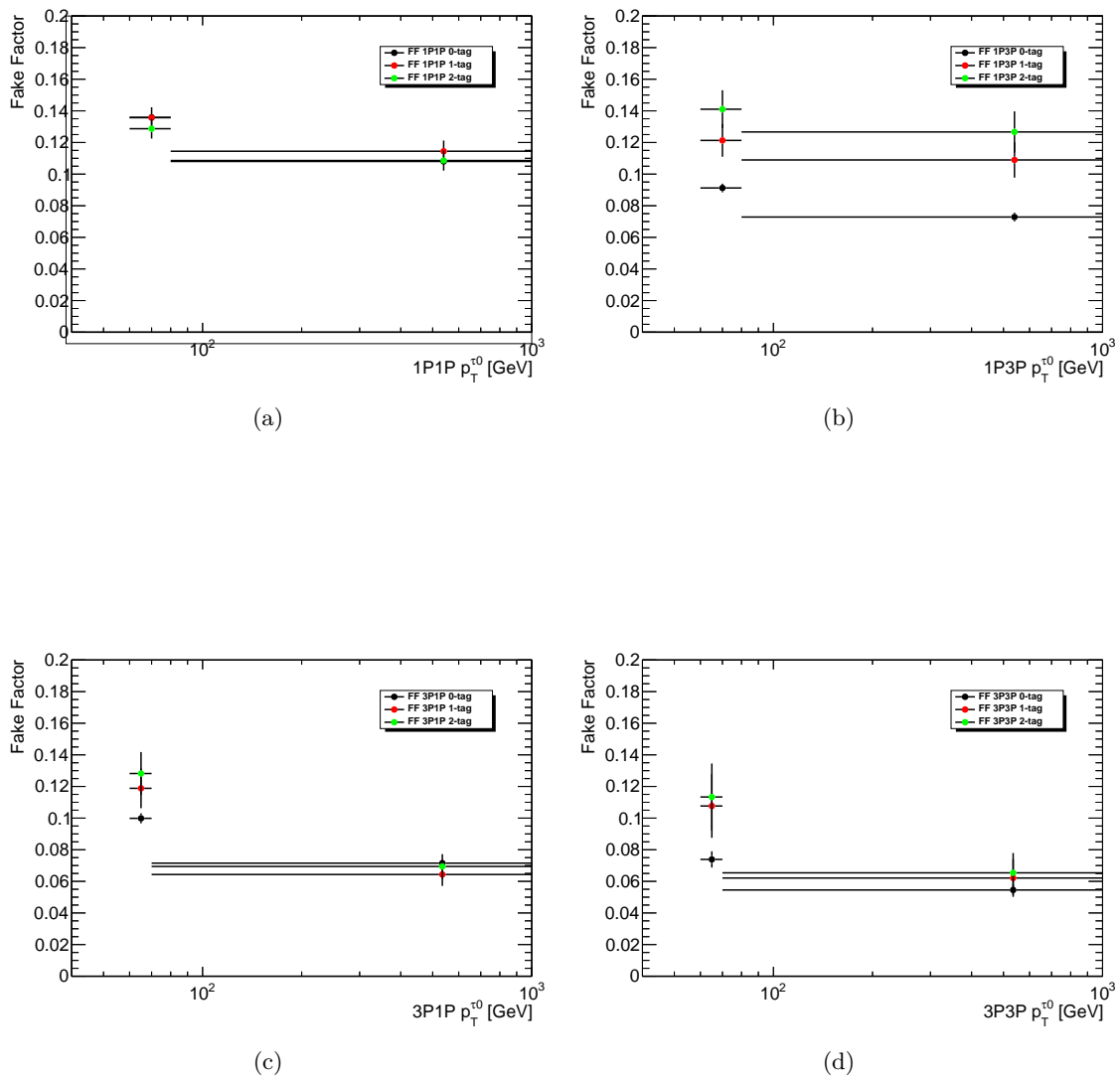
Figure C.1: Fake factor projections onto the leading tau p_T for 1 and 2 b-tag events for τ for 1-prong,1-prong (top left), 1-prong,3-prong (top right), 3,prong,1-prong (bottom left) and 3-prong,3-prong (bottom right) tau pairs in the DTT region, used to determine the multi-jet background in the $\tau_{had}\tau_{had}$ channel.
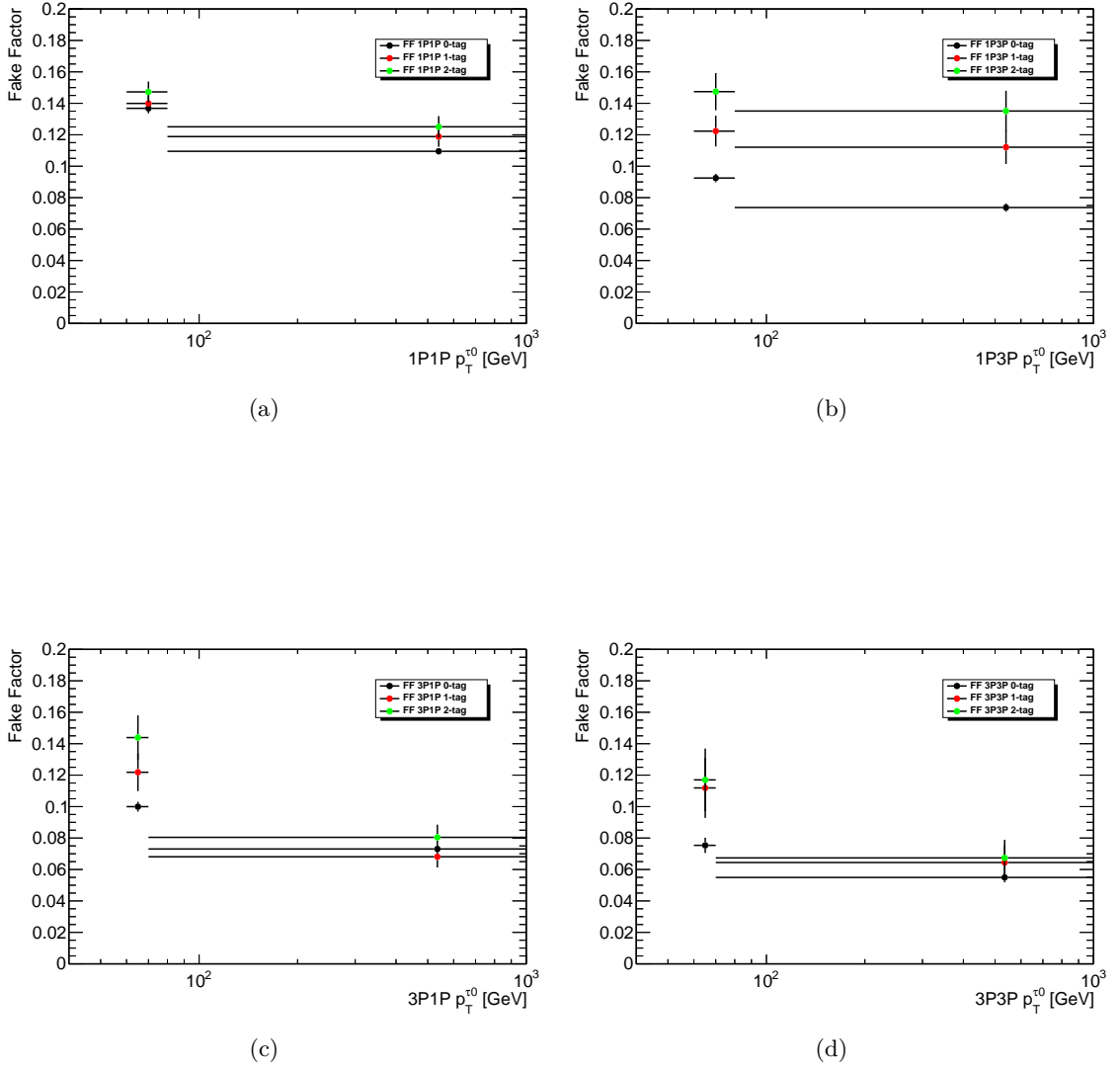
Figure C.2: Monte Carlo subtraction upwards systematic fake factor projections onto the leading tau p_T for 1 and 2 b-tag events for τ for 1-prong,1-prong (top left), 1-prong,3-prong (top right), 3,prong,1-prong (bottom left) and 3-prong,3-prong (bottom right) tau pairs in the DTT region, used to determine the multi-jet background in the $\tau_{\text{had}}\tau_{\text{had}}$ channel.
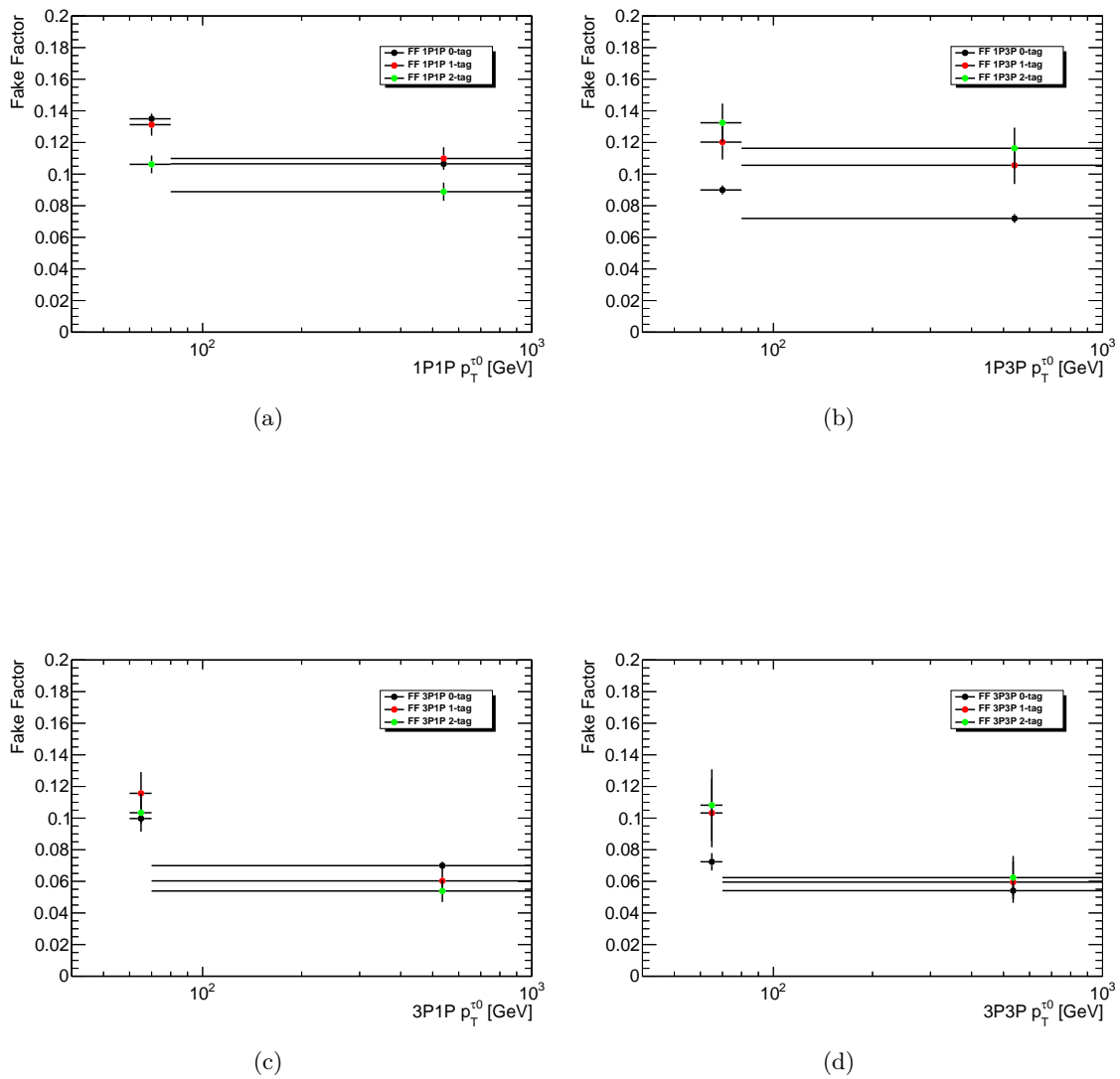
Figure C.3: Monte Carlo subtraction downwards systematic fake factor projections onto the leading tau p_{T} for 1 and 2 b-tag events for τ for 1-prong,1-prong (top left), 1-prong,3-prong (top right), 3,prong,1-prong (bottom left) and 3-prong,3-prong (bottom right) tau pairs in the DTT region, used to determine the multi-jet background in the $\tau_{\mathrm{had}}\tau_{\mathrm{had}}$ channel.

(a)

(b)

(c)
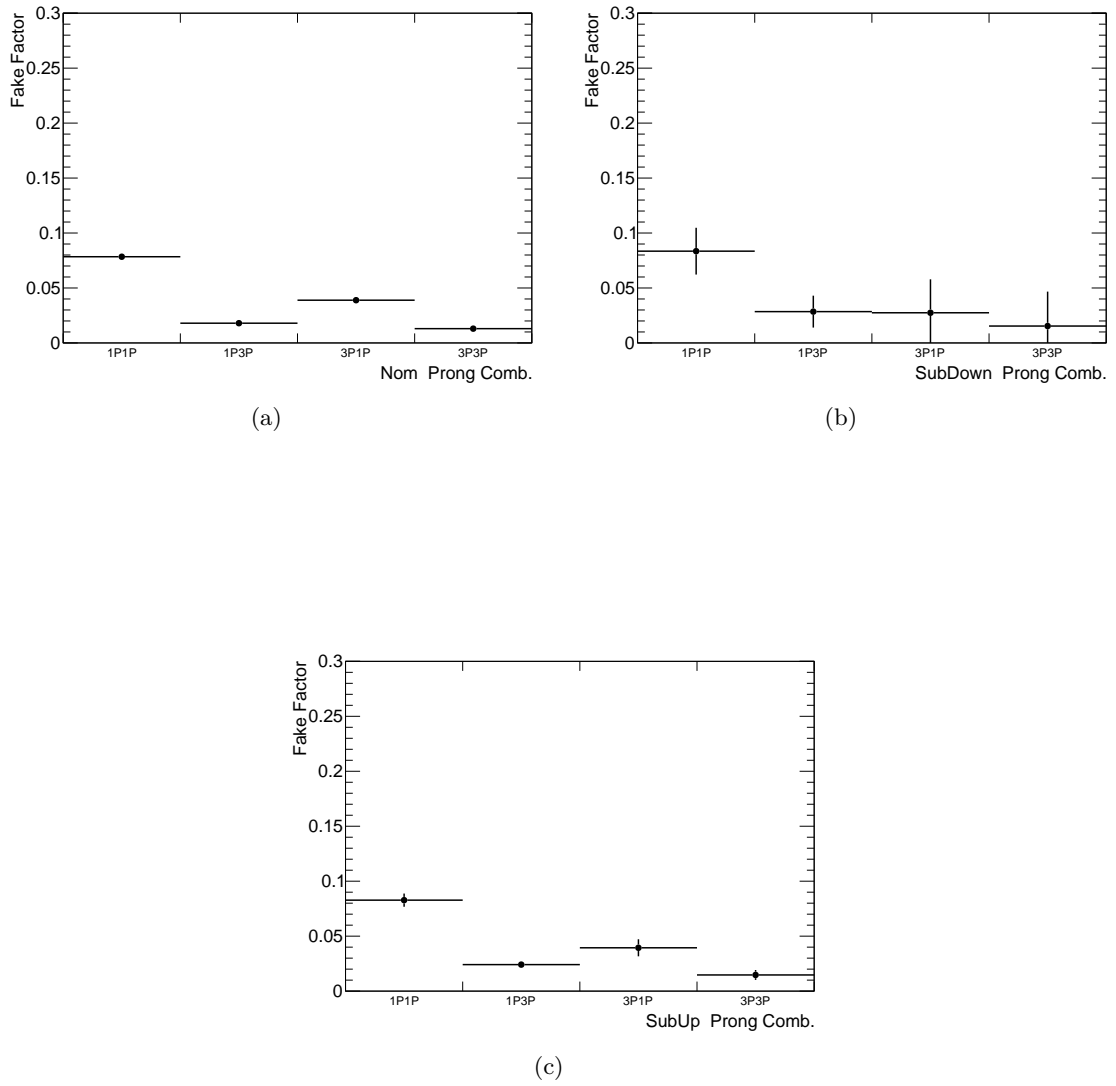
Figure C.4: Single tau trigger fake factors for each prong combination for nominal (top left), MC subtraction upwards variation (top right) and MC subtraction downwards variation (bottom left) used to determine the multi-jet background in the $\tau_{\text{had}}\tau_{\text{had}}$ channel.

(a)

(b)

(c)
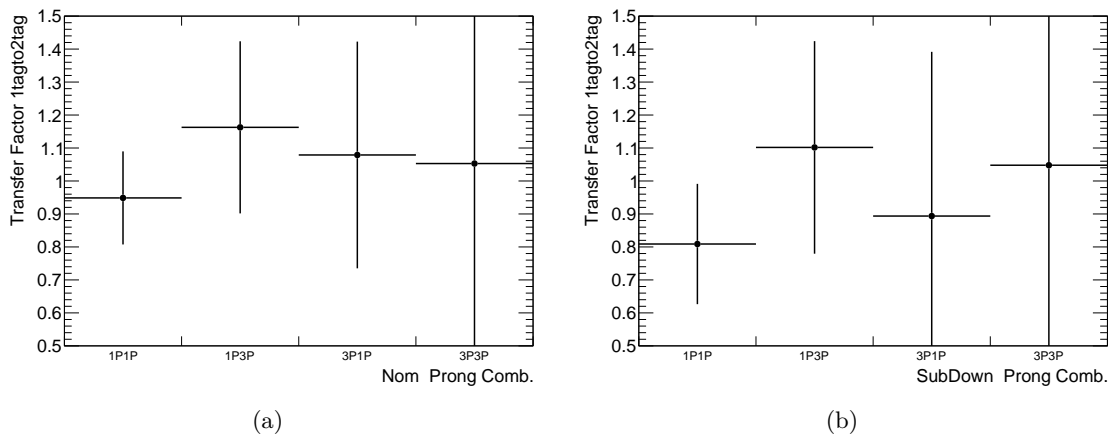
Figure C.5: Transfer factors for each prong combination with nominal (top left), MC subtraction upwards variation (top right) and MC subtraction downwards variation (bottom left) used to extrapolate from 1-tag to 2-tag regions for the multi-jet background in the $\tau_{\mathrm{had}}\tau_{\mathrm{had}}$ channel.

References

[1] "Observation of a new particle in the search for the Standard Model Higgs boson with the ATLAS detector at the LHC". In: *Physics Letters B* 716.1 (2012), pp. 1–29.

[2] "Observation of a new boson at a mass of 125 GeV with the CMS experiment at the LHC". In: *Physics Letters B* 716.1 (2012), pp. 30–61.

[3] G. Aad et al. "The ATLAS Experiment at the CERN Large Hadron Collider". In: *JINST* 3 (2008), S08003.

[4] The CMS Collaboration. "The CMS experiment at the CERN LHC". In: *Journal of Instrumentation* 3.08 (2008), S08004.

[5] Tony Gherghetta and Alex Pomarol. "Bulk fields and supersymmetry in a slice of AdS". In: *Nucl. Phys.* B586 (2000), pp. 141–162. arXiv: `hep-ph/0003129 [hep-ph]`.

[6] Abdesslam Arhrib et al. "Double Neutral Higgs production in the Two-Higgs doublet model at the LHC". In: *JHEP* 08 (2009), p. 035. arXiv: `0906.0387 [hep-ph]`.

[7] Georges Aad et al. "Searches for Higgs boson pair production in the $hh \to bb\tau\tau, \gamma\gamma WW^*, \gamma\gamma bb, bbbb$ channels with the ATLAS detector". In: *Phys. Rev.* D92 (2015), p. 092004. arXiv: `1509.04670 [hep-ex]`.

[8] Georges Aad et al. "Search for Higgs boson pair production in the $b\bar{b}b\bar{b}$ final state from pp collisions at $\sqrt{s} = 8$ TeVwith the ATLAS detector". In: *Eur. Phys. J.* C75.9 (2015), p. 412. arXiv: `1506.00285 [hep-ex]`.

[9] Georges Aad et al. "Search For Higgs Boson Pair Production in the $\gamma\gamma b\bar{b}$ Final State using pp Collision Data at $\sqrt{s} = 8$ TeV from the ATLAS Detector". In: *Phys. Rev. Lett.* 114.8 (2015), p. 081802. arXiv: `1406.5053 [hep-ex]`.

[10] *Search for pair production of Higgs bosons in the two tau leptons and two bottom quarks final state using proton-proton collisions at $\sqrt{s} = 13$ TeV*. Tech. rep. CMS-PAS-HIG-17-002. Geneva: CERN, 2017.

[11]   Savas Dimopoulos and Leonard Susskind. "Mass without scalars". In: *Nuclear Physics B* 155.1 (1979), pp. 237–252.

[12]   Savas Dimopoulos. "Technicoloured signatures". In: *Nuclear Physics B* 168.1 (1980), pp. 69–92.

[13]   Estia Eichten and Kenneth Lane. "Dynamical breaking of weak interaction symmetries". In: *Physics Letters B* 90.1 (1980), pp. 125–130.

[14]   V.D. Angelopoulos et al. "Search for new quarks suggested by the superstring". In: *Nuclear Physics B* 292 (1987), pp. 59–92.

[15]   W. Buchmüller and D. Wyler. "Constraints on SU(5)-type leptoquarks". In: *Physics Letters B* 177.3 (1986), pp. 377–382.

[16]   Howard Georgi and S. L. Glashow. "Unity of All Elementary-Particle Forces". In: *Phys. Rev. Lett.* 32 (8 1974), pp. 438–441.

[17]   Jogesh C. Pati and Abdus Salam. "Lepton Number as the Fourth Color". In: *Phys. Rev.* D10 (1974). [Erratum: Phys. Rev.D11,703(1975)], pp. 275–289.

[18]   Georges Aad et al. "Search for third generation scalar leptoquarks in pp collisions at $\sqrt{s} = 7$ TeV with the ATLAS detector". In: *JHEP* 06 (2013), p. 033. arXiv: `1303.0526 [hep-ex]`.

[19]   Vardan Khachatryan et al. "Search for pair production of third-generation scalar leptoquarks and top squarks in proton–proton collisions at $\sqrt{s}$=8 TeV". In: *Phys. Lett.* B739 (2014), pp. 229–249. arXiv: `1408.0806 [hep-ex]`.

[20]   Morad Aaboud et al. "A search for resonant and non-resonant Higgs boson pair production in the $b\bar{b}\tau^{+}\tau^{-}$ decay channel in *pp* collisions at $\sqrt{s} = 13$ TeV with the ATLAS detector". In: (2018). arXiv: `1808.00336 [hep-ex]`.

[21]   *Reconstruction, Energy Calibration, and Identification of Hadronically Decaying Tau Leptons in the ATLAS Experiment for Run-2 of the LHC*. Tech. rep. ATL-PHYS-PUB-2015-045. Geneva: CERN, 2015.

[22]   Agni Bethani et al. *Search for Pair Production of Scalar Leptoquarks decaying to tau leptons and b-jets with the ATLAS Detector*. Tech. rep. ATL-COM-PHYS-2017-1815. Geneva: CERN, 2017.

[23]   Sheldon L. Glashow. "Partial-symmetries of weak interactions". In: *Nuclear Physics* 22.4 (1961), pp. 579–588.

[24] Steven Weinberg. "A Model of Leptons". In: *Phys. Rev. Lett.* 19 (21 1967), pp. 1264–1266.

[25] S. L. Glashow, J. Iliopoulos and L. Maiani. "Weak Interactions with Lepton-Hadron Symmetry". In: *Phys. Rev. D* 2 (7 1970), pp. 1285–1292.

[26] "Search for elastic muon-neutrino electron scattering". In: *Physics Letters B* 46.1 (1973), pp. 121–124.

[27] "Observation of neutrino-like interactions without muon or electron in the gargamelle neutrino experiment". In: *Physics Letters B* 46.1 (1973), pp. 138–140.

[28] "Observation of neutrino-like interactions without muon or electron in the Gargamelle neutrino experiment". In: *Nuclear Physics B* 73.1 (1974), pp. 1–22.

[29] David J. Gross and Frank Wilczek. "Ultraviolet Behavior of Non-Abelian Gauge Theories". In: *Phys. Rev. Lett.* 30 (26 1973), pp. 1343–1346.

[30] J. J. Aubert et al. "Experimental Observation of a Heavy Particle J". In: *Phys. Rev. Lett.* 33 (23 1974), pp. 1404–1406.

[31] J. -E. Augustin et al. "Discovery of a Narrow Resonance in e^+e^- Annihilation". In: *Phys. Rev. Lett.* 33 (23 1974), pp. 1406–1408.

[32] C. Patrignani et al. "Review of Particle Physics". In: *Chin. Phys.* C40.10 (2016), p. 100001.

[33] G. S. Guralnik, C. R. Hagen and T. W. B. Kibble. "Global Conservation Laws and Massless Particles". In: *Phys. Rev. Lett.* 13 (20 1964), pp. 585–587.

[34] F. Englert and R. Brout. "Broken Symmetry and the Mass of Gauge Vector Mesons". In: *Phys. Rev. Lett.* 13 (9 1964), pp. 321–323.

[35] Peter W. Higgs. "Spontaneous Symmetry Breakdown without Massless Bosons". In: *Phys. Rev.* 145 (4 1966), pp. 1156–1163.

[36] P.W. Higgs. "Broken symmetries, massless particles and gauge fields". In: *Physics Letters* 12.2 (1964), pp. 132–133.

[37] Abdus Salam and J. C. Ward. "Weak and electromagnetic interactions". In: *Il Nuovo Cimento (1955-1965)* 11.4 (1959), pp. 568–577.

[38] Georges Aad et al. "Observation of a new particle in the search for the Standard Model Higgs boson with the ATLAS detector at the LHC". In: *Phys. Lett.* B716 (2012), pp. 1–29. arXiv: 1207.7214 [hep-ex].

[39] Serguei Chatrchyan et al. "Observation of a new boson at a mass of 125 GeV with the CMS experiment at the LHC". In: *Phys. Lett.* B716 (2012), pp. 30–61. arXiv: `1207.7235 [hep-ex]`.

[40] J R Andersen et al. "Handbook of LHC Higgs Cross Sections: 3. Higgs Properties". In: (2013). Ed. by S Heinemeyer et al. arXiv: `1307.1347 [hep-ph]`.

[41] M. Spira et al. "Higgs boson production at the LHC". In: *Nucl. Phys.* B453 (1995), pp. 17–82. arXiv: `hep-ph/9504378 [hep-ph]`.

[42] D. Graudenz, M. Spira and P. M. Zerwas. "QCD corrections to Higgs-boson production at proton-proton colliders". In: *Phys. Rev. Lett.* 70 (10 1993), pp. 1372–1375.

[43] Eric Laenen and Lorenzo Magnea. "Threshold resummation for electroweak annihilation from DIS data". In: *Phys. Lett.* B632 (2006), pp. 270–276. arXiv: `hep-ph/0508284 [hep-ph]`.

[44] Stefano Catani et al. "Soft gluon resummation for Higgs boson production at hadron colliders". In: *JHEP* 07 (2003), p. 028. arXiv: `hep-ph/0306211 [hep-ph]`.

[45] Charalampos Anastasiou et al. "High precision determination of the gluon fusion Higgs boson cross-section at the LHC". In: *JHEP* 05 (2016), p. 058. arXiv: `1602.00695 [hep-ph]`.

[46] Robert V. Harlander and William B. Kilgore. "Next-to-Next-to-Leading Order Higgs Production at Hadron Colliders". In: *Phys. Rev. Lett.* 88 (20 2002), p. 201801.

[47] Charalampos Anastasiou and Kirill Melnikov. "Higgs boson production at hadron colliders in NNLO QCD". In: *Nucl. Phys.* B646 (2002), pp. 220–256. arXiv: `hep-ph/0207004 [hep-ph]`.

[48] V. Ravindran, J. Smith and W. L. van Neerven. "NNLO corrections to the total cross-section for Higgs boson production in hadron hadron collisions". In: *Nucl. Phys.* B665 (2003), pp. 325–366. arXiv: `hep-ph/0302135 [hep-ph]`.

[49] S. Dawson and R. Kauffman. "QCD corrections to Higgs boson production: nonleading terms in the heavy quark limit". In: *Phys. Rev.* D49 (1994), pp. 2298–2309. arXiv: `hep-ph/9310281 [hep-ph]`.

[50] A. Djouadi, M. Spira and P. M. Zerwas. "Production of Higgs bosons in proton colliders: QCD corrections". In: *Phys. Lett.* B264 (1991), pp. 440–446.

[51] Charalampos Anastasiou, Radja Boughezal and Frank Petriello. "Mixed QCD-electroweak corrections to Higgs boson production in gluon fusion". In: *Journal of High Energy Physics* 2009.04 (2009), p. 003.

[52] Valentin Ahrens et al. "Updated Predictions for Higgs Production at the Tevatron and the LHC". In: *Phys. Lett.* B698 (2011), pp. 271–274. arXiv: 1008.3162 [hep-ph].

[53] M. Ciccolini, A. Denner and S. Dittmaier. "Strong and Electroweak Corrections to the Production of a Higgs Boson +2 Jets via Weak Interactions at the Large Hadron Collider". In: *Phys. Rev. Lett.* 99 (16 2007), p. 161803.

[54] M. Ciccolini, Denner A. and Dittmaier S. "Electroweak and QCD corrections to Higgs production via vector-boson fusion at the CERN LHC". In: *Phys. Rev. D* 77 (1 2008), p. 013002.

[55] Paolo Bolzoni et al. "Higgs Boson Production via Vector-Boson Fusion at Next-to-Next-to-Leading Order in QCD". In: *Phys. Rev. Lett.* 105 (1 2010), p. 011801.

[56] Oliver Brein, Robert V. Harlander and Tom J.E. Zirke. "Vh@NNLO: Higgs Strahlung at hadron colliders". In: *Computer Physics Communications* 184.3 (2013), pp. 998–1003.

[57] W. Beenakker et al. "Higgs Radiation Off Top Quarks at the Tevatron and the LHC". In: *Phys. Rev. Lett.* 87 (20 2001), p. 201805.

[58] W. Beenakker et al. "NLO QCD corrections to $t\bar{t}$H production in hadron collisions". In: *Nucl. Phys.* B653 (2003), pp. 151–203. arXiv: hep-ph/0211352 [hep-ph].

[59] L. Reina and S. Dawson. "Next-to-Leading Order Results for $t\bar{t}h$ Production at the Tevatron". In: *Phys. Rev. Lett.* 87 (20 2001), p. 201804.

[60] S. Dawson et al. "Next-to-leading order QCD corrections to $pp \to t\bar{t}h$ at the CERN Large Hadron Collider". In: *Phys. Rev. D* 67 (7 2003), p. 071503.

[61] D. de Florian et al. "Handbook of LHC Higgs Cross Sections: 4. Deciphering the Nature of the Higgs Sector". In: (2016). arXiv: 1610.07922 [hep-ph].

[62] G. Apollinari et al. "High-Luminosity Large Hadron Collider (HL-LHC)". In: *CERN Yellow Rep. Monogr.* 4 (2017), pp. 1–516.

[63] Massimiliano Grazzini et al. "Higgs boson pair production at NNLO with top quark mass effects". In: *JHEP* 05 (2018), p. 059. arXiv: 1803.02463 [hep-ph].

[64] S. Borowka et al. "Higgs Boson Pair Production in Gluon Fusion at Next-to-Leading Order with Full Top-Quark Mass Dependence". In: *Phys. Rev. Lett.* 117 (1 2016), p. 012001.

[65] S. Borowka et al. "Higgs Boson Pair Production in Gluon Fusion at Next-to-Leading Order with Full Top-Quark Mass Dependence". In: *Phys. Rev. Lett.* 117.1 (2016). [Erratum: Phys. Rev. Lett.117,no.7,079901(2016)], p. 012001. arXiv: `1604.06447` `[hep-ph]`.

[66] Abdesslam Arhrib et al. "Search for a light fermiophobic Higgs boson produced via gluon fusion at Hadron Colliders". In: *Phys. Rev.* D78 (2008), p. 075002. arXiv: `0805.1603` `[hep-ph]`.

[67] Eri Asakawa et al. "Higgs boson pair production in new physics models at hadron, lepton, and photon colliders". In: *Phys. Rev.* D82 (2010), p. 115002. arXiv: `1009.4670` `[hep-ph]`.

[68] G. C. Branco et al. "Theory and phenomenology of two-Higgs-doublet models". In: *Phys. Rept.* 516 (2012), pp. 1–102. arXiv: `1106.0034` `[hep-ph]`.

[69] Kaustubh Agashe et al. "Warped Gravitons at the LHC and Beyond". In: *Phys. Rev.* D76 (2007), p. 036006. arXiv: `hep-ph/0701186` `[hep-ph]`.

[70] A. Liam Fitzpatrick et al. "Searching for the Kaluza-Klein Graviton in Bulk RS Models". In: *JHEP* 09 (2007), p. 013. arXiv: `hep-ph/0701150` `[hep-ph]`.

[71] Roberto Contino et al. "Anomalous Couplings in Double Higgs Production". In: *JHEP* 08 (2012), p. 154. arXiv: `1205.5444` `[hep-ph]`.

[72] S. Dawson, A. Ismail and Ian Low. "What's in the loop? The anatomy of double Higgs production". In: *Phys. Rev.* D91.11 (2015), p. 115008. arXiv: `1504.05596` `[hep-ph]`.

[73] R. Grober and M. Muhlleitner. "Composite Higgs Boson Pair Production at the LHC". In: *JHEP* 06 (2011), p. 020. arXiv: `1012.1562` `[hep-ph]`.

[74] Claudio O. Dib, Rogerio Rosenfeld and Alfonso Zerwekh. "Double Higgs production and quadratic divergence cancellation in little Higgs models with T parity". In: *JHEP* 05 (2006), p. 074. arXiv: `hep-ph/0509179` `[hep-ph]`.

[75] T. Plehn, M. Spira and P. M. Zerwas. "Pair production of neutral Higgs particles in gluon-gluon collisions". In: *Nucl. Phys.* B479 (1996). [Erratum: Nucl. Phys.B531,655(1998)], pp. 46–64. arXiv: `hep-ph/9603205` `[hep-ph]`.

[76] A. Djouadi et al. "Production of neutral Higgs boson pairs at LHC". In: *Eur. Phys. J.* C10 (1999), pp. 45–49. arXiv: `hep-ph/9904287 [hep-ph]`.

[77] Junjie Cao et al. "Pair Production of a 125 GeV Higgs Boson in MSSM and NMSSM at the LHC". In: *JHEP* 04 (2013), p. 134. arXiv: `1301.6437 [hep-ph]`.

[78] Dao Thi Nhung et al. "Higher Order Corrections to the Trilinear Higgs Self-Couplings in the Real NMSSM". In: *JHEP* 11 (2013), p. 181. arXiv: `1306.3926 [hep-ph]`.

[79] Ulrich Ellwanger. "Higgs pair production in the NMSSM at the LHC". In: *JHEP* 08 (2013), p. 077. arXiv: `1306.5541 [hep-ph]`.

[80] Lei Wang et al. "Higgs-pair production in littlest Higgs model with T-parity". In: *Phys. Rev.* D76 (2007), p. 017702. arXiv: `0705.3392 [hep-ph]`.

[81] Jose M. No and Michael Ramsey-Musolf. "Probing the Higgs Portal at the LHC Through Resonant di-Higgs Production". In: *Phys. Rev.* D89.9 (2014), p. 095031. arXiv: `1310.6035 [hep-ph]`.

[82] Matthew J. Dolan, Christoph Englert and Michael Spannowsky. "New Physics in LHC Higgs boson pair production". In: *Phys. Rev.* D87.5 (2013), p. 055002. arXiv: `1210.8166 [hep-ph]`.

[83] M. Gillioz et al. "Higgs Low-Energy Theorem (and its corrections) in Composite Models". In: *JHEP* 10 (2012), p. 004. arXiv: `1206.7120 [hep-ph]`.

[84] Lisa Randall and Raman Sundrum. "A Large mass hierarchy from a small extra dimension". In: *Phys. Rev. Lett.* 83 (1999), pp. 3370–3373. arXiv: `hep-ph/9905221 [hep-ph]`.

[85] Maxime Gouzevitch et al. "Scale-invariant resonance tagging in multijet events and new physics in Higgs pair production". In: *JHEP* 07 (2013), p. 148. arXiv: `1303.6636 [hep-ph]`.

[86] Alexandra Oliveira. "Gravity particles from Warped Extra Dimensions, predictions for LHC". In: (2014). arXiv: `1404.0102 [hep-ph]`.

[87] P. M. Ferreira, R. Santos and A. Barroso. "Stability of the tree-level vacuum in two Higgs doublet models against charge or CP spontaneous violation". In: *Phys. Lett.* B603 (2004). [Erratum: Phys. Lett.B629,114(2005)], pp. 219–229. arXiv: `hep-ph/0406231 [hep-ph]`.

[88] I. P. Ivanov. "Minkowski space structure of the Higgs potential in 2HDM". In: *Phys. Rev.* D75 (2007). [Erratum: Phys. Rev.D76,039902(2007)], p. 035001. arXiv: `hep-ph/0609018 [hep-ph]`.

[89] A. Djouadi et al. "The post-Higgs MSSM scenario: Habemus MSSM?" In: *Eur. Phys. J.* C73 (2013), p. 2650. arXiv: `1307.5205 [hep-ph]`.

[90] G. Chalons, A. Djouadi and J. Quevillon. "The neutral Higgs self-couplings in the (h)MSSM". In: *Physics Letters B* 780 (2018), pp. 74–80.

[91] M. Huschle et al. "Measurement of the branching ratio of $\bar{B} \to D^{(*)}\tau^-\bar{\nu}_\tau$ relative to $\bar{B} \to D^{(*)}\ell^-\bar{\nu}_\ell$ decays with hadronic tagging at Belle". In: *Phys. Rev.* D92.7 (2015), p. 072014. arXiv: `1507.03233 [hep-ex]`.

[92] J. P. Lees et al. "Measurement of an Excess of $\bar{B} \to D^{(*)}\tau^-\bar{\nu}_\tau$ Decays and Implications for Charged Higgs Bosons". In: *Phys. Rev.* D88.7 (2013), p. 072012. arXiv: `1303.0571 [hep-ex]`.

[93] Roel Aaij et al. "Measurement of the ratio of branching fractions $\mathcal{B}(\bar{B}^0 \to D^{*+}\tau^-\bar{\nu}_\tau)/\mathcal{B}(\bar{B}^0 \to D^{*+}\mu^-\bar{\nu}_\mu)$". In: *Phys. Rev. Lett.* 115.11 (2015). [Erratum: Phys. Rev. Lett.115,no.15,159901(2015)], p. 111803. arXiv: `1506.08614 [hep-ex]`.

[94] Oliver Sim Bruning et al. *LHC Design Report.* CERN Yellow Reports: Monographs. Geneva: CERN, 2004.

[95] Oliver Sim Bruning et al. *LHC Design Report.* CERN Yellow Reports: Monographs. Geneva: CERN, 2004.

[96] The LHCb Collaboration. "The LHCb Detector at the LHC". In: *Journal of Instrumentation* 3.08 (2008), S08005.

[97] The ALICE Collaboration. "The ALICE experiment at the CERN LHC". In: *Journal of Instrumentation* 3.08 (2008), S08002.

[98] Esma Mobs. "The CERN accelerator complex. Complexe des accélérateurs du CERN". In: (2016). General Photo.

[99] *ATLAS inner detector: Technical Design Report, 1.* Technical Design Report ATLAS. Geneva: CERN, 1997.

[100] S Haywood et al. *ATLAS inner detector: Technical Design Report, 2.* Technical Design Report ATLAS. Geneva: CERN, 1997.

[101] Norbert Wermes and G Hallewel. *ATLAS pixel detector: Technical Design Report.* Technical Design Report ATLAS. Geneva: CERN, 1998.

[102] ATLAS Collaboration. *Track Reconstruction Performance of the ATLAS Inner Detector at $\sqrt{s} = 13$ TeV*. Tech. rep. ATL-PHYS-PUB-2015-018. Geneva: CERN, 2015.

[103] Karolos Potamianos. "The upgraded Pixel detector and the commissioning of the Inner Detector tracking of the ATLAS experiment for Run-2 at the Large Hadron Collider". In: *PoS* EPS-HEP2015 (2015), p. 261. arXiv: `1608.07850 [physics.ins-det]`.

[104] *ATLAS calorimeter performance: Technical Design Report*. Technical Design Report ATLAS. Geneva: CERN, 1996.

[105] Joao Pequenao. "Computer Generated image of the ATLAS calorimeter". 2008.

[106] *ATLAS liquid-argon calorimeter: Technical Design Report*. Technical Design Report ATLAS. Geneva: CERN, 1996.

[107] *ATLAS tile calorimeter: Technical Design Report*. Technical Design Report ATLAS. Geneva: CERN, 1996.

[108] Joao Pequenao. "Computer generated image of the ATLAS Muons subsystem". 2008.

[109] *ATLAS magnet system: Technical Design Report, 1*. Technical Design Report ATLAS. Geneva: CERN, 1997.

[110] *ATLAS central solenoid: Technical Design Report*. Technical Design Report ATLAS. Electronic version not available. Geneva: CERN, 1997.

[111] J P Badiou et al. *ATLAS barrel toroid: Technical Design Report*. Technical Design Report ATLAS. Electronic version not available. Geneva: CERN, 1997.

[112] *ATLAS end-cap toroids: Technical Design Report*. Technical Design Report ATLAS. Electronic version not available. Geneva: CERN, 1997.

[113] Jeremiah Jet Goodson and Robert McCarthy. "Search for Supersymmetry in States with Large Missing Transverse Momentum and Three Leptons including a Z-Boson". Presented 17 Apr 2012.

[114] *ATLAS level-1 trigger: Technical Design Report*. Technical Design Report ATLAS. Geneva: CERN, 1998.

[115] Peter Jenni et al. *ATLAS high-level trigger, data-acquisition and controls: Technical Design Report*. Technical Design Report ATLAS. Geneva: CERN, 2003.

[116] T. Cornelissen et al. "The new ATLAS track reconstruction (NEWT)". In: *J. Phys. Conf. Ser.* 119 (2008), p. 032014.

[117] R. Fruhwirth. "Application of Kalman filtering to track and vertex fitting". In: *Nucl. Instrum. Meth.* A262 (1987), pp. 444–450.

[118] Daniel Wicke. "A New algorithm for solving tracking ambiguities". In: (1999), pp. 219–228.

[119] M. Aaboud et al. "Performance of the ATLAS Track Reconstruction Algorithms in Dense Environments in LHC Run 2". In: *Eur. Phys. J.* C77.10 (2017), p. 673. arXiv: 1704.07983 [hep-ex].

[120] Federico Meloni. "Primary vertex reconstruction with the ATLAS detector". In: *JINST* 11.12 (2016), p. C12060.

[121] "Performance of the ATLAS Inner Detector Track and Vertex Reconstruction in the High Pile-Up LHC Environment". In: (2012).

[122] S. Boutle et al. "Primary vertex reconstruction at the ATLAS experiment". In: *J. Phys. Conf. Ser.* 898.4 (2017), p. 042056.

[123] Morad Aaboud et al. "Reconstruction of primary vertices at the ATLAS experiment in Run 1 proton–proton collisions at the LHC". In: *Eur. Phys. J.* C77.5 (2017), p. 332. arXiv: 1611.10235 [physics.ins-det].

[124] *Vertex Reconstruction Performance of the ATLAS Detector at "$\sqrt{s}$ = 13 TeV"*. Tech. rep. ATL-PHYS-PUB-2015-026. Geneva: CERN, 2015.

[125] Morad Aaboud et al. "Electron efficiency measurements with the ATLAS detector using 2012 LHC proton–proton collision data". In: *Eur. Phys. J.* C77.3 (2017), p. 195. arXiv: 1612.01456 [hep-ex].

[126] Georges Aad et al. "Electron reconstruction and identification efficiency measurements with the ATLAS detector using the 2011 LHC proton-proton collision data". In: *Eur. Phys. J.* C74.7 (2014), p. 2941. arXiv: 1404.2240 [hep-ex].

[127] The ATLAS collaboration. "Electron efficiency measurements with the ATLAS detector using the 2015 LHC proton-proton collision data". In: (2016).

[128] *Electron efficiency measurements with the ATLAS detector using the 2015 LHC proton-proton collision data*. Tech. rep. ATLAS-CONF-2016-024. Geneva: CERN, 2016.

[129] Georges Aad et al. "Measurement of the muon reconstruction performance of the ATLAS detector using 2011 and 2012 LHC proton–proton collision data". In: *Eur. Phys. J.* C74.11 (2014), p. 3130. arXiv: 1407.3935 [hep-ex].

[130] Georges Aad et al. "Muon reconstruction performance of the ATLAS detector in proton–proton collision data at $\sqrt{s}$ =13 TeV". In: *Eur. Phys. J.* C76.5 (2016), p. 292. arXiv: `1603.05598 [hep-ex]`.

[131] John E. Huth et al. "Toward a standardization of jet definitions". In: *1990 DPF Summer Study on High-energy Physics: Research Directions for the Decade (Snowmass 90) Snowmass, Colorado, June 25-July 13, 1990*. 1990, pp. 0134–136.

[132] Matteo Cacciari, Gavin P. Salam and Gregory Soyez. "The Anti-k(t) jet clustering algorithm". In: *JHEP* 04 (2008), p. 063. arXiv: `0802.1189 [hep-ph]`.

[133] Matteo Cacciari and Gavin P. Salam. "Dispelling the N^3 myth for the k_t jet-finder". In: *Phys. Lett.* B641 (2006), pp. 57–61. arXiv: `hep-ph/0512210 [hep-ph]`.

[134] W. Lampl et al. "Calorimeter clustering algorithms: Description and performance". In: (2008).

[135] Georges Aad et al. "Topological cell clustering in the ATLAS calorimeters and its performance in LHC Run 1". In: *Eur. Phys. J.* C77 (2017), p. 490. arXiv: `1603.02934 [hep-ex]`.

[136] *Properties of Jets and Inputs to Jet Reconstruction and Calibration with the ATLAS Detector Using Proton-Proton Collisions at $\sqrt{s} = 13$ TeV*. Tech. rep. ATL-PHYS-PUB-2015-036. Geneva: CERN, 2015.

[137] *Jet Calibration and Systematic Uncertainties for Jets Reconstructed in the ATLAS Detector at $\sqrt{s} = 13$ TeV*. Tech. rep. ATL-PHYS-PUB-2015-015. Geneva: CERN, 2015.

[138] M. Aaboud et al. "Jet energy scale measurements and their systematic uncertainties in proton-proton collisions at $\sqrt{s} = 13$ TeV with the ATLAS detector". In: *Phys. Rev.* D96.7 (2017), p. 072002. arXiv: `1703.09665 [hep-ex]`.

[139] The ATLAS collaboration. "Tagging and suppression of pileup jets". In: (2014).

[140] K G Tomiwa. "Performance of Jet Vertex Tagger in suppression of pileup jets and E_T^{miss} in ATLAS detector". In: *Journal of Physics: Conference Series* 802.1 (2017), p. 012012.

[141] *b-tagging in dense environments*. Tech. rep. ATL-PHYS-PUB-2014-014. Geneva: CERN, 2014.

[142] *Optimisation of the ATLAS b-tagging performance for the 2016 LHC Run*. Tech. rep. ATL-PHYS-PUB-2016-012. Geneva: CERN, 2016.

[143] *Commissioning of the ATLAS high-performance b-tagging algorithms in the 7 TeV collision data.* Tech. rep. ATLAS-CONF-2011-102. Geneva: CERN, 2011.

[144] Giacinto Piacquadio and Christian Weiser. "A new inclusive secondary vertex algorithm for b-jet tagging in ATLAS". In: *J. Phys. Conf. Ser.* 119 (2008), p. 032032.

[145] *Expected performance of the ATLAS b-tagging algorithms in Run-2.* Tech. rep. ATL-PHYS-PUB-2015-022. Geneva: CERN, 2015.

[146] Georges Aad et al. "Performance of *b*-Jet Identification in the ATLAS Experiment". In: *JINST* 11.04 (2016), P04008. arXiv: `1512.01094 [hep-ex]`.

[147] T Barillari et al. *Local Hadronic Calibration.* Tech. rep. ATL-LARG-PUB-2009-001-2. ATL-COM-LARG-2008-006. ATL-LARG-PUB-2009-001. Due to a report-number conflict with another document, the report-number ATL-LARG-PUB-2009-001-2 has been assigned. Geneva: CERN, 2008.

[148] The ATLAS collaboration. "Measurement of the tau lepton reconstruction and identification performance in the ATLAS experiment using *pp* collisions at $\sqrt{s} = 13$ TeV". In: (2017).

[149] Georges Aad et al. "Reconstruction of hadronic decay products of tau leptons with the ATLAS experiment". In: *Eur. Phys. J.* C76.5 (2016), p. 295. arXiv: `1512.05955 [hep-ex]`.

[150] Morad Aaboud et al. "Performance of missing transverse momentum reconstruction with the ATLAS detector using proton-proton collisions at $\sqrt{s} = 13$ TeV". In: (2018). arXiv: `1802.08168 [hep-ex]`.

[151] *Performance of missing transverse momentum reconstruction for the ATLAS detector in the first proton-proton collisions at at $\sqrt{s}= 13$ TeV.* Tech. rep. ATL-PHYS-PUB-2015-027. Geneva: CERN, 2015.

[152] D W Miller, A Schwartzman and D Su. *Pile-up jet energy scale corrections using the jet-vertex fraction method.* Tech. rep. ATL-PHYS-INT-2009-090. Geneva: CERN, 2009.

[153] R.K. Ellis et al. "Higgs decay to +−A possible signature of intermediate mass Higgs bosons at high energy hadron colliders". In: *Nuclear Physics B* 297.2 (1988), pp. 221–243.

[154] G. Aad et al. "Expected Performance of the ATLAS Experiment - Detector, Trigger and Physics". In: (2009). arXiv: `0901.0512 [hep-ex]`.

[155] The CMS Collaboration. "CMS Physics Technical Design Report, Volume II: Physics Performance". In: *Journal of Physics G: Nuclear and Particle Physics* 34.6 (2007), p. 995.

[156] A. Elagin et al. "A New Mass Reconstruction Technique for Resonances Decaying to di-tau". In: *Nucl. Instrum. Meth.* A654 (2011), pp. 481–489. arXiv: `1012.4686` `[hep-ex]`.

[157] *The ATLAS Tau Trigger in Run 2*. Tech. rep. ATLAS-CONF-2017-061. Geneva: CERN, 2017.

[158] Andreas Hocker et al. "TMVA - Toolkit for Multivariate Data Analysis". In: *PoS* ACAT (2007), p. 040. arXiv: `physics/0703039` `[PHYSICS]`.

[159] L. Breiman et al. *Classification and Regression Trees*. Monterey, CA: Wadsworth and Brooks, 1984.

[160] Yoav Freund and Robert E Schapire. "A Decision-Theoretic Generalization of On-Line Learning and an Application to Boosting". In: *Journal of Computer and System Sciences* 55.1 (1997), pp. 119–139.

[161] Jerome H. Friedman. "Stochastic gradient boosting". In: *Computational Statistics Data Analysis* 38.4 (2002). Nonlinear Methods and Data Mining, pp. 367–378.

[162] A L Read. "Presentation of search results: the CL s technique". In: *Journal of Physics G: Nuclear and Particle Physics* 28.10 (2002), p. 2693.

[163] Glen Cowan et al. "Asymptotic formulae for likelihood-based tests of new physics". In: *Eur. Phys. J.* C71 (2011). [Erratum: Eur. Phys. J.C73,2501(2013)], p. 1554. arXiv: `1007.1727` `[physics.data-an]`.

[164] Kyle Cranmer. "Practical Statistics for the LHC". In: *Proceedings, 2011 European School of High-Energy Physics (ESHEP 2011): Cheile Gradistei, Romania, September 7-20, 2011.* [,247(2015)]. 2015, pp. 267–308. arXiv: `1503.07622` `[physics.data-an]`.

[165] Eilam Gross. *Practical Statistics for High Energy Physics.*

[166] Thomas Junk. "Confidence level computation for combining searches with small statistics". In: *Nuclear Instruments and Methods in Physics Research Section A: Accelerators, Spectrometers, Detectors and Associated Equipment* 434.2 (1999), pp. 435–443.

[167] A L Read. "Presentation of search results: the CL s technique". In: *Journal of Physics G: Nuclear and Particle Physics* 28.10 (2002), p. 2693.

[168]   Wouter Verkerke. *Practical Statistics for High Particle Physicists.*

[169]   T. Gleisberg et al. "Event generation with SHERPA 1.1". In: *JHEP* 02 (2009), p. 007. arXiv: `0811.4622 [hep-ph]`.

[170]   Morad Aaboud et al. "Luminosity determination in pp collisions at $\sqrt{s} = 8$ TeV using the ATLAS detector at the LHC". In: *Eur. Phys. J.* C76.12 (2016), p. 653. arXiv: `1608.03953 [hep-ex]`.

[171]   Georges Aad et al. "Measurement of the WW cross section in $\sqrt{s} = 7$ TeV *pp* collisions with ATLAS". In: *Phys. Rev. Lett.* 107 (2011), p. 041802. arXiv: `1104.5225 [hep-ex]`.

[172]   Georges Aad et al. "Measurement of the WW cross section in $\sqrt{s} = 7$ TeV *pp* collisions with the ATLAS detector and limits on anomalous gauge couplings". In: *Phys. Lett.* B712 (2012), pp. 289–308. arXiv: `1203.6232 [hep-ex]`.

[173]   Alessandra Betti. Private Communication. 1st June 2018.

[174]   Agni Bethani et al. *Searches for resonant and non-resonant di-Higgs production in the bb-tautau decay channel in pp collisions at sqrt(s)=13 TeV with the ATLAS detector.* Tech. rep. ATL-COM-PHYS-2017-007. Geneva: CERN, 2017.

[175]   Tanumoy Mandal, Subhadip Mitra and Satyajit Seth. "Pair Production of Scalar Leptoquarks at the LHC to NLO Parton Shower Accuracy". In: *Phys. Rev.* D93.3 (2016), p. 035018. arXiv: `1506.07369 [hep-ph]`.

[176]   J. Alwall et al. "The automated computation of tree-level and next-to-leading order differential cross sections, and their matching to parton shower simulations". In: *Journal of High Energy Physics* 2014.7 (2014), p. 79.

[177]   Mikael Martensson. Private Communication. 1st June 2018.

[178]   Emily Graham. Private Communication. 1st June 2018.

[179]   *Combination of searches for Higgs boson pair production in proton-proton collisions at $\sqrt{s} = 13$ TeV.* Tech. rep. CMS-PAS-HIG-17-030. Geneva: CERN, 2018.